Homogenization method for topology optimization of a coupled thermal fluid-structures built with composite materials

Godfred Oheneba Agyekum

Université Paris Cité

École doctorale de Sciences Mathématiques de Paris Centre, n° 386
Laboratoire Jacques-Louis Lions

Homogenization method for topology optimization of a coupled thermal fluid-structures built with composite materials

Par Godfred Oheneba Agyekum

Thèse de doctorat de spécialité Mathématiques appliquées

Dirigée par François Jouve
Et Laurent Cangémi

Présentée et soutenue publiquement le 25 octobre 2022

Devant un jury composé de :

Pierre Duysinx,	Professeur, Université de Liège	Rapporteur
Yann Monerie,	Professeur, Université de Montpellier	Rapporteur
Grégoire Allaire,	Professeur, École Polytechnique	Examinateur
Laurent Cangémi,	Ingénieur de recherche, IFPen	Co-encadrant de thèse
Anita Catapano,	Maître de conférences, Bordeaux INP	Examinatrice
François Jouve,	Professeur, Université Paris Cité	Directeur de Thèse
Joseph Morlier,	Professeur, ISAE-SUPAERO	Examinateur
Delphine Sinoquet,	Ingénieur de recherche, IFPen	Invitée

Table des matières

Table des figures

Liste des tableaux

Abstract

This work is devoted to shape and topology optimization of multi-scale and multi-physics systems, motivated by the development of advanced technologies in the energy industry. Evaluation of the load sensitivities of arbitrary objective functionals are computed for a weakly coupled thermal fluid-structure systems. A novel homogenization-based gradient-type algorithm is employed for solving generic constrained topology optimization problems without the need for explicit boundary description or tracking. Motivated by the need for enforcing non-mixing constraints in the design of liquid-liquid heat exchangers, Biot-Darcy's model is employed to provide a continuous and consistent treatment of design-dependent fluid-pressure loads ; its provides a computationally inexpensive evaluation of load sensitivities using the adjoint method. All these ingredients allowed us to implement a variety of 2-d and 3-d multiphysics topology optimization test cases : from single, double or three physics problems in 2-d, to moderately large-scale 3-d test cases for structural design, fluid-structure loaded design and thermal fluid-structure interacting systems. This approach could allow in future works to develop new workflow for the design of thermal fluid-elastic systems characterized by multi-scale patterns such as industrial heat exchangers.

Keywords— Topology optimization, multi-scale, relaxed formulation, theory of homogenization, porous medium, adjoint methods, fluid-structure interaction, convective heat transfer.

Résumé

Cette thèse est consacrée à l'optimisation topologique de forme et de la topologie de systèmes multi-échelles et multi-physiques, motivés par le développement de nouvelles technologies dans le domaine de l'énergie. Nous calculons les dérivéees de forme de fonctions coût arbitraires pour un modèle fluide, thermique et mécanique faiblement couplé. Nous introduisons un nouvel algorithme de type gradient adapté à la résolution de problèmes d'optimisation de formes composites sous contraintes qui ne requiert pas une description explicite de la frontière. Nous introduisons ensuite un modèle de type Biot-Darcy pour assurer un traitement continu et cohérent de formes sous chargement hydro-thermo dynamiques : cette technique nous a ainsi permis d'imposer une contrainte de non-mélange de phases et fournit une évaluation peu coûteuse en calcul des sensibilités à l'aide de la méthode adjointe, pour une application à l'optimisation d'échangeurs de chaleur. Tous ces ingrédients ont été employés pour traiter une variété de cas tests d'optimisation de formes pour des systèmes multi-échelles et multi-physiques 2-d et 3-d. Nous avons considéré des problèmes à une seule, deux ou bien trois physiques couplées en 2-d, et des problèmes de tailles relativement élevées en 3-d pour la mécanique, de la forme de systèmes en interaction thermo poro-méchanique. Cette approche pourrait permettre, dans des travaux futurs, de développer l'optimisation de profil d'échangeurs thermiques pour le stockage d'énergie.

Mots-clés— Optimisation topologique, multi-échelles, milieux poreux, milieux périodiques, homogénéisation, méthode adjointe, fluide-structure, conduction thermique

Introduction-Résumé de la thèse

Cette thèse est consacrée à l'optimisation topologique de forme et de la topologie de systèmes multi-physiques et multi-échelles, motivés par des applications technologiques avancées dans l'industrie de l'énergie. En raison de nombreuses contraintes industrielles qui sont détaillées ci-après, nous employons d'emblée la méthode d'homogénéisation qui est particulièrement adaptée à l'optimisation topologique de matériaux architecturés présentant une microstructure composite (périodique ou non) et permettant d'optimiser le comportement poro-diffuso-mécanique des structures de type échangeurs thermiques ou réacteurs électrochimiques.

L'optimisation de forme est l'art mathématique de générer des formes "optimales" qui répondent le mieux à un objectif proposé. Dans le contexte industriel, il s'agit de concevoir des systèmes physiques qui atteignent des performances optimales, comme par exemple : quelle est la forme de la structure la plus rigide utilisant une quantité donnée de matière, ou quel profil d'échangeur choisir pour optimiser les échanges de chaleur ou de masse entre un objet solide résistant mécaniquement et une phase fluide, ou quelle distribution de fluides permet de réaliser le meilleur transfert de chaleur, ou quel profil aérodynamique choisir pour générer une force de portance voulue ? Ces questions sont des problèmes industriels très classiques souvent rencontrées dans de nombreuses technologies de pointe telles que l'aérospatiale, l'aéronautique, l'automobile, la micro-mécanique, le génie civil, ou l'industrie de l'énergie.

0.1 De l'Optimisation de formes à la topologie

L'optimisation de formes suscite depuis longtemeps un vif intérêt, l'impressionnante littérature qui traite de ce sujet peut en témoigner. L'établissement de ses bases théoriques remonte aux débuts des années 1900 avec les travaux de Michell en 1904 [1] et Hadamard in 1905 [2]. De nombreux travaux ont conduit au développement de la méthode comme les travaux de O. Pironneau [3], J Céa [4], D. Chénais [5], J. Sokolowski et J.P. Zolésio [6], Murat-Tartar [7, 8], M.P. Bendsøe [9] ou Cherkaev-Kohn [10], pour n'en nommer que quelques-uns ainsi que les références que ces articles ou livres contiennent. Ci-dessous, nous passons en revue un bref historique des méthodes d'optimisation et la plupart ont entre-temps atteint un état de maturité. Leur popularité en tant qu'outils de conception pour trouver des solutions de matériaux fonctionnels couplant plusieurs physiques ne cesse de croître.

L'optimisation de formes peut se diviser en deux grandes familles : la méthode de variations de frontière (ou sizing) et l'optimisation de formes topologique (ou layout optimization). La méthode de variations de frontière est basée au préalable sur des courbes ou surfaces, utilisées pour interpoler l'ensemble des frontières de formes admissibles (ou compatibles) d'une structure initiale donnée, explicitement capturée par un maillage avec une topologie fixée. En faisant varier les frontières de formes compatibles, on peut rechercher une meilleure solution parmi l'ensemble de toutes les solutions obtenues par transformation homéomorphe de la structure initiale. Initiée par Hadamard

en 1905 [2], la méthode consiste à déplacer la frontière le long de la normale et à en calculer la variation induite sur la fonctionnelle : voir Figure 1, pour un example de variation de frontière. La variation des frontières est définie par rapport à ses courbes ou surfaces lisses, dont nous modifions ses paramètres afin d'atteindre des performances optimales par rapport à un objectif (ou à une fonction coût) donné(e). Cependant, la définition préalable de la structure comme sa topologie, est choisie et figée durant tout le processus d'optimisation et par conséquent, un domaine ne peut être comparé qu'avec un domaine de connectivité semblable : il est difficile d'y créer un trou ou d'ajouter une partie à l'extérieur de ses frontières (en fait c'est même impossible en général, sauf pour la méthode "*bubble*" [11]). La difficulté, c'est qu'il n'existe aucune transformation entre des domaines de topologies distinctes, à savoir, avec des trous en nombre et connections distinctes. Une simple transformation isomorphe du domaine est inapte à générer des topologies différentes (voir la discussion de Chénais D. dans [12]). La difficulté principale, c'est que la méthode de variation des frontières est mal equipée pour capturer la complexité topologique possible de la forme car elle impose des conditions de régularité sur la frontière à optimiser qui ne sont pas toujours vérifiées.

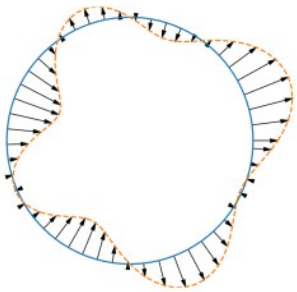

Figure 1 – La méthode de variation de frontière de Hadamard (Figure tirée de [13]). En bleue, la frontière de la structure initiale et en pointillé orange, la variation de la frontière le long de la normale : il s'agit d'évaluer la sensibilité du problème d'optimisation par rapport à de petites déformations de la forme.

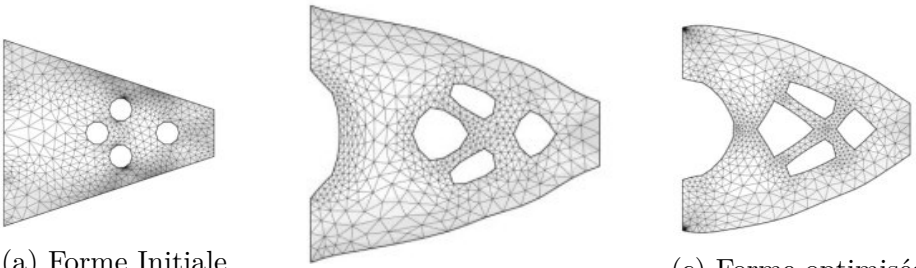

(a) Forme Initiale (b) Forme intermédiare (c) Forme optimisée

Figure 2 – La méthode de variation de frontière de Hadamard basée sur la déformation du maillage (figure tirée de [13]). L'optimisation de la forme d'une console 2-d en flexion. Les changements topologiques sont difficiles à traiter numériquement : les formes initiales et finales ont le même nombre de trous.

Il est bien connu que créer des trous (ou modifier la topologie) peut considérablement améliorer les performances d'une solution optimale trouvée. La variation des frontières fournit une solution optimale qui n'est que le meilleur optimum pour un nombre fixe de trous : une solution sous-optimale, voir Figure 2. L'optimisation topologique permet de modifier plus fondamentalement la nature de la structure. Il n'y a aucune hypothèse sur la définition préalable des paramètres. Ainsi, les caractéristiques de la structure, telles que sa topologie, sont arbitrairement choisies et libres tout au long du processus d'optimisation et donc, un domaine peut être comparé à un domaine de connectivité différente : des trous de n'importe quelle forme et de n'importe quelle taille dans le domaine. Cette méthode a été discutée par F. Murat et L. Tartar dans [7, 8], et [14], popularisé par les travaux de M.P. Bendsøe et N. Kikuchi [15], qui ont été les premiers à traiter numériquement un problème réel (ou physique) en utilisant cette approche dans la conception de structures. Formuler le problème de conception en termes de répartition optimale du matériau disponible est une autre possibilité, qui est satisfaisante car aucune hypothèse n'est requise sur la solution. L'établissement de la théorie mathématique générale des problèmes de domaine variable a donné lieu à plusieurs travaux, dont les plus importantes et les plus connus sont ceux proposés par F. Murat et L. Tartar [7, 8], et ceux de Kohn et Strang [16] et Lurie et CherKaev [17]. Historiquement, le premier travail important lié aux méthodes d'optimisation topologique dans un contexte modèle est la méthode des treillis introduite par Michell dans [1] en 1904 (voir Prager et Rozvany, [18]). Brièvement, cette méthode consiste à construire des structures à partir de barres assemblées en treillis. Chaque barre pouvant soutenir un champ de contraintes tendu ou compressé. La structure optimale est solution d'un problème de minimisation de poids lorsque le champ de contraintes varie dans l'ensemble des champs statiquement admissibles. Cette méthode a l'avantage de construire des solutions explicites pour des problèmes d'optimisation de formes simplifiés et sert donc de référence et de comparaison : voir Figure 3 et Figure 4. Tartar et Murat ont été les premiers à introduire la théorie de l'homogénéisation pour évaluer les propriétés de la microstructure poreuse. Pour déterminer la topologie d'une structure, ils commencent par rechercher la fonction caractéristique du sous-domaine occupé par la matière : un problème "0-1", à savoir, matériel ou vide, mais ce problème est mal posé car l'existence et l'unicité de la solution ne sont pas obtenues en général. Le lecteur est renvoyé aux contre-exemples typiques présentés dans [19], pour modéliser des problèmes de contrôle par les coefficients d'une fonction objective, dépendant de la solution d'une équation aux dérivées partielles linéaire. Leur idée est alors de relaxer le problème en utilisant les méthodes d'homogénéisation. Cela revient physiquement à perforer certaines parties du domaine par un grand nombre de petits trous de géométrie appropriée, à savoir, permettre des mélanges fait du vide et de matériau à une échelle beaucoup plus petite que le maillage utilisé pour le calcul réel. Ce processus d'élargissement de l'espace de solutions statiquement admissibles, afin d'obtenir un problème bien posé, est ce que nous appelons la relaxation : elle permet d'introduire un cadre mathématique plus général pour trouver la solution, d'assurer son existence et de la calculer grâce à un procédé numérique. Kohn et Strang ont montré que pour ces problèmes, la relaxation revenait à calculer la quasi-convexification de certaines fonctionnelles. Dans tous les cas, il s'agit de reformuler le problème de façon à ce qu'il soit bien posé sans changer sa nature physique. Ces deux méthodes, l'une introduite par Murat-Tartar,

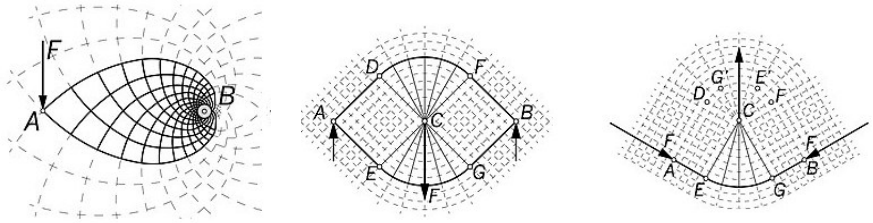

(a) (b) (c)

Figure 3 – La méthode des treillis de Michell (figure extraite de wiki/Michell_structures). (a) Une seule force F appliquée à A, et agissant perpendiculairement à la droite (AB), (b) Une seule force F appliquée à C centré entre les supports aux points A et B (une solution globale), (c) Poutre à charge centrale avec une force éloignée de la ligne droite entre les supports, construction similaire à (b).

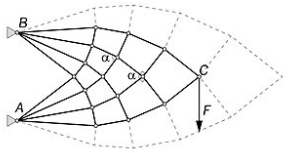

Figure 4 – Treillis Michell discrets ou treillis Prager (figure extraite de wiki/Michell). Méthode du cercle des déplacements relatifs pour arriver à la topologie optimale de telles treillis (typiquement des consoles en flexion).

l'autre par Kohn et Strang, sont liées et complémentaires. Elles constituent les outils de base nécessaires à la résolution des problèmes d'optimisation de forme topologique.

D'un point de vue numérique, l'optimisation topologique des structures élastiques débute avec les travaux de M.P. Bendsøe et N. Kikuchi [15]. La méthode qu'ils proposent pour résoudre le problème de conception, et qui est connue sous le nom de méthode d'homogénéisation, se fonde sur les idées de distribution optimale de matière et sur l'introduction d'une microstructure poreuse (voir Figure 5) dont ils déterminent les propriétés macroscopiques en fonction de la densité grâce à la théorie de l'homogénéisation des microstructures périodiques. Dans [15], Bendsøe et Kikuchi introduisent une microstructure périodique dont la porosité (qui varie) provient d'une perforation rectangulaire au sein de la cellule de base, à savoir, sa longueur m_1 et sa largeur m_2 pour chacun des éléments finis (voir Figure 6). Ainsi, les variables de conception du problème numérique sont les paramètres de longueur m_1 et de largeur m_2 de la perforation de la cellule de base au sein de chaque élément fini. Comme le matériau macroscopique est orthotrope, l'orientation de la microstructure locale joue un rôle fondamental et l'angle d'orthotropie est également une variable de conception du problème. Par conséquent, ce problème d'optimisation numérique est de très grande taille puisqu'il est composé de trois variables de conception pour chaque élément fini. Pour aborder un si grand

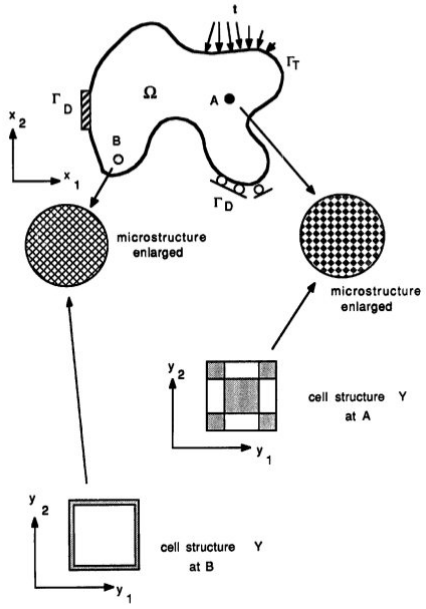

FIGURE 5 – Une structure avec une microstructure composite (figure extraite de [15]).

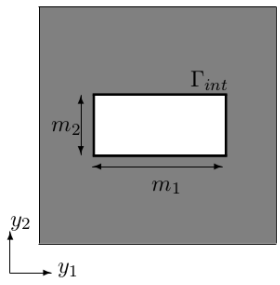

FIGURE 6 – Cellule périodique orthotrope (figure tirée de [20]).

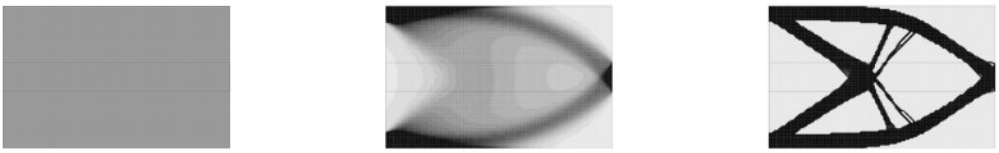

(a) (b) (c)

Figure 7 – Optimisation topologique d'une console en 2-d par une méthode d'homogénéisation (figure obtenu à partir du code source décrit dans [29]). (a) Domaine initial, (b) Densité optimale du matériau composite, séquentiellement laminés de rang 2, (c) Densité penalisée : microstructures suboptimales après pénalisation de la solution (b).

problème, M.P Bendsøe et N. Kikuchi adoptent une formulation très simple qui est de minimiser la compliance (ou l'énergie potentielle) des forces appliquées à une structure, soumise à une contrainte de volume de matière limitée et dans un cadre 2-d, à savoir, seules les structures planes sont étudiées. Etant donnée la formulation simple du problème qui ne comprend qu'une seule contrainte, l'optimisation des variables de conception est réalisée avec une technique de critère d'optimalité. Pour l'angle d'orthotropie, ce critère est basé sur une procédure de type bissection-Newton et s'avère peu efficace. Les résultats numériques de cette première étude ne présentent pas une silhouette claire de la structure optimale. Pour de meilleurs résultats, le schéma de mise à jour de l'angle orthotropie est révisé par Bendsøe [21] et par Suzuki et Kikuchi [22, 23]. Ils remarquent grâce à une étude de Pedersen [24], que l'angle d'orthotropie doit être aligné sur les directions principales de contraintes. La preuve de ce critère d'optimalité n'a été apportée que plus tard par les études théoriques d'Allaire et Kohn [25] et par Gibianski et Cherkaev [26]. D'autres contributions ont été apportées, voir [21, 22, 23]. Le choix de la microstructure poreuse a fait l'objet de nombreux débats. L'utilisation des laminés de rang fini dont Avellaneda [27], Kohn [28] et Allaire-Kohn [25], ont montrés l'optimalité pour la compliance minimale, à savoir, les laminés de rang deux en deux dimensions, a donné lieu à une relaxation complète du problème d'optimisation en mécanique des structures, où la solution optimale est assurée et explicitement déterminée. Finalement, la méthode a été étendue à des structures 3-d (Allaire, Bonnetier, Francfort et Jouve [29], Suzuki et Kikuchi [30]). Cependant, la microstructure optimale théorique est difficilement utilisable dans la pratique car elle est largement remplie de matériau composite de densité $\theta \in [0, 1]$ continue comprise entre le solide et le vide. Ces microstructures ne sont ni directement manufacturables ni faciles à interpréter. Ainsi, pour améliorer la séparation entre les régions occupées par le vide et le solide et pour donner lieu à des solutions utilisables dans la pratique, on préfère recourir à des microstructures suboptimales. Elles peuvent être obtenues de plusieurs manières similaires par exemple en pénalisant directement la densité optimale en la forçant à ne prendre que les valeurs 0 ou 1 [25, 29] (voir Figure 7) ou par une projection de la microstructure optimale à une échelle de longueur souhaitée, qui est une question délicate, bien que peu coûteuse en termes de calcul [31] (voir Figure 8).

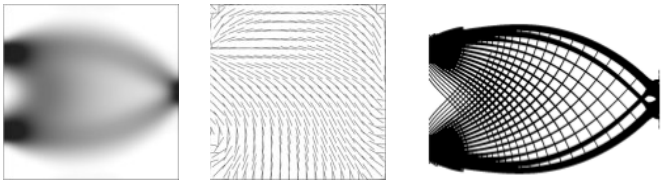

(a) (b) (c)

FIGURE 8 – Optimisation topologique d'une console 2-d en flexion par une méthode d'homogénéisation (figure extraite [20]). (a) Densité optimale du matériau composite de microstructures orthotropes (b) Orientation optimale (c) Forme interprétée

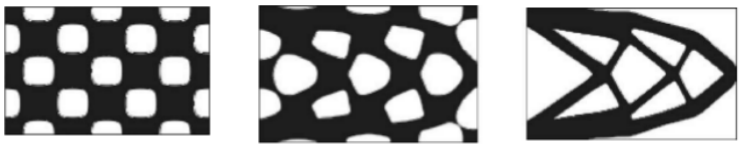

(a) (b) (c)

FIGURE 9 – La méthode de variation de frontières de Hadamard utilisant la méthode des lignes de niveaux pour l'optimisation de la forme d'une console 2-d en flexion (figure extraite de [39]) : (a) Design initial, (b) Design intermédiaire, (c) Design optimisé. Les changements topologiques sont possibles : certains trous ont fusionné entre l'initialisation et la forme finale.

L'optimisation topologique est une discipline très large qui comprend de nombreuses autres méthodes mathématiques et numériques, telles que la méthode du gradient topologique [11, 32], les méthodes par lignes de niveaux qui ne sont pas spécifiquement basées sur la méthode de Hadamard [33, 34, 35], les méthodes de changement de phase [36], les méthodes d'optimisation topologique dites "évolutionnaires" [37], et enfin les méthodes par densité [38] et par homogénéisation [29, 39]. Par exemple, dans les méthodes par lignes de niveaux, la forme à optimiser n'est pas explicitement discrétisée ou capturée par un maillage (comme c'est le cas dans la méthode de variation de frontières), mais plutôt implicitement décrite comme l'ensemble de valeurs négatives d'une fonction "lignes de niveaux", à savoir, une ligne de niveau et qui évolue sur un maillage fixe. Cela permet de gérer les changements topologiques complexes de la forme optimisée telles que la fusion des trous ou l'effondrement des frontières (voir Figure 9). Cette capacité à gérer les changements topologiques est très souhaitée afin de générer des conceptions optimales, sans aucun a priori sur la forme finale, comme le nombre ou l'emplacement des trous (ou trous et des arches en 3-d). Pour cette raison, les algorithmes basées sur la méthode des lignes de niveaux sont souvent considérés comme des techniques d'optimisation topologique, tandis que ceux basés sur la déformation d'un maillage de la forme est traditionnellement appelée optimisation géométrique. En outre, un autre schéma d'intérêt sont les méthodes par densité (voir Figure 10).

(a) (b) (c)

Figure 10 – Optimisation topologique d'une console 2-d en flexion par une méthode de densité, i.e., la méthode SIMP (Simplified Isotropic Material Penalization) : (a) Design initial, (b) Design intermédiaire, (c) Design optimisé. Figure extraite de [13].

0.2 Quelques défis actuels de l'optimisation topologique pour l'industrie de l'énergie

Habituellement, les concepteurs procèdent par essais-erreurs sucessifs en testant des prototypes dont le design relève du savoir faire et de l'intuition de l'ingénieur. Malheureusement, le workflow utilisé est "manuel", souvent très coûteux et imprécis. Avec l'avènement des ordinateurs permettant de simuler numériquement, les ingénieurs conçoivent les systèmes industriels à l'aide de logiciels de Conception Assistée par Ordinateur (CAO), lesquels permettent d'analyser de nombreuses possibilités sans avoir à fabriquer de prototypes, ce qui automatise la recherche de la forme optimale. Ainsi, les industries sont souvent dépendantes de formats CAO du fait de leur compatibilité avec toutes les étapes de conception, de la simulation numérique des processus physiques par des codes industriels, à la fabrication effective par des machines automatisées. Cependant, les méthodes de CAO reposent fortement sur le choix du paramétrage de la géométrie de la forme et donnent généralement de très petites évolutions de la géométrie initialement proposée. Ceci est acceptable pour des innovations incrémentales dans la mesure où ces petites modifications peuvent apporter des gains substantiels de performances. Mais, on imagine facilement que des performances encore meilleures pourraient être obtenues grâce à l'optimisation topologique puisqu'elle pourrait permettre de rechercher de nouvelles conceptions très innovantes parmi des ensembles de formes beaucoup plus libres.

De plus, l'essor de la fabrication additive depuis les années 1990 a permis à l'industrie d'être capable de fabriquer des designs de plus en plus complexes à peine décrit par les logiciels CAO, qui nourrit aujourd'hui un enthousiasme renouvelé pour l'optimisation topologique. De nombreuses technologies de pointe telles que les échangeurs de chaleur pour le stockage de l'énergie, les systèmes de refroidissement pour les nouvelles générations de moteurs (ex., moteurs électriques, microturbines, etc.) ou certaines technologies de batterie (ex., les batteries à flux du type redox) reçoivent actuellement beaucoup d'attention et d'efforts émanant de l'industrie de l'énergie et constituent des motivations à long terme à l'origine de ce travail.

Désormais, l'un des principaux défis à relever pour rendre l'optimisation topologique applicable dans un grand nombre d'applications technologiques est la nécessité d'aborder les aspects multiphysiques inhérents, à savoir, des systèmes fluides présen-

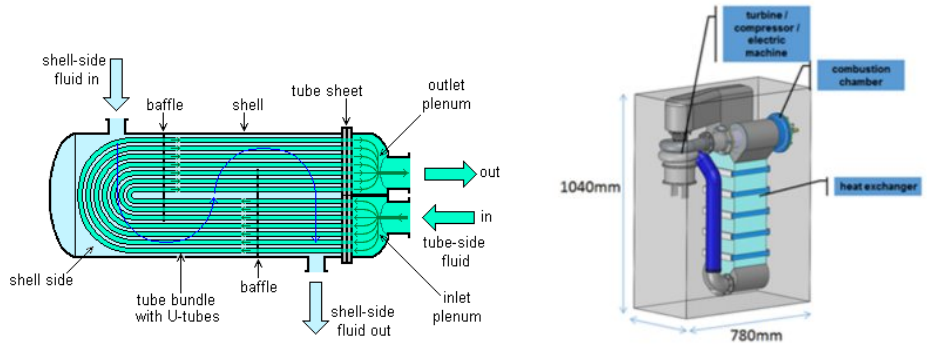

(a) (b)

FIGURE 11 – (a) Echangeur de chaleur (en U), (b) Echangeur de chaleur intégré dans une turbine/compresseur

tant des propriétés hydrauliques, thermiques et mécaniques couplées, i.e., (*i*) identifier la frontière de la forme pour appliquer de telles charges, (*ii*) déterminer la relation entre les charges fluide-thermiques et les variables de conception, i.e., définissant un champ de pression et de température, dépendant de la conception, (*iii*) evaluer de façon efficace la sensibilité des charges hydrauliques et thermiques couplées, lesquelles doivent très souvent être pris en compte simultanément lors de la conception, comme par exemple, pour les composants de nouvelle génération de moteurs.

Parmi ces nouvelles technologies, un problème très représentatif qui attire actuellement une attention considérable dans la communauté de l'optimisation topologique réside dans la conception des échangeurs de chaleur [40, 41, 42, 43, 44, 45], i.e., des dispositifs utilisés dans les moteurs pour refroidir des fluides chauds en les transportant à proximité de certains gaz ou liquides réfrigérants ou de stocker de l'énergie par AACAES (Advanced Adiabatic-Compressed Air Energy Storage), pour diverses applications telles que les moteurs à combustion, la climatisation, la production d'énergie, ou les microturbines. Les échangeurs de chaleur industriels comprennent généralement de nombreux tubes et ailettes façonnés afin de maximiser la surface d'échange entre la phase chaude et froide (voir Figure 11.(a)). Naturellement, diverses contraintes de conception multiphysiques supplémentaires entrent en jeu, telles que la nécessité de contrôler la perte de charge induite par le système sur le fluide d'entrée, ou la résistance mécanique de l'ensemble de la structure sous chargements de pression et de température élevés. Notons que la topologie et les performances des structures optimisées sont directement liées à l'amplitude, à l'emplacement et à la direction des chargements en pression et température, lesquels varient avec la conception. On soupçonne que de nombreux autres composants des moteurs à combustion pourraient également bénéficier d'une optimisation de leur forme et de leur topologie, comme le système de refroidissement interne d'une turbine ou d'un compresseur (voir Figure 11.(b)).

0.3 Cadre de la thèse

À ce jour, la méthode d'homogénéisation utilisée comme optimisation topologique n'est pas encore totalement mature pour de véritables applications industrielles. La plupart des cas-tests présentés dans la littérature concernent plutôt exclusivement l'élasticité linéaire [25, 29, 31, 46], l'écoulement fluide [47], avec très peu de cas-tests 3-d à grande échelle [20, 29]. Ce n'est que récemment que la méthode est appliquée à des physiques plus compliquées telles que l'électrochimie [48]. Cette tendance est également visible dans la communauté d'optimisation topologique par les méthodes de densité, qui présente également un nombre croissant de travaux sur des applications multidisciplinaires [49, 50, 51, 52, 53, 54].

Ici, notre objectif est de mettre en place des outils de modélisation et des méthodologies pour l'optimisation topologique des systèmes multi-échelles et multiphysiques afin de générer des matériaux architecturés, en gardant à l'esprit les exigences industrielles à plus long terme. Par «exigences industrielles», on entend plusieurs technologies de pointe identifiées dans l'industrie de l'énergie qui ont guidé nos recherches et qui sont décrites dans les cinq paragraphes suivants.

Systèmes multiphysiques

Comme mentionné ci-dessus, motivé par les applications industrielles, il existe une demande croissante d'optimisation topologique des systèmes impliquant plusieurs physiques en interaction. Notre étude portera sur les systèmes présentant des propriétés fluides, thermiques et mécaniques couplées. Mathématiquement, ceux-ci sont caractérisés par un ensemble de variables physiques notées comme suit dans tout le manuscrit :

- p pour le champ de pression associé à la phase fluide traversant le système,
- T pour le champ de température dans la phase solide et fluide,
- u pour le champ de déplacement homogénéisé élastique des structures mécaniques solides mise en jeu dans le système.

Ces variables sont déterminées mathématiquement comme les solutions d'un ensemble d'équations aux dérivées partielles (EDPs), qui sont elles-mêmes issues de choix de la modélisation physique. Un cadre académique pour la caractérisation de, p, T et u, suffisamment représentatif pour nos applications, est décrit dans le chapitre 4.

En termes d'applications, une partie importante de notre travail est de remplacer la conception "monolithique" des échangeurs de chaleur ou transfert de masse entre une structure solide et un milieu fluide par des microstructures générant des matériaux poreux localement périodiques, à savoir, des matériaux architecturés (ou fonctionnels). Une étude 2-d, d'optimisation composite de structures chargées en fluide (ou pression), suivant une loi d'écoulement de type Biot-Darcy est proposée au chapitre 3, où nous optimisons la forme et la topologie de divers problèmes de conception et notamment celui d'un problème de transfert de masse.

Optimisation sous contraintes

La plupart des systèmes industriels présentent une variété de cahiers des charges qui doivent être satisfait dans des conditions d'utilisation réelles. Par exemple, la contrainte mécanique globale où la température d'une structure solide peuvent être amenées à rester en dessous d'une certaine limite afin d'éviter une fatigue ou une rupture prématurées. En d'autres termes, un problème d'optimisation se réduit à déterminer la forme d'un système qui réalise les meilleures performances, soumis à un ensemble de contraintes physiques. De tels problèmes sont modélisés de manière générique par des programmes mathématiques de la forme :

$$\begin{aligned} &\min_{\theta} J^*(\theta, p(\theta), T(\theta), u(\theta)) \\ s.t &\begin{cases} g_i(\theta, p(\theta), T(\theta), u(\theta)) = 0 \quad 1 \leq i \leq m, \\ h_j(\theta, , p(\theta), T(\theta), u(\theta)) \leq 0 \quad 1 \leq j \leq n, \end{cases} \end{aligned} \tag{1}$$

où θ désigne la densité de matériau à optimiser, typiquement la proportion de phase solide dans le mélange fabriqué avec uniquement du matériau solide et du vide en proportions θ et $1-\theta$, à une échelle beaucoup plus petite que le maillage utilisé pour le calcul numérique (par ex., la densité des microstructures générant des matériaux poreux localement périodiques). J^* fait référence à la fonction objective (qui est relaxée), quantifiant les performances du système et que l'on cherche à minimiser. Les fonctions objectives classiques couramment rencontrées en optimisation de forme incluent la compliance du système mécanique, le déplacement u tel que u soit aussi proche que possible d'un déplacement cible u_0 donné, ou la chaleur emmagasinée dans un système thermique. Les fonctions g_i et h_j modélisent des contraintes d'égalité et d'inégalité : elles renvoient à des valeurs cibles que certaines quantités physiques doivent atteindre (par ex., fraction volumique du solide) ou bien ne doivent pas dépasser (par ex., une limite imposée sur la température du système). La fonction objectif J^* et les contraintes g_i , h_j dépendent de la variable de conception θ et des variables physiques $p(\theta)$, $T(\theta)$ et $u(\theta)$, qui dépendent eux-mêmes de θ.

La variable de conception θ appartient à un espace fonctionnel $L^\infty(\Omega; [0,1])$, qui appartient à un espace euclidien $\mathbb{R}^N$ après discrétisation, ce qui permet de résoudre des programmes mathématiques de type (2) contraintes par des méthodes très classiques d'optimisation du premier ordre [29, 55, 56, 57]. La plupart des travaux disponibles utilisant la méthode d'homogénéisation convertissent (2) en un problème de minimisation sans contrainte en ajoutant des termes de pénalisation à la fonction objectif J^*, par exemple, une technique couramment employée à cet égard est la méthode du Lagrangien augmenté [20, 29, 49]. Des méthodes, telles que les méthodes de densité ou de lignes de niveaux ont été utilisées avec succès dans un grand nombre de travaux [45, 47, 49, 50]. Dans le chapitre 2, un nouvel algorithme de type gradient est décrit pour la résolution de problèmes d'optimisation topologique composite sous contraintes par la méthode d'homogénéisation.

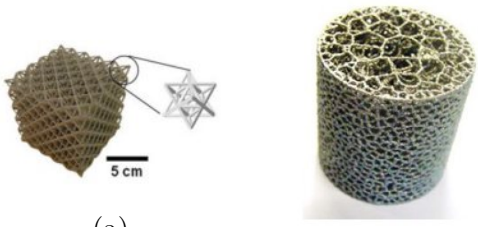

(a) (b)

Figure 12 – (a) Exemple de matériau architecturé à microstructure fixe et (b) à microstructure variable.

Non-intrusifs

Pour les applications industrielles à long terme, une motivation importante dans notre travail est de fournir des contributions à certains sujets de base qui ont été discutés pendant plusieurs années. En effet, à travers le concept d'optimisation topologique, nous visons à : (*i*) apporter une contribution à la compréhension et à la modélisation des mécanismes physiques sous-jacents au comportement poro-diffuso mécanique, dans les procédés et outils de production d'énergie, tels que les échangeurs de chaleur, les systèmes de refroidissement ou certaines technologies de batteries, (*ii*) déployer une analyse multi-physique et multi-échelle de ces comportements, et (*iii*) développer des outils, des méthodologies et des technologies de dimensionnement autour de la production et de l'utilisation de l'énergie. En particulier, ce travail s'inscrit en ligne directe avec le développement de produits technologiques, impliquant des problématiques de mécanique et de transfert, comme les échanges de chaleur ou les échanges de masse. De façon générale, en lien direct avec la thèse, nous souhaitons développer des méthodes d'optimisation d'échangeurs grâce au concept de matériau architecturé, dont la fabrication est rendue aujourd'hui relativement accessible par l'explosion des technologies de fabrication additive.

Problématique

L'objectif de ce travail est de mettre en place les bases d'une approche d'optimisation topologique de matériaux architecturés présentant une microstructure composite (périodique ou non) (voir Figure 12) et permettant d'optimiser le comportement poro-diffuso-mécanique des structures de type échangeurs thermiques ou réacteurs électrochimiques. Il s'agit de chercher une microstructure idéale permettant d'optimiser les échanges et le flux thermique de la pièce ainsi que son comportement mécanique, lorsque que cette dernière est soumise à des variations de pression et de température associées à son cycle de fonctionnement.

D'un point de vue global, la problématique scientifique est double. Le premier enjeu est de pouvoir caractériser le comportement poro-diffuso-mécanique de ce type de matériau à l'échelle macroscopique sous forme de lois «homogénéisées», à partir des

caractéristiques locales du matériau et du fluide considéré. Le second consiste à mettre en place une procédure d'optimisation topologique adéquate pour la recherche de la microstructure, permettant de répondre au mieux à des objectifs de fonctionnalité définis par la problématique technologique. En l'occurrence, dans le cadre de la recherche de solutions technologiques innovantes d'échangeurs permettant de fusionner une fonction structurale à une fonction de transfert de masse ou de transfert thermique, il s'agira de minimiser les déformations de la pièce tout en augmentant ses capacités d'échange entre le fluide et le solide. D'autres objectifs peuvent être ajoutés comme la minimisation de la contrainte locale en fonction d'un critère de contrainte admissible par le matériau constitutif. D'un point de vue méthodologique, on utilise une approche simplifiée pour chaque physique :

- pour la mécanique des solides ou des fluides qui implique des notions cinématiques de conservation du mouvement,
- pour le transfert de température ou de masse.

Il s'agit de poser les bases d'une approche globale d'optimisation topologique multiphysique qui pourra ensuite être améliorée et perfectionnée en fonction des besoins spécifiques à chaque technologie (batteries ou échangeurs thermiques).

0.4 Résumé par chapitre

Chapitre 1 : Homogénéisation

Ce chapitre préliminaire introduit brièvement la théorie de l'homogénéisation dans le cas de l'élasticité linéaire. Le cadre mathématique de la théorie de l'homogénéisation est introduit. Dans la section 1, nous décrivons les théories bien établies nécessaires à la mise en œuvre du "workflow" d'optimisation topologique par la méthode d'homogénéisation. Ensuite, dans la section 2, nous introduisons le contexte et le cadre de base d'optimisation topologique présentant une microstructure composite (périodique ou non). Nous énonçons soigneusement le problème original d'optimisation de forme ainsi que sa forme relaxée. Son effet est d'autoriser des matériaux composites, microperforés comme conceptions admissibles : nous nous intéressons ici aux matériaux composites, constitués de deux phases isotropes.

Chapitre 2 : Optimisation topologique par homogénéisation des structures 2-d et 3-d

Le modèle d'élasticité linéaire et le contexte général d'optimisation de forme sont introduits. Ce chapitre décrit l'optimisation topologique par la méthode d'homogénéisation des structures constituées de microstructures isotropes, modulées en 2-d et 3-d, générant des matériaux poreux localement périodiques. Ici, les composites sont périodiquement perforés par des cellules hexagonales en 2-d et des tétrakaidecaèdres en 3-d. Cette classe de microstructures périodiques modulées est connue pour être isotrope (ou

du moins très proche d'un comportement isotrope), ce qui les rend d'un grand intérêt pour l'optimisation de forme. Il n'est pas nécessaire de les orienter localement dans le domaine, ce qui simplifie le processus d'optimisation. Leur géométrie est paramétrée par un seul paramètre, la densité du matériau et seule la densité du matériau doit être optimisée. À ce titre le processus d'optimisation est très proche de la méthode SIMP (Simplified Isotropic Material Penalization). Néanmoins, nous rappelons qu'aucun matériau fictif n'est utilisé ici, le tenseur d'élasticité homogénéisé du matériau composite isotrope doit être calculé (c'est-à-dire qu'il n'est pas approximé par une loi de puissance de la densité) et pris en compte lors du processus d'optimisation.

Chapitre 3 : Optimisation topologique par la méthode d'homogénéisation de structures chargées en fluide 2-d

Ce chapitre introduit un modèle fluide-structure en interaction simplifié qui sera d'intérêt tout au long de ce travail : les variables u et p sont la solution de deux équations d'état faiblement couplées au sens où chacune d'elles peut être résolue successivement et indépendamment. Ce modèle est basé sur l'équation de Biot-Darcy pour l'écoulement du fluide, formulée en pression, et la poro-élasticité linéaire pour le déplacement élastique. On cherche à minimiser la somme des compliances élastique et fluide-élastique. Une nouveauté importante de cette partie est la dérivation de la fonction objectif qui dépend à la fois des variables d'état u et p. La fonction objectif est convertie en un problème de minimisation sans contrainte (il faut lire le chapitre 2 pour plus de détails) en ajoutant des termes de pénalisation à la fonction objectif : c'est la méthode du Lagrangien augmenté.

L'essentiel du contenu de ce chapitre est communiquée dans l'article suivant en cours de soumission : G.O. Agyekum, F. Jouve et L. Cangémi, Topology Optimization of Fluidic Pressure Loaded Structures using the Biot-Darcy Method.

Chapitre 4 : Optimisation topologique par la méthode d'homogénéisation pour un modèle thermo poro-mécanique en 2-d

L'une des motivations ultimes guidant ce travail est l'optimisation des structures mécaniques soumises à des sollicitations thermiques et refroidies par des fluides. Dans ce chapitre, nous étudions l'optimisation topologique pour un modèle faiblement couplé de propagation de la chaleur et d'intéraction fluide-structure dans un régime de petites déformations. Il est basé sur le modèle de Biot-Darcy déjà vu au chapitre 3, sur l'équation de convection-diffusion pour la propagation de la chaleur dans les domaines fluide et solide, et sur le système thermo poro-mécanique d'élasticité linéaire. On cherche à minimiser plusieurs fonctions de coût arbitraires en 2-d.

Chapitre 5 : Vers des applications 3d et industrielles : implémentation pour une variété de cas tests numériques

Ce chapitre tente de démontrer la capacité de la méthode d'optimisation topologique par la méthode d'homogénéisation, à savoir, l'algorithme minimisation alterné à traiter de cas tests numériques qui approchent des applications industrielles plus avancées. Du point de vue numérique, l'extension de l'algorithme d'optimisation de forme décrit dans le chapitre 3 au chapitre 4 de 2-d à 3-d est simple. Cependant, plusieurs ingrédients supplémentaires sont nécessaires pour obtenir une efficacité satisfaisante.

Chapitre 6 : Annexe

Nous fournissons dans cette annexe des microstructures composites construites avec une cellule orthotrope, dans lesquelles la géométrie de la cellule périodique correspondante est orthotrope, à savoir, anisotrope.

Introduction-Summary of thesis

This thesis is devoted to shape and topology optimization of multi-scale and multi-physics systems, motivated by the development of advanced technologies in the energy field. Due to several industrial constraints that are detailed hereafter, we consider from the get go the homogenization method for such purpose. The objective is to set up a numerical workflow to design multi-scale coupled thermal fluid-structures using homogenization based-topology optimization method, motivated by the development of architected materials.

Shape optimization is the mathematical art of generating shapes or layouts that best fulfill a proposed objective. Industrial applications are generally concerned with the issue of determining physical systems that achieve optimal performance, e.g : what is the shape of the most rigid structure for a given prescribed volume fraction ? ; how to design the shape of a thermal fluid-elastic loaded systems characterized by multi-scale patterns such as industrial heat exchangers ? ; what composite design does achieve the best heat transfer ?. These are very classical questions of industrial interest often encountered in many advanced technologies in the field of engineering such as aerospace, aeronautic, automobile, micro-mechanic, civil engineering, energy industry, et cetera.

0.5 Shape to topology optimization

shape optimization is today a major issue in structural design and as such, impressive literature that deals with this matter can attest to this. The establishment of its theoretical basics dates back to the beginning of the 1900s with the works of Michell in 1904 [1] and Hadamard in 1905 [2]. Much work has led to the development of the method such as the works of O. Pironneau [3], J Céa [4], D. Chénais [5], J. Sokolowski and J.P. Zolésio [6], Murat-Tartar [7, 8], M.P. Bendsøe [9] or Cherkaev-Kohn [10], to cite a few as well as the references that these articles or books contain. Below, we review a brief history of shape and topology optimization methods and most have meanwhile attained a mature state. Their popularity as design tools for achieving solutions to a wide variety of problems involving single/multi-physics is growing consistently.

Shape optimization can be divided into two large families : methods based on boundary motion (or sizing problem) and topology optimization (or layout optimization). Boundary variation techniques are based on *a priori* chosen curves/surfaces, which are used to interpolate the set of admissible boundary shapes of a prescribed structure explicitly captured on a mesh, where its topology is fixed. By moving its boundaries, one can find an optimal solution in the set of admissible boundary shapes, which is obtained by homeomorphic transformation of the boundaries of the initial structure. Initiated by Hadamard in 1905 [2], it consists in moving the boundary along the normal and to compute the resulting variation on the functional : see Figure 13, for an example of boundary variation. The moving boundaries of the structure are defined with respect to its smooth curves/surfaces, which we modify its parameters in order to achieve optimal performance with respect to a given objective or cost function. Prior

definition of the structure based on parametrized curves/surfaces and characteristics, such as its topology, are chosen and fixed throughout the optimization process and, thus, a domain can only be compared to a domain of similar connectivity.

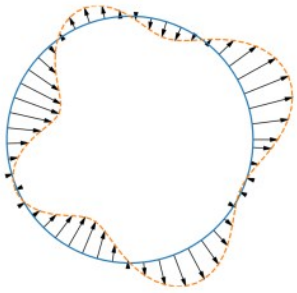

FIGURE 13 – Boundary variation method of Hadamard (Figure from [13]). In blue scheme, the initial boundary of the structure and in dotted orange, the resulting boundary variation along the normal.

It is difficult to create a hole or to add a part outside its boundaries (this is even impossible to achieve, accept in the "*bubble*" method [11]). The difficulty is that there is no map between domains of different topologies, namely, with more or less number of holes and separate connections. A simple isomorphic transformation of the domain is unable to generate different topologies (see the discussion from D. Chénais in [12]). The main difficulty is that boundary variation schemes are ill equipped to capture the possible topological complexity of the shape because of the required smoothness assumptions on the boundary of the domain, which do not permit hole punching. Moreover, the existence of a solution is not always ensured due to the required smoothness assumptions on the boundary of the domain.

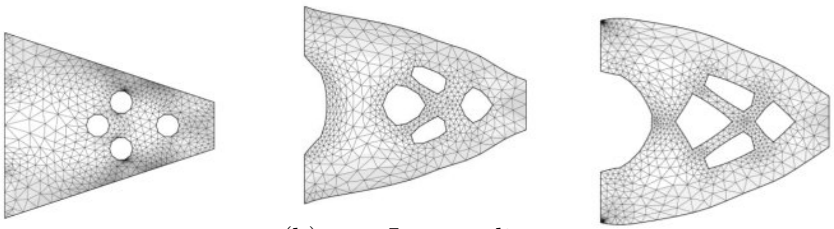

(a) Initial shape (b) Intermediate shape (c) Optimal shape

FIGURE 14 – Boundary variation method of Hadamard based on mesh deformation (Figure from [13]). Shape optimization of a 2-d cantilever in flexion.

It is widely acknowledged that creating holes (namely, changing the topology) may drastically improve the performance of a candidate optimal shape but we do not know in advance the required holes punching. Boundary motion schemes provide an optimal solution which is only the best optimum for a fixed number of holes : a sub-optimal

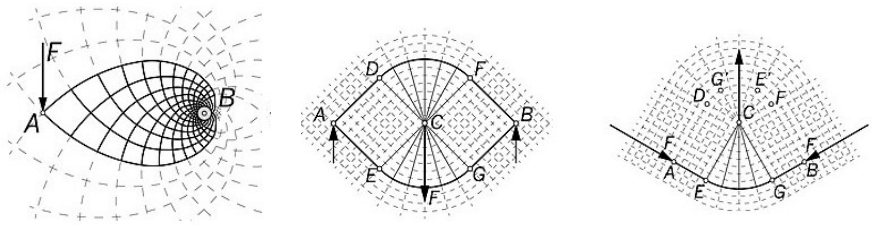

(a) (b) (c)

Figure 15 – Michell trusses method (Figure from wiki/Michell_structures). (a) A single force F applied at A, and acting at right angle to the line AB, (b) A single force F applied at C centered between supports at points A and B (full space solution), (c) Centrally-loaded beam with force away from the straight line between supports, construction similar to (b).

solution, see Figure 14, for an example. Topology optimization allows to modify more fundamentally the nature of the structure. There is no assumption on the prior definition of the structure parameters and characteristics, such as its topology, are arbitrarily chosen and freed throughout the optimization process and thus, a domain can be compared to a domain of different connectivity, i.e., allow for holes of any shape and any size within the design region. This method has been discussed by F. Murat and L. Tartar in [7, 8], and [14], popularized by the works of M.P. Bendsøe and N. Kikuchi [15], who were first to numerically treat a realistic problem using this approach in structural design. Formulate the design problem in terms of optimal distribution of available material is a possible alternative, which is satisfactory because no assumption is required on the solution. The establishment of the general mathematical theory of problems of variable domain designs has given rise to several works, of which the most important and well-known are those proposed by F. Murat and L. Tartar [7, 8], and those of by Kohn and Strang [16] and Lurie and CherKaev [17]. Historically, the first important work related to topology optimization methods in structural model design is the frame (today called truss) method introduced by Michell [1] in 1904 (see, Prager and Rozvany, [18]). Briefly, the method consists of constructing structures from bars assembled into trusses (or lattices). Each bar can support a stress field of the same sign (tension or compression). The optimal structure is a solution of a weight minimization problem when the stress field varies in the set of all statically admissible tensor. This method has the advantage of building explicit solutions for simplified shape optimization problems and therefore serves as a reference and comparison : see, Figure 15 and Figure 16.

Tartar and Murat were first to introduced the theory of homogenization to assess the properties of a porous microstructure. To determine the topology of a structure, they used characteristic functions to characterize the sub-domain occupied by the material : i.e., a bang-bang problem (material or void) ; but the resulting formulation is generally ill-posed. The reader is referred to the typical counter-examples presented in [19] for model problems of control through the coefficients of an objective functional depending on the solution of a linear partial differential equation. Their idea is then to relax the

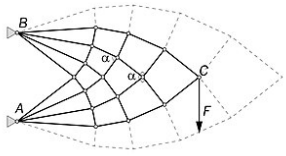

FIGURE 16 – Discrete Michell trusses or Prager trusses (Figure from wiki/Michell_structures). Method of the circle of relative displacements to arrive with optimal topology of such trusses (typically cantilevers).

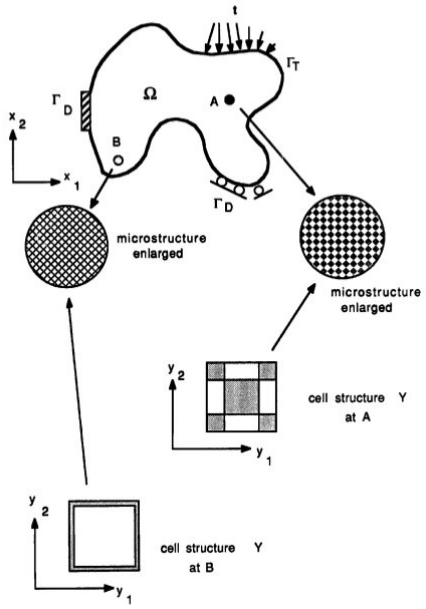

FIGURE 17 – A structure with composite microstructure (Figure from [15]).

problem using homogenization methods. In physical terms, admissible designs should now include arbitrary micro-perforations of the material within the design domain, namely, allow for fine mixtures of void and material on a scale which is much smaller than the mesh used for the actual computation. This process of enlarging the space of admissible designs in order to get a well posed problem is what we called relaxation. Thus, the relaxation allows to introduce a more general mathematical framework, where existence of a solution is ensured and determined using numerical computation. Kohn and Strang showed that for these problems, relaxation amounts to compute the quasi-convexification of some functionals. In all, the idea is to recast the original problem in order to get a well posed problem without changing one's physical nature. These two methods, one introduced by Murat-Tartar, the other by Kohn and Strang are related and complementary. They constitute the basic tools for the resolution of shape optimization problems.

In numerical point of view, topology optimization of elastic structures started with

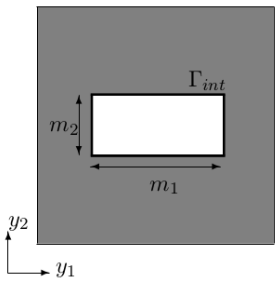

Figure 18 – Orthotropic periodic cell (Figure from [20]).

the works of M.P. Bendsøe and N. Kikuchi [15]. To solve the design problem they proposed the homogenization method, which is based on the ideas of optimal material distribution, relaxation and on the introduction of a porous microstructure (see Figure 17, for an example), of which they determined the effective macroscopic properties with respect to the material density using the theory of periodic homogenization. In [15], Bendsøe and Kikuchi introduced a periodic microstructure, of which the periodic pattern is a square cell perforated by rectangular hole of volume the size of porosity : i.e., proportion of void (see, Figure 18). In [15], the microstructures are built with orthotropic cells which are parametrized by the dimensions of the rectangular hole, i.e. : its length m_1 and width m_2 for each finite elements. Hence, the design variables of the optimization problem are the design parameters m_1, m_2 of the basic microscopic periodic cell. As the macroscopic material is orthotropic, the orientation of the local microstructure plays a key role and the orthotropic angle is also a design variable of the optimization problem. Thus, the numerical optimization problem is very large since it is composed of three design variables by each finite element. To tackle such a large problem, M.P. Bendsøe and N. Kikuchi adopted a very simple formulation which is to minimize the compliance (or energy of the applied force) of a structure, which is submitted to a volume constraint and only in the plane setting. Given the simple formulation of the problem which include only one constraint, a meaningful optimality criteria was proposed to optimize the design variables. For the orthotropic angle, bisection-Newton method was proposed and turns out to be inefficient. The numerical results of this first study did not showcase a clear silhouette of the optimal structure.

For better results, the orthotropic angle update scheme is reviewed by Bendsøe [21] and by Suzuki and Kikuchi [22, 23]. They notice through Pedersen's study [24], that the orthotropic angle must be aligned with the principal directions of the stress tensor. The proof of this optimality criteria was brought only later by the theoretical studies of Allaire and Kohn [25] and by Gibianski and Cherkaev [26]. Others contributions have been brought, see [21, 22, 23]. The choice of the porous microstructure has been the subject of much debate. The use of finite rank sequential laminates by Avellaneda [27], Kohn [28] and Allaire-Kohn [25], showed the optimality for the minimum compliance distribution, i.e., the complete relaxation of the original design problem is given by class of rank-2 sequential laminated microstructures (in 2-d setting), where optimal

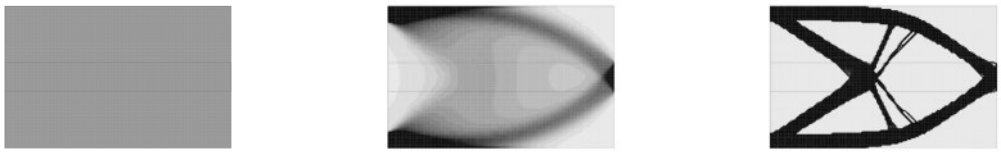

(a) (b) (c)

FIGURE 19 – Topology optimization of a 2-d cantilever using homogenization method (Figure obtained from the source code described in [29]). (a) Initial design, (b) Optimal density of composite material made of rank-2 sequential laminates, (c) The penalized density : sub-optimal microstructure after penalization of the solution (b).

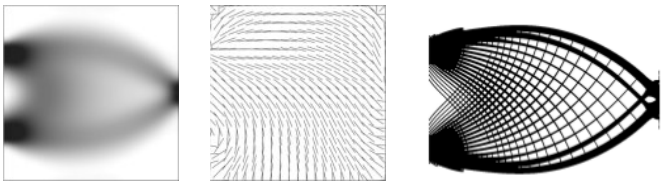

(a) (b) (c)

FIGURE 20 – Topology optimization of a 2-d cantilever using homogenization method (Figure from [20]). (a) Optimal density of composite material periodically perforated by orthotropic cells, (b) Optimal orientation wrt. (a), (c) Projected density : sub-optimal microstructure after projection at a desired length-scale of the solution (a).

solution is ensured and determined using numerical computation [46, 58]. Finally, the method was extended to 3-d structural design problems (Allaire, Bonnetier, Francfort and Jouve [29], Suzuki and Kikuchi [30]). However, the theoretical optimal microstructure can be difficult to handle for engineering practice because it is largely filled with composite material of density between the solid and the void, namely,the material density θ belongs to interval $[0, 1]$. These microstructures are neither manufacturable nor easy to physically interpret. Hence, to improve the separation between the regions occupied by the solid and the void, and to come up with solutions more usable in practice, it can be preferable to resort to sub-optimal microstructures. They can be obtained in several similar ways, for example by directly penalizing the optimal density by forcing it to take only the values 0 or 1 [25, 29] (see, Figure 19) or by projection of the optimal microstructure at a desired length-scale, which is delicate issue, albeit computationally cheap [31] (see, Figure 20).

Shape and topology optimization is actually a rather large field which includes many other methods, such as the topological gradient method [11, 32], level-set methods [33, 34, 35], phase field methods [36], evolutionary topology optimization [37], density methods [38] and by homogenization [29, 39]. For instance, in the level set methods, the shape to be optimized is not discretized explicitly by a mesh (like is the case in boundary variation methods), but rather described implicitly as the negative value set of a level-

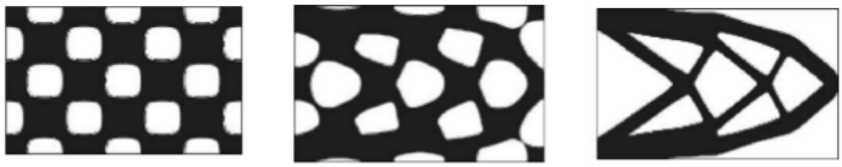

(a) (b) (c)

Figure 21 – Hadamard's method of boundary variation implemented for the optimization of the shape of a 2-d cantilever beam with the level set method (Figure from [39]) : (a) Initial design, (b) Intermediate design, (c) Final design. Topological changes are handled : some holes have merged from the initial to the final design.

(a) (b) (c)

Figure 22 – Topology optimization of a 2-d cantilever using SIMP (Isotropic Material Penalization) method (Figure taken from [13]) : (a) Initial design, (b) Intermediate design, (c) Final design.

set function and evolved on a fixed mesh ; this allows to handle complex topological changes of the optimized shape such as holes merging or boundaries collapsing (see, Figure 21). This ability to handle topological changes is very much desired in order to generate optimal designs without any *a priori* on the final shape, such as the number or the location of holes (or holes and arches in 3-d). As such the level set method used in conjunction with the method of Hadamard is often referred to as a topology optimization method, while the one based on mesh deformation is called geometric optimization. Also, another schemes of interest are the density based methods (see, Figure 22).

0.6 Some current challenges in shape and topology optimization for the energy industry

Generally, engineers proceed by tryouts in which prototypes are tested successively in order to achieve an optimal design, where the expertise and intuitions of the engineer are key. Unfortunately, the workflow is done manually, often inefficient, cumbersome and provides expensive evaluation. With the advent of computers enabling to simulate numerically, today engineers devise industrial systems most often with the assistance of Computer Aided Design (CAD) based geometry optimization software programs. Industries have been very much dependent on CAD formats because of their full compatibility with all stages of the design process, from physical numerical simulations on

commercial software to actual manufacturing by automated machines. However, CAD methods heavily rely on a parameterization choice of the shape geometry, and usually yield very small design updates of the initially proposed geometry. Such is fine for industrial applications to the extent that these small modifications may yield substantial gains of performance. However, it is easily imagined that even better performance could be obtained thanks to topology optimization since it could allow to seek very innovative new designs among much more unconstrained sets of shapes.

In addition, the rise of additive manufacturing since the 1990s has enabled the industry to be capable of fabricating more and more complex designs hardly described by CAD parameterizations, which feeds today a renewed enthusiasm for topology optimization. Many advanced technologies such as heat exchangers for energy storage, re-cooling systems for new generation of engines (e.g., electric engines, microturbines, etc.) or certain battery technologies (e.g., redox type flow batteries) are receiving currently a generous amount of effort issued from energy industry and constitute some long term motivations at origin of this work.

Now, one of the key challenges to overcome in order to make topology optimization applicable to such advanced energy systems is the need for tackling inherent multiphysics aspects : coupled fluid, thermal, and mechanical constraints, which pose several unique challenges : e.g., (i) identifying the structural boundary to apply such loads, (ii) determining the relationship between the fluid-thermal loads and the design variables, i.e., defining a design-dependent and continuous thermal-pressure field, (iii) efficient calculation of the thermal-pressure load sensitivities and so on, which must very often be accounted for simultaneously when designing for instance new generation of engines components.

Among these advanced technologies, a very representative issue drawing currently a substantial amount of attention in the topology optimization community lies in the design of heat exchangers [40, 41, 42, 43, 44, 45] : these are devices that can be used to cool down hot engine fluids by conveying them in the vicinity of some refrigerating gas or liquid, or to store energy per Advanced Adiabatic-Compressed Air Energy Storage (AA-CAES), for various applications such as combustion engines, air conditioning, power production, microturbines, and so on. Industrial heat exchangers usually include many tubes and fins shaped in order to maximize the exchange surface area between hot and cold phase (see, Figure 23.(a)). Naturally, various additional multiphysics design constraints come into play, such as the need for controlling the loss of pressure induced by the system on the input fluid, or the mechanical resistance of the whole structure to the elevated thermal-pressure loads. Note, the topology and performance of the optimized structures are directly related to the magnitude, location, and direction of the thermal-pressure loads which vary with the design. It is suspected that many other components of combustion engines could benefit as well from shape and topology optimization, such as the internal cooling channels system of turbine/compressor (see, Figure 23.(b)).

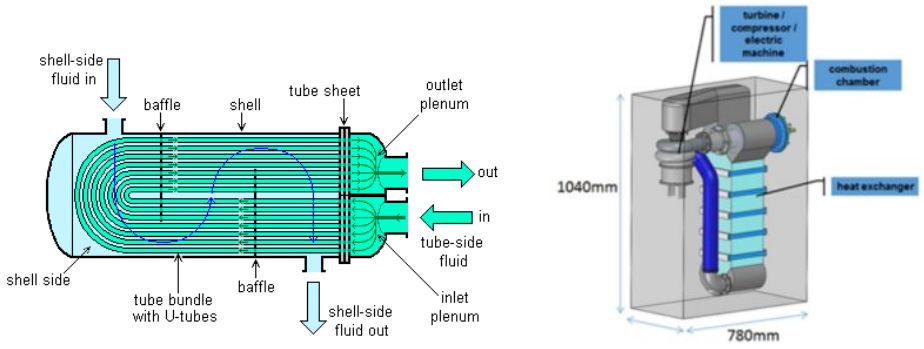

(a) (b)

Figure 23 – (a) U-tube heat exchanger, (b) Heat exchanger integrated in turbine/compressor.

0.7 Scope of the thesis

To date, the homogenization method used as a topology optimization is not yet completely mature for true industrial applications. Most of the test cases featured in the literature are rather exclusively concerned with linear elasticity [25, 29, 31, 46], fluid flow [47], with very few large scale 3-d test cases [20, 29]. It is only relatively recently that the method is being applied on more complicated physics such as electrochemical [48]. This trend is also visible in the density based topology optimization community which also features an increasing number of works on multidisciplinary applications [49, 50, 51, 52, 53, 54].

Here, our objective is set up modelling tools and methodologies for shape and topology optimization of multi-scale and multiphysics systems to generate architected materials, keeping in view longer term industrial requirements. By specific "industrial requirements", it is meant several identified advanced technologies in the energy industry that have guided our research and which are described in the next five paragraphs.

Multiphysics systems

As aforementioned, motivated by the industrial applications, there is an increasing demand for topology optimization of systems involving several interacting physics. Our study shall focus on systems featuring coupled fluid, thermal and mechanical properties. Mathematically, these are characterized by a set of physical variables denoted as follows in this entire manuscript :

- p for the pressure field associated to the fluid phase flowing through the system ;
- T for the temperature field in solid and fluid phase ;
- u for the homogenized displacement field of solid mechanical structures.

These variables are mathematically determined as the solutions of a set of Partial

Differential Equations (PDEs), which are themselves derived from physical modelling choices. An academic setting for the characterization of p, T and u, sufficiently generic for our purposes, shall be described in chapter 4.

A significant motivation of the present work is to replace the "monolithic" design of heat exchangers or mass transfer between a solid structure and a fluid medium by microstructures generating porous locally periodic materials, namely, architected (or functional) materials. A 2-d study for the optimization of fluid-pressure loaded structures using Biot-Darcy model is proposed in chapter 3. This conceptual shift makes it possible to envisage gains in terms of exchange capacity between the two media.

Constrained optimization

Most industrial systems feature a variety of load specifications that must be satisfied in realistic conditions of use. For instance, the overall mechanical stress or the temperature of a solid structure may be required to remain below a given bound in order to avoid premature fatigue. In other words, a design optimization problem reduces to determine the shape of a system that achieves the best performance subject to a given set of physical constraints. Such problems can generically be modeled as mathematical programs of the form

$$\begin{aligned} &\min_{\theta} J^*(\theta, p(\theta), T(\theta), u(\theta)) \\ s.t &\begin{cases} g_i(\theta, , p(\theta), T(\theta), u(\theta)) = 0 \quad 1 \leq i \leq m, \\ h_j(\theta, , p(\theta), T(\theta), u(\theta)) \leq 0 \quad 1 \leq j \leq n, \end{cases} \end{aligned} \tag{2}$$

where θ denotes the material density to be optimized, typically the proportion of solid phase for fine mixtures of void and material on a scale which is much smaller than the mesh used for the actual computation, e.g., the density for microstructures generating porous locally periodic materials. J^* refers to a relaxed given cost function which quantifies the system performance and which is to be minimized. Classical cost functions commonly encountered in shape optimization include the compliance of a mechanical structure, the displacement u such that u is as close as possible to a target displacement u_0 given, or the heat stored into a thermal system. Equality and inequality constraints g_i and h_j model physical load specifications ; they refer to some physical quantities need to be reach (e.g., volume fraction solid in the porous medium) or should not exceed (e.g. an upper bound limit for the overall temperature). Both objective function J^* and constraints g_i , h_j depend on the design variable θ and on the physical variables $p(\theta)$, $T(\theta)$, and $u(\theta)$, which depend themselves on θ through physical state equations.

The design variable θ belongs to some function space $L^\infty(\Omega; [0, 1])$, which belongs to some euclidean space $\mathbb{R}^N$ after discretization, which makes mathematical program of the form of (2) solvable with a meaningful optimality criteria [29, 55, 56, 57]. Most available works using the homogenization method convert (2) into an unconstrained minimization problem by adding penalization terms to the objective function J^*, e.g., as in the Augmented Lagrangian Method [20, 29, 49]. Less complex methods, such

as the density-based methods or level-set methods have been used with some success in few published works [45, 47, 49, 50]. However, these methods still present some unsatisfying qualities for industrial goals : e.g., the density based are physically less rigorous, while with level set methods, finely graded microstructures can not be build. In chapter 2, novel gradient-based type algorithm is described for the resolution of constrained optimization problems adapted to the context of homogenization method.

Non-intrusiveness

For long term industrial applications, a significant motivation of this work is to provide some contributions to some basic topics that have been discussed for several years. Indeed, through the concept of topology optimization, we aim to : (i) provide a contribution to the understanding and modeling of physical mechanisms underlying the behavior of fluid-structure interactions in the energy production processes and tools, such as heat exchangers, re-cooling systems or certain battery technologies, (ii) deploy a multi-physic and multi-scale analysis of these behaviors, and (iii) develop sizing tools, methodologies and technologies around energy production and use.

Moreover, most exchanger technologies imply a co-operation between a fluid phase and a solid phase (or infrastructure) ; the fluid often playing the role of calorie carrier or species carrier. Meanwhile, the solid can transfer calories, store heat or transfer species in the case of an electrode. Also, the solid phase plays a fundamental role of structural encapsulation, often overlooked in the design of systems not experiencing strong mechanical pressures. Thus, the processes or technologies mentioned above present a common analogy in terms of physical problem at a fundamental level : optimize heat or mass exchanges between a solid phase mechanically strong enough and fluid phase. In general, we aim to develop optimization methods of systems or structures under hot and cold pressure loads, thanks to the concept of architected materials whose manufacture is made today relatively accessible through appearance of mature addictive manufacturing technologies ; which are able to build finely graded microstructures or lattice materials allowing to consider the implementation of integrated functional materials.

Problematic

The objective of this work is to establish the bases of a topology optimization approach for architected materials, through the homogenization method ; having a composite microstructure generating porous locally periodic materials, allowing to optimize the mechanical behavior of "porous-diffusion" structures of type heat exchangers or electrochemical reactors. It is about looking for an optimal composite microstructure allowing to maximize the surface exchange between the solid and fluid phases, and the thermal flow within the structure, as well as its mechanical behavior, when the latter is subjected to pressure and thermal variations associated with its operating cycle. The so called architected (or lattice materials) correspond to materials with complex internal arrangement (Figure 24). We can imagine for instance structures made of bars assem-

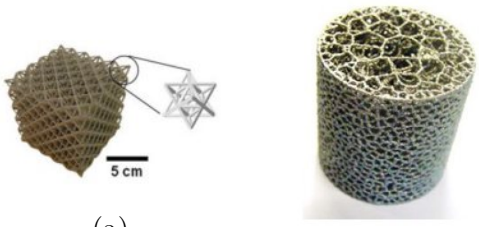

(a) (b)

FIGURE 24 – (a) A lattice material with fixed, (b) and with an arbitrary microstructure.

bled into trusses or membranes, whose intrinsic arrangement meets a specific objective or cost function associated to a certain physic (e.g., mechanical, thermal, flow, ...).

From a global point of view, the scientific problem is twofold. The first stake is to be able to characterize the "porous-diffusion" mechanical behavior of this type of material at macroscopic level in the form of "*homogenized*" laws, from the local characteristics of the material and the fluid considered. The second, consists in setting up the right topology optimization technique for the research of a microstructure that best meets some performance requirements of a system defined by the technological problem. As it happens, in the context of research for innovative technological solutions for exchangers allowing to merge a structural function to mass or temperature transfer function ; it will be to minimize the deformations of the system while increasing its exchange capacities (i.e., surfaces) between the solid and the fluid phases. Other objectives can be added such as minimizing the local stress with respect to stress criterion admissible by the effective material. From a methodological point of view, at first, we use a simplified approach for each physical :

- for solid or fluid mechanics which involves kinematic notions of conservation of the movement ;
- for temperature or mass transfer.

This is to lay the basics of a global approach to multiphysics topology optimization which can then be improved and perfected according to the specific needs of each technology (e.g., heat exchangers or batteries).

0.8 Summary of chapters

Chapter 1 : Homogenization

This preliminary chapter introduces briefly the homogenization theory in the case of linear elasticity. The mathematical framework of the homogenization theory is introduced. In section 1, we outline well-established theories required for an implementation workflow of topology optimization using homogenization method. Next, in section 2, we introduced the background context and material on design optimization with the homogenization method. We carefully state the original shape optimization problem

as well as its relaxed formulation. Its effect is to allow for microperforated composites as admissible designs : we focus here on composite materials, made of two isotropic phases.

Chapter 2 : Homogenization-based topology optimization of 2-d and 3-d structures built with isotropic composite materials

The linear elasticity model and its shape optimization context are being introduced ; this chapter describes a shape optimization based on homogenization method to optimize structures made of modulated isotropic composite microstructures in 2-d and 3-d, generating porous locally periodic materials. Here, the composites are periodically perforated by hexagonal cells in 2-d and tetrakaidecahedron cell in 3-d. This class of modulated periodic microstructures is known to be isotropic microstructures (or at-least very close to one), which make them of high interest for shape optimization. There is no need to orientate them locally in the domain, which simplifies the optimization process. Their geometry is parametrized by only one parameter, the material density, only the material density has to be optimized and as such the optimization process is very close to the SIMP method. Nevertheless, we recall that no fictitious material is used here, the homogenized elasticity tensor of the isotropic composite material has to be computed (i.e., it is not approximated by a power law of the density) and taken into account during the optimization process.

Chapter 3 : Homogenization-based topology optimization of 2-D fluidic pressure loaded structures built with isotropic composite materials

This chapter introduces a simplified fluid-structure model which shall be of interest throughout this whole work : the variables u and p are the solution to two state equations which are weakly coupled in the sense that each of them can be solved successively and independently. This model is based on Biot-Darcy equation for the fluid flow and pressure and linear poro-elasticity for the elastic displacement. We seek minimizers of the sum of the elastic and fluid-elastic compliances.

A significant novelty of this part is the derivation of the objective function which depends upon both the state variables u and p ; the objective function is convert into an unconstrained minimization problem (one should read chapter 2 for details) by adding penalization terms to the objective function : it is the Augmented Lagrangian Method.

Most of the content of this chapter is in the preliminary version of an article : G.O. Agyekum, F. Jouve and L. Cangémi, Topology Optimization of Fluidic Pressure Loaded Structures using the Biot-Darcy Method.

Chapter 4 : Homogenization-based topology optimization for a thermal fluid-structure model in plan setting

One of the ultimate motivations guiding this work is the optimization of mechanical structures subjected to thermal loads and cooled down by fluids. In this chapter, we investigate topology optimization for a weakly coupled model of heat propagation, fluid flow and structure deformation. It is based on the Biot-Darcy model already seen in chapter 3, on the convection-diffusion equation for heat propagation in both fluid and solid domains, and on the linearized poro-diffuso-elasticity system for the mechanical displacement of the solid domain. We seek minimizers of the several arbitrary objective functionals in plan setting.

Chapter 5 : Towards 3-d and industrial applications : Implementation for a variety of numerical test case

This chapter attempts to demonstrate the ability of multiphysics shape optimization by the homogenization method, namely, alternate minimization method, to deal with 3-d problems approaching industrial test cases. From the numerical point of view, the extension of the shape optimization algorithm outlined in chapter 3 to chapter 4 from 2-d to 3-d is straightforward. However, several additional ingredients are required in order to achieve a satisfactory efficiency.

Chapter 6 : Appendix

We provide in this appendix, composite microstructures built with orthotropic cell, in which the geometry of the corresponding periodic cell is orthotropic, namely, anisotropic.

Première partie

Preliminaries

Chapitre 1

Homogenization

We briefly present the homogenization theory in the case of linear elasticity. The reader should refer to the textbook [59], for more details and explanations.

1.1 Definition of *H*-convergence

In this section, the general theory of homogenization is introduced without any special assumptions on the geometry, namely, periodicity or randomness. The H-convergence is a generalization of the so called G-convergence, which is restricted to symmetric operators introduced by Spagnolo [60, 61], and De Giorgi and Spagnolo [62]. H-convergence is due to Tartar [63], and Murat and Tartar [64]. A characteristic feature of the H-convergence theory is a systematic use of weak convergence in Sobolev spaces. We recall its main results in the following.

1.1.1 Strong and weak convergences

We briefly recalled some classical results on strong and weak convergences in the Sobolev spaces ; the reader should refer to textbooks [59], for more details and proofs of all statements presented in this subsection. Let Ω be an open subset in $\mathbb{R}^N$. For $1 \leq p \leq +\infty$, the Lebesgue space $L^p(\Omega)$ of all measurable functions u in Ω, with finite norm defined by

$$||u||_{L^p(\Omega)} := \begin{cases} (\int_\Omega |u(x)|^p \, dx)^{\frac{1}{p}} & \text{for } 1 \leq p < +\infty, \\ ess \; sup_{x\in\Omega} \, |u(x)| & \text{for } p = +\infty \end{cases}$$

is Banach space, i.e., a complete normed space, where two types of convergences coexist ; the strong and the weak convergences. Suppose $(u_\epsilon)_{\epsilon>0}$, a sequence of functions indexed by a sequence of real parameters $\epsilon > 0$ going to zero. The strong convergence is associated to the above norm, i.e., a sequence u_ϵ is said to converge strongly in $L^p(\Omega)$ to a limit u if $\lim_{\epsilon\to 0} ||u_\epsilon - u||_{L^p(\Omega)} = 0$, and is denoted by an arrow, i.e. :

$$u_\epsilon \to u \quad \text{in } L^p(\Omega) \text{ strongly.}$$

On the other hand, the weak convergence in $L^p(\Omega)$ is associated to test functions in its dual space $L^{p'}(\Omega)$, with $\frac{1}{p} + \frac{1}{p'} = 1$. More precisely, for $1 \leq p < +\infty$, a sequence u_ϵ is said to converge weakly in $L^p(\Omega)$ to a limit u if, for any test function $\phi \in L^{p'}(\Omega)$, its satisfies

$$\lim_{\epsilon\to 0} \int_\Omega u_\epsilon(x)\phi(x) \, dx = \int_\Omega u(x)\phi(x) \, dx, \tag{1.1}$$

and is denoted by an harpoon, i.e. :

$$u_\epsilon \rightharpoonup u \quad \text{in } L^p(\Omega) \text{ weakly.}$$

For $p = +\infty$, since the dual of $L^\infty(\Omega)$ is not $L^1(\Omega)$, u_ϵ is said to converge weakly*, i.e., a sequence u_ϵ is said to converge weakly* to u, if for any test function $\phi \in L^1(\Omega)$, its satisfies (1.1).

For a general purpose, we recall the definition of the convergence in the sense of distribution, namely,

Definition 1.1.1. *A sequence $(u_\epsilon)_\epsilon \in L^1_{loc}(\Omega)$ is said to converge in the sense of distributions to u if,*

$$\forall \phi \in \mathcal{D}(\Omega), \lim_\epsilon \int_\Omega u_\epsilon(x)\phi(x)\, dx = \int_\Omega u(x)\phi(x)\, dx, \tag{1.2}$$

where $\mathcal{D}$ is the set of smooth functions with compact support in Ω.

Lemma 1.1.1. *Let $(u_\epsilon)_{\epsilon>0}$ be a bounded sequence in $L^p(\Omega)$, with $1 < p \leq +\infty$, i.e., there exits a positive constant C, which does not depend on ϵ, such that $||u_\epsilon||_{L^p(\Omega)} \leq C$.*

Then, there exist a subsequence $(u_{\epsilon'})_{\epsilon'>0}$ and a limit u such that $(u_{\epsilon'})_{\epsilon'>0}$ converges weakly to u in $L^p(\Omega)$ if, $1 < p < +\infty$, or converges weakly if, $p = +\infty$.*

Note that, $p = 1$ is excluded : indeed, Lemma 1.1.1 is not true for $p = 1$; strong convergence implies weak convergence but converse is not true (e.g., $u_\epsilon(x) = \sin\left(\frac{x_1}{\epsilon}\right)$, where x_1 is first coordinate of x). In a physical point of view, the strong convergence is more or less the pointwise convergence, while the weak convergence is a notion of convergence *"in average"* (up to fluctuations of zero-mean). The connection between strong convergence and pointwise convergence is given by

Lemma 1.1.2. *Let Ω be a bounded subset in $\mathbb{R}^N$. Let u_ϵ be a sequence converging strongly to a limit u in $L^p(\Omega)$, $1 \leq p \leq +\infty$. Then, there exists a subsequence, still denoted u_ϵ, and a function $h(x) \in L^p(\Omega)$, such that, for this subsequence,*

$$\begin{aligned} u_\epsilon(x) &\to u(x) \quad \textit{almost everywhere in } \Omega, \\ |u_\epsilon(x)| &\leq h(x) \quad \textit{almost everywhere in } \Omega. \end{aligned}$$

Lemma 1.1.3. *Let Ω be a bounded open set in $\mathbb{R}^N$. For $1 < p \leq +\infty$, let u_ϵ be a bounded sequence in $L^p(\Omega)$ such that*

$$u_\epsilon(x) \to u(x) \quad \textit{almost everywhere in } \Omega,$$

then the sequence u_ϵ converges strongly to u in any $L^q(\Omega)$, with $1 \leq q < p$.

As a consequence, the product of two strongly converging sequences does also converge strongly (in a different Lebesgue space) to a product of the two limits. But, unfortunately, the same is no longer true for the product two weakly converging sequences, which has no reason to converge weakly to the product of the two weak limits, e.g., $u_\epsilon(x) = \sin\left(\frac{x_1}{\epsilon}\right)$ converges weakly to zero in any $L^p(\Omega)$, with $1 \leq p < +\infty$, while the product $(u_\epsilon)^2$ converges weakly to $1/2$ in any $L^p(\Omega)$. In general, if u_ϵ is a sequence converging weakly in $L^p(\Omega)$ to a limit u, and if f is a nonlinear function, then the sequence $f(u_\epsilon)$ usually does not converge weakly (or in any sense) to $f(u)$. This is the main difficulty with the weak convergence (for more details, see [65]). Nevertheless, it is possible to pass to the limit in the product of one strongly and one weakly converging sequence.

Lemma 1.1.4. *Let Ω be a bounded open set in $\mathbb{R}^N$. Let u_ϵ be a sequence converging strongly to a limit u in $L^p(\Omega)$, $1 \leq p \leq +\infty$. Let v_ϵ be a sequence converging weakly to a limit v in $L^{p'}$ (weakly* if $p' = +\infty$), with $\frac{1}{p} + \frac{1}{p'} = 1$. Then, the product $u_\epsilon v_\epsilon$ converges to uv in the sense of distributions.*

Thanks to interpolation inequalities, a strong convergence and a weak convergence can be *"interpolated"* to obtain another strong convergence in an intermediate Lebesgue space. For details, one should refer to the textbook [59].

1.1.2 *H*-convergence

For future studies, we briefly recalled some theorems and results in the case of linear elasticity ; the reader should refer to the textbook [59], for more theoretical results of the homogenization theory, which is far more general.

The behaviour of an elastic phase is modelized through a positive definite fourth order tensor, i.e., its Hooke's law A. Let $\mathcal{M}_N^4$ be the set of fourth order tensors acting on symmetric matrices of order N, e.g., $A \in \mathcal{M}_N^4$. For any two positive constants $\alpha > 0$ and $\beta > 0$, we define the subspace of $\mathcal{M}_N^4$ made of coercive fourth order tensors with coercive inverses, i.e., the set of admissible Hooke's laws :

$$\mathcal{M}_{\alpha,\beta} = \left\{ A \in \mathcal{M}_N^4 \text{ such that } \forall \xi \in \mathcal{M}_N^s,\ A\xi \ :\ \xi \geq \alpha|\xi|^2 \text{ and } A^{-1}\xi \ :\ \xi \geq \beta|\xi|^2 \right\}$$

H-convergence is a notion of convergence for the coefficients of an elliptic partial differential equation, which is defined through some convergence properties of the solution of this equation.

Definition 1.1.2. *A sequence of Hooke's laws $A^\epsilon(x)$ in $L^\infty(\Omega; \mathcal{M}_{\alpha,\beta})$ is said to converge in the sense of homogenization, or simply to H-converge to an homogenized Hooke's law $A^*(x) \in L^\infty(\Omega; \mathcal{M}_{\alpha,\beta})$ if, for any right hand side $f \in H^{-1}(\Omega)^N$, the sequence u_ϵ of solutions of*

$$\begin{cases} -div(A^\epsilon(x)e(u_\epsilon)(x)) = f \quad in\ \Omega \\ u_\epsilon = 0 \quad on\ \partial\Omega \end{cases} \tag{1.3}$$

satisfies,

$$\begin{cases} u_\epsilon \rightharpoonup u \quad weakly\ in\ H^1(\Omega)^N \\ A^\epsilon e(u_\epsilon) \rightharpoonup A^* e(u) \quad weakly\ in\ L^2(\Omega; \mathcal{M}_N^s), \end{cases} \tag{1.4}$$

where u is the solution of the homogenized equation

$$\begin{cases} -div(A^*(x)e(u)(x)) = f \quad in\ \Omega \\ u = 0 \quad on\ \partial\Omega \end{cases} \tag{1.5}$$

This definition makes sense because of the following sequential compactness theorem from Tartar and Murat [64] : any bounded sequence of $\mathcal{M}_{\alpha,\beta}$ admits a H-convergence subsequence.

Theorem 1.1.5. *For any sequence $A^\epsilon(x)$ of Hooke's laws in $L^\infty(\Omega;\mathcal{M}_{\alpha,\beta})$, there exists a subsequence, still denoted by $A^\epsilon(x)$, and an homogenized Hooke's law $A^*(x) \in L^\infty(\Omega;\mathcal{M}_{\alpha,\beta})$ such that $A^\epsilon(x)$ H-converges to $A^*(x)$.*

A proof of Theorem 1.1.5 is given in [63], is typically a compactness result since it proves the existence of an H-limit for a subsequence of a bounded sequence, but it delivers no explicit formula for this limit. This is in sharp contrast to periodic homogenization (see Subsection 1.1.3) where the entire sequence is converging to an H-limit defined by an explicit formula (up to solving the cell problems).

1.1.3 Periodic homogenization

In this section, the H-convergence method is applied to periodic homogenization and gives a rigorous proof of convergence to the homogenized limit introduced in subsection 1.1.3.

Let $Y = (0,1)^N$ be the unit periodic cube. To take into account the periodic boundary conditions, we identify Y with the unit N -dimensional torus (this is done by gluing together opposite faces of Y). This unit torus is a smooth compact manifold without boundary. In the sequel, a periodic function in Y is actually defined, through this identification, as a function on the unit torus (this has the advantage that the periodicity is somehow built-in).

For $1 \leq p \leq +\infty$, we define the Lebesgue space $L^p_\#(Y)$ of measurable and p-summable functions on the unit torus. Identifying the torus with Y, is equivalent to define as a space of Y-periodic functions in $\mathbb{R}^N$ by

$$L^p_\#(Y) = \left\{ f \in L^p_{loc}(\mathbb{R}^N) \text{ such that } f \text{ is } Y\text{-periodic} \right\} \tag{1.6}$$

equipped with the norm $||f||_{L^p_\#(Y)}$. Similarly, let $H^1_\#(Y)$ be the Sobolev space of functions defined on the periodic cell Y, which are, along with their first derivatives, measurable and squared summable. By the same identification, we have

$$H^1_\#(Y) = \left\{ f \in H^1_{loc}(\mathbb{R}^N) \text{ such that } f \text{ is } Y\text{-periodic} \right\} \tag{1.7}$$

equipped with the norm $||f||_{H^1_\#(Y)}$. Also, let $H^1_\#(Y)/\mathbb{R}$ be the quotient space defined as the space of classes of functions in $H^1_\#(Y)$ equal up to an additive constant. In the context of H-convergence, let $A \in L^\infty(Y;\mathcal{M}_{\alpha,\beta})$ be Y-periodic admissible Hooke's law and $A^\epsilon(x)$ be the sequence of admissible Hooke's laws defined by

$$A^\epsilon(x) = A(\frac{x}{\epsilon}) \tag{1.8}$$

where A(y) is a Y-periodic Hooke's law, which belongs to $L^\infty_\#(Y;\mathcal{M}_{\alpha,\beta})$.

Note that, Theorem 1.1.5 ensures that the sequence $A^\epsilon(x)$ admits a subsequence that H-converges. In fact, according to Theorem 1.1.5, the whole sequence H-converges,

and in the particular case of periodic homogenization, there exists an explicit formula for its H-limit $A^*(x)$.

Theorem 1.1.6. *The sequence $A^\epsilon(x)$ defined in (1.8), H-converges to a constant homogenized fourth order tensor $A^*(x) \in \mathcal{M}_{\alpha,\beta}$ defined by its entries*

$$A^*_{ijkl} = \int_Y A(y)(e_{ij} + e(w_{ij}) \ : \ (e_{kl} + e(w_{kl}) \, dy, \tag{1.9}$$

where $e_{ij} = \frac{1}{2}(e_i \otimes_j + e_j \otimes e_i)$ is the canonical basis of the symmetric tensors of order 2, and w_{ij} is the family of unique solutions in $H^1_\#(Y)/\mathbb{R}$ of the cell problems

$$\begin{cases} -div(A(y)(e_{ij} + e(w_{ij}))) = 0 & \text{in } Y, \\ y \to w_{ij}(y) & Y\text{-periodic} \end{cases} \tag{1.10}$$

We emphasize that, in Theorem 1.1.6, the entire sequence A^ϵ H-converges to A^* (not merely a subsequence, as is the case in Theorem 1.1.5). In addition, a particular interest of Theorem 1.1.6, relies on the fact that any H-limit can be reached by a converging sequence of periodic Hooke's laws : i.e., at each point x, a general H-limit $A^*(x)$ is attained as the limit of a sequence of periodic homogenized fourth order tensors.

Theorem 1.1.7. *Let $A^\epsilon(x)$ be a sequence of Hooke's laws in $L^\infty(\Omega; \mathcal{M}_{\alpha,\beta})$, which H-converges to a limit $A^*(x)$. For any x in Ω and any sufficiently small positive $h > 0$, let $A^*_{x,\epsilon,h}$ be the periodic homogenized fourth order tensor defined by its entries*

$$(A^*_{x,\epsilon,h})_{ijkl} = \int_Y A^\epsilon(x + hy)(e_{ij} + e(w^{ij}_{x,\epsilon,h})) \ : \ (e_{kl} + e(w^{kl}_{x,\epsilon,h})) \, dy,$$

where $w^{ij}_{x,\epsilon,h}$ is the family of unique solutions in $H^1_\#(Y)/\mathbb{R}$ of the cell problems

$$\begin{cases} -div(A^\epsilon(e_{ij} + e(w^{ij}_{x,\epsilon,h}))) = 0 & \text{in } Y, \\ y \to w^{ij}_{x,\epsilon,h}(y) & Y\text{-periodic} \end{cases} \tag{1.11}$$

There exists a subsequence h going to zero such that, for almost every $x \in \Omega$

$$\lim_{h\to 0} \lim_{\epsilon \to 0} A^*_{x,\epsilon,h} = A^*(x)$$

remark 1. *Theorem 1.1.7 implies that the set of all periodic H-limits, as defined by Theorem 1.1.6 is dense in the set of pointwise values of general H-limits ; the values taken by periodic H-limits are not different from those obtained in the general case.*

In particular, periodic homogenization is ideal when studying modulated cellular structures. Indeed, let us consider a periodic cell whose design is parametrized by finite parameters $p \in \mathbb{R}^{n_p}$. Thanks to Theorem 1.1.6, the homogenized Hooke's law $A^*(p)$ of the cell can be computed for any parameters p. For instance, let Ω be the domain tiled by periodic cells of size ϵ, $p^\epsilon(x) : \Omega \to \mathbb{R}^{n_p}$ be the function of parameters of the periodic cells, i.e., a piecewise constant function, and we assume that, p^ϵ converges weakly to p. Let $A^\epsilon(x) \in L^\infty(\Omega; \mathcal{M}_{\alpha,\beta})$ be the Hooke's law of this modulated cellular structure. Then, Theorem 1.1.7 ensures that the sequence $A^\epsilon(p^\epsilon(x))$ H-converges to the Hooke's law $A^*(p(x))$.

remark 2. *Note that, all theorems and results of the homogenization theory in the particular case of linear elasticity hold true in the case of conductivity, i.e., thermal or potential.*

Now, we have all the results in order to compute effective Hooke's laws using the homogenization method for modulated cellular structures ; however, there are few other questions to be answered before using the homogenization theory to any linear elastic problem. Indeed, Definition 1.1.2 is given for particular boundary conditions ; it can be extended to others. In addition, we give in the following results in order to be able to compute some quantities, like energy and eigenfrequencies. We emphasize that, this present work should be approached within such a background.

1.1.4 Irrelevance of the boundary conditions

Proposition 1.1.8. *Let $A^\epsilon(x)$ be a sequence of Hooke 's laws in $L^\infty(\Omega;\mathcal{M}_{\alpha,\beta})$, that H-converges to the limit $A^*(x)$. Any sequence z_ϵ, such that*

$$\begin{cases} -div(A^\epsilon e(z_\epsilon)) = f_\epsilon \to f \quad \textit{strongly in } H^{-1}_{loc}(\Omega)^N \\ z_\epsilon \rightharpoonup z \quad \textit{weakly in } H^1_{loc}(\Omega)^N, \end{cases} \tag{1.12}$$

satisfies,

$$A^\epsilon e(z_\epsilon) \rightharpoonup A^* e(z) \quad \textit{weakly in } L^2(\Omega;\mathcal{M}^s_N)$$

This implies that the main result of H-convergence (i.e., the existence of an homogenized behavior) still holds true for sequences z_ϵ, that do not satisfy any precise boundary conditions on $\partial\Omega$. We recall that, the product two weakly converging sequences has no reason to converge weakly to the product of the two weak limits, but, it is possible to pass to the limit in the product of one strongly and one weakly converging sequence. The div-curl lemma and its generalization state that if, the derivatives verify some convergence, the product converge in the sense of distributions.

Lemma 1.1.9. *Let u_ϵ and v_ϵ be two sequences in $L^2(\Omega;\mathcal{M}^s_N)$, such that,*

$$\begin{cases} u_\epsilon \rightharpoonup u & \textit{weakly in } L^2(\Omega;\mathcal{M}^s_N), \\ div(u_\epsilon) \rightharpoonup div(u) & \textit{weakly in } H^{-1}(\Omega)^N \end{cases}$$

and

$$\begin{cases} v_\epsilon \rightharpoonup v & \textit{weakly in } L^2(\Omega;\mathcal{M}^s_N), \\ \frac{\partial v_{\epsilon,jl}}{\partial x_i \partial x_k} + \frac{\partial v_{\epsilon,ik}}{\partial x_j \partial x_l} - \frac{\partial v_{\epsilon,jk}}{\partial x_i \partial x_l} - \frac{\partial v_{\epsilon,il}}{\partial x_j \partial x_k} \to \frac{\partial v_{jl}}{\partial x_i \partial x_k} + \frac{\partial v_{ik}}{\partial x_j \partial x_l} - \frac{\partial v_{jk}}{\partial x_i \partial x_l} - \frac{\partial v_{il}}{\partial x_j \partial x_k} & \textit{strongly in } H^{-2}(\Omega), \\ \forall i,j,k,l \in \{1,...,N\} \end{cases} \tag{1.13}$$

Then,

$$u_\epsilon \,:\, v_\epsilon \rightharpoonup u \,:\, v \quad \textit{in the sense of distributions.}$$

The compensated term comes from the fact that, specific derivatives of each sequence converge in order to compensate each other. The second condition in (1.13) is automatically satisfied for sequences of symmetric matrices v_ϵ, which are strain tensors : i.e., v_ϵ can be written as $v_\epsilon = \frac{1}{2}(\nabla a_\epsilon + \nabla a^T)$. Indeed this linear combination of partial derivatives is equal to zero for such matrices.

Démonstration. We give here a proof of Proposition 1.1.9 : Let ω be a compact subset in Ω. As z_ϵ converges weakly to z in $H^1_{loc}(\Omega)^N$, $e(z_\epsilon)$ converges weakly to $e(z)$ in $L^2_{loc}(\Omega)^N$. Moreover, $\nabla \wedge e(z_\epsilon) = \nabla \wedge e(z) = 0$. As z_ϵ is bounded in $H^1(\omega)^N$, the product $A^\epsilon e(u_\epsilon)$ is bounded in $L^2(\omega)^N$ and so, converges weakly to σ in $L^2(\omega)^N$, up to a subsequence still denoted by $A^\epsilon e(u_\epsilon)$. The strong convergence of the divergence of the product is an assumption of the proposition.

Now, the objective is to proof that $\sigma = A^* e(u)$ in ω. Let $\phi \in \mathcal{D}(\Omega)$ be a smooth function with compact support in Ω, such that, $\phi \equiv 1$ in ω. Let $\lambda \in \mathcal{M}^s_N$ be a symmetric matrix, and w be defined by $w(x) = \phi(x)\lambda x$, then, we get $e(w(x)) = \lambda$ in ω. Next, let w_ϵ be the test function in $H^1_0(\Omega)^N$, satisfying

$$\begin{cases} -div(A^\epsilon e(w_\epsilon)) = -div(A^* e(w)) & \text{in } \Omega, \\ w_\epsilon = 0 & \text{on } \partial\Omega \end{cases}$$

Thanks to the H-convergence of A^ϵ, we get

$$\begin{cases} w_\epsilon \rightharpoonup w & \text{weakly in } H^1_0(\Omega)^N, \\ A^\epsilon e(w_\epsilon) \rightharpoonup A^* e(w) & \text{weakly in } L^2(\Omega; \mathcal{M}^s_N), \\ e(w_\epsilon) \rightharpoonup e(w) & \text{weakly in } L^2(\Omega)^N \end{cases}$$

Moreover, $e(w_\epsilon)$ satisfies the second condition of (1.13), since it is a strain tensor. In addition, as

$$-div(A^\epsilon e(w_\epsilon)) = -div(A^* e(w)),$$

its implies that,

$$div(A^\epsilon e(w_\epsilon)) \to div(A^* e(w)) \quad \text{strongly in } H^{-1}(\Omega)^N$$

Since, A^ϵ belongs to $\mathcal{M}_{\alpha,\beta}$, so is A^*. We then get

$$A^\epsilon(e(z_\epsilon) - e(w_\epsilon)) \ : \ (e(z_\epsilon) - e(w_\epsilon)) \geq \alpha |(e(z_\epsilon) - e(w_\epsilon))|^2 \quad \text{almost everywhere in } \omega.$$

By application of Lemma 1.1.9 (also known as *div-curl lemma*), we get

$$(\sigma - A^*\lambda) \ : \ (e(z) - \lambda) \geq 0 \quad \text{almost everywhere in } \omega.$$

Furthermore, let x_0 be a point in ω where the above inequality holds. By taking $\lambda = e(z)(x_0) + t\mu$, with $t > 0$ and $\mu \in \mathcal{M}^s_N$, we get

$$\begin{aligned} (\sigma(x_0) - A^*\lambda) \ : \ (e(z)(x_0) - \lambda) &= (\sigma(x_0) - (A^* e(z)(x_0) + tA^*\mu)) \ : \ (e(z)(x_0) - (e(z)(x_0) + t\mu)) \\ &= -(\sigma(x_0) - (A^* e(z)(x_0) + tA^*\mu)) \ : \ t\mu \\ &= -t(\sigma(x_0) - A^* e(z)(x_0)) \ : \ \mu + t^2|\mu|^2 \end{aligned}$$

So, by dividing the equality by $t > 0$, and tending t to zero, we get

$$-(\sigma(x_0) - A^*e(z)(x_0)) \ : \ \mu \geq 0$$

Finally, since this inequality holds for any $\mu \in \mathcal{M}_N^s$, we get that

$$|(\sigma(x_0) - A^*e(z)(x_0))|^2 = 0 \quad \text{for } \mu = (\sigma(x_0) - A^*e(z)(x_0))$$

And so

$$\sigma(x) = A^*e(z)(x) \quad \text{almost everywhere in } \omega$$

Hence, all converging subsequences of $A^\epsilon e(z_\epsilon)$ converges to the same limit for any subset $\omega \subset \Omega$; the entire sequence converges weakly to $A^*e(z)(x)$ in $L^2_{loc}(\Omega; \mathcal{M}_N^s)$. □

1.1.5 Convergence of the energy

In the shape optimization community, one of the classical objective function often encountered in linear elasticity problems is the energy (or compliance) function, which consists in minimizing the compliance of the final structure, namely, maximizing the rigidity of the final structure. For a sequence of structures, whose Hooke's laws H-converge to A^*, the following proposition ensures that its energies converges to the energy of the homogenized structure.

Proposition 1.1.10. *Let $A^\epsilon(x)$ be a sequence of Hooke 's laws in $L^\infty(\Omega; \mathcal{M}_{\alpha,\beta})$, that H-converges to $A^*(x)$. For any right hand side $f \in H^{-1}(\Omega)^N$, the sequence u_ϵ of solutions of*

$$\begin{cases} -div(A^\epsilon(x)e(u_\epsilon)(x)) = f(x) & \text{in } \Omega, \\ u_\epsilon = 0 & \text{on } \partial\Omega \end{cases} \tag{1.14}$$

satisfies,

$$A^\epsilon e(u_\epsilon) \ : \ e(u_\epsilon) \rightharpoonup A^*e(u) \ : \ e(u) \quad \text{in the sense of distributions}$$

and

$$\int_\Omega A^\epsilon e(u_\epsilon) \ : \ e(u_\epsilon)\, dx \to \int_\Omega A^*e(u) \ : \ e(u)\, dx$$

where u is the weak limit of u_ϵ in $H_0^1(\Omega)^N$ and the solution of the homogenized equation

$$\begin{cases} -div(A^*(x)e(u)(x)) = f(x) & \text{in } \Omega, \\ u = 0 & \text{on } \partial\Omega \end{cases} \tag{1.15}$$

By virtue of this result, the energy convergence is a consequence of H-convergence.

Démonstration. We give here a proof of Proposition 1.1.10 to illustrate a simple application of Lemma 1.1.9 : Since by assumption, $A^\epsilon(x)$ H-converges to $A^*(x)$, we get

$$A^\epsilon e(u_\epsilon) \rightharpoonup A^*e(u) \quad \text{in } L^2(\Omega; \mathcal{M}_N^s)$$

Moreover, for all $x \in \Omega$, we get

$$-div(A^\epsilon(x)e(u_\epsilon)(x)) = f(x) = -div(A^*(x)e(u)(x)),$$

hence,

$$div(A^\epsilon(x)e(u_\epsilon)(x)) \to div(A^*(x)e(u)(x)) \quad \text{strongly in } H^{-1}(\Omega)^N$$

In addition, since

$$u_\epsilon \rightharpoonup u \quad \text{in } H_0^1(\Omega)^N,$$

we get

$$e(u_\epsilon) \rightharpoonup e(u) \quad \text{in } L^2(\Omega; \mathcal{M}_N^s)$$

Besides, $e(u_\epsilon)$ satisfies the second condition of Lemma 1.1.10, since it is strain tensor. By application of the generalized div-curl Lemma 1.1.10, we get

$$A^\epsilon e(u_\epsilon) \ : \ e(u_\epsilon) \rightharpoonup A^* e(u) \ : \ e(u) \quad \text{in the sense of distributions}$$

Now, for the second result, we recall that u_ϵ converges weakly to u in $H^1(\Omega)^N$, thus

$$\int_\Omega f \ . \ u_\epsilon \ dx \to \int_\Omega f \ . \ u \ dx$$

Next, a simple integration by parts of the elasticity problems gives respectively

$$\int_\Omega A^\epsilon e(u_\epsilon) \ : \ e(u_\epsilon) \ dx = \int_\Omega f \ . \ u_\epsilon \ dx,$$
$$\int_\Omega A^* e(u) \ : \ e(u) \ dx = \int_\Omega f \ . \ u \ dx,$$

which leads to the desired result. □

remark 3. *The second result of the Proposition1.1.10, can be extended to other boundary conditions only if they are fixed, in order to proceed to the integration by parts of the elasticity problems. This present work is approached within such background for any elasticity problems.*

1.1.6 Corrector results

In the case of linear elasticity, we assume that the stress and the strain are always linked together through the Hooke's law, no matter their values. However, in practice, several phenomena (e.g., plasticity or buckling) may occur when the stress exceeds some threshold. Hence, in shape optimization, it would be relevant to estimate the limit, if it exists, of

$$\int_\Omega k(x)|\sigma_\epsilon(x)|^2 \ dx, \tag{1.16}$$

where $k(x)$, is a non-negative function : a weight factor, in which the evaluation of the stress can be localized.

We recall that, σ_ϵ converges weakly to σ in $L^2(\Omega;\mathcal{M}_N^s)$ and that the product of two weakly converging sequences has no reason to converge weakly to the product of the two weak limits. Hence to pass to the limit in (1.16), strong convergence is needed for the sequence σ_ϵ. In mechanical point of view, this means that, in a composite, the microstructure induces local stress, which unfortunately, the homogenized (or averaging) stress does not take into account. To circumvent this issue, amplification (or corrector) factors are required to estimate local stress from the average one.

Definition 1.1.3. *Let $(X^{ij})_{1\leq i,j\leq N}$ be the family of functions in $H^1(\Omega)^N$ defined by its entries*

$$X_k^{ij} = x_j\delta_{ik}, \tag{1.17}$$

and in particular,

$$e(X^{ij}) = e_{ij}, \tag{1.18}$$

Definition 1.1.4. *Let $A^\epsilon(x)$ be a sequence of Hooke's laws in $L^2(\Omega;\mathcal{M}_{\alpha,\beta})$, that H-converges to A^* and let $(w_\epsilon^{ij})_{1\leq i,j\leq N}$ be a family of functions in $H^1(\Omega)^N$, such that,*

$$\begin{aligned} w_\epsilon^{ij} &\rightharpoonup X^{ij} \quad \text{weakly in } H^1(\Omega)^N \\ g_\epsilon^{ij} = div(A^\epsilon e(w_\epsilon^{ij})) &\to div(A^* e_{ij}) \quad \text{strongly in } H^{-1}(\Omega)^N \end{aligned} \tag{1.19}$$

The fourth order tensor W^ϵ, defined by its entries

$$W_{ijkl}^\epsilon = (e(w_\epsilon^{ij}))_{kl}$$

is called corrector tensor.

The existence of w_ϵ^{ij}, known as correctors (or oscillating test functions) is at the heart of the proof of Theorem 1.1.6, by Tartar and Murat [64]. They are introduced in the proof to define the homogenized tensor A^*; it is involved in the correction of A^*, in order to compute the strong limit of the stress. We emphasize they are not uniquely defined, but only up to a strongly convergent additive term, which leads to the following lemma.

Lemma 1.1.11. *Let A^ϵ be a sequence of Hooke's laws in $L^2(\Omega;\mathcal{M}_{\alpha,\beta})$, that H-converges to A^*. If, there exist two corrector tensors W^ϵ and $\tilde{W}^\epsilon$, then their difference converges strongly to zero in $L^2_{loc}(\Omega;\mathcal{M}_N^4)$.*

In the periodic case, there exists an explicit formula for the correctors w_ϵ^{ij}, they are defined through the family of correctors w_{ij}, solutions to the cell problem (1.10)

$$w_\epsilon^{ij} = X^{ij} + \epsilon w_{ij}(\frac{x}{\epsilon}) \tag{1.20}$$

Thus,

$$e(w_\epsilon^{ij}) = e_{ij} + e_y(w_{ij})(\frac{x}{\epsilon})$$

Indeed, by rescaling the cell problem (1.10), we get

$$div(e(w_\epsilon^{ij}) = 0 = div(e_{ij}) \quad \text{in } \Omega$$

Since, A^* is homogeneous in Ω for the periodic case, and the correctors w_ϵ^{ij} satisfy (1.19), we get

$$W_{ijkl}^\epsilon = I_{ijkl}^4 + (e_y(w_{ij})(\frac{x}{\epsilon}))_{kl},$$

where I^4 is the fourth order identity tensor and e_y the operator e with respect to the periodic variable $y \in Y$.

Lemma 1.1.12. *Let A^ϵ be a sequence of Hooke's laws in $L^\infty(\Omega; \mathcal{M}_{\alpha,\beta})$, that H-converges to A^*. Then, we have*

$$\begin{aligned} W^\epsilon &\rightharpoonup I^4 \quad \text{weakly in } L^2(\Omega; \mathcal{M}_N^4) \\ A^\epsilon W^\epsilon &\rightharpoonup A^* \quad \text{weakly in } L^2(\Omega; \mathcal{M}_N^4) \\ (W^\epsilon)^T A^\epsilon W^\epsilon &\rightharpoonup A^* \quad \text{in sense of distribution in } \mathcal{D}'(\Omega; \mathcal{M}_N^4) \end{aligned} \tag{1.21}$$

Theorem 1.1.13. *Let A^ϵ be a sequence of Hooke's laws in $L^\infty(\Omega; \mathcal{M}_{\alpha,\beta})$, that H-converges to A^* and u_ϵ be the solution of (1.14), which converges weakly (up to a subsequence still denoted u_ϵ) to u, the solution to the homogenized equation (1.15). Then,*

$$e(u_\epsilon) = W^\epsilon e(u) + r_\epsilon,$$

where, r_ϵ converges strongly to zero in $L^2_{loc}(\Omega; \mathcal{M}_N^s)$.

Thus, from the setting of Theorem 1.16, we get

$$\sigma_\epsilon = A^\epsilon e(u_\epsilon) = W^\epsilon A^\epsilon e(u) + A^\epsilon r_\epsilon = P^\epsilon \sigma + A^\epsilon r_\epsilon,$$

where P^ϵ is a fourth order tensor defined by

$$P^\epsilon = A^\epsilon W^\epsilon A^{*-1}$$

Thanks to Lemma 1.1.12, we get

$$P^\epsilon \rightharpoonup I^4 \quad \text{weakly in } L^2(\Omega; \mathcal{M}_N^4)$$

Hence, the objective function defined by (1.16), can then be rewritten

$$J_\epsilon = \int_\Omega k(x)|\sigma_\epsilon|^2 \, dx = \int_\Omega k(x)|P^\epsilon \sigma|^2 + 2\int_\Omega k(x)(P^\epsilon \sigma \ : \ A^\epsilon r_\epsilon) \, dx + \int_\Omega k(x)|A^\epsilon r_\epsilon|^2 \tag{1.22}$$

Proposition 1.1.14. *In the case of periodic homogenization, the objective defined by (1.16), converges when ϵ tends to zero, to*

$$J = \int_\omega k(x) P^* \sigma \, . \, \sigma \, dx,$$

where is the associated constraint tensor to the displacement u and P^* is defined by

$$P^* = \int_Y A(y)W(y)A^{*-1}A(y)W(y)A^{*-1} \, dy$$

Before displaying a proof of Proposition 1.1.14, we recall the following lemma in [59].

Lemma 1.1.15. *Let $f(y) \in L^2_{\#}(Y)$ be a periodic function. The sequence f_ϵ, defined by*

$$f_\epsilon(x) = f(\frac{x}{\epsilon}),$$

converges weakly in $L^2_{loc}(\mathbb{R}^N)$ to the average

$$\frac{1}{|Y|}\int_Y f(y)\, dy$$

Démonstration. We give here a proof of Proposition 1.1.14 : thanks to Meyers theorem (see, Theorem 1.3.41 in [59]), the displacement u_ϵ, solution of (1.14) is known to belong to $W^{1,p}_0(\Omega)$, with $p > 2$ (i.e., the Meyers exponent is independent of ϵ). Thus, $e(u_\epsilon)$ is L^p-bounded. Likewise, the family of correctors, solution to the cell problem (1.10) belong to $W^{1,p}_0(\Omega)$ and thus, W^ϵ is $L^p(\Omega)$-bounded.

In addition, by assumption, $e(u)$ is L^∞-bounded. Hence, $r_\epsilon = e(u_\epsilon) - W^\epsilon e(u)$ is L^p-bounded. Moreover, by assumption, r_ϵ converges strongly to zero in $L^2_{loc}(\Omega; \mathcal{M}^s_N)$, and thanks to Lemma 1.2.5 in [59], it also converges strongly to zero in $L^2(\Omega; \mathcal{M}^s_N)$.

Now, by assumption, A^ϵ is L^∞-bounded and thus, the third term of (1.22) also converges strongly to zero in $L^2(\Omega; \mathcal{M}^s_N)$. Likewise, since σ is L^∞-bounded, the second term of (1.22) converges strongly to zero in $L^2(\Omega; \mathcal{M}^s_N)$. Finally, using Lemma 1.1.15, leads to desired result. □

The term amplification tensor stands for the fact that the L^2 norm of the homogenized stress σ is amplified by this tensor in order to reach the convergence.

remark 4. *In Proposition 1.1.14, other assumptions could be chosen, like regularity on the solutions w_{ij}, of cell problem (1.10), leading to W^ϵ to be L^∞-bounded. However, microstructures featuring sharp corners are used in this thesis and thus, such assumption can not be considered here.*

The following subsection is concerned with the application of the homogenization theory to the modelling of eigenvalue problems : it gives convergence result for the eigenfrequencies.

1.1.7 Eigenfrequencies

Let Ω be a bounded subset in $\mathbb{R}^N$ and $A^* \in L^\infty(\Omega; \mathcal{M}_{\alpha,\beta})$ be an admissible Hooke's law. We recall that, the spectral problem in linear elasticity reads as

$$\begin{cases} -div(A^*(x)e(u)(x)) = \lambda\rho(x)u(x) & \text{in } \Omega \\ u = 0 & \text{on } \partial\Omega, \end{cases} \tag{1.23}$$

where the unknown $\lambda > 0$, is an eigenvalue, and $u \in H_0^1(\Omega)^N$, the associated eigenvector. There is a countable infinite number of solutions λ : i.e., the eigenvalues are a positive unbounded sequence ; they are indexed by increasing order.

Theorem 1.1.16. *Let A^ϵ be a sequence of Hooke's laws in $L^\infty(\Omega; \mathcal{M}_{\alpha,\beta})$, that H-converges to A^*. Let $\rho_\epsilon(x)$ be a sequence of positive functions, such that*

$$0 < \rho_- \leq \rho_\epsilon(x) \leq \rho_+ < +\infty,$$

which converges weakly in $L^\infty(\Omega)$ to a limit $\rho(x)$. Let $(\lambda_\epsilon^m)_{m\geq 1}$ be the eigenvalues, indexed by increasing order, and $(u_\epsilon^m)_{m\geq 1}$ be the associated normalized eigenvectors (i.e., $||u_\epsilon^m||_{L^2(\Omega)^N} = 1$) of the spectral problem*

$$\begin{cases} -div(A^\epsilon(x)e(u_\epsilon^m)(x)) = \lambda_\epsilon^m \rho_\epsilon(x) u_\epsilon^m(x) & \text{in } \Omega \\ u_\epsilon^m = 0 & \text{on } \partial\Omega, \end{cases} \tag{1.24}$$

Then, for any fixed $m \geq 1$,

$$\lim_{\epsilon\to 0} \lambda_\epsilon^m = \lambda^m,$$

and, up to a subsequence still denoted u_ϵ^m, converges weakly in $H_0^1(\Omega)^N$ to a limit u^m, a normalized eigenvector associated to λ^m, which are solutions to the homogenized eigenvalue problem

$$\begin{cases} -div(A^*(x)e(u^m)(x)) = \lambda \rho(x) u^m(x) & \text{in } \Omega \\ u^m = 0 & \text{on } \partial\Omega, \end{cases} \tag{1.25}$$

and $(\lambda^m)_{m\geq 1}$ is the complete family of eigenvalues of (1.23), indexed in increasing order.

We emphasize that several eigenvectors may be associated to the same eigenvalue, and so the convergence of the sequence u_ϵ^m can only be ensured up to a subsequence.

1.2 Composite material

Let A and B be two isotropic solid phases in $\mathcal{M}_{\alpha,\beta}$, with shear moduli denoted respectively, μ_A, and μ_B, and with Lamé coefficients denoted respectively, λ_A, and λ_B. We assume that

$$0 < \mu_B \leq \mu_A, \quad \text{and} \quad 0 < \lambda_B \leq \lambda_A$$

Let $\chi_\epsilon(x)$ be a family of characteristic functions in $L^\infty(\Omega; \{0,1\})$, that converges weakly* to the limit $\theta(x) \in L^\infty(\Omega; [0,1])$ and let $A^\epsilon(x)$ be a sequence of Hooke's laws in $L^\infty(\Omega; \mathcal{M}_{\alpha,\beta})$, defined by

$$A^\epsilon(x) = \chi_\epsilon(x)A + (1 - \chi_\epsilon(x))B$$

Thanks to Theorem 1.1.5, the sequence A^ϵ admits a subsequence still denoted A^ϵ, that H-converges to a limit A^* in $L^\infty(\Omega; \mathcal{M}_{\alpha,\beta})$. The H-limit A^*, is the homogenized tensor of the composite material made of phase A, in proportions $\theta(x)$ and phase B, in proportions $1 - \theta(x)$, with a microstructure defined by the sequence $(\chi_\epsilon(x))_\epsilon$.

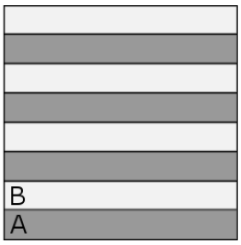

FIGURE 1.1 – Counter example : a composite made of equal layers of phases A and B, non-isotropic.

Definition 1.2.1. *Let $\theta(x) \in L^\infty(\Omega; [0,1])$ be the density function. The set $\mathcal{G}_\theta$ of composite material made of phase A, in proportions $\theta(x)$ and phase B, in proportions $1-\theta(x)$ is defined as the set of all H-limits A^*, associated to θ.*

In general, there is no formula for the H-limit A^* of A^ϵ. Hence, the set $\mathcal{G}_\theta$ can not be explicitly characterized : this is a huge limitation to perform shape optimization with the whole set of composite materials. To circumvent this issue, a solution consists in reducing the set of admissible composites to family of composites for which the effective elastic properties can be computed. Below, we introduced a particular class of composites : the sequential laminates and then, we recall the Hashin-Shtrikman bounds on the elastic properties of isotropic composites from $\mathcal{G}_\theta$, which will serve as reference. Finally, we briefly present the design of microstructures, an important research field in shape optimization.

remark 5. *The H-limit A^*, is not a Hooke's law defined by*

$$\theta(x)A + (1-\theta(x))B.$$

Indeed, if such was the case, this would imply that the local microstructure of the composite does not affect its homogenized elastic behaviour. Only the proportions of each phase (i.e., $\theta(x)$ for A, and $(1-\theta(x))$ for B) would control the homogenized Hooke's law and as such, A^* would be isotropic, which is is obviously false. A counter example is to consider a composite made of equal layers of phases A and B in the direction $(1,0)$: see Figure 1.1, it will collapse for a vertical load but will stay very strong for a horizontal load : it is then not isotropic.

1.2.1 Sequential laminates

Single laminated composites

A single laminated composite relies on the following result of H-convergence : see Lemma 1.4.10 in textbook [59].

Lemma 1.2.1. *Let $\chi_\epsilon(x_1)$ be a sequence of characteristic functions in $L^\infty(\mathbb{R};\{0,1\})$, that converges weakly* to a limit $\theta(x_1) \in L^\infty(\mathbb{R};[0,1])$. Let $A^\epsilon(x)$ be a sequence of fourth order tensors in $L^\infty(\Omega;\mathcal{M}_{\alpha,\beta})$ defined by*

$$A^\epsilon(x) = \chi_\epsilon(x)A + (1-\chi_\epsilon(x))B$$

Then, A^ϵ H-converges to a limit $A^*(x_1) \in L^\infty(\Omega;\mathcal{M}_{\alpha,\beta)}$, which depends only on x_1, defined by

$$\theta(x_1)(A^*(x_1)-B)^{-1} = (A-B)^{-1} + (1-\theta(x_1))f_B(e_1),$$

where $f_B(e_1)$, is a positive non definite fourth order tensor defined, for any symmetric matrix ξ by

$$f_B(e_1)\xi \;:\; \xi = \frac{1}{\mu_B}(|\xi e_1|^2 - (\xi e_1 \,.\, e_1)^2) + \frac{1}{\mu_B+\lambda_B}(\xi e_1 \,.\, e_1)e_1 \otimes e_1 \tag{1.26}$$

The composite A^* is said to be a single lamination in the direction e_1, of the two phases A and B in proportions θ and $(1-\theta)$, respectively. The single laminated composites define a whole family of composite materials parametrized by the proportion of lamination θ and the direction of lamination : its can also be laminated, i.e., single laminated composite generating an enlarged family of composite materials.

Sequential laminated composites

Lemma 1.2.2. *Let $(e_i)_{1\le i\le p}$ be a set of unit vectors and let θ be a volumic fraction in $[0,1]$. For any collection of non-negative real numbers $(m_i)_{1\le i\le p}$ in $[0,1]$, satisfying*

$$\sum_{i=1}^{p} m_i = 1,$$

there exists a rank-p sequential laminate A_p^*, with matrix A and core B in proportions θ and $(1-\theta)$, respectively, with lamination directions $(e_i)_{1\le i\le p}$, such that :

$$(1-\theta)(A_p^*-B)^{-1} = (B-A)^{-1} + \theta\sum_{i=1}^{p} m_i f_A(e_i),$$

where f_A is given by (1.26). The numbers $(m_i)_{1\le i\le p}$ are called the lamination parameters.

See Figure 1.2 for the display of a sequential construction of sequence of composite materials converging to a rank-2 laminate. The first lamination between the two phases A and B is done in the direction e_1 (see, Figure 1.2(a)) ; it is a single laminated composite seen as an homogenized material. This is a key point in the proof of the explicit formula of the elastic properties of the sequential laminates. Next, a change of scale is performed on the size ϵ of the single laminated composite in the same direction e_1 : see, Figure 1.2(b). Finally, this new effective material is laminated in direction e_2 with the previous matrix A : see, 1.2(c).

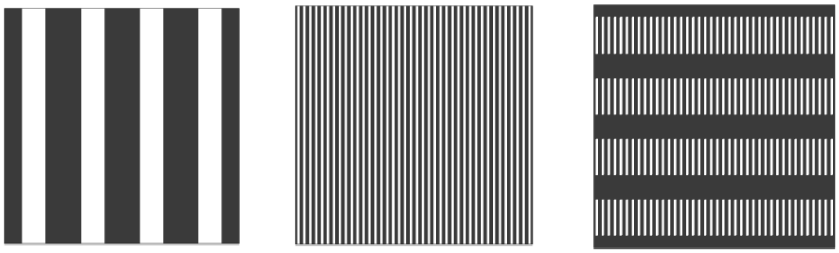

(a) First lamination, in direction e_1 (b) Change of scale, in direction e_1 (c) Second lamination, in direction e_2

FIGURE 1.2 – An example of a sequential laminated construction of sequence of composite materials

We emphasize that without a change of scale between two laminations, the constructed composite will not converge to a sequential laminates. The process for laminated composites of higher ranks is exactly the same : the new material is seen as an effective material, thanks to a change of scale, then laminated in the appropriate direction.

1.2.2 Hashin Shtrikman bounds

There exist optimal bounds called the Hashin-Shtrikman bounds on the shear and bulk moduli. There were introduced by Hashin and Shtrikman [66] : it was proven by Francfort and Murat [67] that they can be reached by sequential laminates.

Theorem 1.2.3. *Let A^* be an isotropic homogenized tensor in $\mathcal{G}_\theta$ of composite materials made of two phases A and B in proportions θ and $(1-\theta)$, respectively, i.e. :*

$$A^* = 2\mu^* I_4 + (\kappa^* - \frac{2\mu^*}{N}) I_2 \otimes I_2,$$

where κ^* and μ^*, are its bulk and shear moduli, respectively. Then, κ^* and μ^* satisfy

$$\kappa_l \leq \kappa^* \leq \kappa_u,$$

with,

$$\kappa_l = \kappa_B + \frac{\theta}{\frac{1}{\kappa_A - \kappa_B} + \frac{N(1-\theta)}{N\kappa_B + 2(N-1)\mu_B}}, \quad \kappa_u = \kappa_A + \frac{1-\theta}{\frac{1}{\kappa_B - \kappa_A} + \frac{N\theta}{N\kappa_A + 2(N-1)\mu_A}} \tag{1.27}$$

$$\mu_l \leq \mu^* \leq \mu_u,$$

with,

$$\mu_l = \mu_B + \frac{\theta}{\frac{1}{\mu_A - \mu_B} + \frac{2N(N-1)(1-\theta)(\kappa_B + 2\mu_B)}{(N(N-1)-2)\mu_B(N\kappa_B + 2(N-1)\mu_B)}}, \quad \mu_u = \mu_A + \frac{1-\theta}{\frac{1}{\mu_B - \mu_A} + \frac{2N(N-1)\theta(\kappa_A + 2\mu_A)}{(N(N-1)-2)\mu_A(N\kappa_A + 2(N-1)\mu_A)}} \tag{1.28}$$

remark 6. *These bounds were first established by Hashin-Shtrikman in 3-D [66]. A rigorous proof is due Francfort and Murat [67] completed by Kohn-Milton [68].*

remark 7. *These bounds are more accurate than the arithmetic and harmonic means (or Paul or Voigt and Reuss bounds) defined by :*

$$\frac{1}{\kappa_h} = \frac{1-\theta}{\kappa_B} + \frac{\theta}{\kappa_A} \quad \text{and} \quad \kappa_a = (1-\theta)\kappa_B + \theta\kappa_A,$$
$$\frac{1}{\mu_h} = \frac{1-\theta}{\mu_B} + \frac{\theta}{\mu_A} \quad \text{and} \quad \mu_a = (1-\theta)\mu_B + \theta\mu_A$$

Indeed, we have

$$\kappa_h \leq \kappa_l \leq \kappa^* \leq \kappa_u \leq \kappa_a,$$
$$\mu_h \leq \mu_l \leq \mu^* \leq \mu_u \leq \mu_a$$

Let A_m^* be an isotropic homogenized tensor, where the bulk modulus is either κ_h or κ_a and/or the shear modulus either μ_h or μ_a. Then, A_m^* is not in $\mathcal{G}_\theta$. The bounds formed by the harmonic and arithmetic means are therefore not optimal.

In addition, the Hashin-Shtrikman bounds are optimal : see, Francfort and Murat [67], according to the following proposition.

Proposition 1.2.4. *There exists an isotropic composite material, a rank-m sequential laminate denoted $A^{*l}_{L_{iso}}$, corresponding to the two lower bounds of Hashin-Shtrikman, such that*

$$A^{*l}_{L_{iso}} = 2\mu_l I_4 + (\kappa_l - \frac{2\mu_l}{N}) I_2 \otimes I_2$$

and likewise, a sequential laminate denoted $A^{*u}_{L_{iso}}$ corresponding to the two upper bounds of Hashin-Shtrikman, such that

$$A^{*u}_{L_{iso}} = 2\mu_u I_4 + (\kappa_u - \frac{2\mu_u}{N}) I_2 \otimes I_2$$

They are defined by their rank $m = 2$, in 2-D and $m = 6$, in 3-D, their lamination parameters

$$m_i = \frac{1}{m},\ 1 \leq i \leq m$$

and their lamination directions $(e_i)_{1\leq i\leq m}$, formed from the vectors starting from the origin and pointing towards the m equidistributed points on the unit upper semi-circle in 2-D and on the unit upper semi-sphere in 3-D.

remark 8. *the second lower bound, which intervenes in Proposition 1.2.4 is obtained by exchanging the role of the two phases A and B in the definition of the lower bound (1.27-1.28). Likewise, the second upper bound is obtained in the same way.*

This proposition shows that the Hashin-Shtrikman bounds are optimal because they can be reached by sequential laminated composite belonging to $\mathcal{G}_\theta$. In the following, we set the upper Hashin Shtrikman bounds as references for composite materials. Moreover, in this present work, composite materials are assumed to be made of an isotropic phase A and void : i.e., the phase B is considered to tend to zero. Hence, in this particular case, the the upper Hashin-Shtrikman bounds κ_u and μ_u are given by :

$$\begin{cases} \kappa_u = \frac{\kappa_A \mu_A \theta}{\kappa_A + \mu_A - \kappa_A \theta}, \quad \mu_u = \frac{\kappa_A \mu_A \theta}{2(\kappa_A+\mu_A) - (\kappa_A + 2\mu_A)\theta} & \text{in 2-D,} \\ \kappa_u = \frac{4\kappa_A \mu_A \theta}{3\kappa_A + 4\mu_A - 3\kappa_A \theta}, \quad \mu_u = \frac{(9\kappa_A + 8\mu_A)\mu_A \theta}{5(3\kappa_A+4\mu_A) - 6(\kappa_A+2\mu_A)\theta} & \text{in 3-D} \end{cases} \tag{1.29}$$

These bounds are obtained when the couple (κ_B, μ_B) tends to zero in the bounds (κ_l, μ_l) and (κ_u, μ_u) of (1.27-1.28) : the first couple (κ_l, μ_l) is tending towards zero, while the second (κ_u, μ_u) is tending towards the written limits above in 2-D and 3-D. For the remainder of this manuscript, we denote by (κ_{HS}, μ_{HS}), the upper Hashin-Shtrikman bounds : i.e., (κ_u, μ_u).

The SIMP method

In the Solid Isotropic Material with Penalization (SIMP) method, the Hooke's law is represented as a power law of the density : the maximal exponent is 3. The bulk and the shear moduli with respect to the density are respectively displayed by Figure 1.3 for three values of the exponent : 1 (linear law), 2 (quadratic law) and 3 (cubic law) ; and as a reference, the upper Hashin-Shtrikman bounds for a composite made of an isotropic material and void is also displayed.

The linear and quadratic materials are above the upper Hashin-Shtrikman bounds for any density ; they are fictitious material in the sense that, no composite material reach those elastic properties for the same density. Meanwhile, the cubic one satisfies the Hashin-Shtrikman bounds for density lower than 70% : up to this point, the cubic material may match composite material. However, we do not have any information of which kind of microstructure it could be. Nevertheless, for greater densities, the cubic material also turns out to be fictitious. Hence, the SIMP method is not appropriate for shape optimization with microstructures. The penalization part is mandatory in order to reach real material (by opposition with fictitious materials), i.e., void and solid material.

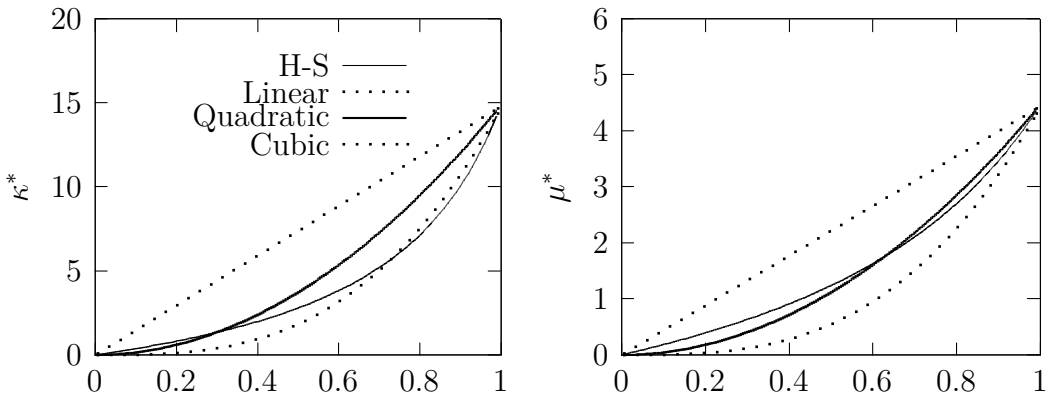

Figure 1.3 – The bulk κ^* (left) and shear μ^* (right) moduli in 2-D, wrt. the upper Hashin-Shtrikman bounds (H-S) and the three values of the exponent : 1 (linear law), 2 (quadratic law) and 3 (cubic law)

1.2.3 Design of a periodic microstructure

As aforementioned, the set $\mathcal{G}_\theta$ is very large and can not be explicitly characterized : there exists an infinite choice of microstructures. To choose an adapted class of composites for a given minimization problem is not an easy task, see the textbook [69] for more details about composite materials in numerous physical domains.

In the shape optimization community, microstructures have been theoretically elaborated in order to reach some specific properties, like the sequential laminates, the coated confocal ellipsoid [70] or the Vigdergauz cells [71]. Other microstructures have also been optimized using shape optimization methods : see [72] and [73], or [74] for isotropic microstructures, also, see [75] for optimized cells for permeability fluids or [76] for optimization of biomaterials.

In this work, the chosen periodic microstructures should satisfy some criteria. Firstly, it should be manufacturable using additive manufacturing process. This imply that the microstructure can feature only one scale of material : a rank-2 or more laminated composite are then excluded. For 3-D microstructures, other constraints have to be taken into account depending on the process of fabrication : e.g., for metal additive manufacturing, the microstructure has to be drilled from end to end, otherwise metallic powder could be trapped in the final structure. Secondly, only lattice material is considered, i.e., a mixing of an isotropic elastic phase and void. Thirdly, the geometry of the microstructure has to be easily parametrizable to perform the optimization process only over few parameters. Finally, the microstructure should explore within the realm of the possible, a large range of elastic properties. In particular, it has to reach complete void and full material : e.g., this excludes a square perforated with an ellipse.

1.3 Shape optimization and homogenization

This section is essentially composed of reminders of existing results in shape optimization using homogenization methods. An adequate class of admissible designs is introduced, which is precisely the concern of the theory of homogenization. The announced goal is to devise the least compliant structure compatible with the loads for a given weight of the structure, namely, to maximize the rigidity of an elastic structure under a weight constraint. We content ourselves to recall the main results detailed in [29], by Allaire, Bonnetier, Francfort and Jouve. These results will be useful for a good understanding of various related subjects that we discuss hereafter. The complete proof sometimes very technical, can be found in [29]. The reader should also refer to [25, 46], for more details and explanations about the homogenization based topology optimization.

1.3.1 The original optimal design problem

Consider a bounded domain Ω, in $\mathbb{R}^N$ subject to "smooth enough" surface loadings f (e.g., $f \in H^{-1/2}(\partial\Omega)^N$ satisfying a compatibility condition of equilibrium) on its boundary $\partial\Omega$. Part of the domain is occupied by an isotropic linearly elastic material with elasticity

$$A = (\kappa - \frac{2\mu}{N}) I_N \otimes I_N + 2\mu I_{2N}, \quad 0 < \kappa, \mu < +\infty, \tag{1.30}$$

while the remaining part of Ω is void. Let χ be the characteristic function of the part Ω_χ, occupied by the elastic material. Whenever Ω_χ is a smooth enough open subdomain of Ω such that $\partial\Omega_\chi$ contains the part of $\partial\Omega$ where f is not zero, the elasticity problem in Ω_χ is well-posed, i.e., the following set of equations

$$\begin{cases} \sigma = Ae(u) \quad e(u) = \frac{1}{2}(\nabla u + \nabla^t u), \\ div(\sigma) = 0 \quad \text{in } \Omega_\chi, \\ \sigma \,.\, n = f \quad \text{on } \partial\Omega_\chi \cap \partial\Omega, \\ \sigma \,.\, n = 0 \quad \text{on } \partial\Omega_\chi \setminus \partial\Omega. \end{cases} \tag{1.31}$$

has a unique solution $u \in H^1(\Omega_\chi)^N$ (up to a rigid displacement field). Here, u is the displacement vector and σ is the associated Cauchy stress field, uniquely defined in $L^2(\Omega_\chi; \mathbb{R}_s^{N^2})$.

As such, σ can be extended to an element of $L^2(\Omega; \mathbb{R}_s^{N^2})$, which further realizes the minimum of the complementary energy over all statically admissible stress fields, namely :

$$c(\chi) := \int_\Omega A^{-1}\sigma \,.\, \sigma \, dx = \min_{\tau \in \Sigma(\chi)} \int_\Omega A^{-1}\tau \,.\, \tau \, dx, \tag{1.32}$$

where the set $\Sigma(\chi)$ is defined by :

$$\Sigma(\chi) = \Big\{ \tau \in L^2(\Omega; \mathbb{R}_s^{N^2}) \mid div(\tau) = 0 \text{ in } \Omega;\ \tau \,.\, n = f \text{ on } \partial\Omega;\ \tau(x) = 0 \text{ a.e. where } \chi(x) = 0 \Big\}. \tag{1.33}$$

The quantity $c(\chi)$, defined by (1.32) is called the compliance of the body and a straightforward integration by parts demonstrates that

$$c(\chi) = \int_{\partial\Omega} f \,.\, u \; dx,$$

where u is the solution of the system (1.31). When $\chi(x)$ is the characteristic function of an arbitrary measurable subset of Ω (not necessarily open), the existence of σ is no longer guaranteed. A generalized compliance may however be defined as

$$c(\chi) := \inf_{\tau \in \Sigma(\chi)} \int_{\Omega} A^{-1}\tau \,.\, \tau \; dx, \tag{1.34}$$

with $\Sigma(\chi)$ is defined by (1.33) (note that, the infimum is not necessarily attained).

The goal of the optimal design is devise the least compliant structure compatible with the loads for a given weight of the structure. Thus, the range of compliances $c(\chi)$ for all characteristic functions χ such that

$$\int_{\Omega} \chi(x) \; dx = \Theta, \quad 0 < \Theta \leq |\Omega|,$$

is investigated and the optimal design reads as

$$I := \inf \Big\{ c(\chi) \mid \chi \in L^{\infty}(\Omega; \{0,1\}); \quad \int_{\Omega} \chi(x) \; dx = \Theta \Big\}. \tag{1.35}$$

The optimal design problem defined in (1.35) is difficult to handle since it is constrained by

$$\int_{\Omega} \chi(x) \; dx = \Theta. \tag{1.36}$$

Such a constraint is routinely handled in elementary calculus of variations through the introduction of a positive Lagrange multiplier. Thus, (1.35) is replaced by

$$I(\ell) := \inf_{\chi \in L^{\infty}(\Omega;\{0,1\})} \Big\{ c(\chi) + \ell \int_{\Omega} \chi(x) \; dx \Big\}, \tag{1.37}$$

in the hope that there exists a positive value ℓ for which the volume constraint (1.36) is met. That it is not so obvious in the case at hand, and as such it should be justified. We are unfortunately helpless in the matter as detailed in [29]. Thus, we content ourselves with the above unconstrained version of the original optimization problem.

remark 9. *For sake of simplicity, we consider only the case where surface loads are applied. A straightforward modification of the model would however permit the consideration of volume forces or the clamping of part of the boundary $\partial\Omega$ (i.e., the enforcement of a Dirichlet boundary condition $u = 0$). The reader is referred to the numerical examples presented in chapter 2, which include different types of boundary conditions. The above optimization problem is usually referred to as a "single load" problem. This means that the elastic structure is optimized for a single configuration of loading forces and may well be totally inadequate for other loads. Its quite often more realistic to investigate "multiple loads" problem which amounts to an optimization of the structure for*

several configurations, i.e., various surface loadings $f_1, ..., f_p$ are given and we consider the minimization problem

$$I_p(\ell) := \inf_{\chi \in L^\infty(\Omega;\{0,1\})} \Big\{ \sum_{i=1}^{p} c_i(\chi) + \ell \int_\Omega \chi(x) \Big\}, \tag{1.38}$$

where $c_i(\chi)$ is the generalized compliance defined by (1.34) for the boundary condition f_i.

It is well-known since the seminar counter-examples of Murat [19], that problems of the type (1.35) or (1.37) do not generally admit solution to the extent that minimizers do not exist among characteristic functions. The problem must be relaxed : allow for micro-perforated composite as admissible designs and the optimum is achieved by a composite or generalized design. This is due to the fact that composite designs, made of very small microstructures can always outperform genuine designs made of plain material.

1.3.2 The relaxed optimal design problem

A composite design is described by the local density $\theta(x) \in L^\infty(\Omega; [0,1])$ of material and an homogenized elasticity tensor $A^*(x)$ that depends on the microstructure at the point $x \in \Omega$. The homogenized or macroscopic displacement u^* of the structure is then solution of the following set of equations

$$\begin{cases} \sigma = A^* e(u^*) \quad e(u^*) = \frac{1}{2}(\nabla u^* + \nabla^t u^*), \\ div(\sigma) = 0 \quad \text{in } \Omega, \\ \sigma \,.\, n = f \quad \text{on } \Gamma_N, \\ \sigma \,.\, n = 0 \quad \text{on } \partial\Omega \setminus \Gamma_N, \end{cases} \tag{1.39}$$

such that Γ_N contains the part of $\partial\Omega$ where f is non zero. We emphasize that the problem is now defined on the whole working space Ω and no longer on a design Ω_χ. Thus, the minimization problem (1.37) is replaced by

$$I^*(\ell) := \min_{\tau \in \Sigma(\Omega)} \Big\{ \min_{0 \le \theta \le 1} \Big\{ c^*(\theta) + \ell \int_\Omega \theta \, dx \Big\} \Big\}, \tag{1.40}$$

where $\Sigma(\Omega)$ is defined by

$$\Sigma(\Omega) = \Big\{ \tau \in L^2(\Omega; \mathbb{R}_s^{N^2}) \mid div(\tau) = 0 \text{ in } \Omega;\ \tau \,.\, n = f \text{ on } \partial\Omega \Big\}. \tag{1.41}$$

and $c^*(\theta)$ is defined by

$$c^*(\theta) = \min_{A^*(x) \in \mathcal{G}_{\theta(x)}} \int_\Omega A^{*-1}\tau \,.\tau \, dx, \tag{1.42}$$

where we recall that, $\mathcal{G}_{\theta(x)}$ is the set of effective or homogenized Hooke's laws for microstructures of density $\theta(x)$. The quantity $c^*(\theta)$, defined by (1.42) is called the

relaxed or homogenized compliance for a perforated composite material obtained by mixing the material A with holes in proportions $\theta(x)$ and $1-\theta(x)$.

The main difficulties in the homogenized formulation defined by (1.40) are first to compute the relaxed compliance $c^*(\theta)$, which may be different from the original compliance $c(\chi)$ and then the most important, is to give a complete and explicit description of the set of admissible Hooke's laws $\mathcal{G}_\theta$. Unfortunately as aforementioned, the set of effective tensors resulting from the mixture in fixed volume fraction of two elastic materials is unknown for the general case of non-defined underlaying microstructures topologies. This obstacle is alleviated in the particular case where the objective functional is the elastic compliance because its minimum can be computed among a well-known subset of the full set of effective tensors, namely that of a sequential laminates (see [29] for more details). To circumvent these obstacles, following the lead of [20, 77], we propose to limit the set of admissible composite designs to microstructures for which the Hooke's law can be numerically computed (typically, periodic composites with a hexagonal cells in 2-d and tetrakaidecahedron cell in 3-d).

This work should approached within such background. We content ourselves with the relaxed version (1.40) of the original optimization problem (1.35). As such, we denote by u, the homogenized displacement solution of (1.39).

Deuxième partie

Contribution

Chapitre 2

Homogenization-based topology optimization of 2-D and 3-D structures built with isotropic composite materials

2.1 Introduction

In this chapter, homogenization based topology optimization method is presented to optimize elastic structures made of modulated isotropic materials in 2-d and 3-d. We seek minimizers among composites made of microstructures periodically perforated by hexagonal cells in 2-d and tetrakaidecahedron cell in 3-d ; such microstructures in 2-d or 3-d are of high interest because there is no need to orientate them locally in the domain, which simplifies the optimization process as well as the deshomogenization process. Moreover, the geometry of the periodic cell is parametrized by only one parameter : the material density θ. Hence, only the density has to be optimized, which makes the optimization process similar to the density-based approach : e.g, the SIMP method. Nevertheless, the homogenization-based approach relies on true composite materials ; the homogenized elasticity tensor has to be computed and taken into account during the optimization process, which makes it more rigorous than the SIMP approach, which relies on fictitious material approximated by a power law of the density.

In the next section, isotropic 2-d and 3-d periodic cells are introduced : we compute their homogenized elasticity tensor as well as the corresponding stress amplification tensor. Next in section 3, we present the optimization algorithm based on the gradient descent method. Several objective functions are investigated : the minimum compliance in single-load and multiple-loads, the minimum displacement for a given target, the minimum L^2-norm of the stress tensor and the maximization of the first eigenfrequency. In section 4, we briefly recall the deshomogenization process introduced in [20], for the post-treatment of the composite solutions. We only seek minimizers among composites made of microstructures periodically perforated by isotropic cells.

2.2 Isotropic periodic microstructures

In this section, three isotropic microstructures in 2-d and one in 3-d are presented. For sake of simplicity, only one parameter is retained here to modulate the isotropic lattice material : the material density θ. Other equivalent parameters could be chosen, as the width of the bars, also more parameters could have been retained in order to design a morphing between different types of isotropic cells.

2.2.1 Cell designs

A composite design is described by the local density $\theta(x)$ of the material and the homogenized tensor $A^*(x)$ that depends on the microstructure at the point $x \in \Omega$ in the design domain. We restrict ourselves and restrain our analysis to a simple class of composites already investigated in [20]. Herein, the composites are periodically perforated by hexagonal cells in 2-d and by tetrakaidecahedron cell in 3-d.

Classical honeycomb

We denote by Y, the classical honeycomb cell, namely, a regular hexagon perforated by an hexagonal hole (see, Figure 2.1(a)). The design cell Y is parametrized by one parameter, its density $\theta \in [0, 1]$, which varies from void (i.e., $\theta = 0$) to full material (i.e., $\theta = 1$). Let m be the relative width of the bars of Y in $[0, \frac{\sqrt{3}}{2}]$, defined by

$$m = \frac{\sqrt{3}}{2}(1 - \sqrt{1 - \theta}), \tag{2.1}$$

where m is density-dependent, varying from 0 to $\frac{\sqrt{3}}{2}$.

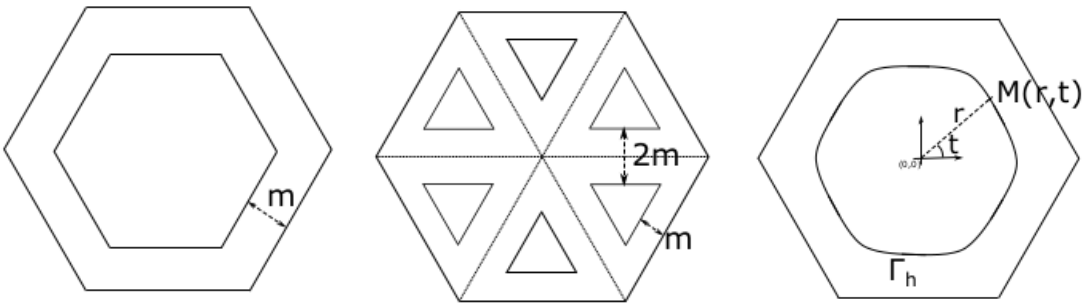

(a) Classical honeycomb (b) Reinforced honeycomb (c) Smooth honeycomb

Figure 2.1 – Isotropic design cells in 2-d (images taken from [20])

Reinforced honeycomb

Let Y be the reinforced honeycomb cell, namely, a regular hexagon perforated by triangle-like truss holes. The design cell Y is characterized by its three diagonals, where its periodic pattern can be seen as a truss of three groups of parallel bars ; all the bars are of same width, equally spaced and oriented : the angle between two bars of different groups is equal to $\frac{\pi}{3}$ (see, Figure 2.1.b). Like wise, Y is parametrized by its density θ, which varies from void to full material. Let m be the relative width of the bars of Y in $[0, \frac{1}{2\sqrt{3}}]$, defined by

$$m = \frac{1}{2\sqrt{3}}(1 - \sqrt{1 - \theta}), \tag{2.2}$$

where likewise, m is density-dependent, varying from 0 to $\frac{1}{2\sqrt{3}}$.

Smooth honeycomb

We denote by Y, the periodic smooth honeycomb cell ; similar to the classical honeycomb, except that the interiors corners of its regular hexagon hole are rounded (see Figure 2.1(c)). Consequently, when the density $\theta \in [0, 1]$, tends to one, its central smooth hexagon hole tends to a circle with a diameter going to zero. However, because

of its rounded corners, the smooth honeycomb can not reach completely void (i.e., θ going to zero is excluded). In addition, the design cell Y is not parametrized using its density θ, for practical reason ; but, another parameter $h \in [0,1]$, homogeneous to a distance. Indeed, in order to design this kind of cell, a parametric curve Γ_h, depending on h is introduced and represents the boundary of its smooth central hole. We introduce some notations before giving its polar equation. Let $v(t) = (\cos(t), \sin(t))^T$ and n_i, with $i \in \{0,1,2\}$ represent the normal vectors of the three diagonals of Y, defined by

$$n_0 = \begin{pmatrix} 0 \\ 1 \end{pmatrix}, \quad n_1 = \begin{pmatrix} \frac{\sqrt{3}}{2} \\ \frac{1}{2} \end{pmatrix}, \quad n_2 = \begin{pmatrix} \frac{\sqrt{3}}{2} \\ -\frac{1}{2} \end{pmatrix}. \tag{2.3}$$

Next, the polar equation of Γ_h is defined by

$$r(t) = h\frac{\sqrt{3}}{2}(\sum_{i=0}^{2} |v(t) \,.\, n_i|^{k(h)})^{\frac{-1}{k(h)}} \quad \text{with } t \in [0, 2\pi], \tag{2.4}$$

where k is positive coefficient, which depends on h : in this work, we took $k(h) = 4 + 20h^2$. We emphasize that h is homogeneous to a distance and it is similar to the parameter

$$m = \frac{\sqrt{3}}{2}(1 - \sqrt{1-\theta}),$$

which denotes the relative width of bars with respect to the size of Y. Thus, these three design cells are parametrized quite the same way. Now, the polar equation of Γ_h relies on the following remarks and can be extended to other polygons. Let $\mathcal{H}$ be a a regular unit hexagon. By definition, $\mathcal{H}$ is the set of all points such that, the maximal distance of a point in $\mathcal{H}$ from the three diagonals is equal to $\frac{\sqrt{3}}{2}$. Let $M(r,t)$ be a point, with its polar coordinate denoted by (r,t). Thus, M is a point in $\mathcal{H}$ if and only if, its polar coordinate (r,t) satisfies

$$r \max_i |v(t) \,.\, n_i| = \frac{\sqrt{3}}{2}. \tag{2.5}$$

Consequently, the polar equation of $\mathcal{H}$ verifies

$$r(t) = \frac{\sqrt{3}}{2}(\max_i |v(t) \,.\, n_i|)^{-1}. \tag{2.6}$$

In addition, we recall that

$$(\sum_{i=0}^{2} |v(t) \,.\, n_i|^{k})^{\frac{-1}{k}} \to_{k\to\infty} \max_i |v(t) \,.\, n_i|. \tag{2.7}$$

The polar equation of Γ_h comes from combining the polar equation of $\mathcal{H}$ and the above limit ; parameter h is added in order to adjust the diameter of its inner hole. The interest of the smooth honeycomb relies on its smooth rounded corners, known to generate lower local concentration stress ([78, 79]), compare to the classical honeycomb.

remark 10. *The structure of the periodic cell $Y(h)$ as well as its Hooke's law are qualitatively similar to the celebrated Vigdergauz hexagonal cell [71], which is known to*

generate extreme composite microstructures, in the sense that they minimize the energy. Moreover, we do not claim that the smooth honeycomb can reach a particular elastic properties. The announced goal consists in reducing the stress concentration localized around the sharp corners of the classical honeycomb.

Tetrakaidecahedron

Isotropic cells are not so easy to design in 3-d, they are bit difficult. But, in [20, 76], a regular tetrakaidecahedron, known as the Kelvin foam was introduced : it is numerically shown to yield an isotropic (or quasi) homogenized Hooke's law. In addition, isotropic cells with particular proprieties were introduced in [67], like the sequential laminates. However, for our purpose, easily parametrizable cell is required ; so we chose from the start to focus on the unit tetrakaidecahedron. Its features fourteen faces : six unit squares and eight regular unit hexagons (see Figure 2.2).

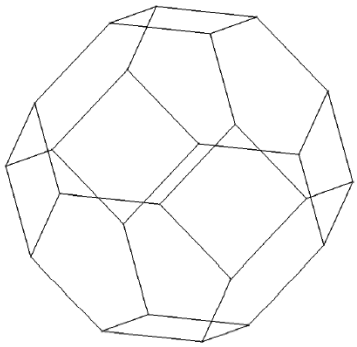

Figure 2.2 – Tetrakaidecahedron : an isotropic design cell in 3-d (image taken from [20]).

Several approaches are possible in order to design a parametrized isotropic cell from this one, with its density θ in $[0, 1]$. A naive approach consists in adding a central tetrakaidecahedron inclusion characterized by its size in $[0, 1]$. However, we should keep in mind that the final structure has to be manufacturable using additive manufacturing processes, including metallic ones : no inclusion is permitted because metal powder could be trapped inside during the process and could be impossible to remove at the end. Consequently, the cell should be drilled from end to end : through holes are drilled from each face to its opposite face (see Figures 2.3 and 2.4).

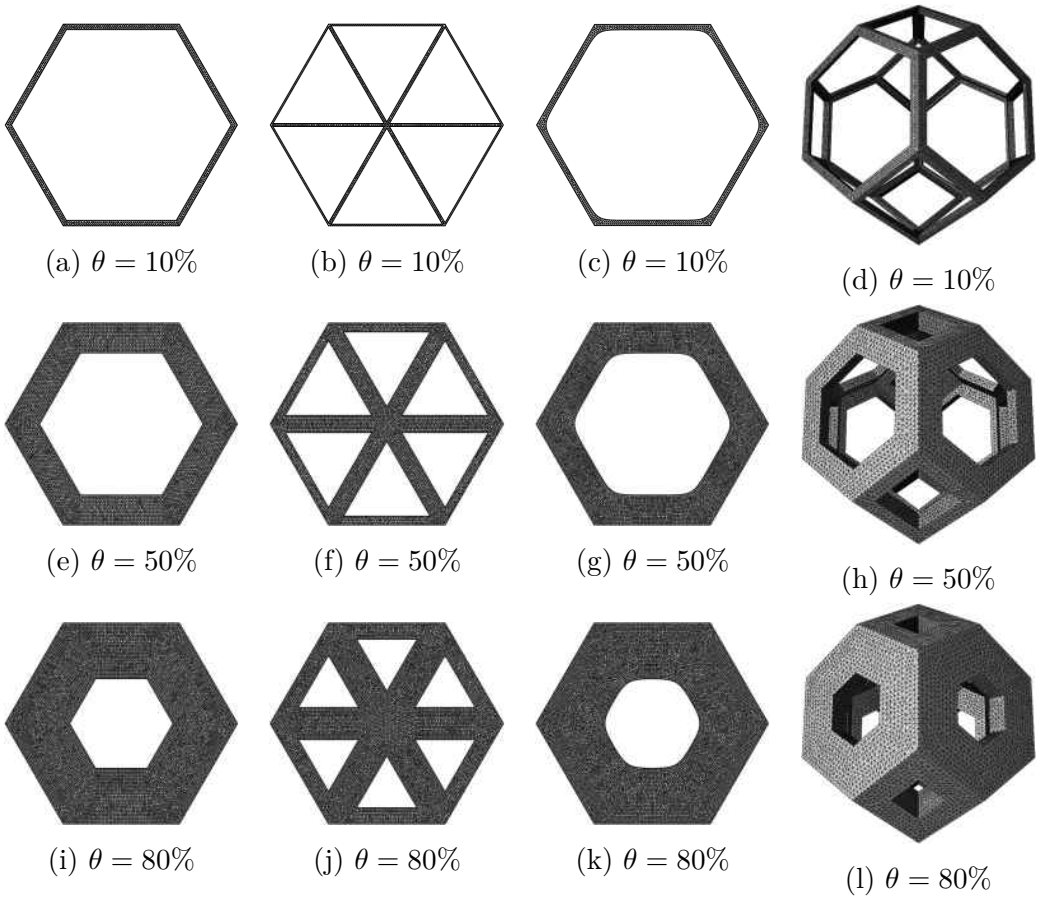

(a) $\theta = 10\%$ (b) $\theta = 10\%$ (c) $\theta = 10\%$ (d) $\theta = 10\%$

(e) $\theta = 50\%$ (f) $\theta = 50\%$ (g) $\theta = 50\%$ (h) $\theta = 50\%$

(i) $\theta = 80\%$ (j) $\theta = 80\%$ (k) $\theta = 80\%$ (l) $\theta = 80\%$

FIGURE 2.3 – Isotropic design cells : classical (first column), reinforced (second column), smooth honeycomb (third column) and Kelvin Foam (fourth column), wrt. their density θ

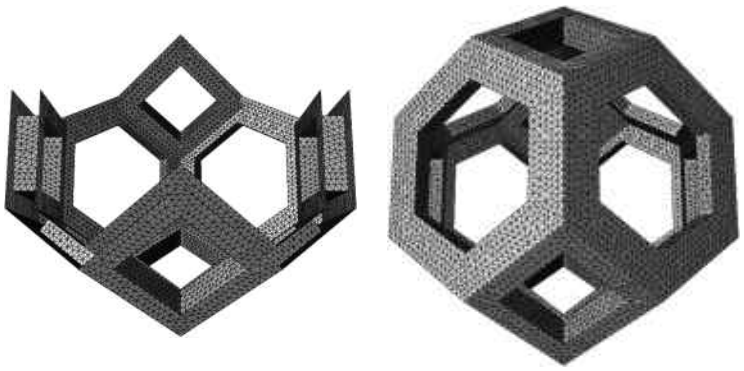

FIGURE 2.4 – Tetrakaidecahedron : clipping (left) and complete (right) design cell in 3-d

2.2.2 The Homogenized Hooke's laws

For sake of clarity, few important results on the theory of homogenization are briefly recalled hereafter, the interested reader should refer to sect. 1.1.3 of chapter 1 or textbook [59] for details. Assume that, in a given macroscopic domain Ω, there is a periodic distribution of holes inside an elastic isotropic phase with constant elastic tensor A defined by :

$$A = 2\mu I_{2N} + (\kappa - \frac{2\mu}{N}) I_N \otimes I_N,$$

where κ and μ are the bulk and shear moduli of the elastic phase A, with its Lamé coefficient defined by $\lambda = \kappa - \frac{2\mu}{N}$. Let $\epsilon > 0$ be the periodicity size, wherein the rescaled periodicity cell is either the regular hexagonal in 2-d (see Figure 2.1) or the regular tetrakaidecahedron in 3-d (see Figure 2.2), denoted by Y. We emphasize that, the periodicity of the cell Y is defined by the displacement along its opposite and parallel faces. Hence, for the hexagonal cells, there are three directions of periodicity and for the tetrakaidecahedron cell, there are seven directions of periodicity. Inside the periodic cell of volume denoted by $|Y|$, let $Y_0 \subset Y$ be the solid phase, where its complement being the hole(s). Let Γ_{int} be the boundary of its complement (i.e., $\Gamma_{int} = \partial(Y \backslash Y_0)$), where its normal vector is denoted by $\boldsymbol{n}$. Whenever ϵ tends to zero, the porous medium can be considered homogeneous, with the effective Hooke's law denoted by $A^*(x)$.

As seen in sect.1.1.3 of chapter 1, to compute the homogenized tensor $A^*(x)$, one needs the so-called correctors w_{ij}, corresponding to the local displacements in the periodic cell Y_0, defined for each pair $(i,j) \in \{1,..,N\}$, as the solutions to the set of equations defined by

$$\begin{cases} div(A(e_{ij} + e(w_{ij}))) = 0 & \text{in } Y_0 \\ A(e_{ij} + e(w_{ij})) \,.\, \boldsymbol{n} = 0 & \text{on } \Gamma_{int} \\ y \mapsto w_{ij}(y) & Y_0 \text{ periodic,} \end{cases} \tag{2.8}$$

where $e_{ij} = \frac{1}{2}(e_i \otimes e_j + e_j \otimes e_i)$ is the basis of the symmetric tensors of order 2 and $\boldsymbol{n}$, the normal vector to Γ_{int}. Thus, the variational formulation associated to (2.8) is defined by : find $w_{ij} \in H^1_{\#}(Y_0, \mathbb{R}^N)$ such that

$$\forall \phi \in H^1_{\#}(Y_0, \mathbb{R}^N) \quad \int_{Y_0} Ae(w_{ij}) \;:\; e(\phi) + \int_{Y_0} Ae_{ij} \;:\; e(\phi) = 0, \tag{2.9}$$

which admits a unique solution (up to a rigid displacement field). The entries of the homogenized tensor $A^*(x)$ is then given in terms of the correctors w_{ij}, solutions of (2.2) given by

$$A^*_{ijkl} = \frac{1}{|Y|} \int_{Y_0} A(e_{ij} + e(w_{ij})) \;:\; (e_{kl} + e(w_{kl}))\, dy \quad \forall i,j,k,l \in \{1,..,N\} \tag{2.10}$$

Where the symbol # denotes the periodicity of the solutions w_{ij}.

remark 11. *We emphasize that in (2.10), the coefficient is divided by the volume $|Y|$: in general, to bypass this point, the periodic cell is design such that its volume $|Y| = 1$. However with intricate cells like the tetrakaidecahedron, its is preferable to design a regular unit cell and if so, one should not forget to rescale the computed coefficients.*

Restricting the analysis to periodic composites is an acceptable limitation because the set of Hooke's laws of periodic composites is dense in the set of all possible Hooke's laws reachable with composites [59]. However, restricting the set of periodic composites to regular hexagonal cells in 2-d or regular tetrakaidecahedron cell in 3-d, is clearly a loss of generality. Exploring a larger range of periodic microstructures is an obvious line of research for future work (see Appendix 5.4, for composite built with orthotropic cell).

We recall that, the homogenized tensor A^* is isotropic, thus, it is given by

$$A^* = 2\mu^* I_{2N} + (\kappa^* - \frac{2\mu^*}{N}) I_N \otimes I_N,$$

where κ^* and μ^* are the bulk and shear moduli of the homogenized Hooke's law A^*, with its Lamé coefficient defined by $\lambda^* = \kappa^* - \frac{2\mu^*}{N}$. Furthermore, its entries are given by

$$\begin{cases} \mu^* = A^*_{ijij} & \\ \lambda^* = A^*_{iijj} & \forall i,j \in \{1,...,N\} \\ \kappa^* = A^*_{iijj} + \frac{2}{N} A^*_{ijij} & \end{cases} \tag{2.11}$$

We recall that, the homogenized tensor A^* is isotropic, thus, it is given by

$$A^* = 2\mu^* I_{2N} + (\kappa^* - \frac{2\mu^*}{N}) I_N \otimes I_N,$$

where κ^* and μ^* are the bulk and shear moduli of the homogenized Hooke's law A^*, with its Lamé coefficient defined by $\lambda^* = \kappa^* - \frac{2\mu^*}{N}$. Furthermore, its entries are given by

$$\begin{cases} \mu^* = A^*_{ijij} & \\ \lambda^* = A^*_{iijj} & \forall i,j \in \{1,...,N\} \\ \kappa^* = A^*_{iijj} + \frac{2}{N} A^*_{ijij} & \end{cases} \tag{2.12}$$

Hashin-Shtrikman bounds

As seen in sect. 1.2.2 of chapter 1, the bulk and the shear moduli of any isotropic two-phase composite material are bounded by the Hashin-Shtrikman bounds [66]. Here, the composite material is obtained by mixture of the elastic phase A and void in proportion θ and $1-\theta$, respectively. We recall that, the upper Hashin-Shtrikman bounds for the homogenized bulk κ_{HS} and shear μ_{HS} moduli are given by

$$\begin{cases} \kappa_{HS} = \frac{\kappa\mu\theta}{\kappa+\mu-\kappa\theta}, \quad \mu_{HS} = \frac{\kappa\mu\theta}{2(\kappa+\mu)-(\kappa+2\mu)\theta} & \text{in 2-D,} \\ \kappa_{HS} = \frac{4\kappa\mu\theta}{3\kappa+4\mu-3\kappa\theta}, \quad \mu_{HS} = \frac{(9\kappa+8\mu)\mu\theta}{5(3\kappa+4\mu)-6(\kappa+2\mu)\theta} & \text{in 3-D} \end{cases} \tag{2.13}$$

Numerical results

Our design cell Y is parametrized by its density θ, thus to perform the topology optimization, one needs to compute the set of effective elasticity tensors $\{A^*(\theta) \mid \theta \in$

$L^\infty(\Omega;[0,1])\}$. Furthermore, since the considered cell is specifically chosen in order to design an isotropic composites, only two coefficients of the homogenized tensor A^* : i.e., A^*_{1122} and A^*_{1212} could be computed in order to fully characterized A^*. However, to confirm the isotropy of the effective tensor A^*, we computed all its entries. In addition, to demonstrate that the hexagonal cells in 2-d and the tetrakaidecahedron cell in 3-d, are isotropic cells (or at least very close to one), the range of the density θ is regularly discretized with 50 elements in 2-d and with 20 elements in 3-d.

The cell problems (2.8) are solved using the software-FreeFem++ [80] : a finite element solver for a family of discrete values of the density $(\theta_i)_{i=0,...,n_s}$, where n_s is the size of the discretization. A linear material model with Young's modulus $\boldsymbol{E} = 12\times10^9 Nm^{-2}$ (i.e., 12GPa) and Poisson's ratio $\nu = 0.35$ were considered. Furthermore, the isotropy of A^* implies some equalities between its coefficients, i.e. :

$$\forall i,j,k,l,p \in \{1,...,N\} \quad \begin{cases} A^*_{iijk} = 0 \\ A^*_{iiii} = A^*_{jjjj} \\ A^*_{iijj} = A^*_{kkll} \\ A^*_{iiii} = A^*_{ijij} + A^*_{llpp} \end{cases} \tag{2.14}$$

Figures 2.5 to 2.7 depict the relative errors to the above equalities (2.14), computed for a discrete sample of material density θ for the hexagonal cells in 2-d and the tetrakaidecahedron cell in 3-d.

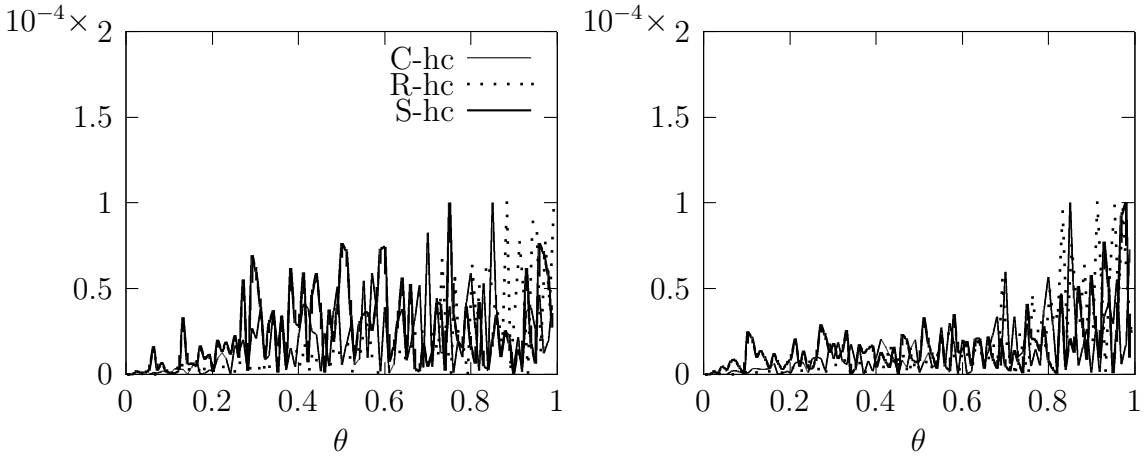

Figure 2.5 – The residual of $|A^*_{1112}|$ (left) and $|A^*_{2212}|$ (right), with respect to the hexagonal cells in 2-d : Classical honeycomb (C-hc), Reinforced honeycomb (R-hc) and Smooth honeycomb (S-hc)

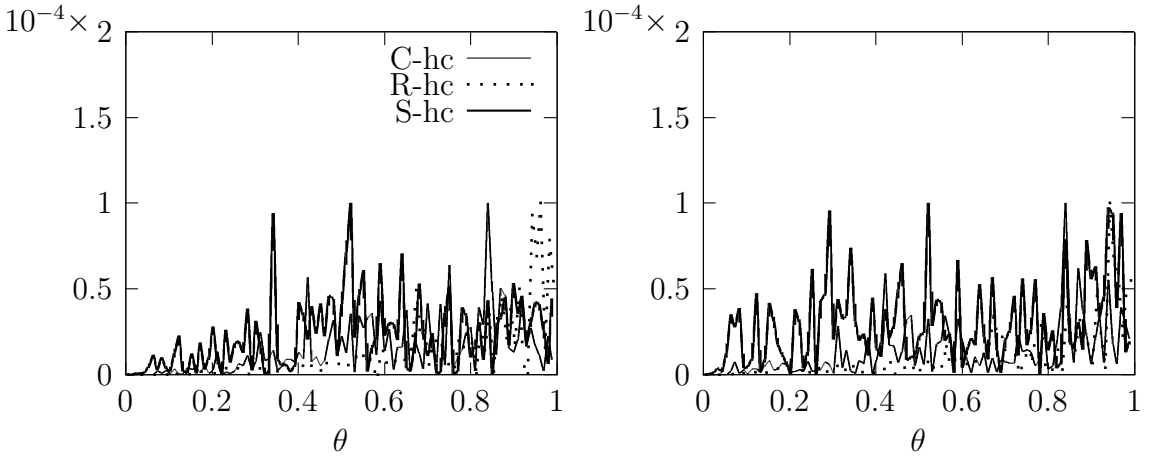

FIGURE 2.6 – The residual of $|A^*_{1111} - A^*_{2222}|$ (left) and $|A^*_{1212} - A^*_{1122} - A^*_{1111}|$ (right) , with respect to the hexagonal cells in 2-d : Classical honeycomb (C-hc), Reinforced honeycomb (R-hc) and Smooth honeycomb (S-hc)

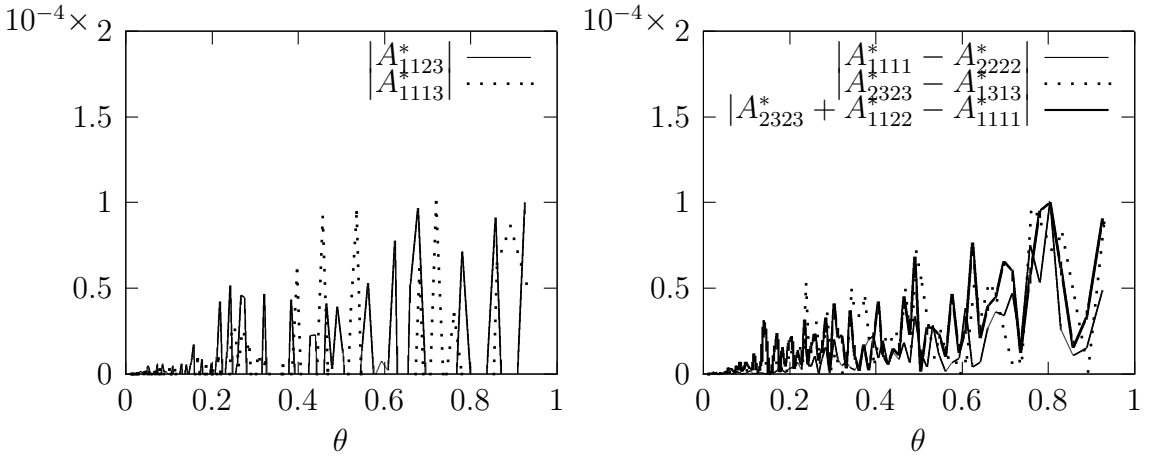

FIGURE 2.7 – The residual errors with respect to the tetrakaidecahedron cell in 3-d

Since, any isotropic two-phase composite material is bounded by the Hashin-Shtrikman bounds [66], the homogenized bulk κ^* and shear μ^* moduli of the effective Hooke's law A^* were also computed in order to confirm the boundedness. In each case, the coefficients are smooth increasing functions of the material density θ, which ensures that the optimization process will converge : one can see that the homogenized bulk of the classical and smooth honeycomb cells are very closed to the upper Hashin-Shtrikman bound : see Figures 2.8 and 2.9 for the numerical results.

remark 12. *We emphasize that, the void (i.e., $\theta = 0$) is fill with a very compliant material, like is the case in the SIMP method, in order to avoid singularities of the effective tensor when the elasticity problem is solved; its elastic phase A_{min} is equal to ϵA, wherein, we took $\epsilon = 10^{-4}$: it is numerically proven that, any value ϵ different from zero works fine.*

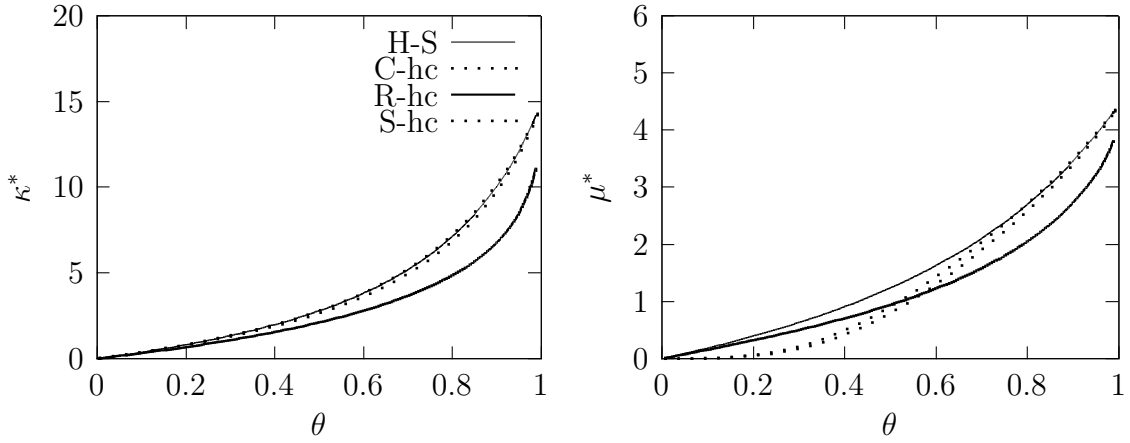

Figure 2.8 – The bulk κ^* (left) and shear μ^* (right) moduli wrt. the hexagonal cells in 2-d : classical honeycomb (C-hc), reinforced honeycomb (R-hc) and smooth honeycomb (S-hc), and with the upper Hashin-Shtrikman bounds (H-S) set as reference

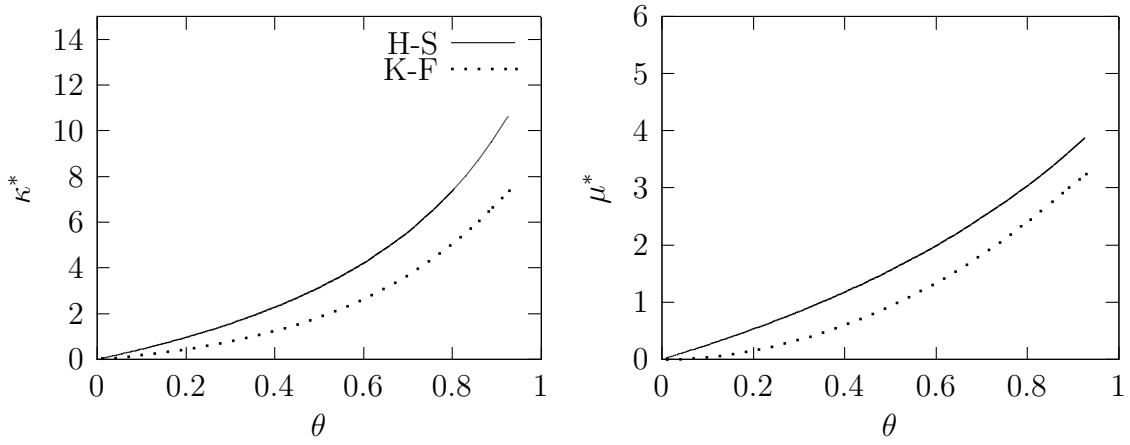

Figure 2.9 – The bulk κ^* (left) and shear μ^* (right) moduli wrt. the tetrakaidecahedron cell, i.e. : Kelvin foam (K-F), and the upper Hashin-Shtrikman bounds (H-S) set as reference

2.2.3 Corrector matrices

As seen in sect. 1.1.6 of chapter 1, the microscopic heterogeneities may cause stress concentration. The real stress distribution $\sigma_\epsilon = A^\epsilon e(u_\epsilon)$ of the microstructure of period ϵ is different from the macroscopic homogenized stress $\sigma_* = A^* e(u)$. This is due to the fact that the stress σ_ϵ for a microstructure of size ϵ does not converge strongly to the homogenized stress σ_*, when ϵ tends to zero (see [59] for details). Hence, a stress amplification factor may be introduced in order to compute the L^2-norm of the homogenized stress σ_* : this is not a pointwise maximum, as it could be requested in the case of plasticity or buckling of an elastic material : see section 1.1.6. We recall

from sect. 1.1.6 of chapter 1 that, the entries of the corrector tensor W are given by

$$W_{ijkl} = I^4_{ijkl} + e(w_{ij})_{kl},$$

where $(w_{ij})_{i,j=1,...,N}$ are the correctors, solutions of the cell problem (2.8). With the amplification factor P^* is given by

$$P^*(\theta) = \frac{1}{|Y|}\int_{Y_0} AW(y)A^{*-1}\, AW(y)A^{*-1}\, dy$$

The entries of amplification tensor $P^*(\theta)$ has been computed for the hexagonal cells in 2-d and tetrakaidecahedron cell on the same scheme as its homogenized one for a discrete values of θ, displayed by Figure 2.10.

Numerical results

The amplification tensor $P^*(\theta)$ has been computed for the hexagonal cells in 2-d, on the same scheme as the homogenized tensor $A^*(\theta)$ for a discrete values $(\theta_i)_{i=1,...,n_s}$ of the density. Let $\sigma_1 = 1\ .e_{11}$ and $\sigma_2 = \frac{\sqrt{2}}{2}(e_{12} + e_{21})$ be the unit stress in direction x_1 and in the plan x_1x_2, respectively. Assume that, a unit square is fulfilled with the above microstructure and that the homogenized stress σ^* is equal to σ_1 (or σ_2). Then, the L^2-norm of the corrected stress can be computed using the amplification tensor defined by :

$$P^*(\theta) = \begin{cases} P^*_{1111} & \textit{if } \sigma^* = \sigma_1 \\ P^*_{1212} & \textit{if } \sigma^* = \sigma_2 \end{cases}$$

Figure 2.10 depicts the above results computed for a discrete values $(\theta_i)_{i=1,...,n_s}$: for small densities, the L^2-norm of the corrected stress blows up. This is due to the fact that the local stress in the thin bars can not be approximated by the homogenized stress. Conversely, for high densities, the L^2-norm of the corrected stress converge to the L^2-norm of the homogenized stress, which is one. The amplification factor of the reinforced honeycomb is the lowest of the hexagonal cells in 2-d, followed by the smooth honeycomb and then the classical one.

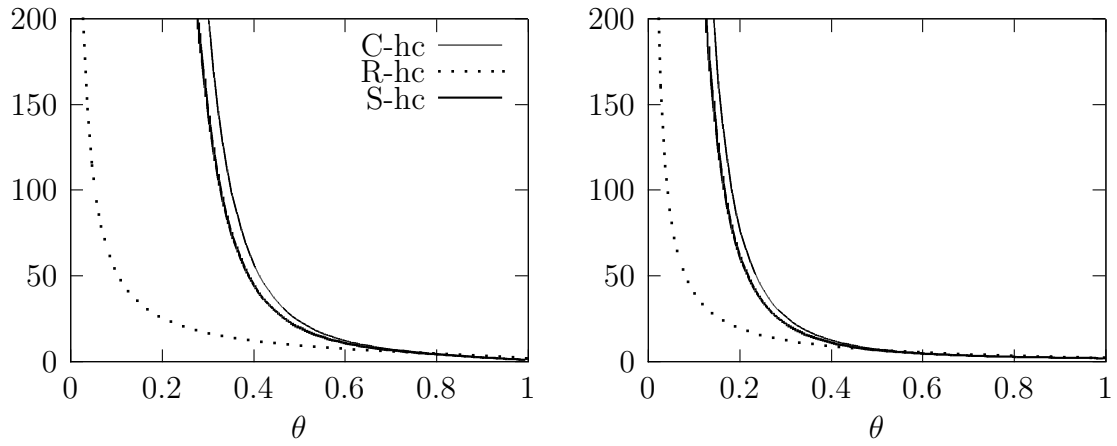

Figure 2.10 – The compression load P^*_{1111} (left) and the shear load P^*_{1212} (right) : L^2-norm of the corrected stress wrt the density of the hexagonal cells in 2-d.

2.3 Topology optimization of structures built with composite materials periodically perforated by isotropic cells

Let $J^*(\theta)$ be the relaxed objective function for composite materials periodically perforated by hexagonal cells in 2-d or tetrakaidecahedron cell in 3-d, where θ is the design variable : the density of composite materials periodically built with isotropic cells, parametrized by θ (see Figure 2.3). Here, in all the design problems presented, we assume that the volume is constrained to a volume fraction Θ given by :

$$\Theta = \frac{1}{|\Omega|}\int_\Omega \theta(x)\, dx, \tag{2.15}$$

Consequently, the minimization problem reads as :

$$\min_{\substack{0\le\theta\le 1 \\ \frac{1}{|\Omega|}\int_\Omega \theta\, dx=\Theta}} J^*(\theta) \tag{2.16}$$

2.3.1 The minimum compliance : single load case

Herein, we seek minimizers of the sum of elastic compliance and of the weight of a solid structure under specified loading, with its relaxed objective function defined by :

$$J^*(\theta) := \int_{\Gamma_N} f\ .\ u\ ds = \min_{\tau\in H_0}\Big\{\min_{A^*(x)\in G_\theta}\int_\Omega A^{*-1}\tau\ .\tau\ dx\Big\}, \tag{2.17}$$

where H_0 is defined as fellow :

$$H_0 = \left\{\tau\in L^2(\Omega;\mathcal{M}_2^s)\ |\ \begin{cases} -div(\tau) = 0 & \text{in } \Omega \\ \tau\ .\ n = f & \text{on } \Gamma_N \\ \tau\ .\ n = 0 & \text{on } \Gamma \end{cases}\right\} \tag{2.18}$$

where $\Gamma = \partial\Omega \backslash \Gamma_N$ is the free part of boundary $\partial\Omega$. As aforementioned, we explicitly compute the optimization process on a subset of all possible Hooke's laws G_θ, i.e. : composite periodically perforated by hexagonal cells in 2-d and tetrakaidecahedron cell in 3-d. Therefore, the set of effective elasticity tensors $\{A^*(\theta) \mid \theta \in L^\infty(\Omega, [0,1]\}$ has to be characterized. The proposed strategy consists in computing the material properties for a discrete sample of parameters values and using the collected data to construct a surrogate model for the constitutive law (by a simple linear interpolation). Consequently, the optimization problem defined by (2.16), can be recast as a minimization problem over the stress field σ in H_0 and density field θ in $L^\infty(\Omega; [0,1])$:

$$\inf_{\substack{\sigma \in H_0 \\ \theta \in L^\infty(\Omega;[0,1]) \\ \frac{1}{|\Omega|}\int_\Omega \theta \, dx = \Theta}} \int_\Omega A^{*-1}\sigma \, . \sigma \, dx \tag{2.19}$$

The problem is then solved using the alternate minimization algorithm [59], which consists in minimizing successively the stress tensor through the solving of the elasticity problem and density θ through a projected gradient method : it is an algorithm based on *optimality criteria*. Next, the corresponding Lagrangian, which is an augmented function of the objective function is introduced, that is :

$$\mathcal{L}(\theta, \sigma, \ell) = \int_\Omega A^{*-1}\sigma \, . \, \sigma \, dx + \ell(\int_\Omega \theta \, dx - \Theta), \tag{2.20}$$

in the hope that there exists a positive Lagrange multiplier ℓ, for which the volume constraint in (2.15) is met.

remark 13. *For sake of simplicity, we consider only the case where surface loads are applied. A straightforward modification of the model would however permit the consideration of volume forces or the clamping of part of the boundary $\partial\Omega$ (i.e., the enforcement of a Dirichlet boundary condition $u = 0$). The reader is referred to the numerical examples presented hereafter, which include different types of boundary conditions. The above optimization problem is usually referred to as a "single load" problem. This means that the elastic structure is optimized for a single configuration of loading forces and may well be totally inadequate for other loads. The reader should refer to section 3 of this chapter for the "multiple loads" problem.*

Minimizing over the stress field

Minimization over the stress field σ, consists in solving the linear elasticity problem (2.18) over the effective tensor $A^*(x)$ for given design $\theta(x)$ of microstructure periodically perforated by the hexagonal cells in 2-d or the tetrakaidecahedron cell in 3-d. Consequently, the linear elasticity problem is recast as a variational problem : find $u \in V(\Gamma_D)$ such that

$$\forall v \in V(\Gamma_D), \quad \int_\Omega A^*(\theta)e(u) \; : \; e(v) \, dx = \int_{\Gamma_N} f \, v \, ds, \tag{2.21}$$

with, $V(\Gamma_D)$ given by

$$V(\Gamma_D) := \{v \in H^1(\Omega;\mathbb{R}^N) \mid v = 0 \text{ on } \Gamma_D\} \tag{2.22}$$

Numerically, P_1 finite elements are used to compute the displacement field u.

Minimizing over the density field

For a given stress tensor σ, the minimization over the density field θ is performed using the projected gradient algorithm. As the optimization problem (2.19) is self-adjoint, the descend direction is given by solving the bilinear equation :

$$\left\langle \frac{\partial \mathcal{L}}{\partial \theta}(\theta,\sigma,\ell), h \right\rangle = -\int_\Omega \left(\frac{\partial A^*}{\partial \theta} A^{*-1}\sigma \ : \ A^{*-1}(\theta)\sigma - \ell \right) h \, dx, \tag{2.23}$$

where the descend direction $h = d\theta$ has to satisfy the inequality

$$\left\langle \frac{\partial \mathcal{L}}{\partial \theta}(\theta,\sigma,\ell), d\theta \right\rangle < 0 \tag{2.24}$$

Which is achieved by choosing

$$d\theta = \left(\frac{\partial A^*}{\partial \theta} A^{*-1}\sigma \ : \ A^{*-1}\sigma - \ell \right) \quad \text{in } \Omega. \tag{2.25}$$

At iteration n, the optimal density θ is then updated by performing the projected gradient :

$$\theta^{n+1} = P_{[0,1]}(\theta^n + \delta d\theta), \tag{2.26}$$

where $\delta > 0$ is the step size and $P_{[0,1]}$ is the projection operator on the interval $[0,1]$. The value of the Lagrange multiplier ℓ is computed at each iteration by a dichotomy process designed to respect the volume constraint. We emphasize that the exact value of ℓ can not be analytically given because of the projection operator : numerically, the partial derivative of the Lagrangian $\frac{\partial \mathcal{L}}{\partial \theta}$ is regularized using an equivalent H^1-norm by solving the following variational formulation :

$$\int_\Omega \left(\frac{\partial \mathcal{L}}{\partial \theta} h + \eta^2 \nabla \frac{\partial \mathcal{L}}{\partial \theta} \cdot \nabla h\right) dx = -\int_\Omega \left(\frac{\partial A^*}{\partial \theta} e(u) \ : \ e(u) - \ell \right) h \, dx, \tag{2.27}$$

where η is a small coefficient, which typically depends on the size of the elements of the mesh : thanks to this coefficient, we are able to numerically regularize the partial derivative on a length scale of order η and to limit the checkerboard effect on the density, similar to those reported in [81, 82, 83]. In practice, we use an adaptive step size δ, which consists in increasing δ by 20%, if the newly computed homogenized structure is accepted (i.e., if current compliance is lower than the previous one), else δ is divided by 2.

remark 14. *We emphasize that the derivative $\frac{\partial A^*}{\partial \theta}$ with respect the material density θ is computed using the difference finite method and a simple linear interpolation over the surrogate model.*

Volume constraint.

As explained in [29], we do not known how to determine ℓ beforehand. As such, an alternative computations were performed, where the Lagrange multiplier ℓ is adjusted at each iteration, so that the corresponding value of the optimal density satisfies the volume constraint. In other words, once the stress σ is computed through (2.18), we determine θ through (2.26) and then ℓ is determined through a simple iterative procedure, namely by dichotomy.

Complete optimization algorithm

The optimization algorithm is an iterative method structured as follows :

1. Initialization of the design variable θ such that :

$$\forall x \in \Omega \quad \theta^0(x) = \frac{\Theta}{\int_\Omega 1 \, dx}$$

2. Iteration until convergence, for $n \geq 0$:
   (a) Computation of the stress tensor σ^n through the linear elasticity problem (2.18) with design shape $(\theta^n(x), A^*(x))$
   (b) Computation of the descend direction $d\theta^n$ for the stress tensor σ^n using formula (2.27)
   (c) Updating the design variable θ^{n+1} using formulas (2.25-2.26) for the descend direction $d\theta^n$ and then updating the design $(\theta^{n+1}(x), A^*(x))$, by linear interpolation.

Note that, the alternate direction algorithm is apparented to the two known methods in [15, 22, 25].

Convergence criterion.

The above procedure is iterated until the quantity

$$\max\left((\max_i(|\theta_i^{n+1} - \theta_i^n|), 1 - \frac{\int_\Omega A^{*-1}(\theta^{n+1})\sigma^{n+1} \ : \ \sigma^{n+1} \, dx + \ell \int_\Omega \theta^{n+1} \, dx}{\int_\Omega A^{*-1}(\theta^n)\sigma^n \ : \ \sigma^n \, dx + \ell \int_\Omega \theta^n \, dx}\right)$$

becomes smaller than a preset threshold. About 160 iterations are required to reach a criterion of order 10^{-5}. Other convergence criteria could be used, for instance the L^2 norm of $\sigma^{n+1} - \sigma^n$.

Singularities in the composite Hooke's law.

The homogenized Hooke's laws computed at each iteration turn out to be singular, an undesired feature when solving problems of linear elasticity. This singular behaviour

has several sources. First, we note that the effective tensor is equal to zero when the density vanishes. Implicitly, the corresponding stress field should vanish simultaneously. This problem, which occurs in 2-d and 3-d is easily circumvented by imposing a positive threshold on the density. In practice, the smallest admissible value of θ is fixed at $1.e{-}3$. Numerical experiments suggest that the choice of 10^{-3} is not important.

Numerical results

We now present several numerical examples to show the efficacy and robustness of the proposed method. The algorithm has been implemented in FreeFem++[80], where all unknowns are discretized using P_1 finite elements and the stress field is averaged on each cell. The working space Ω is discretized with triangular elements in 2-d and tetrahedral elements in 3-d. All the computations are performed with a linear material model with Young's modulus $\boldsymbol{E} = 12 \times 10^9 Nm^{-2}$ (i.e., 12GPa) and Poisson's ratio $\nu = 0.35$. The void is replaced with a very compliant material in order to avoid singularities of the effective tensor when the elasticity problem is solved. The calculations are initialized with composite periodically perforated by hexagonal cells in 2-d or tetrakaidecahedron cell in 3-d : we attempted several computations with other initial shapes and obtained similar designs. The method seems stable with respect to the choice of initial configurations, although the number of iterations required for convergence may be greatly affected.

The 2-D cantilever

We start with a test case already been investigated by several authors [9, 20, 29] ; it has become a sort a benchmark for layout optimization algorithms. The workspace Ω is a rectangle of dimensions 1.6×1, discretized with 22000 element mesh. The structure to be found is submitted to a vertical load applied at middle of the right vertical side on a zone width $\frac{1}{10}$, while the left side is clamped : see 2.11, for schematic of this test case. The volume constraint is set to $\Theta = 35\%$ of the volume $|\Omega|$.

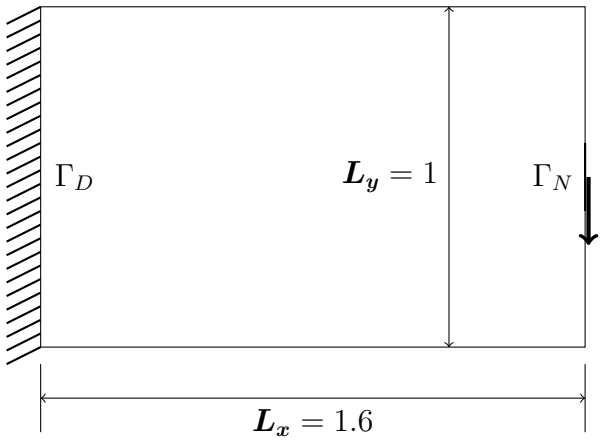

Figure 2.11 – Setting for the 2-d cantilever test case of Section 2.3.1

Figure 2.12 depicts the output of the algorithm computed for the three hexagonal cells, i.e. : the classical, reinforced and smooth honeycomb, while Figure 2.13 (as benchmark) shows the optimal density computed for composite made of rank-2 sequential laminates (obtained from the source code described in [29]).

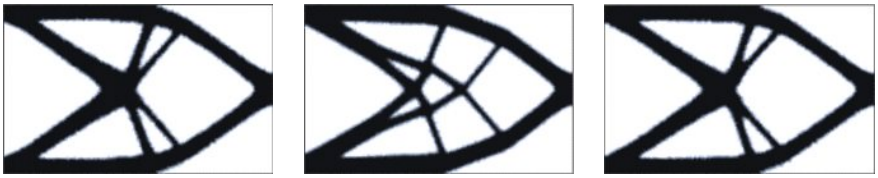

(a) C-hc (b) R-hc (c) S-hc

FIGURE 2.12 – Optimal density associated to the hexagonal cells in 2-d : Classical honeycomb (C-hc), Reinforced honeycomb (R-hc) and Smooth honeycomb (S-hc), for the 2-d cantilever test case 2.3.1

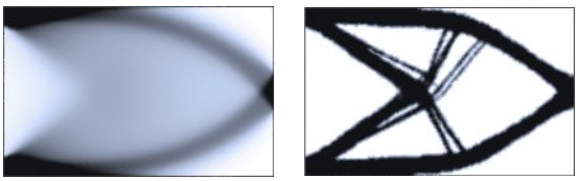

(a) (b)

FIGURE 2.13 – Optimal density (left) and penalized density (right), for the sub-optimal microstructure after penalization of the solution built with rank-2 sequential laminates [29]

It is noted that the structures built with the hexagonal cells are autopenalized, namely, they are black and white structures. The classical and smooth honeycomb microstructures are quite similar : this can be explained by the fact that their homogenized elasticity tensor are very closed as depicted by Figures 2.8 and 2.9. We emphasize that those structures are local minima, which might explains the differences that exist among the autopenalized structures.

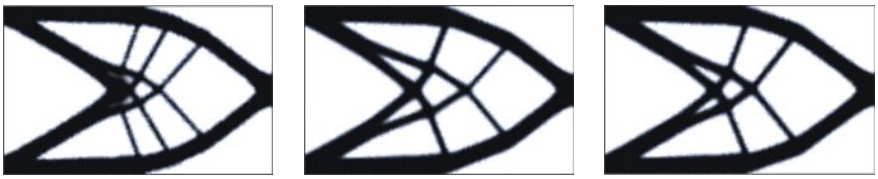

(a) $m = 100$ (b) $m = 1500$ (c) $m = 2000$

FIGURE 2.14 – Optimal design featuring different size m of surrogate model, wrt. the reinforced honeycomb

Here, the collected data used to construct the surrogate model for the constitutive law $\{A^*(\theta_i) \mid (\theta_i)_{1 \leq i \leq m}\}$ (by a simple linear interpolation) was of size $m = 1000$. It is

noted that the compliance of the structures is relatively better for all size $m \geq 100$. However, the topology of result is quite similar for all size $m \geq 100$: see Figure 2.14, for different size m. Figure 2.15 displays the convergence history for this calculations : smooth and relatively fast convergence is observed. As expected, the optimized compliance for the hexagonal cells are almost equal to each other, while the optimal solution built with rank-2 sequential laminates is the lowest.

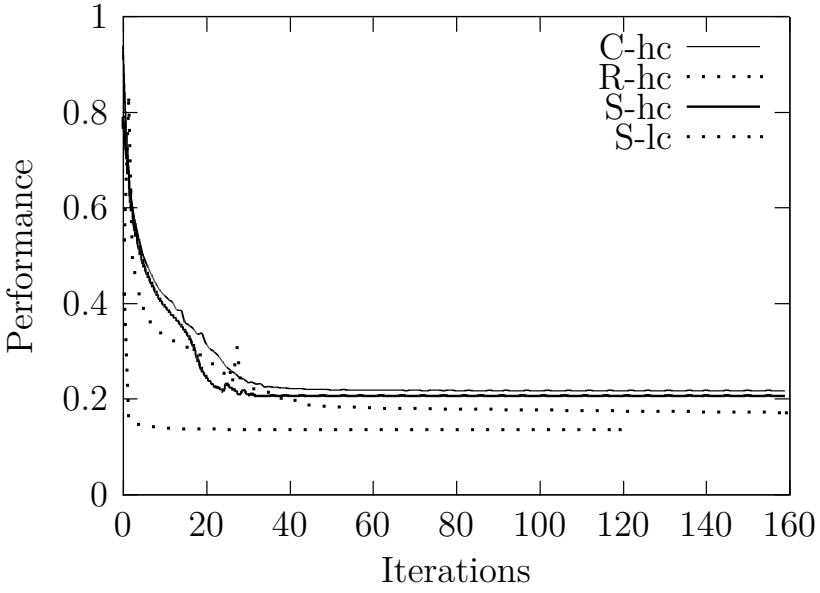

Figure 2.15 – Convergence history wrt. the hexagonal cells : Classical honeycomb (C-hc), Reinforced honeycomb (R-hc) and Smooth honeycomb (S-hc) ; and rank-2 sequential laminated composite (S-lc) for the 2-d cantilever test case

The 2-D bridge

In this second example [20, 29], the workspace Ω is a rectangle of dimensions 2×1.2, discretized with 35100 element mesh. The object to be found is supported at the edges of its lower boundary, on a zone of width $\frac{1}{8}$. A unit vertical load is applied on the middle part of its lower boundary, on a zone of width $\frac{1}{16}$: see 2.16 for a schematic of this test case. The volume constraint is set to $\Theta = 17\%$ of the volume $|\Omega|$.

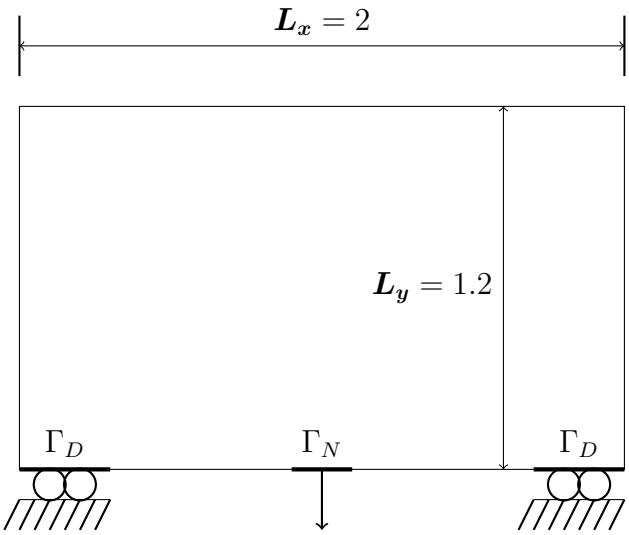

FIGURE 2.16 – Setting for the 2-d bridge test case 2.3.1

Figure 2.17 displays the optimal density computed for the three hexagonal cells in 2-d, while Figure 2.18 for composite made of rank-2 sequential laminates. Again, the topology of the result is similar to that obtained in previous literature [20, 29].

(a) C-hc (b) R-hc (c) S-hc

FIGURE 2.17 – Optimal density associated to the hexagonal cells in 2-d, for the 2-d bridge test case 2.3.1

In addition, the topology of the optimized structures with the classical and smooth honeycomb microstructures are autopenalized, whereas the reinforced honeycomb features grey densities. However, its final compliance is higher than the autopenalized structures : either the optimization process is trapped in a local minimum or the optimization is so slow for this microstructure that is not yet finished. In both cases, the optimized structure is not optimal : other parameters were used but we never reach a better structure.

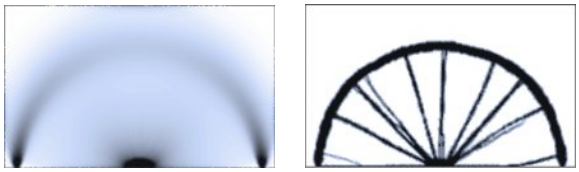

(a) (b)

Figure 2.18 – Optimal density (left) and penalized density (right) in the 2-d bridge test case : sub-optimal microstructure after penalization of the solution built with rank-2 sequential laminates

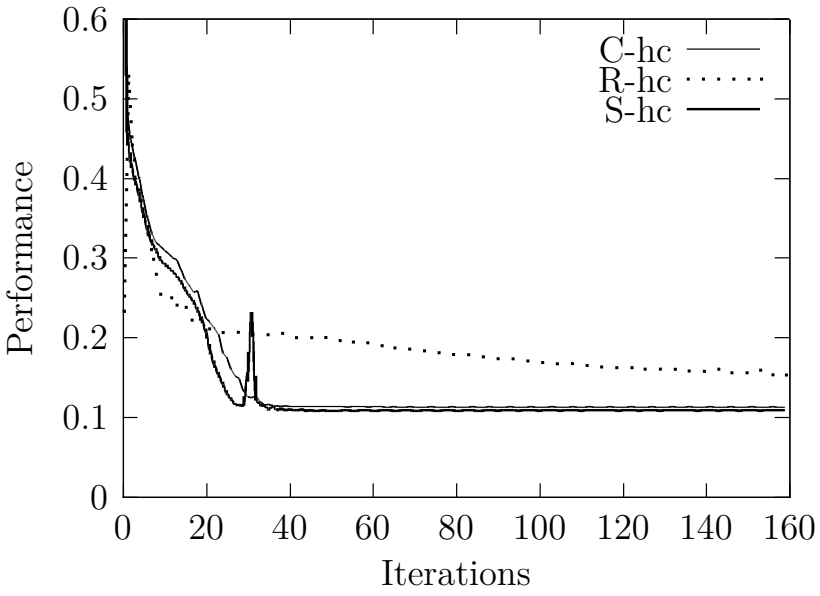

Figure 2.19 – Convergence history wrt. the hexagonal cells : Classical honeycomb (C-hc), Reinforced honeycomb (R-hc) and Smooth honeycomb (S-hc)

The 3-D cantilever

This 3-d example is analog to the first test case 2.3.1, already been investigated in [29]. The working space is a $1.6 \times 1 \times 0.6$ box. The structure to be found is submitted to a vertical load on a small surface of the right vertical side of area $\frac{1}{100}$, while the left side is clamped : see Figure 2.20, for a schematic of this test case. For this calculation, the volume constraint set to $\Theta = 15\%$ of the total domain $|\Omega|$ and we used for all finite element operations a mesh of size 41755 tetrahedral elements.

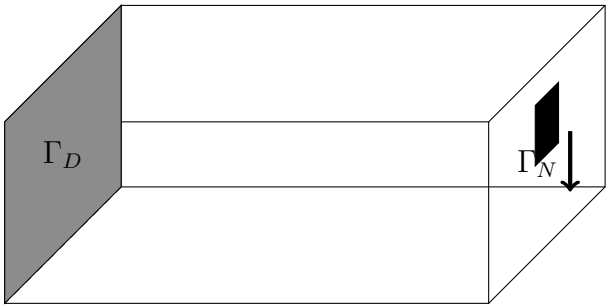

FIGURE 2.20 – Setting for the 3-d cantilever test case of Section 2.3.1

The 3-d pictures are harder to visualize. Figure 2.21 shows the resulting designs for a sweep of iso-surface θ of composite density. In this example, the iso-surfaces are smooth and embedded into each other as θ increases. The total **FreeFEM** running CPU time (2.60 **GHz**) for this calculation is 7986.82 seconds.

(a) $\theta \geq 10\%$ (b) $\theta \geq 25\%$

(c) $\theta \geq 50\%$ (d) $\theta \geq 60\%$

FIGURE 2.21 – Threshold of the domain according to the optimized density θ for 3-d cantilever test case of Section 2.3.1

The 3-D Bridge

This example [20] is analog to the second test case 2.3.1. The workspace is a $2.2 \times 1 \times 1.2$ box. The structure to be found is submitted to a vertical load on a small

surface of the middle lower surface of area $\frac{4}{100}$, while the left and right side surface is clamped : see Figure 2.22, for a schematic of this test case. For this calculation, the volume constraint is set to $\Theta = 25\%$, with the total **FreeFEM** running CPU time (2.60 **GHz**) 20710.9 seconds.

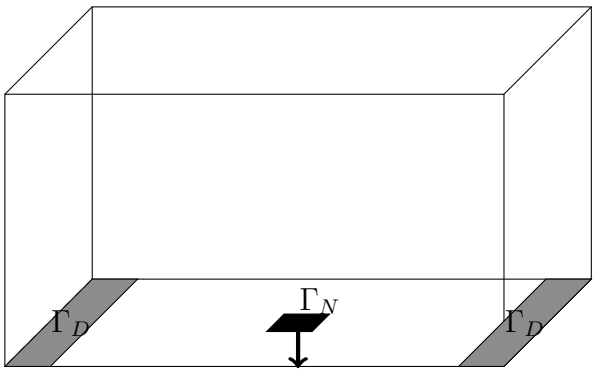

Figure 2.22 – Setting for the 3-d bridge test case of Section 2.3.1

Figure 2.23 represents the resulting designs for a sweep of iso-surface θ of composite density. Like in the 2-d case, the topology of the result is autopenalized.

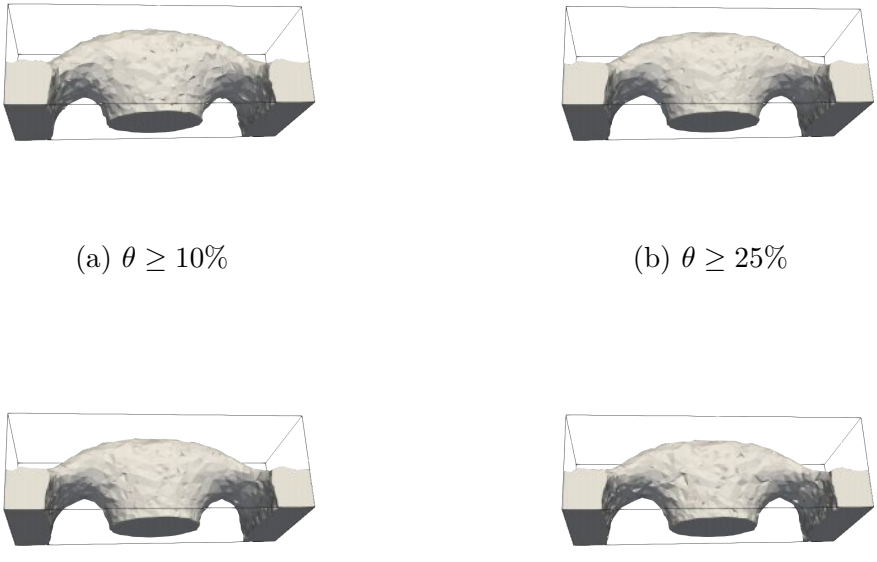

(a) $\theta \geq 10\%$

(b) $\theta \geq 25\%$

(c) $\theta \geq 50\%$

(d) $\theta \geq 70\%$

Figure 2.23 – Threshold of the domain according to the optimized density θ for 3-d Bridge test case of Section 2.3.1

The 3-D L-shape

This example is analog to the 2-d L-shape [20]. The working space is a $1 \times 0.5 \times 0.5$ L-like box (namely, a truncated cubic object). The structure to be found is submitted to a vertical load on a small surface of the right-vertical side of area $\frac{1}{100}$, while the top boundary is clamped.

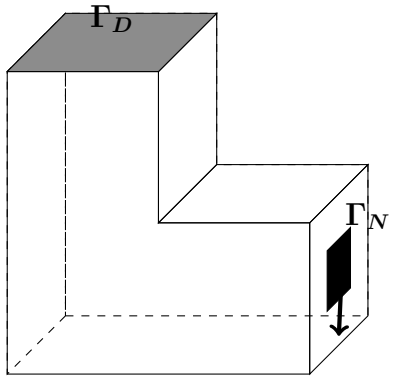

FIGURE 2.24 – Setting for the 3-d L-shape test case of Section 2.3.1. The grey region at the top wall correspond to fixed Dirichlet boundary (i.e.,$u = 0$). The black rectangle at middle-right wall is submitted to a vertical load (i.e., non-homogeneous Neumann boundary condition hold)

Figure 2.25 represents the iso-surface θ for a sweep of threshold of of composite density composite, the iso-surfaces are smooth and embedded into each other as θ increases.

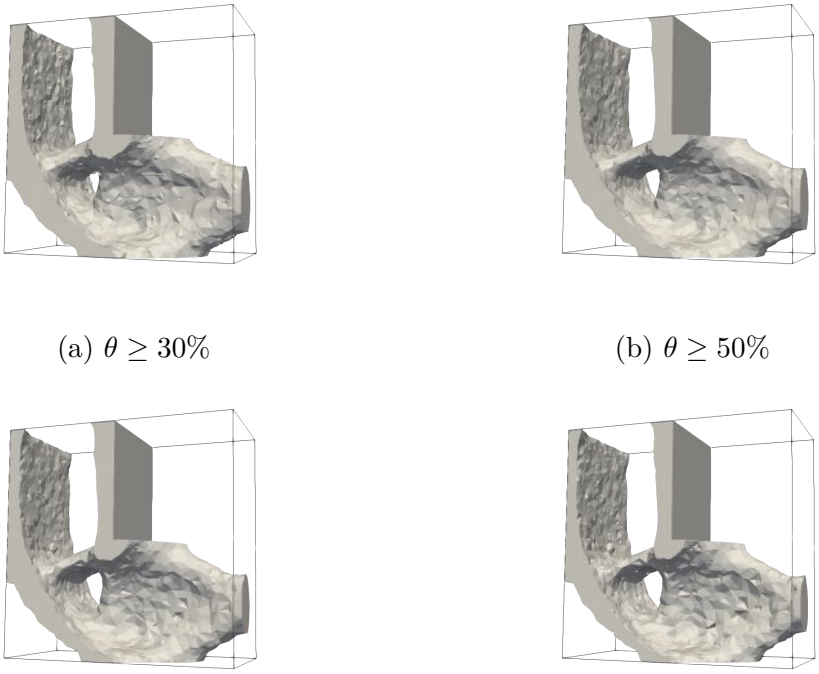

(a) $\theta \geq 30\%$ (b) $\theta \geq 50\%$

(c) $\theta \geq 60\%$ (d) $\theta \geq 70\%$

Figure 2.25 – Threshold of the domain according to the optimized density θ for 3-d L-shape test case of Section 2.3.1

2.3.2 The minimum compliance : multiple loads case

In this section, we investigate "multiple loads" problem which amounts to an optimization of the structure for several configurations, namely, various surface loadings $f_1, .., f_p$ are given and we consider the minimization problem

$$J^*(\theta) = \sum_{i=1}^{p} \int_{\Gamma_{N_i}} f_i \,.\, u_i \, ds = \sum_{i=1}^{p} \min_{\tau \in H_{0,i}} \left\{ \min_{A^*(x) \in G_\theta} \int_\Omega A^{*-1} \tau \,.\tau \, dx \right\}, \tag{2.28}$$

with $H_{0,i}$ defined by :

$$H_{0,i} = \left\{ \tau \in L^2(\Omega; \mathcal{M}_2^s) \mid \begin{cases} -div(\tau) = 0 & \text{in } \Omega \\ \tau \,.\, n = f_i & \text{on } \Gamma_{N_i} \\ \tau \,.\, n = 0 & \text{on } \Gamma \end{cases} \right\} \tag{2.29}$$

Where $\Gamma = \partial\Omega \backslash \cup_i \Gamma_{N_i}$ is the free part of boundary $\partial\Omega$ and $(\Gamma_{N_i})_i$ is the family of surface loading boundaries. As in the single load, this optimization problem can be recast as a minimization over the stress fields σ_i, for each configuration i and over the

density field θ of the microstructure

$$\inf_{\substack{\sigma\in H_{0,i}\\ \theta\in L^\infty(\Omega;[0,1])\\ \frac{1}{|\Omega|}\int_\Omega \theta\, dx=\Theta}} \sum_{i=1}^{p}\int_\Omega A^{*-1}\sigma\ .\sigma\ dx \tag{2.30}$$

Next, the corresponding Lagrangian is introduced

$$\mathcal{L}(\theta,\sigma_i,...,\sigma_p,\ell)=\sum_{i=1}^{p}\int_\Omega A^{*-1}\sigma_i\ .\ \sigma_i\ dx+\ell(\int_\Omega \theta\ dx-\Theta), \tag{2.31}$$

in the hope that there exists a positive Lagrange multiplier ℓ, for which the volume constraint is met. As in the single-load case, minimization over the stress field σ_i, for each configuration consists in solving the linear elasticity problem over the effective tensor $A^*(x)$ separately. Again, the minimization over the density field is performed using the projected gradient algorithm : the problem is still self-adjoint, so the descent step is given by the partial derivative of the Lagrangian $\mathcal{L}$ with respect to the density θ

$$\left\langle \frac{\partial\mathcal{L}}{\partial\theta}(\theta,\sigma_i,...,\sigma_p,\ell),h\right\rangle=\int_\Omega \ell h\ dx-\sum_{i=1}^{p}\int_\Omega\left(\frac{\partial A^*}{\partial\theta}A^{*-1}\sigma_i\ :\ A^{*-1}(\theta)\sigma_i\right)h\ dx, \tag{2.32}$$

where the optimization algorithm is identical to the single load case, except that p configuration of linear elasticity problems have to be solved and the descent step $d\theta$ is given by

$$d\theta=\sum_{i=1}^{p}\frac{\partial A^*}{\partial\theta}A^{*-1}\sigma_i\ :\ A^{*-1}\sigma_i-\ell\quad\text{in }\Omega. \tag{2.33}$$

Numerical results

As previously, the computations were performed over three isotropic hexagonal cells in 2-d and the tetrakaidecahedron cell in 3-d. The above algorithm has been implemented in FreeFem++[80], where all unknowns are discretized using P_1 finite elements and the stress field is averaged on each cell. All the computations are performed with a linear material model with Young's modulus $\boldsymbol{E}=12\text{GPa}$ ($12\times10^9 Nm^{-2}$) and Poisson's ratio $\nu=0.35$.

The 2-D bridge : multiple loads

We start with a test case already been investigated in [20, 29]. The workspace Ω is a rectangle of dimensions 2×1.2 discretized with 35100 element mesh. The object to be found is supported at the edges of its lower boundary, on a zone of width $\frac{1}{8}$. A unit vertical loads are applied separately on the several central part of its lower surface, on a zone of width $\frac{1}{16}$: see Figure 2.26, for a schematic of boundary conditions. For this calculation, the volume constraint set to $\Theta=20\%$.

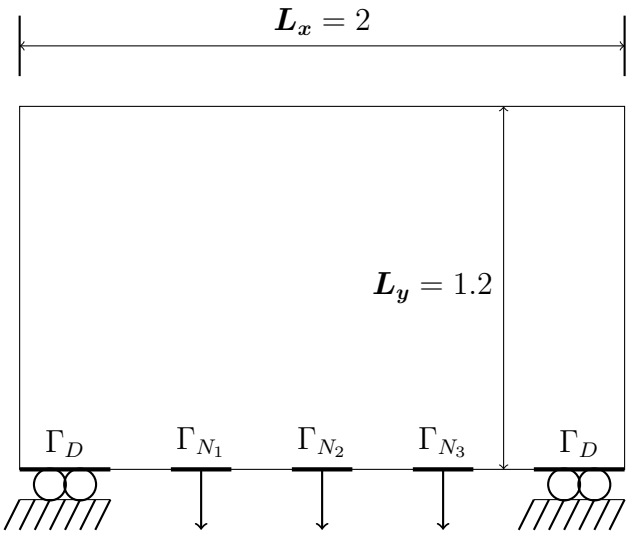

Figure 2.26 – Setting for the bridge in the multiple load case of Section 2.3.2

Figure 2.27 displays the output of the algorithm computed for the three hexagonal cells in 2-d. The topology of the result is similar to that obtained in previous literature [20, 29] for similar problems with different design and optimization settings. Each optimized structure features grey densities ; they are not autopenalized, which attest that isotropic microstructures are efficient for compliance minimization in the multiple load configurations.

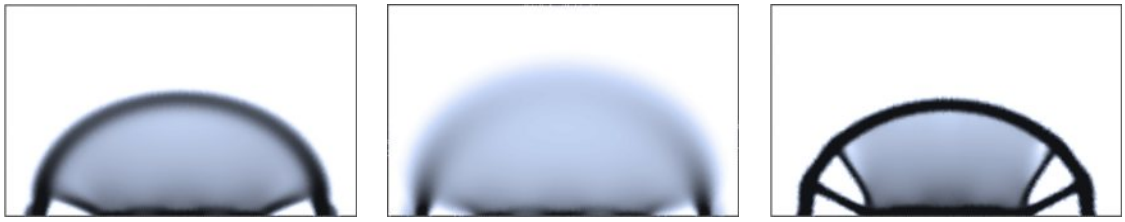

(a) Classical honeycomb (b) Reinforced honeycomb (c) Smooth honeycomb

Figure 2.27 – Optimal density associated to the hexagonal cells in 2-d, in the 2-d bridge test case of Section 2.3.2

Figure 2.3.2, depicts the convergence history for this calculation : smooth and relatively fast convergence is observed for all the three hexagonal cells. We emphasize that the reinforced honeycomb has the lowest compliance curve.

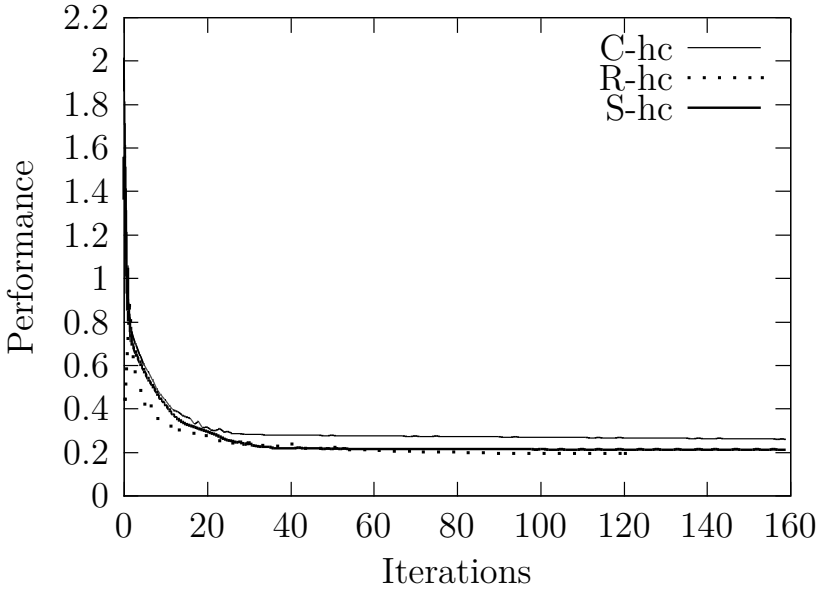

FIGURE 2.28 – Convergence history for the 2-d bridge featuring multiple loads, wrt. the hexagonal cells : Classical honeycomb (C-hc), Reinforced honeycomb (R-hc) and Smooth honeycomb (S-hc)

2.3.3 Displacement optimization

Here, we seek minimizers of a given elastic displacement and of the weight of a solid structure under specified loading. The relaxed objective function is given by

$$J^*(\theta) = \int_{\Gamma_T} (u - u_T)^2 \, ds, \tag{2.34}$$

where u_T is the target displacement : displacement to be found by u. In converse to the minimum compliance, the optimization problem is not self-adjoint ; thus one needs to define the associated adjoint problem, which we define using the Céa method. First, we introduce the following Lagrangian

$$\mathcal{L}(v, q, \theta, \ell) = \int_\Omega A^* e(v) \ : \ e(q) - \int_{\Gamma_N} f \ . \ q \ ds + \int_{\Gamma_T} (v - u_T)^2 \ ds + \ell(\int_\Omega \theta \ dx - \Theta), \tag{2.35}$$

where u_T is the target displacement : displacement to be found by u. In converse to the minimum compliance, the optimization problem is not self-adjoint, thus one needs to define the associated adjoint problem, which we define using the Céa method. First, we introduce the following Lagrangian

$$\mathcal{L}(v, q, \theta, \ell) = \int_\Omega A^* e(v) \ : \ e(q) - \int_{\Gamma_N} f \ . \ q \ ds + \int_{\Gamma_T} (v - u_T)^2 \ ds + \ell(\int_\Omega \theta \ dx - \Theta), \tag{2.36}$$

where $q \in H^1_{\Gamma_N}(\Omega)^N$ is the Lagrange multiplier for the elasticity equation : seen as a constraint in $H^1(\Omega; \mathbb{R}^N)$ such that $\frac{\partial q}{\partial n} = f$ on the boundary Γ_N. Again, ℓ is the Lagrange multiplier for the volume constraint.

Second, we compute the partial derivatives of the Lagrangian $\mathcal{L}$; let $u, p \in H^1_{\Gamma_N}(\Omega)^N$ be a stationary point of $\mathcal{L}$. The partial derivative of $\mathcal{L}$ with respect to q in the direction $\psi \in H^1_{\Gamma_N}(\Omega)^N$ is given by

$$\left\langle \frac{\partial \mathcal{L}}{\partial q}, \psi \right\rangle = \int_\Omega A^*(\theta)e(v) \ : \ e(\psi) - \int_{\Gamma_N} f \ . \ \psi \ ds \tag{2.37}$$

Thus, at the stationary point (u, p), the above derivative vanishes and leads to the variational formulation of the elasticity problem. Next, the partial derivative of $\mathcal{L}$ with respect to v in the direction $\psi \in H^1_{\Gamma_N}(\Omega)^N$ is given by

$$\left\langle \frac{\partial \mathcal{L}}{\partial v}, \psi \right\rangle = \int_\Omega A^*(\theta)e(\psi) \ : \ e(q) + \int_{\Gamma_T} 2(\psi - u_T) \ ds \tag{2.38}$$

At the stationary point (u, p), the above derivative vanishes and leads to the adjoint problem

$$\forall \psi \in H^1_{\Gamma_N}(\Omega)^N \quad \int_\Omega A^*(\theta)e(p) \ : \ e(\psi) = -\int_{\Gamma_T} 2(\psi - u_T) \ ds \tag{2.39}$$

And finally, the partial derivative of $\mathcal{L}$ with respect to θ in direction $h \in L^\infty(\Omega; \mathbb{R})$, at the stationary point (u, p) is given by

$$\left\langle \frac{\partial \mathcal{L}}{\partial \theta}, h \right\rangle = \int_\Omega (\frac{\partial A^*(\theta)}{\partial \theta} e(u) \ : \ e(p) + \ell) h \ dx \tag{2.40}$$

Now, as in the minimum compliance problem, the descent direction $h = d\theta$ has to be selected such that :

$$\left\langle \frac{\partial \mathcal{L}}{\partial \theta}(\theta, u, p, \ell), d\theta \right\rangle < 0, \tag{2.41}$$

which is achieved by choosing

$$d\theta = -\frac{\partial A^*}{\partial \theta} e(u) \ : \ e(p) - \ell \quad \text{in } \Omega. \tag{2.42}$$

At iteration n, the optimal density θ is then updated by performing the projected gradient :

$$\theta^{n+1} = P_{[0,1]}(\theta^n + \delta d\theta), \tag{2.43}$$

where $\delta > 0$ is the step size and $P_{[0,1]}$ is the projection operator on the interval $[0, 1]$. Again, the value of the Lagrange multiplier ℓ is computed at each iteration by a dichotomy process designed to respect the volume constraint.

2.3.4 Stress minimization

In this section, we seek minimizers of the sum of elastic stress and of the weight of a solid structure under specified loading, that is :

$$J^*(\theta) = \int_\Omega P^*(\theta)\sigma \ . \ \sigma \ dx = \int_\Omega P^*(\theta)A^*(\theta)e(u) \ . \ A^*(\theta)e(u) \ dx, \tag{2.44}$$

where $P^*(\theta)$ is the amplification tensor defined in section 2.2.3, while, $\sigma = A^*e(u)$ is the stress tensor (solution of the elasticity problem) and the associated displacement u. In converse to the minimum compliance, the above optimization problem is not self-adjoint, thus, one needs to define the adjoint problem. First, we introduce the Lagrangian

$$\mathcal{L}(v,q,\theta,\ell) = \int_\Omega A^*e(v) \ : \ e(q) - \int_{\Gamma_N} f.q \ ds + \int_\Omega P^*A^*e(v) \ : \ A^*e(v) \ dx + \ell(\int_\Omega \theta \ dx - \Theta),$$

where $q \in H^1_{\Gamma_N}(\Omega)^N$ is the Lagrange multiplier for the elasticity equation and ℓ, the Lagrange multiplier for the volume constraint. Next, we compute the partial derivatives of the Lagrangian $\mathcal{L}$.

Let $u, p \in H^1_{\Gamma_N}(\Omega)^N$ be a stationary point of $\mathcal{L}$. The partial derivative of $\mathcal{L}$ with respect to q in the direction $\psi \in H^1_{\Gamma_N}(\Omega)^N$ is given by

$$\left\langle \frac{\partial \mathcal{L}}{\partial q}, \psi \right\rangle = \int_\Omega A^*(\theta)e(v) \ : \ e(\psi) - \int_{\Gamma_N} f \ . \ \psi \ ds \tag{2.45}$$

which at the stationary point (u,p), vanishes and leads to the variational formulation of the elasticity problem. Next, the partial derivative of $\mathcal{L}$ with respect to v in the direction $\psi \in H^1_{\Gamma_N}(\Omega)^N$ is defined by

$$\left\langle \frac{\partial \mathcal{L}}{\partial v}, \psi \right\rangle = \int_\Omega A^*(\theta)e(\psi) \ : \ e(q) + \int_\Omega 2P^*(\theta)A^*(\theta)e(v) \ : \ A^*(\theta)e(\psi) \ dx \tag{2.46}$$

which at the stationary point (u,p), vanishes and leads to the adjoint problem

$$\forall \psi \in H^1_{\Gamma_N}(\Omega)^N \quad \int_\Omega A^*(\theta)e(p) \ : \ e(\psi) = -2 \int_\Omega P^*(\theta)A^*(\theta)e(u) \ : \ A^*(\theta)e(\psi) \ dx \tag{2.47}$$

Finally, the partial derivative of $\mathcal{L}$ with respect to θ in direction $h \in L^\infty(\Omega;\mathbb{R})$, at the stationary point (u,p) is defined by

$$\begin{aligned} \left\langle \frac{\partial \mathcal{L}}{\partial \theta}, h \right\rangle = & \int_\Omega (\frac{\partial A^*(\theta)}{\partial \theta} e(u) \ : \ e(p) + \ell) h \ dx \\ & + \int_\Omega (\frac{\partial P^*}{\partial \theta} A^*(\theta)e(u) \ : \ A^*(\theta)e(u)) h \ dx \\ & + 2 \int_\Omega (P^*(\theta) \frac{\partial A^*}{\partial \theta} e(u) \ : \ A^*(\theta)e(u)) h \ dx \end{aligned} \tag{2.48}$$

Now, the descent direction $h = d\theta$ has to be selected such that :

$$\left\langle \frac{\partial \mathcal{L}}{\partial \theta}(\theta,u,p,\ell), d\theta \right\rangle < 0, \tag{2.49}$$

which is achieved by choosing

$$\begin{aligned} d\theta = -\Bigg(& \int_\Omega (\frac{\partial A^*(\theta)}{\partial \theta} e(u) \ : \ e(p) + \ell) \ dx \\ & + \int_\Omega \frac{\partial P^*}{\partial \theta} A^*(\theta)e(u) \ : \ A^*(\theta)e(u) \ dx \\ & + 2 \int_\Omega P^*(\theta) \frac{\partial A^*}{\partial \theta} e(u) \ : \ A^*(\theta)e(u) \ dx \Bigg) \end{aligned} \tag{2.50}$$

At iteration n, the optimal density θ is then updated by performing the projected gradient :

$$\theta^{n+1} = P_{[0,1]}(\theta^n + \delta d\theta), \tag{2.51}$$

where $\delta > 0$ is the step size and $P_{[0,1]}$ is the projection operator on the interval $[0, 1]$. Again, the value of the Lagrange multiplier ℓ is computed at each iteration by a dichotomy process designed to respect the volume constraint.

2.3.5 Maximization of the first eigenfrequency

Here, the objective function is :

$$J^*(\theta) = \min_{u \in H^1_{\Gamma_N}(\Omega;\mathbb{R}^N)} \frac{\int_\Omega A^*(\theta)e(u) \ : \ e(u) \ dx}{\int_\Omega \rho\theta|u|^2 \ dx} \tag{2.52}$$

where the objective function $J^*(\theta)$ is the first eigenvalue ω_1^2, solution to the homogenized spectral problem :

$$\begin{cases} -div(A^*(x)e(u)) = \omega^2 \rho_A \theta(x) u & \text{in } \Omega \\ A^*(x)e(u) \ . \ n = 0 & \text{on } \Gamma_N \\ u = 0 & \text{on } \Gamma_D, \end{cases} \tag{2.53}$$

where ρ_A is the material density of the elastic phase A. The objective function is Gateaux differentiable (see Lemma 5.2.16 in [59]) and the descend direction $d\theta$ is defined by

$$d\theta = -\frac{1}{\int_\Omega \rho_A \theta|u|^2}\left(\frac{\partial A^*(\theta)}{\partial \theta}e(u) \ : \ e(u) + \omega_1^2 \rho_A |u|^2\right) - \ell \tag{2.54}$$

Again, as in the minimum compliance problem, the alternate minimization algorithm is used to compute the optimization problem :

1. Initialization of the design variable θ such that :

$$\forall x \in \Omega \quad \theta^0(x) = \frac{\Theta}{\int_\Omega 1 \ dx}$$

2. Iteration until convergence, for $n \geq 0$:
   (a) Computation of the first eigenvalue ω_1^n and the first eigenvector u^n through the spectral problem (2.53) with the design $(\theta^n(x), A^*(x))$
   (b) Computation of the descend direction $d\theta^n$ (2.54) using formula (2.27)
   (c) Updating the design variable θ^{n+1} for the descend direction $d\theta^n$ and updating the design $(\theta^{n+1}(x), A^*(x))$ by linear interpolation.

2.3.6 Discussion

Several benchmark examples were presented to showcase the efficacy and robustness of the proposed method : the alternate minimization algorithm. We computed

the optimization problem over structures built with isotropic composite materials : the hexagonal cells in 2-d and the tetrakaidecahedron cell in 3-d. The microstructure tend to auto-penalize in numerous cases in 2-d. We can only conclude that modulated isotropic microstructures are may be not ideal for a single load minimization problems, e.g., the rank-2 laminates or the orthotropic cell are known to be optimal for a single load compliance minimization problem : they are anisotropic microstructures. Thus, the obtained results with isotropic microstructures sound coherent. For instance, Zhang in [84], introduced a new approach which consists in bounding the gradient of the density of composite with classical honeycomb in order to keep grey densities ; however, the proposed strategy is not ideal, they have no chance to be more optimal than structures optimized with the SIMP or the level-set method.

In converse to single load case, the optimization over isotropic microstructures in the multiple load configurations do not auto-penalized : they appear to be meaningful.

2.4 Deshomogenization process

We recall that in this thesis, we seek minimizers of composite microstructures. However, we should keep in mind that the final structure has to be manufacturable using additive manufacturing processes. This section is essentially composed of reminders of existing results introduced in [20], which consists of methodologies to deshomogenize composite solution. The homogenized structures are not straightforward manufacturable : only the local density of the cells is given but this does not describe a classical shape.

Let ϵ be the size of the hexagonal cells in 2-d or the tetrakaidecahedron cell in 3-d and Ω_ϵ be the resulting sequence of microstructures built with the isotropic cells. Geoffrey-Donders P. in [20], introduced two main approaches in order to construct such a sequence : the first one, is a local approach, where each cell is either the hexagonal cells in 2-d or the tetrakaidecahedron cell in 3-d and the second one is a global approach where the final structure is described through a level-set function. The first approach is said to be time consuming since each cell has to be constructed separately, while the second one is computationally fast.

2.4.1 Local approach

This approach has already been investigated in [20, 84], to project optimal composite structures on explicit cellular structures : the period ϵ is fixed, first and the workspace Ω is paved with the hexagonal cell in 2-d or tetrakaidecahedron cell in 3-d, see Figure 2.29.(b).

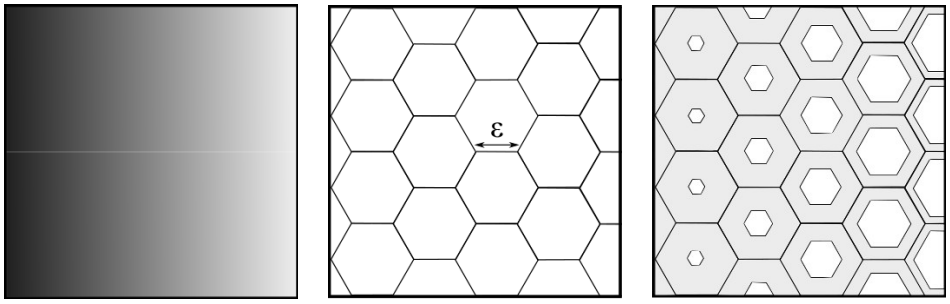

(a) Density field (b) Tessellation of Ω (c) Design of each cell

Figure 2.29 – Local deshomogenization approach : tessellation with honeycomb cells for an arbitrary density field and given periodic size ϵ (image taken from [20])

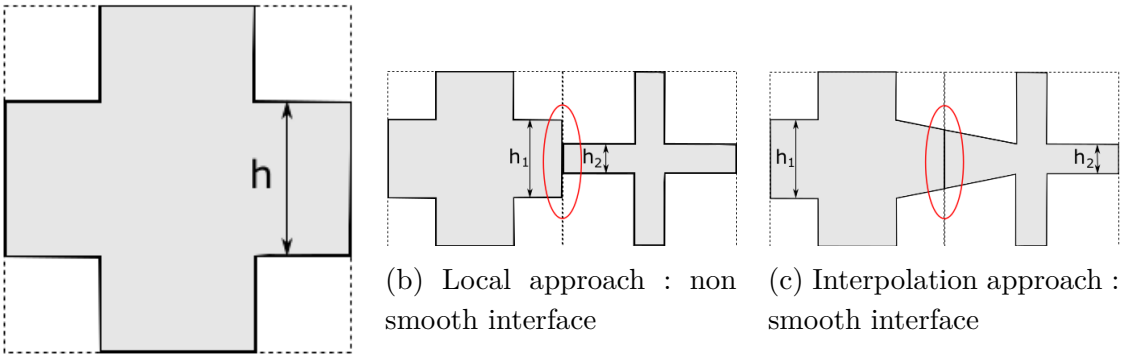

(a) Cross cell

(b) Local approach : non smooth interface

(c) Interpolation approach : smooth interface

Figure 2.30 – Two local strategies to deshomogenize composite solution built with cross cells in 2-D (image taken from [20])

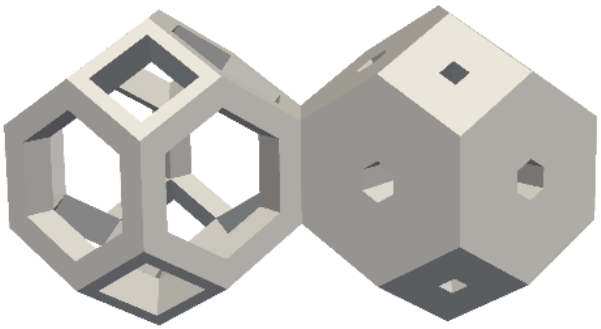

(a) Two adjacent tetrakaidecahedron cells

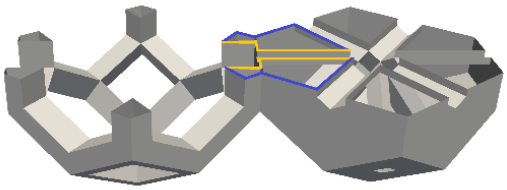

(b) Local approach : non-smooth interface

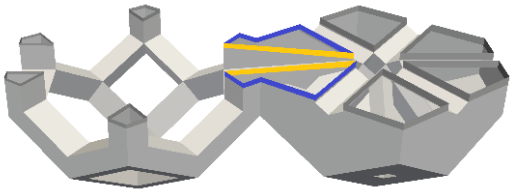

(c) Interpolation approach : smooth interface

FIGURE 2.31 – Two local strategies to deshomogenize composite solution built with tetrakaidecahedron cells in 3-D (image taken from [20])

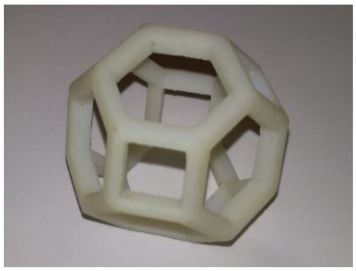

(a) Tetrakaidecahedron cell

(b) Four adjacent cells

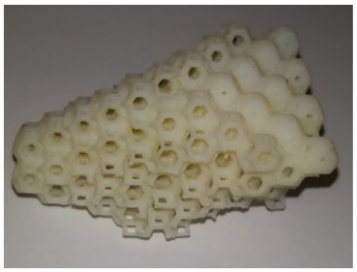

(c) Test structure

FIGURE 2.32 – 3-D printed structures built with modulated tetrakaidecahedron cells (image taken from [20])

2.4.2 Global approach

For the global approach, the resulting sequence of microstructures Ω_ϵ is implicitly characterized by a level-set function ψ_ϵ defined by

$$\psi_\epsilon : x \in \Omega \to \begin{cases} \psi_\epsilon(x) = 0 & \text{if } x \in \partial\Omega_\epsilon \\ \psi_\epsilon(x) < 0 & \text{if } x \in \Omega_\epsilon \\ \psi_\epsilon(x) > 0 & \text{if } x \in \Omega_\epsilon \backslash \Omega \end{cases} \tag{2.55}$$

Level-set function for the reinforced honeycomb cell

We recall that the reinforced honeycomb is a regular hexagon perforated by triangle-like truss holes : it is characterized by its three diagonals, where its periodic pattern can be seen as a truss of three groups of parallel bars of rotation 0, $\frac{\pi}{3}$ and $\frac{2\pi}{3}$ departing from the horizontal axis, respectively (see Figure 2.1.b). The three sets of parallel bars denoted by $\Omega_{\epsilon,i}$ are characterized by the level-set functions $\psi_{\epsilon,i}$, defined by

$$\psi_{\epsilon,i}(x) = -\cos(\frac{2\pi}{\epsilon}\frac{\sqrt{3}}{2}(x_1, x_2)^T \,.\, n_i) + \cos(2\pi\frac{\sqrt{3}}{2}m(x)), \tag{2.56}$$

where $m(x)$ is the relative width of the bar with respect to the density defined in (2.2.1). The complete network of bars Ω_ϵ is then given as the union of the three sets of parallel bars (see Figure 2.33), characterized by the level-set function ψ_ϵ defined by

$$\psi_\epsilon(x) = \min_{i\in\{0,1,2\}} \psi_{\epsilon,i}(x) \tag{2.57}$$

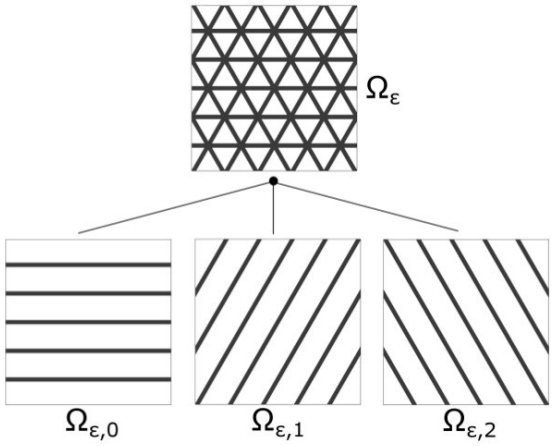

Figure 2.33 – Process to design the reinforced honeycomb using level-set function (image taken from [20])

For a period of size ϵ, parallel bars are at distant $\frac{\sqrt{3}}{2}\epsilon$ of each other : the distant of point $x \in \Omega_\epsilon$ to a diagonal is defined by the scalar product of x and the normal vector n_i. Consequently, thanks to cosine : an even and periodic function, the first term of (2.56) defines the set of parallel bars of normal n_i, with a periodicity equal to $\frac{\sqrt{3}}{2}\epsilon$, while the second term adjusts the local width of the bar with respect to m by thresholding the cosine function at adapted value.

Geoffrey-Donders P. in [20], successfully computed the final structure Ω_ϵ for several periodic size ϵ in $\Omega = [-1, 1]^2$, in the case of a radial :

$$\theta = 1 - 0.5 * (x_1^2 + x_2^2) \tag{2.58}$$

The results are displayed by Figure 2.34 : finely graded microstructures are obtained by decreasing of the periodic size ϵ ; however, the cells are not exactly reinforced honeycomb : the local width of the bar is given by the local density, wherein, the bar's width is smooth in the whole workspace and does not feature any discontinuity.

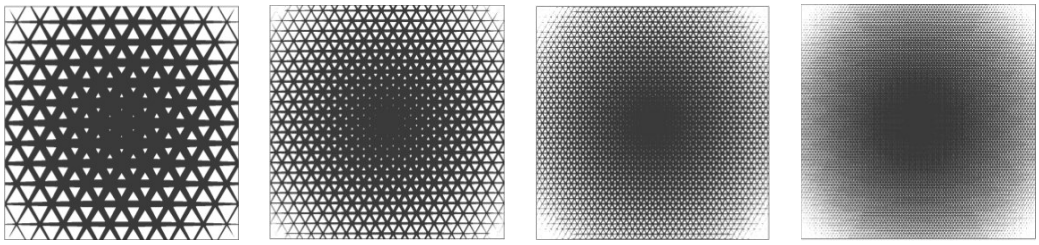

(a) $\epsilon = 1$ (b) $\epsilon = 0.5$ (c) $\epsilon = 0.25$ (d) $\epsilon = 0.125$

FIGURE 2.34 – Projection of a radial density θ over composites built with reinforced honeycomb (image taken from [20])

Level-set function for the classical honeycomb cell

Likewise, let ϵ be the size of the hexagonal cell. We recall that the classical honeycomb is a regular hexagon perforated by an hexagonal hole : it is characterized by its finite segments. Again, the periodic pattern can be seen as three groups of parallel bars of rotation 0, $\frac{\pi}{3}$ and $\frac{2\pi}{3}$ departing from the horizontal axis, see Figure 2.35.

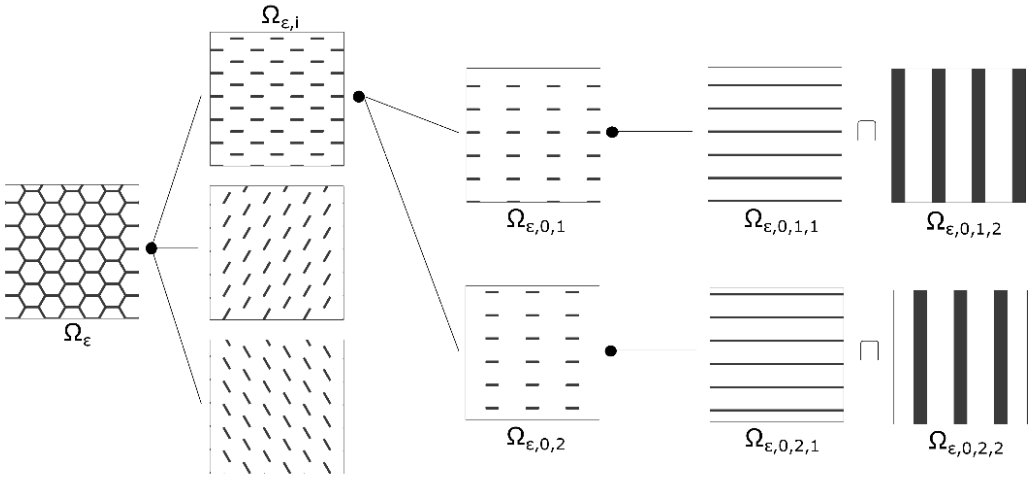

FIGURE 2.35 – Process to design the classical honeycomb using level-set function (image taken from [20])

A set of segments $\Omega_{\epsilon,i}$ in direction n_i can be divided into two subsets of periodic segments : $\Omega_{\epsilon,i,1}$ and $\Omega_{\epsilon,i,2}$, wherein a periodic segment $\Omega_{\epsilon,i,j}$ is described as the intersection between two sets of bars orthogonal to each other : $\Omega_{\epsilon,i,j,1}$ and $\Omega_{\epsilon,i,j,1}$, see Figure

2.35. Where, the first periodic segments $\Omega_{\epsilon,i,j,2}$ is defined by

$$\Omega_{\epsilon,i,j,1}(m) = \{x \in \Omega \mid \cos(\frac{2\pi\sqrt{3}}{\epsilon}(x_1, x_2)^T \,.\, n_i + j\pi) \geq \cos(2\pi\frac{\sqrt{3}}{2}m(x))\} \tag{2.59}$$

with periodic size is equal to $\sqrt{3}\epsilon$ and of bar's width, m dependent. The term $j\pi$ is here to shift the second periodic segments with respect to the first one defined by

$$\Omega_{\epsilon,i,j,2}(m) = \{x \in \Omega \mid \cos(\frac{2\pi}{3\epsilon}(x_1, x_2)^T \,.\, n_i + j\pi + (2\delta_{i,2} - 1)\frac{\pi}{3}) \geq \cos(\frac{\pi}{3})\} \tag{2.60}$$

where $\delta_{i,j}$ is the symbol of Kronecker : this term is here to adjust all the segments together. The origin $(0, 0)$ of Ω corresponds to the upper left corner of the hexagon : level-set description is not unique and can be translated in order to place the origin $(0, 0)$ wherever you want in the periodic cell.

Again, Geoffrey-Donders P. in [20], successfully computed the final structure Ω_ϵ for several periodic size ϵ in $\Omega = [-1, 1]^2$, in the case of a radial given by (2.58). The results are displayed on Figure 2.36 : finely graded microstructures are obtained by decreasing of the periodic size ϵ. Likewise, the cells are not exactly classical honeycomb but the bar's width is smooth in the whole workspace and does not feature any discontinuity.

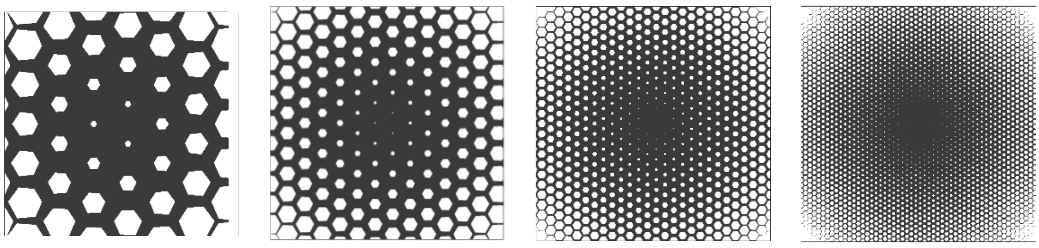

(a) $\epsilon = 1$ (b) $\epsilon = 0.5$ (c) $\epsilon = 0.25$ (d) $\epsilon = 0.125$

Figure 2.36 – Projection of a radial density θ over composites built with classical honeycomb (image taken from [20])

Chapitre 3

Homogenization-based topology optimization of 2-D fluidic pressure loaded structures built with isotropic composite materials

We now introduce a simplified fluid-structure model which shall be of interest throughout this whole work. The variables u and p are the solutions of two state equations which are weakly coupled in the sense that each of them can be solved successively and independently. This model is based on Biot-Darcy equation for the fluid flow and pressure, and linear poro-elasticity for the elastic displacement. We seek minimizers of the sum of the elastic and fluid-elastic compliances.

Most of the content of this chapter is in the preliminary version of an article : AGYEKUM O.G., JOUVE F. and CANGÉMI L., **Topology Optimization of Fluidic Pressure Loaded Structures using the Biot-Darcy Model**.

Abstract

In various applications, design problems involving structures, experience fluidic pressure loads. During topology optimization of such design problems, these loads adapt their direction and location with the evolution of the design, which poses various challenges. A novel approach to optimize the relaxed formulation of such design problems is presented to provide a continuous and consistent treatment of design-dependent pressure loads. Its effect is to allow micro-perforated composite as admissible designs. The porosity of each finite element is related to its density variable using a regular function, yielding a smooth transition between the solid and void phase. A design-dependent pressure field is established using Biot-Darcy's law and the associated PDE is solved using the finite element method. The approach provides a computationally inexpensive evaluation of load sensitivities using the adjoint-variable method. Since it places no assumption on the number of holes cut within the domain, it can be seen as a topology optimization algorithm. Numerical results are presented for various two dimensional problems : we seek minimizers of the sum of the elastic compliance, fluid-elastic compliance and of the weight of a solid structure under fluid-pressure loads.

Keywords— Topology optimization, relaxed formulation, theory of homogenization, porous medium, periodic medium, fluid-structure interaction.

3.1 Introduction

Shape optimization is a major issue in structural design and one of the most challenging aspects is what structural engineers refer to as layout or topology optimization. Its is nowadays well developed field with various methods and most have meanwhile attained a mature state. Moreover, their popularity as design tools for achieving solutions to a wide variety of problems involving single/multi-physics is growing consistently. Among these, design problems involving fluidic pressure loads pose several unique challenges : (i) identifying the structural boundary to apply such loads, (ii) determining the relationship between the fluidic pressure loads and the design variables, i.e., defining a design-dependent and continuous pressure field and (iii) efficient calculation of the fluidic pressure load sensitivities. Such problems can be encountered in the design

of heat-exchangers [40, 41, 42, 43, 44, 45], for various applications such as hot and cold fluids loaded and mechanical structures (e.g., combustion engines, air conditioning, power production or microturbines). Note that, the topology and performance of the optimized structures are directly related to the magnitude, location and direction of the fluidic pressure loads which vary with the design.

In this chapter, we target topology optimization to address the aforementioned challenges in the design of solid structures under fluid-pressure loads for a given weight of the solid. We carefully map the passage from original shape optimization problem to its assumed relaxed formulation, namely, allow a periodic distribution of holes of any shape and any size within the design region. The recipe is deceptive because the issue at stake is truly of a mathematical nature, the collection of admissible periodic holes should be such that meaningful optimality criteria can be proposed. A key problem characteristic is that the fluid-pressure loaded surface is not defined *a priori* but, it can be modified by the optimization process to (for instance) maximize stiffness. The main application of our work is the optimization of architectured materials, also known as lattice materials which are becoming increasingly popular in the context of additive manufacturing. Below, we review the proposed topology optimization (TO) methods that involve fluid-pressure loaded boundaries for structure designs.

In the case of TO, Hammer and Olhoff [40] were first to propose design problems involving pressure loaded structures. Thereafter, several approaches have been proposed to apply and provide a proper treatment of such loads in TO setting, which can be broadly classified into : (*i*) methods using boundary identification schemes [40, 85, 86, 87, 88, 89], (*ii*) level set method based approaches [45, 90, 91, 92], and (*iii*) approaches involving special methods, which avoid detecting the loading surface [93, 94, 95, 96, 97, 98].

Boundary identification techniques in general, are based on *a priori* chosen threshold density ρ_T : iso-density curves/surfaces are identified. Hammer and Olhoff [40] used the iso-density approach to identify the pressure loading facets Γ_{p_b} which they further interpolated via Bézier spline curves to apply the pressure loading. However, as per Du and Olhoff [85], this iso-density (isolines) method may furnish isoline-islands and/or separated isolines. Hence, valid loading facets may not be achieved. In addition, this method requires predefined starting and ending points for the exposed boundary Γ_{p_b} [40]. To circumvent this issue associated with the isolines method, Du and Olhoff [85] proposed a modified isolines technique. In [40, 85], the sensitivities of the pressure load are evaluated with respect to design variable(s) using an efficient finite difference formulation. Lee and Martins [87] presented a method wherein one does not need to define starting and ending points *a priori*. In addition, they provided an analytical approach to calculate load sensitivities. However in [40, 85, 87], the sensitivities of the pressure loads, were confined to only those elements which are exposed to the pressure boundary loads Γ_{p_b}. One should refer to [86, 89] for methods evolving pressure loading boundary Γ_{p_b}. The methods presented in this paragraph do not account for load sensitivities within their TO setting. Furthermore, as per Hammer and Olhoff [40], if the evolving pressure loaded boundary Γ_{p_b} coincides with the edges of the finite elements (**FEs**) then the load sensitivities with respect to design variables vanish or can be disre-

garded. Consequently, Γ_{p_b} no longer remains sensitive to infinitesimal alterations in the design variables unless the threshold value ρ_T is passed and thus, Γ_{p_b} jumps directly to the edges of a next set of **FEs** in the following TO iteration. We emphasize that load sensitivities however may critically affect the optimal material layout of a given design problem, thus, considering load sensitivities in problems involving fluidic pressure loads is highly desirable. In addition, ideally these sensitivities should be straightforward to compute, implement and computationally inexpensive.

In contrast to density-based TO, in the level-set-based approaches, an implicit boundary description is available that can be used to define the pressure load. On the other hand, being based on boundary motion, level-set methods tend to be more dependent on the initial design [45]. Gao et al. [90] (2004) employed a level set function (**LSF**) to represent the structural topology and overcame difficulties associated with the description of boundary curves in an efficient and robust way. Xia et al. [92] (2015), employed two zero-level sets of two **LSFs** to represent the free boundary and the pressure boundary separately. Wang et al. [99] (2016), employed the **D**istance **R**egularized **L**evel **S**et **E**volution (**DRLSE**) (see [91], 2010) to locate the structural boundary. They used the zero level contour of an **LSF** to represent the loading boundary but did not regard load sensitivities. Recently, Feppon et al. [45] (2018), employed a **L**evel **S**et **M**esh **E**volution (**LSME**) to locate the structural boundary. They used Hadamard's method of shape differentiation to solve a coupled thermal fluid-structure. Picelli et al. [100] (2019) proposed a method wherein Laplace's equation is employed to compute hydrostatic fluid-pressure fields, in combination with interface tracking based on a flood fill procedure. Shape sensitivities in conjunction with Ersatz material interpolation approach are used within their method.

Given how difficult is to identify a discrete boundary within density-based TO and obtain consistent sensitivity information, various researchers have employed special/alternative methods (without identifying pressure loading surfaces directly) to design structures experiencing pressure loading. Chen and Kikuchi [94] (2001), presented an approach based on applying a fictitious thermal loading to solve pressure loaded problems. Sigmund and Clausen [96] (2007), employed a mixed displacement-pressure formulation based finite element method in association with three-phase material (fluid/void/solid). Therein, an extra (compressible) void phase is introduced in the given design problem while limiting the volume fraction of the fluid phase and also, the mixed finite element methods have to fulfill the Babuška–Brezzi condition (BB-condition) which guarantees the stability of the element formulation [101]. Bourdin and Chambolle [93] (2003), also used three-phase material to solve such problems. Zheng et al. [89], (2009) introduced a pseudo electric potential to model evolving structural boundaries. In their approach, pressure loads were directly applied upon the edges of finite elements and thus, they did not account for load sensitivities. Additional physical fields or phases are typically introduced in these methods to handle the pressure loading. Recently, Kumar et al, [49] (2020), employed similar strategy based on Darcy's law, to design both structures and compliant mechanisms loaded by design-dependent pressure loads using density-based TO. In addition, D. Hübner et al. [47] (2019), employed similar strategy based on Biot model derived by the homogenization of two decoupled problems : (1) deformation of a porous solid saturated by a slightly compressible static

fluid and (2) Stokes flow through the rigid porous structure. The effective medium properties are given by the drained skeleton elasticity, the Biot stress coupling, the Biot compressibility coefficients, and by the hydraulic permeability of the Darcy flow model. Our method follows a similar strategy based on Biot-Darcy's law to optimize a relaxed (or homogenized) formulation to provide a continuous and consistent treatment of design-dependent fluid-pressure loads, which has not been reported before.

On one hand we carefully map the passage from the original shape optimization problem to its assumed relaxed formulation in a 2-d setting. This permits to introduce micro-perforated composite as admissible designs. Our motivation originates from the observation that many industrial applications in the energy field involve multi-scale designs. For instance, heat exchangers feature periodic patterns visible at a microscopic scale which are geometrically modulated over larger scales. They are integrated into a suitable macroscopic structure so as to maximize the exchange surface between hot and cold phases, while limiting the output pressure loss. We propose a new computational algorithm for two dimensional shape optimization that takes full advantage of a class of periodically perforated composite to design fluidic pressure loaded structures. The presented approach uses Biot-Darcy's law and standard **FEs**, for modeling and providing a suitable treatment of pressure loads. The Biot-Darcy's law is adapted in a manner that the porosity of the finite elements can be taken as design-dependent using a smooth function facilitating smoothness and differentiability. Consequently, prescribed pressure loads are transferred into a design dependent pressure field using a **PDE**, which is further solved using the finite element method. The determined pressure field is used to evaluate consistent nodal forces using the finite element method. This two steps process offers a flexible and tunable method to apply the pressure loads and also, provides distributed load sensitivities, especially in the early stage of optimization. The latter is expected to enhance the exploratory characteristics of the topology optimization process.

Regarding applications, most research on TO involving fluid-pressure loads has thus far focused on compliance minimization problems and the present work should be approached within such background. Several homogenized models exist depending on various scaling regimes assumed by the microstructure pattern (i.e., Darcy, Brinkman, or Stokes regimes, etc.) which makes it unclear which effective model should be used to describe a context featuring all possible regimes simultaneously at different locations in the domain. Thus, using the presented method, we not only design a rigorous fluid-pressure loaded microstructures but also provide a suitable treatment of pressure loads, which suggests the novel potentiality of the method.

In section 2, we present the homogenized fluid-structure models using Biot-Darcy approach. Next, in section 3, we introduce the topology optimization problem formulation for fluid-pressure loaded structures and small-deformation, and the associated sensitivity analysis. In section 4, we present the topology optimization process : it is an alternate direction algorithm, which successively computes the stress field through the solving of a coupled fluid-structure problem for that stress field over the set of composites, periodically perforated by hexagonal cells in 2-d. Finally, in section 5, we present our numerical results : 2-d computations are displayed of various benchmark

design problems involving fluidic pressure loaded structures and small deformation. As a final note, the following new aspects are presented :

- Biot-Darcy's law is used to identify evolving pressure loading boundary which is performed by solving an associated **PDE**,
- the approach facilitates computationally inexpensive evaluation of the load sensitivities using the adjoint-variable method,
- the load sensitivities are derived analytically and consistently considered within the presented approach while synthesizing structures experiencing pressure loading,
- the method avoids explicit description of the pressure loading boundary (which proves cumbersome to extend to 3-D),
- the robustness and efficacy of the approach is demonstrated via various standard design problems related to structures,
- the method employs standard linear **FEs**, without the need for special **FE** formulations.

3.2 The fluid-structure model using Biot-Darcy approach

The material boundary of a given design domain Ω, evolves as the TO progresses while forming an optimum material layout. Therefore, it is challenging especially in the initial stage of the optimization to locate an appropriate loading boundary Γ_{p_b}, for applying the pressure loads. In addition, while designing especially fluid-pressure and small deformation, establishing a design-dependent and continuous pressure field would aid the TO.

From a fluid point of view, it was established in [102], that different regimes can exist within a foam-like composite. These regimes depend on the local Reynolds number evaluated using 3-D simulation of the pore-scale flow. It is shown that, a Darcy regime is established for Reynolds numbers lower than 0.3, while an inertial regime is established for a Reynolds greater than 30, preceded by a transition regime. The complexity of these real flow regimes is not taken into account in our present work and we consider in this first approach a flow of the Darcean type. However, it was established in [102] that, a Darcy-Forchheimer type approach makes it possible to account for all possible regimes. Thus, exploring this sophisticated flow law is an obvious line of research for future work.

Here, Biot-Darcy's law is employed to establish the pressure field as a function of material density θ. Darcy's law defines the ability of a fluid to flow through porous media such as rock, soil or sandstone. It states that fluid flow through a unit area is directly proportional to the pressure drop per unit length ∇p and inversely proportional to the resistance of the porous medium to the flow μ_f ([103]). Mathematically,

$$\boldsymbol{q} := -\frac{\kappa_f}{\mu_f}\nabla p = -K_D^*\nabla p, \tag{3.1}$$

where $\boldsymbol{q}$, κ_f, μ_f, and ∇p represent the flux (ms^{-1}), permeability (m^2), fluid viscosity ($Nm^{-2}s$) and pressure gradient (Nm^{-3}), respectively. Further, $K^{*\,1}$ ($m^4N^{-1}s^{-1}$) is termed as flow coefficient which expresses the ability of a fluid to flow through a porous medium. The flow coefficient is assumed to be related to the material density $\theta(x)$. In order to differentiate between void ($\theta(x) = 0$) and solid ($\theta(x) = 1$) states of a **FE**, and at the same time ensuring a smooth and differentiable transition, $K^*(\theta)$ is modeled using a smooth function, that is :

$$K^*(\theta) := \min\left(\frac{\epsilon_0 + (1-\epsilon_0)(1-\theta)}{\theta}, K_\infty\right), \tag{3.2}$$

where ϵ_0, K_∞ are given thresholds : $\epsilon_0 = 10^{-4}$, $K_\infty = 10^3$. Our intent is to smoothly and continuously distribute the pressure drop over a certain penetration depth of the solid facing the pressure source : the validity of this assumption will be displayed later in our numerical results, where we compare the above function to the homogenized conductivity model computed using the so called cell problems. In addition, the pressure field p is assumed to satisfy a Biot's law defined by

$$p := M^* m - M^* b\, e_{vol}, \tag{3.3}$$

where M^*, m and e_{vol} are smooth enough functions related to the material density $\theta(x)$ given by

$$m(\theta) := (1-\theta)\rho, \quad M^*(\theta) := \frac{1-\theta}{\kappa_v} - \frac{b(\theta) - (1-\theta)}{\kappa_s}, \quad e_{vol}(\theta) := div(u(\theta)), \tag{3.4}$$

where, ρ, κ_v and κ_s represent the density of the flux [2], compressibilty of the void and solid phases ; where $e_{vol}(\theta)$ denotes a volume variation of the solid phase of proportion $\theta(x)$ at each **FE**. The parameters M^* and b are the so called Biot modulus and Biot coefficient. The Biot's law (3.3) is assumed to be related to Darcy's law (3.1) :

$$\boldsymbol{q} := m v_f = -K^* \nabla p, \tag{3.5}$$

where v_f represents the velocity (ms^{-1}) of the flux. Biot-Darcy's law renders a gradual pressure drop from the inner pressure boundary Γ_{p_b} to the outer pressure boundary Γ_{p_0} : the validity of this assumption is checked later in our numerical results. Consequently, equivalent nodal forces appear within the material as well as upon the associated boundaries. This penetrating pressure originating because of Biot-Darcy's law, is a smeared-out version of an applied pressure load on a sharp boundary or interface [3]. We emphasize that, summing up the contributions of penetrating loads gives the resultant load. It is assumed that local differences in the load application have no significant effect on the global behaviour of the structure, in line with the Saint-Venant principle. In addition to the Biot-Darcy equation (3.5), the equation of state model using the law of conservation of mass in view of incompressible fluid is derived :

$$\frac{\partial m}{\partial t} := -div(\boldsymbol{q}) = div(K^* \nabla p) \tag{3.6}$$

1. $K^* = \frac{\kappa_f}{\mu}$ is termed "flow coefficient", noting the fact that this terminology is however sometimes used in literature with a different meaning.

2. mass per unit volume of the fluid

3. used in the approaches based on boundary identification

Consequently, we derived from the Biot's law (3.2), the equation

$$\frac{\partial p}{\partial t} = M\frac{\partial m}{\partial t} - Mb\frac{\partial e_{vol}}{\partial t}, \tag{3.7}$$

Further to Biot-Darcy's law (3.6), we assume for sake of simplicity that our fluid model is continuous, stationary and that, the state equation satisfies the law of conservation of mass (in view of incompressible fluid), that is :

$$\frac{\partial m}{\partial t} = -div(\mathbf{q}) = div(K_D^*\nabla p) = 0 \tag{3.8}$$

where in the particular case of a porous isotropic medium, the Biot's coefficient $b(\theta)$ is explicitly given by

$$b(\theta) := 1 - \frac{\kappa_s(\theta)}{\kappa}, \tag{3.9}$$

where, κ and $\kappa_s(\theta)$ represent the bulk moduli of the solid phase A and the homogenized tensor $A^*(x)$. We emphasize that $A^*(x)$ tends to A when $\theta(x)$ tends to 1, thus, $\kappa_s(\theta)$ tends to κ. This formulation can effectively control the location and depth of penetration of the applied pressure. This present work should be approached within such background : we assume that our fluid-structure model is defined in the particular case of a porous isotropic medium. In order to discuss the precise mathematical settings of our multiphysic system, we introduce the following spaces of functions :

$$V(\Gamma_D^s) := \{v \in H^1(\Omega)^N \mid v = 0 \text{ on } \Gamma_D^s\}, \quad V(\Gamma_D^f) := \{q \in H^1(\Omega) \mid q = 0 \text{ on } \Gamma_D^f\}, \tag{3.10}$$

where Γ_D^s and Γ_D^f represent the homogeneous Dirichlet boundaries for the solid and fluid systems, respectively. We consider the subspace

$$H^{1/2}(\Gamma_N^s) := \{v|_{\Gamma_N^s} \mid v \in V(\Gamma_D^s)\}, \tag{3.11}$$

and its dual space $H^{-1/2}(\Gamma_N^s)$. Using the Biot-Darcy's law (3.8), our fluid model is then defined by

$$\text{(Biot-Darcy)} \begin{cases} -div(K^*\nabla p) = 0 & \text{in } \Omega, \\ \boldsymbol{q}_\Gamma \,.\, \mathbf{n} = f_f & \text{on } \Gamma_N^f, \\ \boldsymbol{q}_\Gamma \,.\, \mathbf{n} = 0 & \text{on } \Gamma^f = \partial\Omega\backslash(\Gamma_D^f \cup \Gamma_N^f), \\ p = p_{in} & \text{on } \Gamma_D^f \end{cases} \tag{3.12}$$

where $f_f \in H^{-1/2}(\Gamma_N^f)$ (satisfies a compatibility condition of equilibrium) is the enforcement of flux load on the part of its boundary Γ_N^f (i.e., the enforcement of a Neumann boundary condition) and p_{in} is the loading pressure on the part of its boundary Γ_D^f (i.e., the enforcement of a Dirichlet boundary condition). Thus, by a straightforward integration by parts, $p \in V(\Gamma_D^f)$ is the unique solution (up to a constant function) to the variational formulation : find $p \in p_{in} + V(\Gamma_D^f)$ such that $\forall q \in V(\Gamma_D^f)$

$$\int_\Omega K^*(\phi)\nabla p \,.\, \nabla q \; dx - \int_{\Gamma_N^f} f_f \; q \; ds = 0 \tag{3.13}$$

Next, we weakly coupled the solution p of the fluid model (3.13) to the linear-elasticity problem defined by

$$\text{(Biot-Coussy)} \begin{cases} -div(\sigma) = -b\nabla p & \text{in } \Omega \\ \sigma \,.\, n = f_s & \text{on } \Gamma_N^s, \\ u = 0 & \text{on } \Gamma_D^s, \\ \sigma \,.\, n = 0 & \text{on } \Gamma^s = \partial\Omega \backslash (\Gamma_N^s \cup \Gamma_D^s), \\ \sigma = A^* e(u) & e(u) = \frac{1}{2}(\nabla u + \nabla^t u), \end{cases} \tag{3.14}$$

where $u \in V(\Gamma_D^s)$ is the unique solution (up to rigid displacement field). Here, u is the homogenized displacement vector and σ is the associated Cauchy stress field. The vector function $f_s \in H^{-1/2}(\Gamma_N^s)$ is the body force applied on its boundary Γ_N^s, with a clamping of part on its boundary Γ_D^s. Wherein, the coupling is weak because the equations are solved consecutively : the Biot-Darcy model, first, then the linear poro-elasticity model. Thus, by a straightforward integration by parts, u is the unique solution to the variational formulation : find $u \in V(\Gamma_D^s)$ such that $\forall v \in V(\Gamma_D^s)$

$$\int_\Omega A^* e(u) \,.\, e(v)\, dx - \int_{\Gamma_N^s} f_s \, v \, ds + \int_\Omega b\nabla p \,.\, v \, dx = 0 \tag{3.15}$$

For the remainder of this chapter, we weakly solve the variational formulations of the fluid-structure model.

3.3 The topology optimization problem formulation for fluidic pressure loaded structures

We follow TO of modulated periodic microstructures using the homogenization method. A composite design is described by the local density $\theta(x)$ of the material and the homogenized tensor $A^*(x)$, that depends on the microstructure at the point $x \in \Omega$ in the working space. We restrict ourselves to 2-d setting and restrain our analysis to a simple class of composites already used in [20] : composites are periodically perforated by an hexagonal cells, namely, classical, reinforced and smooth honeycomb. This class of modulated periodic microstructures is known to be isotropic microstructures (or atleast very close to one) : the validity of this assumption is displayed in chapter 2 section 2.2.1.

3.3.1 The Homogenized Hooke's laws

We denote by Y, the periodic hexagonal cells, i.e., classical, smooth and reinforced honeycomb (see chapter sect.2.2.1, for details). The structure of the hexagonal cell as well as its Hooke's law are qualitatively similar to the celebrated Vigdergauz hexagonal cell [71], which is known to generate extreme composite microstructures, in the sense that they minimize the energy. For sake of clarity, few important results on the theory

of homogenization are recalled hereafter, the interested reader should refer to chapter 2 or the textbook [59], for details and explanations.

Assume that in a given macroscopic domain Ω, there is a periodic distribution of holes inside an elastic isotropic phase, with constant elastic tensor A. The periodicity size is denoted by $\epsilon > 0$, wherein the rescaled periodicity cell is the unit hexagonal cell. Inside this unit periodic cell, the solid phase is the subset Y_0, where its complement being the hole with boundary Γ_{int} (see Figure 2.1). Whenever ϵ tends to zero, the porous medium can be considered homogeneous with an effective (or homogenized) tensor $A^*(x)$. To compute the homogenized tensor A^*, one needs the so-called correctors w_{ij}, corresponding to the local displacements in the periodic cell Y_0, defined for each pair $(i,j) \in \{1,2\}$ as the solutions to

$$\begin{cases} -div(A(e_{ij} + e(w_{ij}))) = 0 & \text{in } Y_0 \\ A(e_{ij} + e(w_{ij})) \,.\, \boldsymbol{n} = 0 & \text{on } \Gamma_{int} \\ y \mapsto w_{ij}(y) & Y_0 \text{ periodic,} \end{cases} \tag{3.16}$$

where $e_{ij} = \frac{1}{2}(e_i \otimes e_j + e_j \otimes e_i)$ is the basis of the symmetric tensors of order 2 and $\boldsymbol{n}$ is the normal vector to the interior boundary Γ_{int} of Y_0. By straightforward integration by part, its associated variational formulation is : find $w_{ij} \in H^1_{\#}(Y_0, \mathbb{R}^2)$ such that

$$\forall \phi \in H^1_{\#}(Y_0, \mathbb{R}^2) \quad \int_{Y_0} Ae(w_{ij}) \;:\; e(\phi) + \int_{Y_0} Ae_{ij} \;:\; e(\phi) = 0, \tag{3.17}$$

which admits a unique solution (up to a rigid displacement field). The entries of the homogenized tensor $A^*(x)$ is then given in terms of the correctors w_{ij}, solutions of (3.17), defined by

$$A^*_{ijkl} = \frac{1}{|Y|} \int_{Y_0} A(e_{ij} + e(w_{ij})) \;:\; (e_{kl} + e(w_{kl}))\, dy \quad \forall i,j,k,l \in \{1,2\} \tag{3.18}$$

where the symbol # denotes the periodicity of the solutions w_{ij}. Likewise, starting from a microscopic description of a problem, one seeks a macroscopic or effective model problem in conductivity. We consider a model problem of fluid flow in a periodic medium : an heterogeneous domain obtained by mixing periodically two different phases, one being the solid phase and the other the void inclusions. Again, to compute the homogenized conductivity tensor K^*, we introduce the so-called cell problems, and since the considered cell Y is specifically chosen in order to design isotropic composites, only one of its coefficient (e.g., $(K^*)_{11}$) could be computed in order to fully characterized K^*, a scalar value ; however to confirm the isotropy, we computed all its coefficients.

We denote by $(e_i)_{i=1,2}$ the canonical basis of $\mathbb{R}^2$. For each unit vector e_i, we consider the following conductivity problem in the periodic cell Y :

$$\begin{cases} -div(K(e_i + \nabla w_i))) = 0 & \text{in } Y \\ y \mapsto w_i(y) & Y \text{ periodic,} \end{cases} \tag{3.19}$$

where $w_i(y)$ is the local variation of pressure created by an averaged (or macroscopic) gradient e_i. The homogenized conductivity tensor K^* is then given in terms of the

correctors w_i, solutions of (3.19), defined by

$$(K^*)_{ij} = \frac{1}{|Y|}\int_Y K(e_i + \nabla w_i) \ : \ (e_j + \nabla w_j)\, dy \quad \forall i,j \in \{1,2\} \tag{3.20}$$

The constant tensor K^* describes the effective or homogenized properties of the heterogeneous microstructure of periodic size ϵ. Note that K^* does not depend on the choice of domain Ω, source term f_f, or boundary condition on $\partial\Omega$.

Numerical results

The constant tensor K^* has been computed for the hexagonal cells in 2-d, on the same scheme as the homogenized tensor $A^*(\theta)$ for a discrete values $(\theta_i)_{i=1,\dots,n}$ of the density. Figure 3.1 displays the homogenized flow coefficient K^* computed for a discrete values of the density with respect to the hexagonal cells and the normalized smooth function given by (3.2). As expected, K^* is a decreasing function with respect to the density θ. It is noted that the residual $|(K^*)_{11} - (K^*)_{22}| \leq 10^{-6}$ and $(K^*)_{12} \leq 10^{-3}$ for three hexagonal cells, which validates the isotropy. We emphasize that the flow coefficient K^* is quite the same for the three hexagonal cells and can be approximated by the normalized smooth function in (3.2).

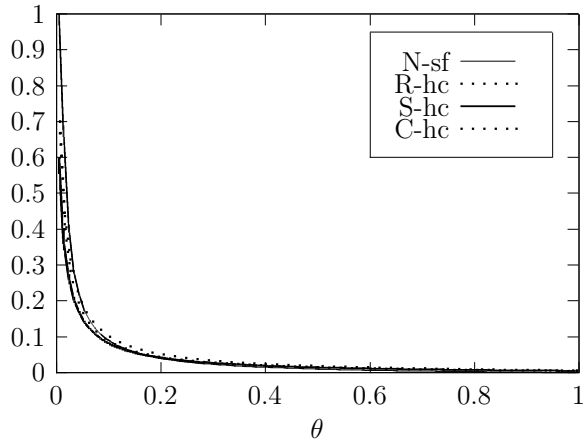

FIGURE 3.1 – The homogenized flow coefficient history wrt. the hexagonal cells : Classical honeycomb (C-hc), Reinforced honeycomb (R-hc) and Smooth honeycomb (S-hc) and the normalized smooth function (N-sf) (3.2)

3.3.2 Problem formulation and sensitivity analysis

In this section, we present the optimization problem formulation associated to fluid-pressure loaded structures and discuss the sensitivity analysis for such design problems. The standard formulation, namely the minimization of compliance is considered to design pressure loaded stiff structures, where the optimization problem is given by the

constrained formulation

$$\min_{\substack{0\leq\theta\leq 1 \\ \frac{1}{|\Omega|}\int_\Omega \theta\, dx=\Theta}} J^*(\theta) \tag{3.21}$$

where, $J^*(\theta)$ is the relaxed objective function defined by

$$J^*(\theta) := \int_{\Gamma_N} f_s \,.\, u\, ds + \int_\Omega (-b\nabla p) \,.\, u\, dx = \min_{\tau\in H_0}\Big\{ \min_{A^*(x)\in G_\theta} \int_\Omega A^{*-1}\tau \,.\tau\, dx\Big\}, \tag{3.22}$$

with H_0 :

$$H_0 = \left\{ \tau \in L^2(\Omega;\mathcal{M}_2^s) \mid \begin{cases} -div(\tau - bpI_2) = 0 & \text{in } \Omega \\ \tau \,.\, n = f_s & \text{on } \Gamma_N^s \\ \tau \,.\, n = 0 & \text{on } \Gamma^s \end{cases} \right\} \tag{3.23}$$

where, $\Gamma^s = \partial\Omega\backslash\Gamma_N^s$ is the free part of boundary $\partial\Omega$. We recall that, we only explicitly compute the optimization process on a subset of of all possible Hooke's laws G_θ, namely, composites periodically perforated by the hexagonal cells. Therefore, the set of effective elasticity tensors $\{A^*(\theta) \mid \theta \in L^\infty(\Omega,[0,1]\}$ has to be characterized. The proposed strategy consists in computing the material properties for a discrete sample of parameter values and using the collected data to construct a surrogate model for the constitutive law (by a simple linear interpolation). Next, the optimization problem (3.21) is recast as follow

$$\min_\theta J^*(\theta) = \min_\theta \int_\Omega A^*(\theta)e(u) \;:\; e(u)\, dx, \tag{3.24}$$

where u is the unique solution to the coupled fluid-elastic problem :

$$\begin{cases} (i) & -div(K^*\nabla p) = 0 \\ (ii) & -div(A^*e(u)) = -b\nabla p \\ (iii) & \frac{1}{|\Omega|}\int_\Omega \theta\, dx = \Theta, \end{cases} \tag{3.25}$$

where Θ, is the prescribed volume fraction. Note that, all mechanical equilibrium equations are satisfied under small deformation assumption. The optimization problem is then solved using the alternate minimization algorithm [29], which consists in minimizing successively the stress tensor through the solving of the coupled fluid-structure problem and then the density θ through a projected gradient method : it is an algorithm based on *optimality criteria*. We emphasize that, the boundary value problems in (3.25) are solved in each iteration in combination with the respective boundary conditions.

In a gradient-based TO, it is essential to determine sensitivities of the objective function and the constraints with respect to the design variable(s). In general, the formulated objective function depends upon both the state variables u, p, solutions to the fluid-mechanical equilibrium equations and the design variable(s). In order to discuss the precise mathematical settings, we introduce the following set of admissible design variables $\mathcal{U}_{ad}$:

$$\mathcal{U}_{ad} := \Big\{ \theta \in L^\infty(\Omega;\mathbb{R}) \mid \theta(x) \in [0,1], \forall x \in \Omega \Big\} \tag{3.26}$$

We define the applications $\theta \to u(\theta)$, $\theta \to p(\theta)$, where $\theta \in \mathcal{U}_{ad}$ is associated to the solution $\{u(\theta), p(\theta)\} \in V(\Gamma_D^s) \times V(\Gamma_D^f)$ of the state equations (under volume constraints) :

$$\begin{cases} (i) & -div(K^*(\theta)\nabla p) = 0 \\ (ii) & -div(A^*(\theta)e(u)) = -b\nabla p \\ (iii) & \frac{1}{|\Omega|}\int_\Omega \theta \, dx = \Theta \end{cases} \tag{3.27}$$

As already known [59], the above maps are continuous and differentiable in $\mathcal{U}_{ad}$, where the directional derivative at θ of $u(\theta)$ and $p(\theta)$ with respect to $\bar{\theta} \in L^\infty(\Omega)$ are defined respectively by

$$\left\langle p'(\theta), \bar{\theta} \right\rangle = \bar{p}, \quad \left\langle u'(\theta), \bar{\theta} \right\rangle = \bar{u}, \tag{3.28}$$

where $\bar{p} \in H_0^1(\Omega)$ and $\bar{u} \in H_0^1(\Omega)^2$ are the unique solutions (up to constant functions) to the system given by

$$\begin{cases} (i) & -div(K^*(\theta)\nabla \bar{p}) = div(\bar{K^*}\nabla p) \\ (ii) & -div(A^*(\theta)e(\bar{u})) = div(\bar{A^*}e(u)) - \bar{b}\nabla p - b\nabla \bar{p}, \end{cases} \tag{3.29}$$

where

$$\bar{K^*} =< (K^*)'(\theta), \bar{\theta} >, \quad \bar{A^*} =< (A^*)'(\theta), \bar{\theta} > \quad \text{and} \quad \bar{b} =< b'(\theta), \bar{\theta} > \tag{3.30}$$

represent the directional derivatives at θ with respect to $\bar{\theta}$.

Démonstration. Here, we only give the main results, the reader is referred to [59] for a complete proof. Let $(\theta, \bar{\theta}) \in \mathcal{U}_{ad} \times L^\infty(\Omega)$. For all $t > 0$ small enough, $\hat{\theta}(t) = \theta + t\bar{\theta}$ belongs to $\mathcal{U}_{ad}$. Thus, $\hat{p}(t) = p(\hat{\theta}(t))$ and $\hat{u}(t) = u(\hat{\theta}(t))$ are solutions to the system given by :

$$\begin{cases} (i) & -div(\hat{K^*}(t)\nabla \hat{p}(t)) = 0 \\ (ii) & -div(\hat{A^*}(t)e(\hat{u}(t))) = -\hat{b}(t)\nabla \hat{p}(t) \end{cases} \tag{3.31}$$

Where,

$$\hat{K^*}(t) = K^*(\hat{\theta}(t)), \quad \hat{A^*}(t) = A^*(\hat{\theta}(t))$$

We then derive the system (3.31) with respect to the variable t and the resulting derivatives are evaluated at $t = 0$ in order to get the obtained system (3.29). □

As already known [59], the objective function :

$$J^*(\theta) = \int_{\Gamma_N} f_s \, . \, u \, ds + \int_\Omega (-b\nabla p) \, . \, u \, dx = \int_{\Gamma_N} j_1(u) \, ds + \int_\Omega j_2(u,p) \, dx \tag{3.32}$$

is differentiable and the directional derivative at θ with respect to $\bar{\theta}$ is given by

$$\left\langle J^{*'}(\theta), \bar{\theta} \right\rangle = \int_{\Gamma_N} j_1'(u)\bar{u} \, ds + \int_\Omega \frac{\partial j_2}{\partial u}(u,p)\bar{u} \, dx + \int_\Omega \frac{\partial j_2}{\partial p}(u,p)\bar{p} \, dx \tag{3.33}$$

where, $\bar{p} \in H_0^1(\Omega)$ and $\bar{u} \in H_0^1(\Omega)^2$ are the unique solutions to (3.29), respectively. Unfortunately, equation (3.33) is **unusable in practice** because we cannot deduce a simple expression of the derivative $J^{*'}(\theta)$. Indeed, $\bar{u}$ and $\bar{p}$ are linear functions with respect to $\bar{\theta}$, which are non-explicit. To circumvent this issue, the presented Biot-Darcy-based TO method facilitates use of adjoint-variable method to determine the sensitivities, which is performed using the Céa method.

We introduced the Lagrange multiplier for the constraints (3.25), associating $\{p(\theta), u(\theta)\}$ to θ, which is the family $\{\underline{p}, \underline{u}, \ell\} \in H_0^1(\Omega) \times H_0^1(\Omega)^2 \times \mathbb{R}^{*+}$, where ℓ is the Lagrange multiplier designed to respect the volume constraint. In addition, an augmented performance function known as the Lagrangian $\mathcal{L}$ can be defined using the objective function and the mechanical state equations defined by

$$\begin{aligned}\mathcal{L}(\hat{\theta}, \hat{u}, \underline{\hat{u}}, \hat{p}, \underline{\hat{p}}, \ell) := J^*(\hat{\theta}) + \int_\Omega \underline{\hat{u}}(-div(A^*(\hat{\theta})e(\hat{u})) + b(\hat{\theta})\nabla\hat{p})\, dx \\ + \int_\Omega \underline{\hat{p}}(-div(K_D^*(\hat{\theta})\nabla\hat{p}))\, dx + \ell(\int_\Omega \hat{\theta}\, dx - \Theta),\end{aligned} \tag{3.34}$$

where, $(\hat{\theta}, \hat{u}, \underline{\hat{u}}, \hat{p}, \underline{\hat{p}}) \in L^\infty(\Omega) \times H_0^1(\Omega;\mathbb{R}^2)^2 \times H_0^1(\Omega;\mathbb{R})^2$ are independent variables. By straightforward integration by parts, we get

$$\begin{aligned}\mathcal{L}(\hat{\theta}, \hat{u}, \underline{\hat{u}}, \hat{p}, \underline{\hat{p}}, \ell) := J^*(\hat{\theta}) + \int_\Omega (A^*(\hat{\theta})e(\hat{u}) \ : \ e(\underline{\hat{u}}) + b(\hat{\theta})\nabla\hat{p} \,.\, \underline{\hat{u}})\, dx \\ + \int_\Omega K_D^*\nabla\hat{p} \,.\, \nabla\underline{\hat{p}}\, dx + \ell(\int_\Omega \hat{\theta}\, dx - \Theta),\end{aligned} \tag{3.35}$$

Next, the sensitivities are evaluated by differentiating (3.35) with respect to u and p in directions $\phi_u \in H^1(\Omega)^2$ and $\phi_p \in H^1(\Omega)$ defined by

$$\left\langle \frac{\partial\mathcal{L}}{\partial u}(\hat{\theta}, ...,), \phi_u \right\rangle = \int_{\Gamma_N} f_s \,.\, \phi_u\, ds - \int_\Omega b(\hat{\theta})\nabla p \,.\, \phi_u + \int_\Omega A^*(\hat{\theta})e(\phi_u) \ : \ e(\underline{\hat{u}})\, dx \tag{3.36}$$

and

$$\left\langle \frac{\partial\mathcal{L}}{\partial p}(\hat{\theta}, ...,), \phi_p \right\rangle = \int_\Omega (-b\nabla\phi_p) \,.\, u\, dx + \int_\Omega b(\hat{\theta})\nabla\phi_p \,.\, \underline{\hat{u}} + \int_\Omega K_D^*\nabla\phi_p \,.\, \nabla\underline{\hat{p}}\, dx \tag{3.37}$$

which when it vanishes, is nothing more than the variational formulation associated to adjoint-state. Furthermore, the derivatives with respect $\underline{u}$ and $\underline{p}$ in directions $\phi_u \in H^1(\Omega)^2$ and $\phi_p \in H^1(\Omega)$ are simply the state equations defined by :

$$\left\langle \frac{\partial\mathcal{L}}{\partial\underline{u}}(\hat{\theta}, \hat{u}, \underline{\hat{u}}, \hat{p}, \underline{\hat{p}}, \ell), \phi_u \right\rangle = \int_\Omega \Big(A^*e(\hat{u}) \ : \ e(\phi_u)\, dx + b\nabla\hat{p} \,.\, \phi_u\Big), \tag{3.38}$$

and

$$\left\langle \frac{\partial\mathcal{L}}{\partial\underline{p}}(\hat{\theta}, \hat{u}, \underline{\hat{u}}, \hat{p}, \underline{\hat{p}}, \ell), \phi_p \right\rangle = \int_\Omega K_D^*\nabla\hat{p} \,.\, \nabla\phi_p\, dx, \tag{3.39}$$

which when it vanishes, is nothing more than the variational formulation associated to state equations (3.25). Finally, the partial derivative of the Lagrangian $\mathcal{L}$ with respect to θ in direction $\bar{\theta} \in L^\infty(\Omega;\mathbb{R})$ at the stationary point $(u, \underline{u}, p, \underline{p})$ is defined by

$$\left\langle \frac{d\mathcal{L}}{d\theta}, \bar{\theta} \right\rangle = \int_\Omega \left(-e(u)^T\frac{\partial A^*}{\partial\theta}e(u) + \Big(\underbrace{e(u)^T\frac{\partial A^*}{\partial\theta}e(\underline{u}) + \frac{\partial K^*}{\partial\theta}\nabla p \,.\, \nabla\underline{p} + \frac{\partial b}{\partial\theta}(\theta)\nabla p \,.\, \underline{u} + \ell}_{\text{Load sensitivities}}\Big)\right)\bar{\theta}\, dx \tag{3.40}$$

3.4 Topology optimization over the set of isotropic periodic composite materials

3.4.1 Alternate minimization method

This section presents the proposed numerical algorithm, which is based on the homogenization method. The key idea is to compute composite designs for the relaxed formulation rather than "classical" designs, which are merely approximately optimal for the original formulation. Our optimization problem is solved using the alternative minimization algorithm. We seek minimizers of sum of the elastic compliance, fluid-elastic compliance and of the weight of a solid structure under fluid-pressure loads.

Minimizing over the stress field.

Minimization over the stress field σ consists in solving the poro-linear elasticity problem (3.14) over the effective tensor $A^*(x)$ for given design θ of microstructure periodically perforated by the hexagonal cells. Consequently, the poro-linear elasticity problem can be recast as a variational problem, that is : find $u \in V(\Gamma_D^s)$ such that

$$\forall v \in V(\Gamma_D^s), \quad \int_\Omega A^*(\theta)e(u) \ : \ e(v)\ dx = \int_{\Gamma_N^s} f_s\ .v\ ds + \int_\Omega (-b\nabla p)\ .\ v\ dx \tag{3.41}$$

which numerically is solved using P_1 finite elements to compute the displacement u.

Minimizing over the density field.

Minimization over the density field θ for a given stress tensor σ, is performed using the projected gradient algorithm. The minimum compliance problem defined by (3.22) is not self-adjoint, thus one needs to define the associated adjoint problem, which we define using the Céa method presented in section 3.3.2. The descend direction $h = d\theta$ is given by solving :

$$\left\langle \frac{\partial \mathcal{L}}{\partial \theta}, h \right\rangle = -\int_\Omega \left(e(u)^T \frac{\partial A^*}{\partial \theta} e(u) - \Big(\underbrace{e(u)^T \frac{\partial A^*}{\partial \theta} e(\underline{u}) + \frac{\partial K_D^*}{\partial \theta} \nabla p\ .\ \nabla \underline{p} + \frac{\partial b}{\partial \theta} \nabla p\ .\ \underline{u} + \ell}_{\text{Load sensitivities}} \Big) \right) h\ dx, \tag{3.42}$$

where the descend direction $h = d\theta$ has to satisfy the inequality given by :

$$\left\langle \frac{\partial \mathcal{L}}{\partial \theta}(\theta, u, \underline{u}, p, \underline{p}, \ell), d\theta \right\rangle < 0 \tag{3.43}$$

which is achieved by choosing

$$d\theta = \left(e(u)^T \frac{\partial A^*}{\partial \theta} e(u) - \Big(\underbrace{e(u)^T \frac{\partial A^*}{\partial \theta} e(\underline{u}) + \frac{\partial K_D^*}{\partial \theta} \nabla p\ .\ \nabla \underline{p} + \frac{\partial b}{\partial \theta}(\theta) \nabla p\ .\ \underline{u} + \ell}_{\text{Load sensitivities}} \Big) \right) \tag{3.44}$$

At iteration n, the optimal density θ is then updated by performing the projected gradient :

$$\theta^{n+1} = P_{[0,1]}(\theta^n + \delta d\theta), \tag{3.45}$$

where $\delta > 0$ is the step size and $P_{[0,1]}$ is the projection operator on the interval $[0, 1]$. The value of the Lagrange multiplier ℓ is computed at each iteration by a dichotomy process designed to respect the volume constraint. We emphasize that the exact value of ℓ can not be analytically given because of the projection operator. Numerically, the partial derivative of the Lagrangian $\frac{\partial \mathcal{L}}{\partial \theta}$ is regularized using an equivalent H^1-norm :

$$\begin{aligned}\int_\Omega (\frac{\partial \mathcal{L}}{\partial \theta} h + \eta^2 \nabla \frac{\partial \mathcal{L}}{\partial \theta} \,.\, \nabla h)\, dx = -\int_\Omega \Bigg(& \frac{\partial A^*}{\partial \theta} e(u) \;:\; e(u) - \frac{\partial A^*}{\partial \theta} e(u) \;:\; e(\underline{u}) \\ & - \frac{\partial K_D^*}{\partial \theta} \nabla p \,.\, \nabla \underline{p} - \frac{\partial b}{\partial \theta} \nabla p \,.\, \underline{u} - \ell \Bigg) h \, dx,\end{aligned} \tag{3.46}$$

where η is a small coefficient, which typically depends on the size of the elements of the mesh : thanks to this coefficient, we are able to numerically regularize the partial derivative on a length scale of order η and to limit the checkerboard effect on the density θ, similar to those reported in [81, 104, 105]. In practice, we use an adaptive step size δ, which consists in increasing δ by 20%, if the newly computed homogenized structure is accepted : if current compliance is lower than the previous one, else δ is divided by 2.

Volume constraint.

As explained in chapter 2, we do not known how to determine ℓ beforehand and as such, an alternative computations were performed, where the Lagrange multiplier ℓ is adjusted at each iteration, so that the corresponding value of the optimal density satisfies the volume constraint. In other words, once the stress σ^n is computed through (3.41), we determine θ^n through (3.45) and then ℓ^n is determined through a simple iterative procedure, namely by dichotomy.

3.4.2 Implementation

This section presents our complete optimization process to perform topology optimization of structures under fluidic pressure loads and some general difficulties related to the homogenization method.

Complete optimization algorithm.

The optimization algorithm is an iterative method, structured as follows :

1. Initialization of the design variable θ such that :

$$\forall x \in \Omega \quad \theta^0(x) = \frac{\Theta}{\int_\Omega 1 \, dx}$$

2. Iteration until convergence, for $n \geq 0$:
   (a) Computation of the state variable p^n through the Biot-Darcy problem (3.12), with design variable $(\theta^n, A^*(x))$
   (b) Computation of the stress tensor σ^n through the poro-linear elasticity problem (3.14), with design shape $(\theta^n, A^*(x))$
   (c) Computation of the descend direction $d\theta^n$ for a given stress tensor σ^n using formulas (3.42)–(3.44)
   (d) Updating the design variable θ^{n+1} using formulas (3.45) for the descend direction $d\theta^n$ and then updating the design $(\theta^{n+1}, A^*(x))$, by linear interpolation.

Note that, the alternate direction algorithm is apparented to the two known methods in [15, 22, 25].

Convergence criterion.

The procedure is iterated until the quantity :

$$max\left((\max_i(|\theta_i^{n+1} - \theta_i^n|), 1 - \frac{\int_\Omega A^{*-1}(\theta^{n+1})\sigma^{n+1} \ : \ \sigma^{n+1}\, dx + \ell \int_\Omega \theta^{n+1}\, dx}{\int_\Omega A^{*-1}(\theta^n)\sigma^n \ : \ \sigma^n\, dx + \ell \int_\Omega \theta^n\, dx}\right)$$

becomes smaller than a preset threshold. About 100 iterations are required to reach a criterion of order 10^{-5}. Other convergence criteria could be used, for instance the L^2 norm of $\sigma^{n+1} - \sigma^n$.

Singularities in the composite Hooke's law.

The homogenized Hooke's laws computed at each iteration turn out to be singular, an undesired feature when solving problems of linear elasticity. This singular behaviour has several sources. First, we note that the effective tensor is equal to zero when the density vanishes. Implicitly, the corresponding stress field should vanish simultaneously. This problem, which occurs in 2-d and 3-d, is easily circumvented by imposing a positive threshold on the density. In practice, the smallest admissible value of θ is fixed at $1.e{-}3$. Numerical experiments suggest that the choice of 10^{-3} is not important.

3.4.3 Numerical results and discussion

This part deviates from the preliminary version of our article to be published ; supplementary test cases are treated. To demonstrate that evaluation of the consistent nodal loads seen in section 2 from the obtained pressure field produces physically correct results, various (benchmark) design problems involving fluid-pressure loaded stiff structures and small deformation are solved to show the efficacy and robustness of the proposed method, while minimizing the sum of the elastic compliance, fluid-elastic compliance and of the weight of a solid structure. Any change in the value of

considered parameters is reported within the definition of the problem formulation. The above algorithm has been implemented in FreeFem++[80], where all the unknowns are discretized using P_1 finite elements. For all our computations, a linear material model with Young's modulus $\boldsymbol{E} = 12\text{Gpa}$ (i.e., $12 \times 10^9 Nm^{-2}$) and Poisson's ratio $\nu = 0.35$ are considered. The void (i.e., $\theta = 0$) is replaced with a very compliant material, like in the **SIMP** approach in order to avoid singularities of the effective tensor when the elasticity problem is solved.

Pressurized arch problem

This example was originally introduced and solved in [49, 89]. The structure to be found is rectangle of dimensions $0.2m \times 0.1m$, fixed at the edges of its left-right bottom on a zone of width $\frac{1}{8}$, while a pressure load $p = 1$ bar (i.e., $1 \times 10^5 Nm^{-2}$) is applied to the bottom and and vanishes on the boundary $\Gamma^f_{p_0}$ (i.e., $p|_{\Gamma^f_{p_0}} = 0$) : see Fig.3.2 for schematic of this test case. For this calculation, the workspace Ω is discretized with 44492 triangular elements and the volume constraint is set to $\Theta = 20\%$. Evidently, prior to the analysis, the force contribution from the prescribed pressure appears only in y-direction.

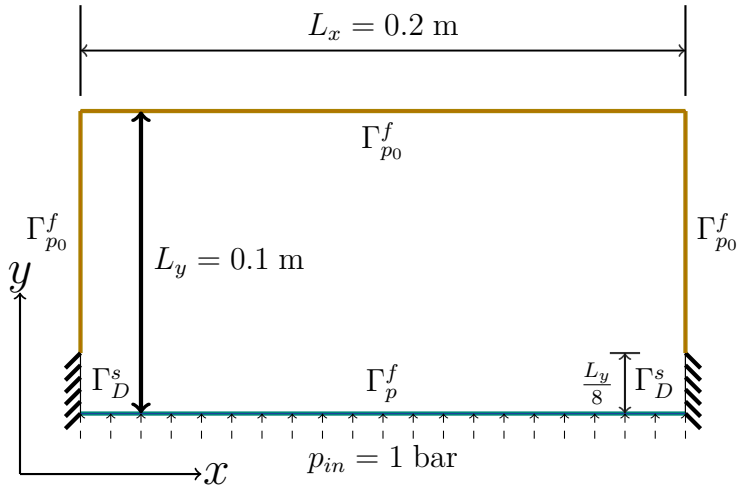

Figure 3.2 – Setting for fluid-elastic compliance minimization problem of Section 3.4.3 issued from [49, 89]

Figure 3.3 shows the output of the alternate minimization algorithm for the three hexagonal cells ; the density θ is represented with a gray scale : areas where $\theta = 1$ are black (pure material), whereas white zones correspond to voids. Although one can guess a "shape" on the edges of the structure, its center contains a large composite zone for all three hexagonal cells. For this later, Figure 3.4 displays the corresponding deformed mesh and pressure field at the final state.

(a) C-hc (b) R-hc (c) S-hc

FIGURE 3.3 – Optimal density for each the hexagonal cell : Classical honeycomb (C-hc), Reinforced honeycomb (R-hc) and Smooth honeycomb (S-hc), for test case of Section 3.4.3

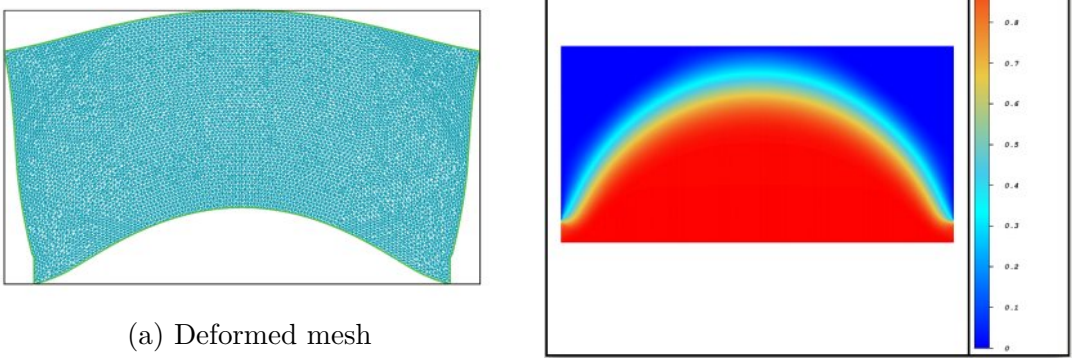

(a) Deformed mesh

(b) Pressure

FIGURE 3.4 – The deformed mesh and pressure field at the final state for test case of Section 3.4.3

Figure 3.5 represents the objective function history for this calculation : smooth and relatively fast convergence is observed. We emphasize that the optimized compliance for each hexagonal cell is quite similar, however the compliance of the reinforced honeycomb is the lowest, followed by the smooth and then classical one.

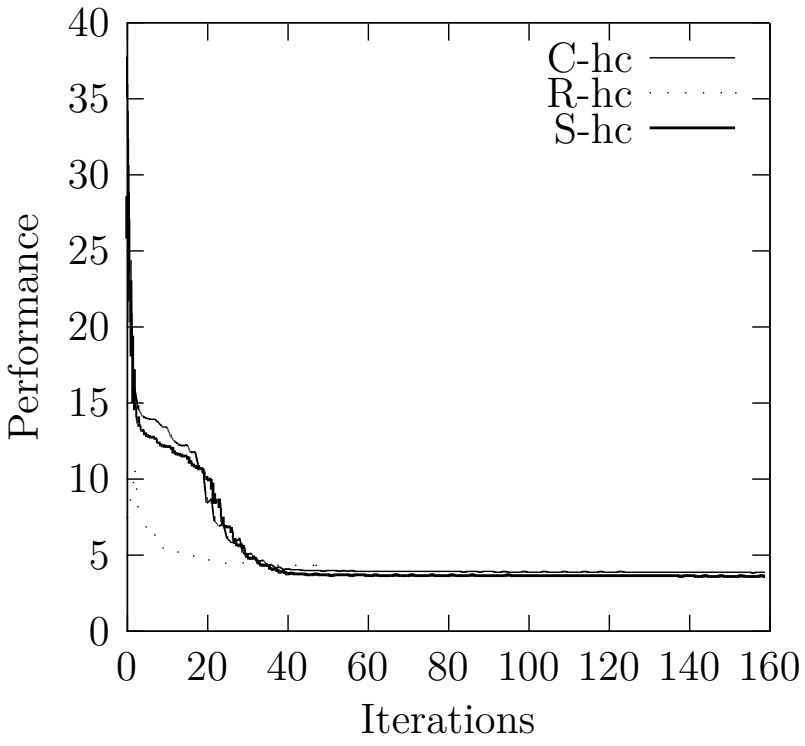

Figure 3.5 – Convergence history for each hexagonal cell : Classical honeycomb (C-hc), Reinforced honeycomb (R-hc) and Smooth honeycomb (S-hc)

Pressurized piston problem

This second test case was originally introduced and solved in [49, 93]. The workspace is a $0.12m \times 0.04m$ rectangle, fixed on the boundary Γ_D^s, while submitted to pressure load $p = 1$ bar on the upper boundary Γ_p^f and vanishes on boundary $\Gamma_{p_0}^f$: see Figure 3.6 for a schematic of the test case. For this calculation, the volume fraction is set to $\Theta = 25\%$. It is desired to find a stiffest optimum design "shape" which can convey the applied pressure loads on the upper boundary to the lower fixed support readily.

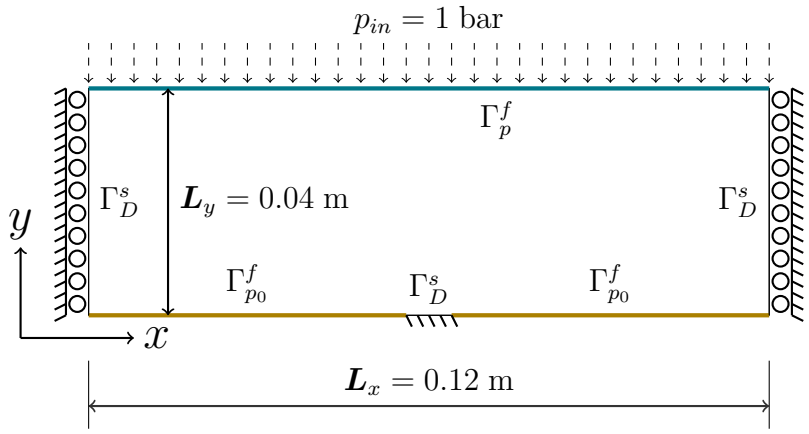

FIGURE 3.6 – Setting for fluid-elastic compliance minimization problem of Section 3.4.3 issued from [49, 93]

Figure 3.7 displays the optimized density for each hexagonal cell. The topology of the result is similar to that obtained in previous literature [49, 87, 99, 100], for similar problems with different design and optimization settings. It is noted that, from a relatively diffused initial interface, the boundary exposed to pressure loading is gradually formed during the optimization process. Although one can guess a "shape" on the edges of the structure, its center contains a large composite zone for all three hexagonal cells. For this latter, Figure 3.8 depicts the deformed mesh and pressure field at the final state.

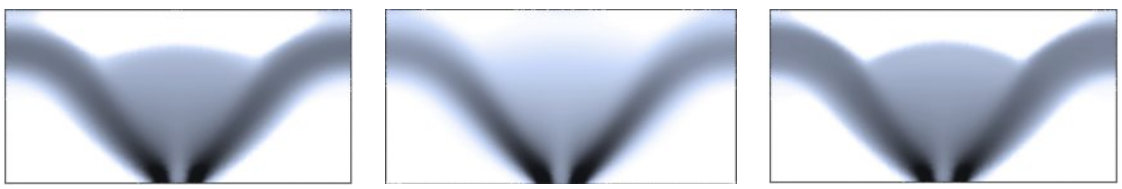

(a) C-hc (b) R-hc (c) S-hc

FIGURE 3.7 – Optimal density for each hexagonal cell : Classical honeycomb (C-hc), Reinforced honeycomb (R-hc) and Smooth honeycomb (S-hc)

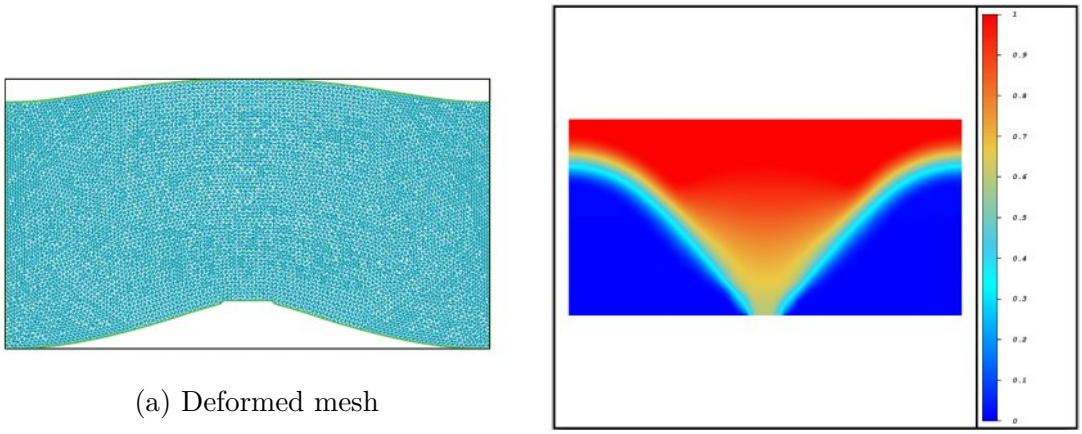

(a) Deformed mesh

(b) Pressure

Figure 3.8 – Deformed mesh (left) and the pressure field (right) at the final state

Figure 3.9 represents the objective function history for this calculation. We emphasize that the optimized compliance for each hexagonal cell is quite similar. However, the compliance of the reinforced honeycomb is the lowest ; smooth and relatively rapid convergence is observed.

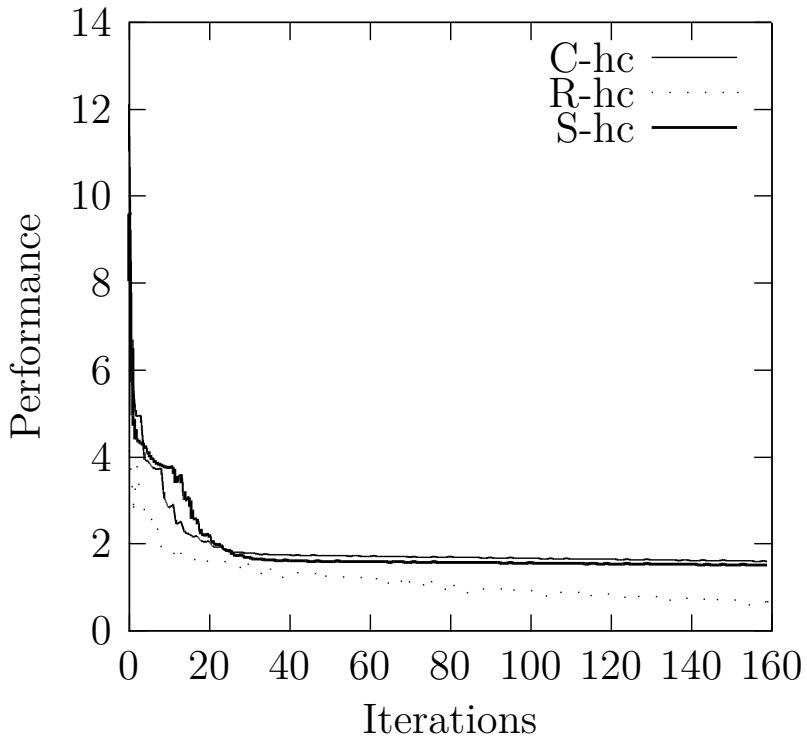

Figure 3.9 – Convergence history for each hexagonal cell : Classical honeycomb (C-hc), Reinforced honeycomb (R-hc) and Smooth honeycomb (S-hc)

Pressurized MBB

In this test case, the structure to be found is submitted to pressure load $p_{in} = 1$ bar on the boundary Γ_p^f, while its boundary Γ_D^s is clamped. The workspace Ω is sketched on Figure 3.10 : a rectangle of dimensions $0.3m \times 0.1m$. The domain is discretized with 43440 triangular elements, where the volume fraction is set to $\Theta = 30\%$. Note that, this example has already been investigated by several authors in the case of structural design under mechanical loading.

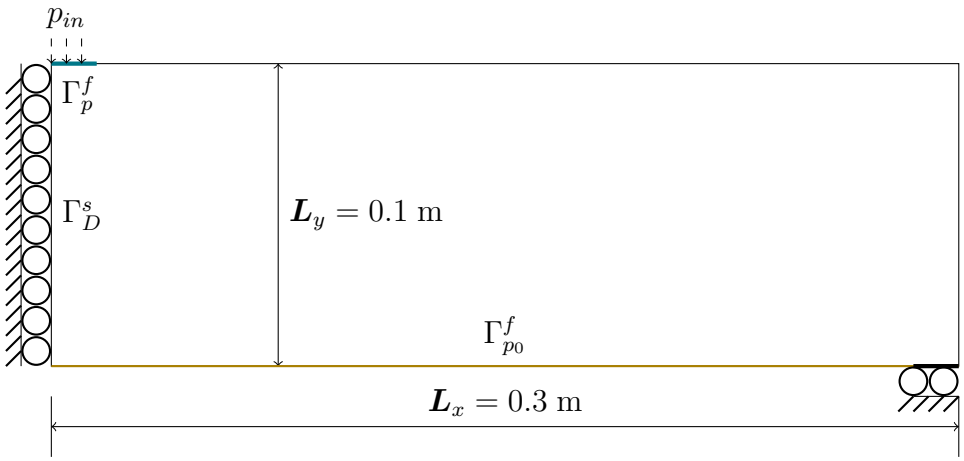

FIGURE 3.10 – Setting for fluid-elastic compliance minimization problem of test case 3.4.3

On Figure 3.11, we display the topology of the optimal design and the resulting von Mises stress, pressure field and deformed mesh under pressure loads at the final state : only the composite perforated by smooth honeycomb cell is displayed but the topology of the result remains valid for all the three hexagonal cells. We emphasize that, the topology is similar to that obtained in the case of mechanical load. On Figure 3.12 , we plot the convergence history for this calculation : smooth and relatively fast convergence is observed.

(a) Density

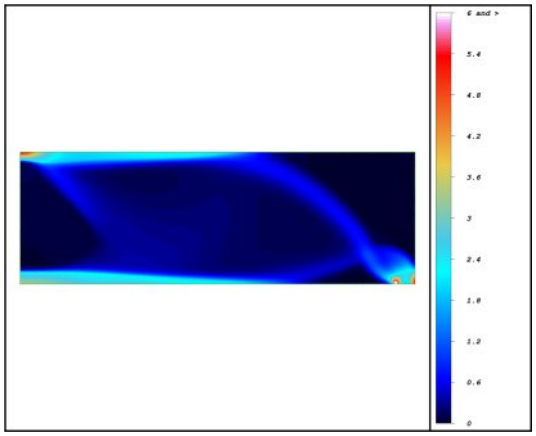

(b) von Mises

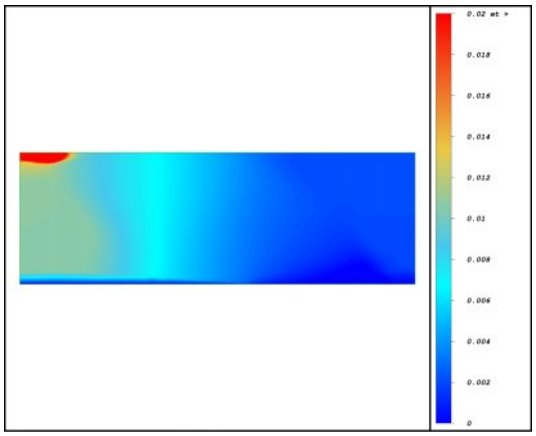

(c) Pressure

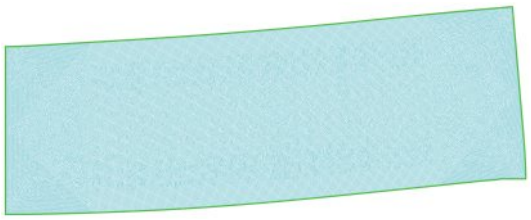

(d) Deformed mesh

Figure 3.11 – (a) The optimal density, (b) von Mises stress, (c) pressure field, and (d) deformed mesh for test case 3.4.3

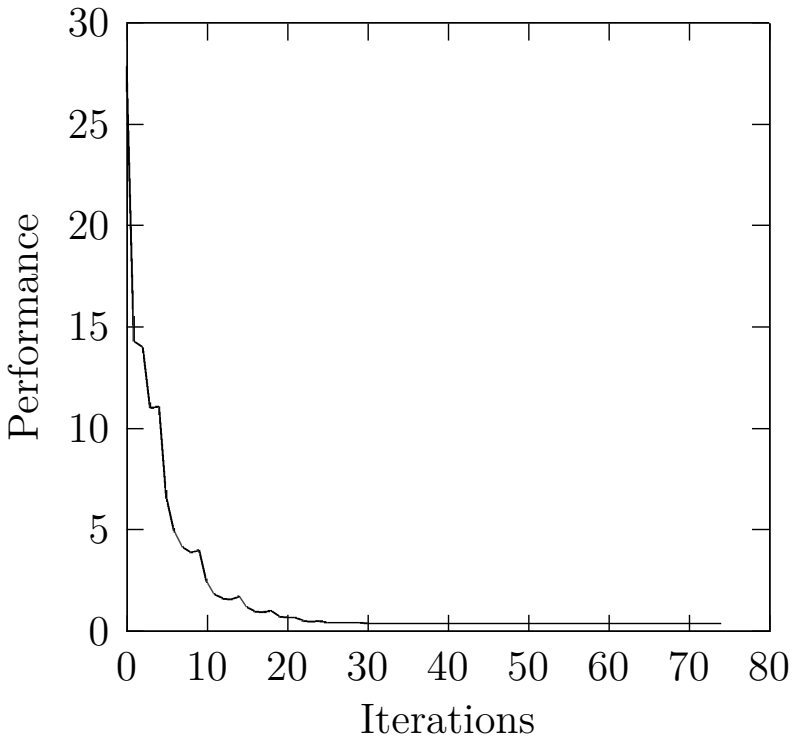

FIGURE 3.12 – Convergence history fluid-elastic compliance minimization problem of test case 3.4.3

Fluid-pressure exchange problem

This example is an attempt to compute a more realistic structure. The structure to be found is a unit box with cavities. The setup is seen in Figure 3.13 and consists of a fluid of density $\boldsymbol{q}_{0,1}$, entering at the middle-left part of the domain, with the corresponding outlet pressure p_0 on the opposite middle-right side ; where as another fluid of density $\boldsymbol{q}_{0,2}$ is located at the upper-middle side of the domain, with the corresponding outlet pressure p_0 at the opposite lower-middle side. All the other boundaries in this device are insulated from the outside : zero Neumann boundary conditions hold for the pressure (i.e., $\frac{\partial p}{\partial n} = 0$), while homogeneous Dirichlet boundary conditions are applied on all four corners of the unit box, on a zone of width $\frac{L_x}{30}$. The numerical values of the parameters involved are displayed on Figure 3.15.

Our aim is to achieve a trade-off between the minimization of the compliance imposed by the fluid and the maximization of the hydraulic strain energy, subject to the volume constraint, that is :

$$J^*(\theta, u(\theta)) = \alpha \underbrace{\left(\int_\Omega A^* e(u) \ : \ e(u) \, dx \right)}_{\text{Elastic strain energy}} + (1-\alpha) \underbrace{\left(- \int_\Omega K^* \nabla p \, . \, \nabla p \, dx \right)}_{\text{Hydraulic strain energy}}, \quad s.t. \left\{ \frac{1}{|\Omega|} \int_\Omega \theta \, dx = \Theta \right. \tag{3.47}$$

where $\alpha \in [0,1]$ is termed as a weighting factor : it measures the relative weight given to each term in (3.47). The objective functional $J^*(\theta, u(\theta))$ corresponds to the internal energy stored inside the structure, under volume constraint (or not). For this optimization problem, the corresponding Lagrangian $\mathcal{L}$ is :

$$\begin{aligned}\mathcal{L}(\hat{\theta}, \hat{u}, \underline{\hat{u}}, \hat{p}, \underline{\hat{p}}, \ell) := J^*(\hat{\theta}, u(\hat{\theta})) + \int_\Omega (A^*(\hat{\theta}) e(\hat{u}) \ : \ e(\underline{\hat{u}}) + b(\hat{\theta}) \nabla \hat{p} \ . \ \underline{\hat{u}}) \ dx \\ + \int_\Omega K^* \nabla \hat{p} \ . \ \nabla \underline{\hat{p}} \ dx + \ell(\int_\Omega \hat{\theta} \ dx - \Theta),\end{aligned} \tag{3.48}$$

and the corresponding partial derivative of the Lagrangian $\mathcal{L}$ with respect to θ in direction $\bar{\theta} \in L^\infty(\Omega; \mathbb{R})$ at the stationary point $(u, \underline{u}, p, \underline{p})$ reads :

$$\begin{aligned}\left\langle \frac{d\mathcal{L}}{d\theta}, \bar{\theta} \right\rangle = \int_\Omega \Bigg(- \alpha \ e(u)^T \frac{\partial A^*}{\partial \theta} e(u) + (1-\alpha) \int_\Omega - \frac{\partial K^*}{\partial \theta} \nabla p \ \nabla p \ dx \\ + \Bigg(\underbrace{e(u)^T \frac{\partial A^*}{\partial \theta} e(\underline{u}) + \frac{\partial K^*}{\partial \theta} \nabla p \ . \ \nabla \underline{p} + \frac{\partial b}{\partial \theta} \nabla p \ . \ \underline{u} + \ell}_{\text{Load sensitivities}} \Bigg) \Bigg) \bar{\theta} \ dx\end{aligned} \tag{3.49}$$

where the formulas needed for the sensitivities and the definition of the adjoint systems read : for u, in direction $\phi_u \in H^1(\Omega)^N$, we get

$$\left\langle \frac{\partial \mathcal{L}}{\partial u}, \phi_u \right\rangle = \alpha \Bigg(\int_{\Gamma_N} f_s \ . \ \phi_u \ ds - \int_\Omega b \nabla p \ . \ \phi_u \ dx \Bigg) + \int_\Omega A^* e(\phi_u) \ : \ e(\underline{\hat{u}}) \ dx \tag{3.50}$$

and for p, in direction $\phi_p \in H^1(\Omega)$, we get

$$\begin{aligned}\left\langle \frac{\partial \mathcal{L}}{\partial p}, \phi_p \right\rangle = -\alpha \int_\Omega b \nabla \phi_p \ . \ u \ dx - 2(1-\alpha) \int_\Omega K^* \nabla p \ . \ \nabla \phi_p \ dx \\ + \int_\Omega b(\hat{\theta}) \nabla \phi_p \ . \ \underline{\hat{u}} \ dx + \int_\Omega K^* \nabla \phi_p \ . \ \nabla \underline{\hat{p}} \ dx\end{aligned} \tag{3.51}$$

which when it vanishes, is nothing more than the variational formulation associated to adjoint-systems.

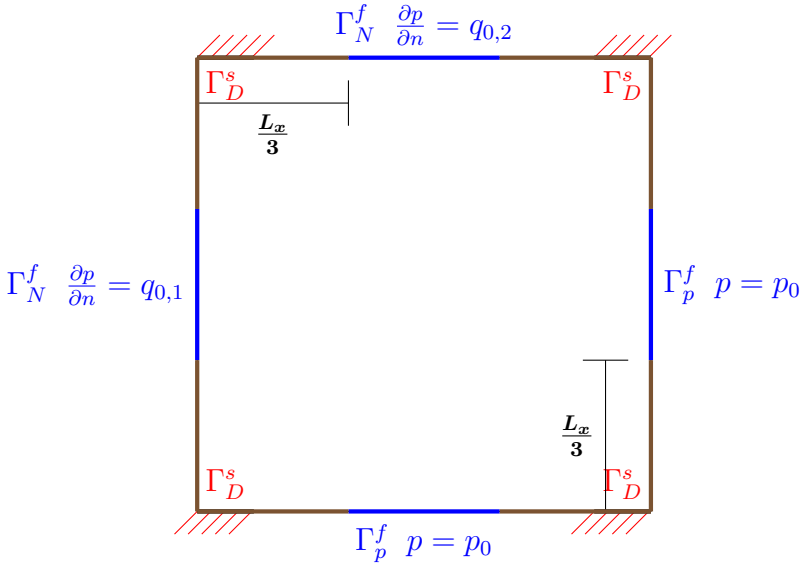

FIGURE 3.13 – Setting of the fluidic pressure exchange problem of Section . The brown layers at the walls stand for zero Neumann boundary conditions for the pressure (i.e., $\frac{\partial p}{\partial n} = 0$).

p_0	$\boldsymbol{q}_{0,1}$	$\boldsymbol{q}_{0,2}$
0.55	1	1

FIGURE 3.14 – Numerical values of the physical parameters in the fluidic pressure exchange problem of Section 3.13

Here, we consider to two configurations, i.e. : (i) a test case with volume constraint set to $\Theta = 20\%$, first and (ii) test case without volume constraint, second, for several values of α. For this calculation, we consider only the smooth honeycomb but the topology of the result remains valid for all hexagonal cells in 2-d.

Figure 3.15 to Figure 3.16 display the optimal densities for a sweep of α for the two configurations, i.e. : with or without volume constraint. Very interestingly, we retrieve the fact that the topology of the results is a tunnel-like dome with composite zone, where the force contribution induced by the fluid appears in all directions, which evidently, prior to the analysis is expected. For this latter, the corresponding objective history for the two configurations are depicted on Figure 3.17 to Figure 3.18. On Figure 3.19, we plot the final volume with respect to α for the second configuration, while on Figure 3.20, we show the convergence history for $\alpha = 1/2$ in both configurations. On Figure 3.21, we display the corresponding pressure field for both configurations, with $\alpha = 1/2$.

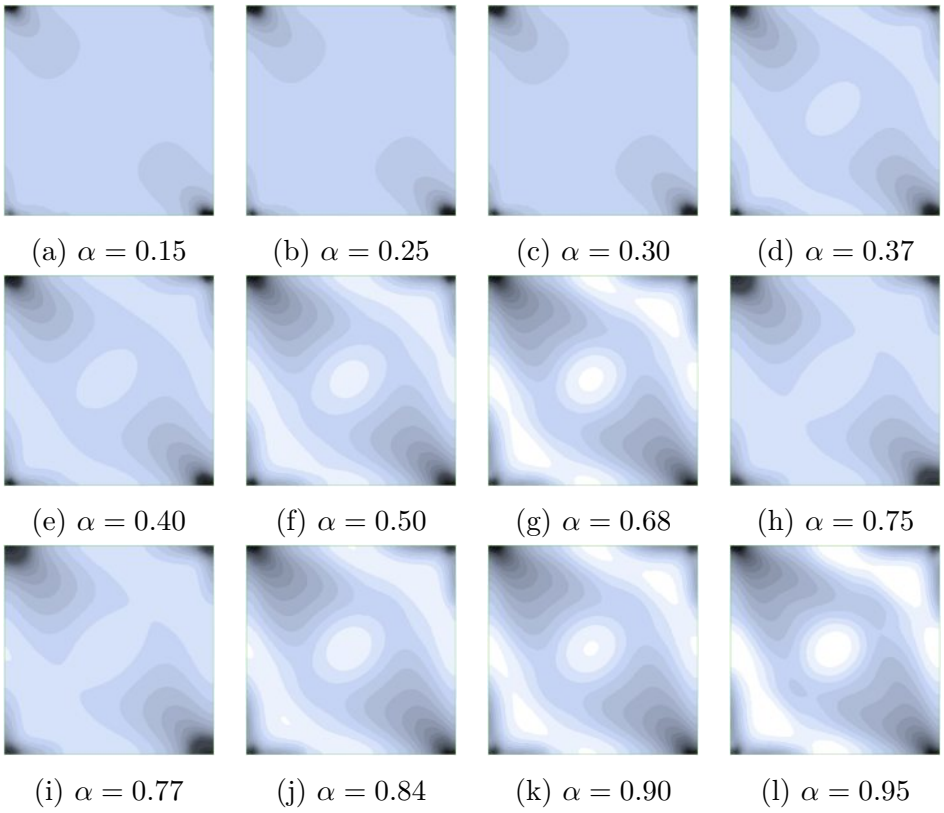

(a) $\alpha = 0.15$ (b) $\alpha = 0.25$ (c) $\alpha = 0.30$ (d) $\alpha = 0.37$

(e) $\alpha = 0.40$ (f) $\alpha = 0.50$ (g) $\alpha = 0.68$ (h) $\alpha = 0.75$

(i) $\alpha = 0.77$ (j) $\alpha = 0.84$ (k) $\alpha = 0.90$ (l) $\alpha = 0.95$

Figure 3.15 – The Optimal densities for a sweep of α, with volume fraction $\Theta = 20\%$

We note that, in both configurations, namely when the optimization is subjected to a volume constraint or not, the topology of the optimal design is α dependent, namely, for all $\alpha \in (0, 0.40)$, the topology tends to maximize the hydraulic strain energy, which in process minimize the output pressure, whereas for all $\alpha \in [0.40, 1)$, the topology of the result tends to achieve a trade-off between the minimization of the compliance induced by the fluid and the maximization of the hydraulic strain energy, which evidently is what we intent to achieve for this optimization problem. However, in the second configuration, we emphasize a gain of volume fraction but not necessarily a gain in performance, see Figure 3.19.

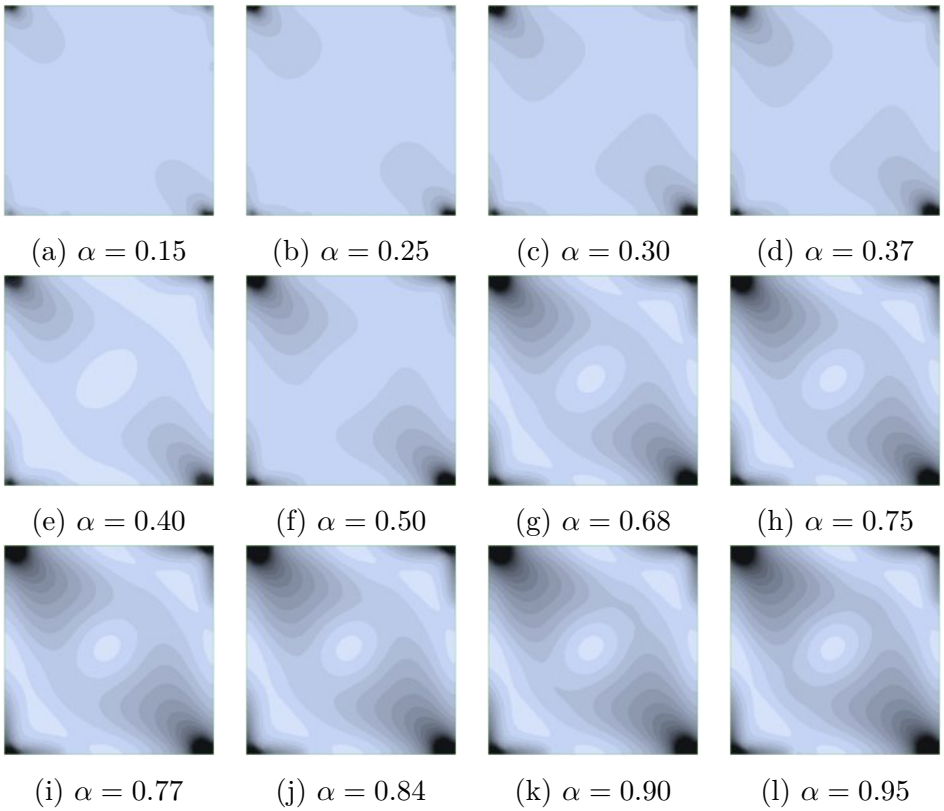

(a) $\alpha = 0.15$ (b) $\alpha = 0.25$ (c) $\alpha = 0.30$ (d) $\alpha = 0.37$

(e) $\alpha = 0.40$ (f) $\alpha = 0.50$ (g) $\alpha = 0.68$ (h) $\alpha = 0.75$

(i) $\alpha = 0.77$ (j) $\alpha = 0.84$ (k) $\alpha = 0.90$ (l) $\alpha = 0.95$

FIGURE 3.16 – The Optimal densities for a sweep of α, without volume constraint

α	0.25	0.30	0.40	0.50	0.77	0.84	0.90	0.95
$J^*(\alpha)$	-0.07	-0.07	-0.05	0.03	0.06	0.41	0.97	0.16

FIGURE 3.17 – The converged objective function wrt. α, with volume fraction $\Theta = 20\%$

α	0.25	0.30	0.40	0.50	0.77	0.84	0.90	0.95
$J^*(\alpha)$	-0.08	-0.08	-0.06	-0.45	0.01	0.03	0.04	0.05

FIGURE 3.18 – The converged objective function wrt. α, without volume constraint

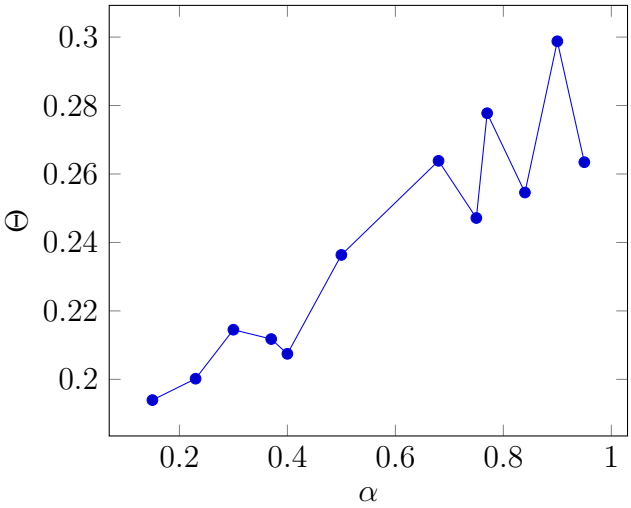

Figure 3.19 – The final volume history wrt. α, in the second configuration, i.e., without volume constraint.

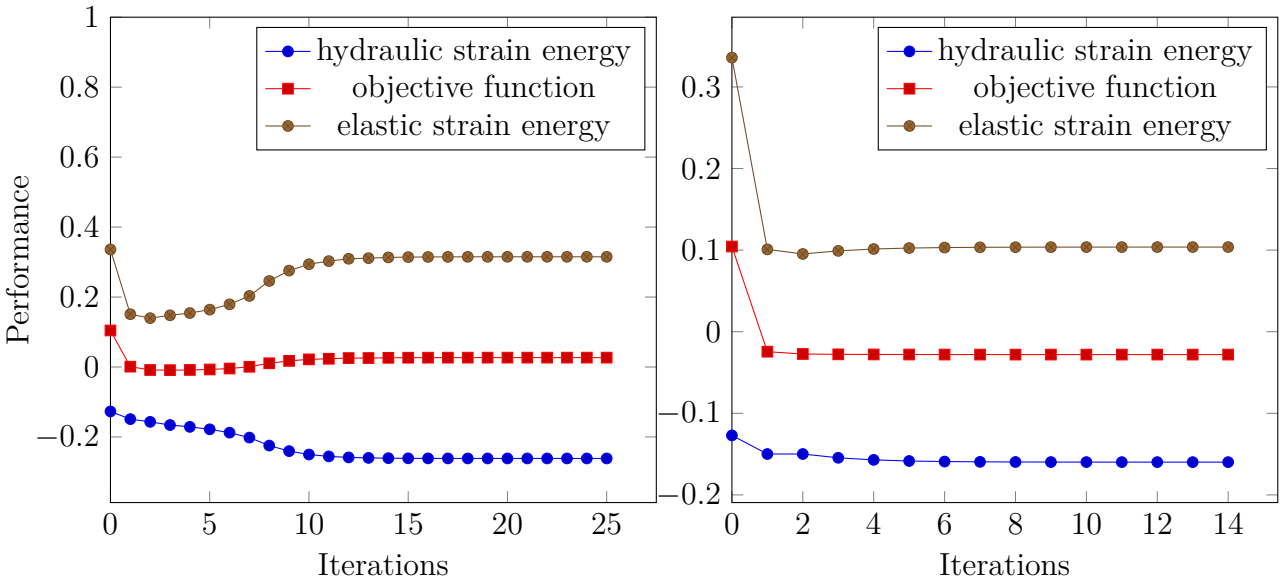

Figure 3.20 – The convergence history wrt. $\alpha = 1/2$, in both configurations,i.e. : with (left) and without (right) volume constraint.

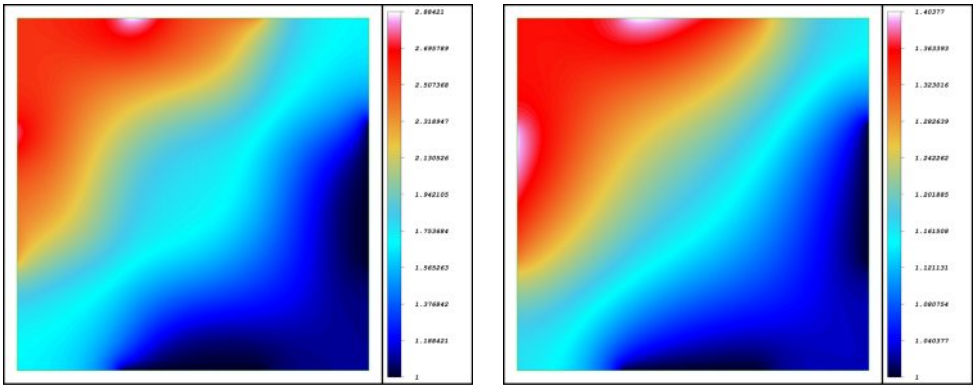

(a) with volume constraint (b) without volume constraint

FIGURE 3.21 – The pressure field at final state for both configuration : with and without volume constraint, for $\alpha = 1/2$

3.5 Conclusion and perspectives

In this work, a novel approach to perform topology optimization of design problems involving fluidic pressure loaded structures was presented using the homogenization method. The approach permits use of standard finite element formulation and does not require explicit boundary description or tracking. As pressure loads vary with the shape and location of the exposed structural boundary, a main challenge in such problems is to determine design-dependent pressure field and its design sensitivities. In the proposed method, Biot-Darcy's law is used to define the design dependent pressure field by solving an associated **PDE** using the standard finite element method. The porosity of each **FE** is related to its material density via a smooth enough function to ensure a smooth transition between void and solid elements. The Biot coefficient is also related to material density, explicitly defined in the case of isotropic porous medium, where the determined pressure field is further used to find the consistent nodal loads. In the early stage of the optimization, the obtained nodal loads are spread out within the design domain and thus, may enhance exploratory characteristics of the formulation and thereby the ability of the optimization process to find well-performing solutions. Furthermore, the Biot-Darcy's parameters, selected a priori to the optimization, affect the topologies of the final density. The method facilitates analytical calculation of the load sensitivities with respect to the design variables using the computationally inexpensive adjoint-variable method. This availability of load sensitivities is an important advantage over various earlier approaches to handle pressure loads in topology optimization. In addition, it is noticed that consideration of load sensitivities within the approach does alter the final density designs, and that the load sensitivities terms are particularly important when designing pressure loaded structures. Moreover, in contrast to methods that use explicit boundary tracking, the proposed Biot-Darcy method offers the potential for relatively straightforward extension to 3-D problems. The effectiveness and robustness of the proposed method is verified by minimizing the sum of the elastic and fluid-elastic compliance, and of the weight of a solid structure under pressure loads. The method allows relocation of the fluidic pressure-loaded boundary

during optimization, and smooth and steady convergence is observed. Extension to 3-D structures and to liquid-liquid heat exchangers problems are presented in chapter 5.

Chapitre 4

Topology optimization of thermal fluid-loaded structures built with isotropic composite materials

We now introduce a simplified thermal fluid-structure model which shall be of interest throughout this whole work. The variables u, p and T are the solutions of three state equations which are weakly coupled in the sense that each of them can be solved successively and independently. This model is based on Biot-Darcy equation for the fluid flow and pressure, the convection-diffusion equation for the temperature variable and linear poro-elasticity for the elastic displacement. We seek minimizers of arbitrary objective functions.

Most of the content of this chapter is in the preliminary version of an article : Agyekum Oheneba G., Jouve F. and Cangémi L., **Topology Optimization of a Coupled Thermal Fluid-Structure Problem**.

4.1 Introduction

One of the ultimate motivations guiding this thesis is the optimization of mechanical structures subjected to thermal loads and cooled down by fluids. In this chapter, we investigate homogenization based topology optimization method for a weakly coupled model of heat propagation, fluid flow and structure deformation. This model is detailed in section 4.2 and serves as a basis for all the numerical shape optimization test cases considered hereafter. It is based on the Biot-Darcy model already seen in chapter 3, on the convection-diffusion equation for heat propagation in both fluid and solid domains, and on the linearized poro-elasticity system for the mechanical displacement of the solid domain. Our main result is the use of an alternate direction algorithm, which successively computes the stress field through the solving of a coupled thermal fluid-structure problem for that stress field over the set of composites periodically perforated by hexagonal cells in 2-d and the use of the adjoint variable method to compute the sensitivities of an arbitrary objective functionals in volume : part of these are given in chapter 3. These formulas are implemented and verified numerically on 2-d test cases. Our 2-d numerical test cases involve either one, two or three of the aforementioned physics simultaneously ; more complex numerical test cases including 3-d problems being specifically detailed in chapter 5.

4.2 Setting of the three-physic problem

Let Ω be a fixed domain in $\mathbb{R}^N$ ($N = 2$ or 3 in applications), fill with composite periodically perforated by the hexagonal cells in 2-d and tetrakaidecahedron cell in 3-d, characterized by one parameter θ, i.e., the material density, which is to be optimized. Throughout this chapter, the normal vector $\boldsymbol{n}$ to $\partial\Omega$ is pointing outward to the domain Ω. The domain Ω is described by three physical variables which are governed by three coupled models :

- the motion of the fluid inside the domain Ω described by the pressure field p, satisfying the Biot-Darcy's law
- the diffusion of heat inside the whole domain Ω, and its transport by convection in the fluid domain, resulting in a temperature field T ;

- the deformation of the solid phase, as a result of the stress exerted by the fluid part and of the dilation induced by thermoelastic effects, characterized by a mechanical displacement u

The physical equations chosen for the modeling of the state variables p, T and u with their relevant set of boundary conditions are described in strong form in section 4.2.1 to section 4.2.3. The homogenization based topology optimization setting is then introduced in 4.2.7. Notation for the setting of boundary conditions as well as for all the physical parameters involved in the state equations are summarized respectively in Figure 4.1.

Ω	Whole domain fill with composite
$\partial\Omega = \Gamma_T^D \cup \Gamma_T^N \cup \Gamma_T$	Boundary of the global domain Ω
Γ_T^D	Dirichlet (isothermal) boundary condition for the temperature variable ($T = T_0$) on Γ_T^D
Γ_T^N	Neumann (adiabatic or isoflux) boundary condition for the temperature variable $-k_f^* \frac{\partial T_f}{\partial \boldsymbol{n}} = h$ on Γ_T^N and $-k_s^* \frac{\partial T_s}{\partial \boldsymbol{n}} = h$ on Γ_T^N
$\partial\Omega = \Gamma_D^s \cup \Gamma_N^s \cup \Gamma^s$	Boundary of the solid domain
Γ_D^s	Dirichlet boundary for the solid variable u
Γ_N^s	Neumann boundary for the solid variable u
$\partial\Omega = \Gamma_D^f \cup \Gamma_N^f \cup \Gamma^f$	Boundary of the fluid domain
Γ_D^f	Dirichlet (inlet) boundary for the fluid variable ($p\vert_{\Gamma_D^f} = p_{in}$)
Γ_N^f	Neumann (outlet) boundary for the fluid variable ($\frac{\partial p}{\partial \boldsymbol{n}}\vert_{\Gamma_N^f} = 0$)
Γ_T	Free boundary for the temperature variable T
Γ^s	Free boundary for the solid variable u

FIGURE 4.1 – The workspace Ω with its boundary conditions

4.2.1 Hydraulic law of type Biot-Darcy for the pressure variable

As already mentioned in section 3.2, Biot-Darcy law is employed to establish the pressure field p as a function of material density θ. It states that fluid flow through a unit area is directly proportional to the pressure drop per unit length ∇p and inversely proportional to the resistance of the porous medium to the flow μ :

$$\boldsymbol{q} := -\frac{\kappa_f}{\mu_f}\nabla p = -K_D^* \nabla p, \tag{4.1}$$

where $\boldsymbol{q}$, κ_f, μ_f, and ∇p represent the flux (ms^{-1}), permeability (m^2), fluid viscosity ($Nm^{-2}s$) and pressure gradient (Nm^{-3}). The flow coefficient K_D^* is assumed to be related to the material density θ : see section 3.2 for more details. In addition, the pressure field p is assumed to satisfy a Biot's law :

$$p := M^* m - M^* b e_{vol}(u), \tag{4.2}$$

where M^*, m, b and $e_{vol}(u)$ are smooth enough functions related to the material density :

$$m(\theta) := (1-\theta)\rho, \quad M^*(\theta) := \frac{1-\theta}{\kappa_v} - \frac{b(\theta)-(1-\theta)}{\kappa_s}, \quad e_{vol}(u) := \nabla \,.\, u. \tag{4.3}$$

Wherein, ρ, κ_v, and κ_s represent the density of the flux, compressibilty of the void and solid phases ; where $e_{vol}(u) = div(u)$, denotes a volume variation of the solid phase. Furthermore, the Biot's law (4.2) is assumed to be related to Darcy's law :

$$\boldsymbol{q} := m v_f = -K_D^* \nabla p, \tag{4.4}$$

where v_f represents the velocity (ms^{-1}) of the flux. Biot-Darcy law renders a gradual pressure drop from the inner pressure boundary $\Gamma^f_{p_{in},D}$ to the outer pressure boundary $\Gamma^f_{p_{out},D}$. Furthermore, the Biot-Darcy law (4.1) is assumed to satisfy the law of conservation of mass (in view of incompressible fluid) :

$$\frac{\partial m}{\partial t} = -div(\boldsymbol{q}) = div(K_D^* \nabla p) = 0 \tag{4.5}$$

Consequently, the pressure field p satisfies :

$$\text{(Biot-Darcy)} \begin{cases} -div(K_D^* \nabla p) = 0 & \text{in } \Omega, \\ \boldsymbol{q}_\Gamma \,.\, \mathbf{n} = f_f & \text{on } \Gamma^f_N, \\ \boldsymbol{q}_\Gamma \,.\, \mathbf{n} = 0 & \text{on } \Gamma^f = \partial\Omega \backslash (\Gamma^f_D \cup \Gamma^f_N), \\ p = p_0 & \text{on } \Gamma^f_D \end{cases} \tag{4.6}$$

In (4.6), f_f is an applied Neumann isoflux condition for the pressure variable p ; the boundary of the fluid phase is the disjoint reunion

$$\partial\Omega = \Gamma^f_D \cup \Gamma^f_N \cup \Gamma^f$$

of a Dirichlet (or inlet) part Γ^f_D where the flow enters with a given $p = p_0$, a Neumann (or outlet) part Γ^f_N where normal stress is observed, and free interface Γ^f of $\partial\Omega$. At this stage it is assumed that the deformation of the solid domain is sufficiently small so that no slip boundary conditions hold on : $\boldsymbol{q}_\Gamma \,.\, \mathbf{n} = 0$. Therefore, the variable p depend solely on the material density $\theta(x)$, for all $x \in \Omega$.

$v_f \in H^1(\Omega;\mathbb{R}^N)$	Fluid velocity
$p \in H^1(\Omega)$	Fluid pressure
$\mu_f \in \mathbb{R}_+^*$	Fluid viscosity
$\rho \in \mathbb{R}_+^*$	Fluid density
$f_f \in H^{1/2}(\Gamma_N^f)$	Neumann (adiabatic or isoflux) condition for the pressure p
$p_0 \in H^{1/2}(\Gamma_D^f)$	Input inlet or outlet pressure
$m \in \mathbb{R}_+^*$	Mass of the fluid
$M^* \in L^\infty(\Omega;\mathbb{R}_+^*)$	Biot modulus
$b \in L^\infty(\Omega;\mathbb{R}_+^*)$	Biot coefficient
$K_D^* \in L^\infty(\Omega;\mathbb{R}_+^*)$	Homogenized permeability of type Darcy
$T \in H^1(\Omega)$	Temperature field
$T_s \in H^1(\Omega)$	Restriction of T to the solid phase
$T_f \in H^1(\Omega)$	Restriction of T to the fluid phase
$T_0 \in H^{1/2}(\Omega)$	Input temperature on the total boundary
$c_p \in \mathbb{R}_+^*$	Heat capacity of the fluid
$k_f^* \in \mathbb{R}_+^*$	Homogenized conductivity in fluid phase
$k_s^* \in \mathbb{R}_+^*$	Homogenized conductivity in solid phase
$h_{vol}^* \in \mathbb{R}_+^*$	Thermal exchange parameter at interface solid/fluid
$h \in H^{1/2}(\Gamma_T^N)$	Input entering heat flux on the total boundaries
$u \in H^1(\Omega;\mathbb{R}^N)$	Homogenized elastic displacement field
$T_{ref} \in \mathbb{R}_+^*$	Reference temperature in the solid
$\alpha \in \mathbb{R}_+^*$	Thermal expansion coefficient
$u_0 \in H^{1/2}(\Gamma_D^s;\mathbb{R}^N)$	Prescribed displacement
$f_s \in L^2(\Gamma_N^s;\mathbb{R}^N)$	Input traction force

FIGURE 4.2 – Physical parameters considered in the weakly coupled model

4.2.2 Convection diffusion for the temperature variable

The fluid velocity v_f determines the physical behavior of the temperature T in the whole domain Ω as a result of convection and diffusion effects inside the fluid domain

and of pure diffusion inside the solid domain : we recall that, when ϵ tends to 0, the periodic microstructure Ω_ϵ tends to an homogeneous domain Ω fill with fine mixtures of solid and void/fluid phases. Denoting by k^* and k_s^* the thermal conductivity inside the fluid and solid phases respectively, and by c_p the thermal capacity of the fluid, the temperature field T is determined by the convection-diffusion equations :

$$\begin{cases} -div(k_f^*\nabla T_f) + h_{vol}^*(T_s - T_f) + \phi(\rho c_p)_f T_f' + \phi(\rho c_p)_f v_f \nabla T_f = 0 & \text{in } \Omega, \\ -div(k_s^*\nabla T_s) + h_{vol}^*(T_f - T_s) + \phi(\rho c_p)_s T_s' = 0 & \text{in } \Omega, \\ T = T_0 & \text{on } \Gamma_T^D, \\ -k_f^*\frac{\partial T_f}{\partial \boldsymbol{n}} = -k_s^*\frac{\partial T_s}{\partial \boldsymbol{n}} = h & \text{on } \Gamma_T^N, \\ T_f = T_s & \text{on } \Gamma_T^D, \\ -k_f^*\frac{\partial T_f}{\partial \boldsymbol{n}} = -k_s^*\frac{\partial T_s}{\partial \boldsymbol{n}} = 0 & \text{on } \Gamma_T \end{cases} \tag{4.7}$$

where we use the subscripts $_f$ and $_s$ for the restrictions T_f and T_s of T to fluid and solid phases in Ω. The boundary $\partial\Omega = \Gamma_T^D \cup \Gamma_T^N \cup \Gamma_T$ is split into a Dirichlet part, where a temperature T_0 is imposed on Γ_T^D and a Neumann part where a given incoming heat flux h is applied on Γ_T^N. The physical parameter h_{vol}^* is a thermal exchange at interface solid and fluid/void phases.

The convection-diffusion equations (4.7) can be recast as thermal Biot-Darcy equation :

$$\begin{cases} -div(k_f^*\nabla T_f) + h_{vol}^*(T_s - T_f) + (c_p m)_f T_f' + (-c_p K_D^*\nabla p)_f \nabla T_f = 0 & \text{in } \Omega, \\ -div(k_s^*\nabla T_s) + h_{vol}^*(T_f - T_s) + (c_p m)_s T_s' = 0 & \text{in } \Omega, \\ T = T_0 & \text{on } \Gamma_T^D, \\ -k_f^*\frac{\partial T_f}{\partial \boldsymbol{n}} = -k_s^*\frac{\partial T_s}{\partial \boldsymbol{n}} = h & \text{on } \Gamma_T^N, \end{cases} \tag{4.8}$$

where $\phi\rho v_f = m v_f = -K_D^*\nabla p$ satisfies the Darcy law (4.1). Consequently, for the remainder of this work, our convection-diffusion model is given by (4.8), which we assumed stationary :

$$\begin{cases} -div(k_f^*\nabla T_f) + h_{vol}^*(T_s - T_f) + (-c_p K_D^*\nabla p)_f \nabla T_f = 0 & \text{in } \Omega, \\ -div(k_s^*\nabla T_s) + h_{vol}^*(T_f - T_s) = 0 & \text{in } \Omega, \\ T = T_0 & \text{on } \Gamma_T^D, \\ -k_f^*\frac{\partial T_f}{\partial \boldsymbol{n}} = -k_s^*\frac{\partial T_s}{\partial \boldsymbol{n}} = h & \text{on } \Gamma_T^N, \end{cases}$$

Similar to the Biot-Darcy model (4.6), starting from a microscopic description of a problem, one seeks a macroscopic or effective model problem in conductivity. We consider a model problem of thermal flow in a periodic medium : an heterogeneous domain obtained by mixing periodically two different phases, one being the solid phase and the other the void inclusions. As in chapter 3, section 3.3.1, to compute the homogenized conductivity tensor k^*, we introduce the so-called cell problems, and since the considered cell Y is specifically chosen in order to design isotropic composites, only one of its coefficient (e.g., $(k^*)_{11}$) could be computed in order to fully characterized k^*, a scalar value : see 3.3.1, for details.

The homogenized heat transfer coefficient h_{vol} $(W.m^{-3}.K^{-1})$, is a volumetric coefficient that is related to the convective exchange coefficient h_{s-f} $(W.m^{-2}.K^{-1})$, which in turn is related to the surface exchange :

$$h_{vol} = h_{s-f}.a_c \tag{4.9}$$

$$h_{s-f} = \frac{\boldsymbol{q}_{s\mapsto f}}{(T_s - T_f).S_\Gamma} \tag{4.10}$$

where $\boldsymbol{q}_{s\mapsto f}(W)$, is the averaged heat transfer over the entire surface $S_\Gamma(m^2)$. S_Γ is the surface of the solid that is in contact with the fluid and a_c, is the specific surface area : defined as the total lateral surface area of the cell Y (e.g., the hexagonal cells in 2d or tetrakaidecahedron in 3d).

remark 15. *In various applications where convective heat transfer cannot be neglected (e.g., heat exchanger, solar receiver design, etc...), the condition of local equilibrium is no longer valid [106] : the pores are not small enough, when the thermal properties differ widely or when convective transport is important. Hence, many authors took initiative to describe and emphasize separate transport equations for each phase when the assumption of local thermal equilibrium failed to be valid ; this work should be approached within such a background.*

4.2.3 Thermoelasticity with fluid structure interaction for the elastic variable

Finally, the pressure variable p and the temperature T together determine the displacement u of the solid in Ω, which is assumed to be an isotropic thermoelastic composite material with homogenized Lamé coefficients λ^*, μ^*, thermal expansion parameter α and temperature at rest T_{ref}. The homogenized elastic displacement u is characterized by the equations of linear thermal poro-elasticity of type Biot-Coussy :

$$\begin{cases} -div(\sigma(u, T_s)) = -b\nabla p & \text{in } \Omega, \\ u = u_0 & \text{on } \Gamma^s_D, \\ \sigma(u, T_s)\boldsymbol{n} = f_s & \text{on } \Gamma^s_N, \end{cases} \tag{4.11}$$

where the homogenized stress tensor is given by

$$\sigma(u, T) = A^*\Big(e(u) - \alpha(T_s - T_{ref})I\Big) \quad \text{with } A^*e(u) = 2\mu^* e(u) + \lambda^* \mathrm{Tr}(e(u))I, \tag{4.12}$$

and where, $-b\nabla p$ and I are the coupled fluid resulting from the pressure and the identity matrix. In (4.11), the boundary $\partial\Omega$ is split into respectively a Dirichlet part Γ^s_D where a displacement $u = u_0$ is prescribed, a Neumann part Γ^s_N where a stress f_s is imposed, and a free part Γ^s.

remark 16. *The above model is a simplified version of a genuine thermal fluid-solid coupling between the solid and fluid phases. A more accurate description of fluid-structure interaction would feature a transition regime and inertia regime :*

$$\boldsymbol{q} := mv_f + \rho C_{for} v_f^2$$

where C_{for} is a inertia parameter of the fluid flow, called Forchheimer coefficient. It is noted that in the work by Kumar and Jobic [102], 3-D numerical simulations at pore scale were performed to study the pressure drop characteristics ; fluid flow through open cell foam was performed in three different regimes : Darcy regime, transition regime and inertia regime. They showed that these effects can no longer be neglected when the number of Reynolds increases, i.e. for example when the pore size increases. They revealed a Darcean regime with a low Reynolds number and a non-linear regime dependent on flow velocity after a transition zone.

For sake of simplicity, we opted for simplified version, which is justifiable insofar as we wish to obtain a first qualitative result of microstructure without however, sizing accurately as possible the system. Hence, the Forchheimer coefficient C_{for} is neglected and in (4.8), the thermal exchange h^*_{vol} is taken constant.

Thanks to this simplification, the system (4.6) to (4.11) is only weakly coupled : its resolution is achieved by solving first the fluid system (4.6), then using the fluid stress resulting from the pressure p in the heat transfer equation (4.8), and finally using the fluid stress and the temperature T_s to solve (4.11).

4.2.4 Shape optimization setting

The final goal of the thesis is the resolution of relaxed unconstrained version of the original optimization problems of the form

$$\begin{aligned} &\min_{\theta} J^*(\theta, p(\theta), T(\theta), u(\theta)) \\ \text{s.t} &\begin{cases} g_i(\theta, p(\theta), T(\theta), u(\theta)) = 0, & 1 \leq i \leq p, \\ h_j(\theta, p(\theta), T(\theta), u(\theta)) \leq 0, & 1 \leq j \leq q, \end{cases} \end{aligned} \tag{4.13}$$

where J^*, g_i and h_j are arbitrary relaxed shape objective and constraint functionals set by a user. For its resolution, we shall rely on the alternative minimization algorithm detailed in chapter 3, which (like any other first order optimization method) requires the knowledge of the shape derivatives of the above functionals : adjoint variable method is used to determine sensitivities of the objective function and constraints with respect to the design variable θ. In the context of the adjoint variable method (reviewed in chapter 3, section 3.3.2), this means computing the Fréchet (or directional) derivative of the mapping

$$\theta \mapsto J^*(\theta, p(\theta), T(\theta), u(\theta)),$$

where we recall that θ is material density belonging in general to $\mathcal{U}_{ad}$, defined by

$$\mathcal{U}_{ad} := \left\{ \theta \in L^\infty(\Omega; \mathbb{R}^*_+) \mid \theta(x) \in [0,1], \forall x \in \Omega \right\}$$

4.2.5 A fully Lagrangian setting for computing shape derivatives of arbitrary objective functionals

Although very common and widely used in the literature (e.g., see [107]), an issue with Céa's method as exposed in Chapter 3 sect. 3.3.2(see also [59]) is that the computation of the shape derivatives depend very much on the assumptions made on the nature of the considered objective functional J^*. Different type of functionals may lead to different strong forms for the adjoint equations (see Chapter 2 sect. (2.3.3) to (2.3.5), where this fact is exemplified), which imposes to redo the analytical derivation whenever the objective function is modified, and to update the numerical implementation accordingly.

Again as in chapter 3 sect.3.3.2, we use a fully Lagrangian setting to derive rigorously the shape derivative of very general objective functionals in the simplified setting of (3.25) to (4.11). The shape sensitivities of the state variables $p(\theta)$, $T(\theta)$ and $u(\theta)$ are calculated first, in order to obtain the shape derivative of an arbitrary objective functional in volume form. Then, under sufficient regularity assumptions, the well-known Céa method together with suitable augmented Lagrangian functional yield general shape derivative formulas.

A modified objective functional and Lagrangian derivative of the state variables

Again, the starting remark is that the relaxed functional J^*, although appearing naturally in the formulation of the optimization problem (4.13) is not so convenient for the mathematical analysis. Indeed, the domain of definition of $J^*(\theta, ., ., .)$ is a $V(\Gamma_D^f) \times V(\Gamma_T^D) \times V(\Gamma_D^s)$, functional space which depends on the first argument θ. In order to discuss the precise mathematical settings of our multiphysic system, we introduce the functional spaces which are required for the thermal fluid-structure interaction, i.e., for the pressure variable p

$$V(\Gamma_D^f) = \{q \in H^1(\Omega) \mid q = 0 \text{ on } \Gamma_D^f\},$$

temperature variable T

$$V(\Gamma_T^D) := \{S \in H^1(\Omega) \mid S = 0 \text{ on } \Gamma_T^D\},$$

and for the displacement u

$$V(\Gamma_D^s) := \{v \in H^1(\Omega)^N \mid v = 0 \text{ on } \Gamma_D^s\}$$

We consider the subspace

$$H^{1/2}(\Gamma_N^s) = \{v|_{\Gamma_N^s} \mid v \in V(\Gamma_D^s)\}$$

and its dual space $H^{-1/2}(\Gamma_N^s)$; as well the affine spaces associated to the non-homogeneous Dirichlet boundary data $u_0 \in H^{1/2}(\Gamma_D^s; \mathbb{R}^N)$, $p_{in} \in H^{1/2}(\Gamma_D^f; \mathbb{R})$ and $T_0 \in H^{1/2}(\Gamma_T^D; \mathbb{R})$ featured in (3.25) to (4.11). The state variables p, T, u are the solutions to the following

variational problems : for the Biot-Darcy equation (3.25), find $p \in p_{in} + V(\Gamma_D^f)$ such that :

$$\forall q \in V(\Gamma_D^f) \quad \int_\Omega K_D^* \nabla p \,.\, \nabla q + \int_{\Gamma_N^f} f_f \; q \; dx = 0, \tag{4.14}$$

for the thermal equation (4.2.2), find $T \in T_0 + V(\Gamma_T^D)$ such that

$$\begin{cases} \int_\Omega k_s^* \nabla T \,.\, \nabla S \; dx + \int_{\Gamma_{T,N}} hS \; ds + \int_\Omega h_{vol}^* (T_f - T) S \; dx = 0, \\ \int_\Omega k_f^* \nabla T \,.\, \nabla S \; dx + \int_{\Gamma_{T,N}} hS \; ds + \int_\Omega h_{vol}^* (T_s - T) S \; dx + \int_\Omega (-c_p S K_D^* \nabla p) \,.\, \nabla T \; dx = 0, \end{cases} \tag{4.15}$$

for the thermal poro-linear elasticity equations (4.11), find $u \in u_0 + V(\Gamma_D^s)$ such that

$$\forall v \in V(\Gamma_D^s) \quad \int_\Omega \sigma(u, T_s) e(v) \; dx - \int_{\Gamma_N^s} f_s \,.\, v \; ds + \int_\Omega b \nabla p \,.\, v \; dx = 0 \tag{4.16}$$

remark 17. *Let us comment on the well-posedness of the coupled system of variational problems (4.14) to (4.16). As in Chapter 3 sect.3.3.2, the volumic source terms are assumed to enjoy H^1 regularity in the domain. The surface fluxes h and f_s in (4.8) and (4.11) are assumed to belong to L^2 spaces. The variational formulation of the thermal equations (4.8) is not well-posed in utter generality because of the lack of coercivity induced by the advection term $\int_\Omega (-c_p K_D^* \nabla p) \nabla T_f$ (4.2.2) and of the presence of inhomogeneous Dirichlet boundary conditions. However, in usual applications [45], it is customary to impose a Dirichlet boundary condition $T = T_{0,f}$ at the inlet of the computational domain (where $-K_D^* \nabla p \,.\, \boldsymbol{n} < 0$) and a Neumann boundary condition $-k_f^* \nabla T \,.\, \boldsymbol{n} = 0$. This together with the incompressibility condition $-div(K_D^* \nabla p) = 0$ is easily shown to imply the coercivity of the bilinear form featured in (4.15) ; see e.g. [59].*

Eventually, the well-posedness of the linear elasticity problem (4.16) results from the Lax-Milgram theorem. In the above context, we aim at solving the minimization problem (4.13) where the pressure $p(\theta)$, temperature $T(\theta)$ and elastic displacement $u(\theta)$ are the solutions to (4.6) to (4.11).

In order to address the sensitivity of an arbitrary objective function, the classical idea is to work within a Lagrangian framework. Therefore, we consider the corresponding Lagrangian, which is an augmented function of the objective function :

$$\begin{aligned} \mathcal{L}(\hat{\theta}, \hat{u}, \underline{\hat{u}}, \hat{p}, \underline{\hat{p}}, \hat{T}, \underline{\hat{T}}, \ell) := J^*(\hat{\theta}) &+ \int_\Omega \underline{\hat{u}} (-div(\sigma(\hat{u}, \hat{T}) + b(\hat{\theta}) \nabla \hat{p}) \; dx \\ &+ \int_\Omega \underline{\hat{T}} (-div(k_f^* \nabla \hat{T}_f) + (-c_p K_D^* \nabla \hat{p}) \nabla \hat{T}_f - div(k_s^* \nabla \hat{T}_s)) \\ &+ \int_\Omega \underline{\hat{p}} (-div(K_D^*(\hat{\theta}) \nabla \hat{p})) \; dx + \ell(\int_\Omega \hat{\theta} \; dx - \Theta), \end{aligned} \tag{4.17}$$

where, $(\hat{\theta}, \hat{u}, \underline{\hat{u}}, \hat{p}, \underline{\hat{p}}, \hat{T}, \underline{\hat{T}}) \in L^\infty(\Omega) \times H_0^1(\Omega; \mathbb{R}^2)^2 \times H_0^1(\Omega; \mathbb{R})^2 \times H_0^1(\Omega; \mathbb{R})^2$ are independent variables. We emphasize that the objective function $J^*(\hat{\theta})$ depends upon the

state variables u, p and T. By straightforward integration by parts, we get

$$\begin{aligned}\mathcal{L}(\hat{\theta},\hat{u},\underline{\hat{u}},\hat{p},\underline{\hat{p}},\ell) = J^*(\hat{\theta}) + \int_\Omega (\sigma(\hat{u},\hat{T}) \ : \ e(\underline{\hat{u}}) + b(\hat{\theta})\nabla\hat{p} \ . \ \underline{\hat{u}})\ dx \\ + \int_\Omega k_f^*\nabla\hat{T}_f \ . \ \nabla\underline{\hat{T}} + \int_\Omega k_s^*\nabla\hat{T}_s \ . \ \nabla\underline{\hat{T}} + \int_\Omega (-c_p\underline{\hat{T}}K_D^*\nabla\hat{p})\nabla\hat{T}_f \\ + \int_\Omega K_D^*\nabla\hat{p} \ . \ \nabla\underline{\hat{p}}\ dx + \ell(\int_\Omega \hat{\theta}\ dx - \Theta),\end{aligned} \tag{4.18}$$

Again, we point out that J^* is assumed smooth enough functional, elsewise we cannot apply the Céa method.

4.2.6 Sensitivity analysis for the three-physic problem

In a gradient-based topology optimization, it is essential to determine sensitivities of the objective functional and the constraints with respect to the design variable(s). The sensitivities are evaluated by differentiating the above augmented objective function (4.18) with respect to state variables u, p and T in directions $\phi_u \in H^1(\Omega)^2$, $\phi_p \in H^1(\Omega)$ and $\phi_T \in H^1(\Omega)$. Let $(u,\underline{u}) \in H^1_{\Gamma_N}(\Omega)^N$ be a stationary point of $\mathcal{L}$. The derivative of equation (4.18) with respect to u in direction $\phi_u \in H^1(\Omega)^N$ is given by :

$$\left\langle \frac{\partial\mathcal{L}}{\partial u}, \phi_u \right\rangle = < \frac{\partial J^*}{\partial u}, \phi_u > + \int_\Omega (< \frac{\partial\sigma}{\partial u}, \phi_u > : \ e(\underline{\hat{u}}))\ dx, \tag{4.19}$$

while the derivative with respect to p in direction $\phi_p \in H^1(\Omega)$ is given by :

$$\left\langle \frac{\partial\mathcal{L}}{\partial p}, \phi_p \right\rangle = < \frac{\partial J^*}{\partial p}, \phi_p > + \int_\Omega b\nabla\phi_p \ . \ \underline{\hat{u}}\ dx + \int_\Omega (-c_p\underline{\hat{T}}K_D^*\nabla\phi_p)\nabla\hat{T}_f + \int_\Omega K_D^*\nabla\phi_p \ . \ \nabla\underline{\hat{p}}\ dx, \tag{4.20}$$

and the derivative with respect to T in direction $\phi_T \in H^1(\Omega)$ is given by

$$\begin{aligned}\left\langle \frac{\partial\mathcal{L}}{\partial T}, \phi_T \right\rangle = < \frac{\partial J^*}{\partial T}, \phi_T > + \int_\Omega < \frac{\partial\sigma}{\partial T}, \phi_T > : \ e(\underline{\hat{u}})\ dx + \int_\Omega k_f^*\nabla(\phi_T)_f \ . \ \nabla\underline{\hat{T}}\ dx \\ + \int_\Omega k_s^*\nabla(\phi_T)_s \ . \ \nabla\underline{\hat{T}} + \int_\Omega (-c_p\underline{\hat{T}}K_D^*\nabla\hat{p})\nabla(\phi_T)_f\ dx,\end{aligned} \tag{4.21}$$

which when equation (4.19) to (4.21) vanish, are nothing more than the variational formulation associated to the adjoint-states. Furthermore, the derivatives with respect $\underline{u}$, $\underline{p}$ and $\underline{T}$ in directions $\phi_u \in H^1(\Omega)^2$, $\phi_p \in H^1(\Omega)$ and $\phi_T \in H^1(\Omega)$ are simply the state equations defined by :

$$\left\langle \frac{\partial\mathcal{L}}{\partial\underline{u}}, \phi_u \right\rangle = \int_\Omega (\sigma(\hat{u},\hat{T}) \ : \ e(\phi_u) + b(\hat{\theta})\nabla\hat{p} \ . \ \phi_u)\ dx, \tag{4.22}$$

$$\left\langle \frac{\partial\mathcal{L}}{\partial\underline{p}}, \phi_p \right\rangle = \int_\Omega K_D^*\nabla\hat{p} \ . \ \nabla\phi_p\ dx, \tag{4.23}$$

and

$$\left\langle \frac{\partial \mathcal{L}}{\partial \underline{T}}, \phi_T \right\rangle = \int_\Omega k_f^* \nabla \hat{T}_f \,.\, \nabla \phi_T + \int_\Omega k_s^* \nabla \hat{T}_s \,.\, \nabla \phi_T + \int_\Omega (-c_p \phi_T K_D^* \nabla \hat{p}) \nabla \hat{T}_f \, dx, \quad (4.24)$$

which when it vanishes, is nothing more than the variational formulation associated to the state equations (4.8)-(4.11). Finally, the partial derivative of the Lagrangian $\mathcal{L}$ with respect to θ in direction $\bar{\theta} \in L^\infty(\Omega; \mathbb{R})$ at the stationary point $(u, \underline{u}, p, \underline{p}, T, \underline{T})$ is defined by

$$\begin{aligned} \left\langle \frac{d\mathcal{L}}{d\theta}, \bar{\theta} \right\rangle =< \frac{\partial J^*}{\partial \theta}, \bar{\theta} > + \int_\Omega \Bigg((\frac{\partial \sigma}{\partial \theta} \ : \ e(\underline{\hat{u}}) + \frac{\partial b}{\partial \theta} \nabla \hat{p} \,.\, \underline{\hat{u}}) \, dx + \int_\Omega \frac{\partial K_D^*}{\partial \theta} \nabla \hat{p} \,.\, \nabla \underline{\hat{p}} \, dx \\ + \frac{\partial k_f^*}{\partial \theta} \nabla \hat{T}_f \,.\, \nabla \underline{\hat{T}} + \frac{\partial k_s^*}{\partial \theta} \nabla \hat{T}_s \,.\, \nabla \underline{\hat{T}} + (-c_p \underline{\hat{T}} \frac{\partial K_D^*}{\partial \theta} \nabla \hat{p}) \nabla \hat{T}_f + \ell \Bigg) \bar{\theta} \, dx \end{aligned} \quad (4.25)$$

remark 18. *The variational problem (4.18) makes sense for general objective functions which are smooth enough. Let us point out that they may lead to different adjoint equations (4.19)-(4.21), which is the way they are obtained with Céa's method (this is one of the reasons why the sensitivity analysis must be repeated from the beginning when changing the type of the objective functional). For instance, if we consider an objective functional depending on $u(\theta)$ and $p(\theta)$ through a volume integral :*

$$J^*(\theta) = \int_\Omega j_s(u) \, dx + \int_\Omega j_f(p) \, dx$$

for two $\mathcal{C}^2$ functions j_s, j_f : $L^\infty(\Omega) \to \mathbb{R}$ with bounded second order derivatives, then

$$< (J^*)'(\theta), \bar{\theta} >= \int_\Omega j_s'(u)\bar{u} + \int_\Omega j_f'(p)\bar{p}, \quad (4.26)$$

where $\bar{u} \in H_0^1(\Omega)^N$ and $\bar{p} \in H_0^1(\Omega)$ are solution to some strong form. Unfortunately, equation (4.26) is unusable in practice because we cannot deduce a simple expression of the derivative $(J^*)'(\theta)$. Indeed, $\bar{u}$ and $\bar{p}$ are linear functions with respect to $\bar{\theta}$, which are non-explicit. To circumvent this issue, the adjoint variables $\underline{u}$ and $\underline{p}$ allow to obtain an expression independent of $\bar{u}$ and $\bar{p}$.

4.2.7 Alternate minimization method

We now briefly describe how the methodology presented in Chapter 3 sect.3.3.2 applies to the weakly coupled multiphysics system of (4.6) to (4.11). The key idea is to compute composite designs for the relaxed formulation rather than "classical" designs, which are merely approximately optimal for the original formulation, i.e. : the proposed numerical algorithm is the concern of the theory of homogenization. Our optimization problem (4.13) is solved using the alternative minimization algorithm.

Minimizing over the stress field

Minimization over the stress field σ consists in solving the thermal poro-linear elasticity problem (4.11) over the effective tensor $A^*(x)$, for given design shape θ of microstructure periodically perforated by the hexagonal cells in 2-d and tetrakaideca-hedron cell in 3-d. Consequently, the thermal poro-linear elasticity problem (4.11) can be recast as a variational problem :

$$v \in V(\Gamma_D^s), \quad \int_\Omega \sigma(u,T) \ : \ e(v)\ dx = \int_{\Gamma_N^s} f_s\ .v\ ds + \int_\Omega (-b\nabla p)\ .\ v\ dx \tag{4.27}$$

Which numerically, is solved using P_1 finite elements to compute the displacement vector field u.

Minimizing over the density field

Minimization over the density field θ for a given stress tensor σ is performed using the projected gradient algorithm. As the minimization problem (4.13) is not self-adjoint, one needs to define the associated adjoint problem, which is performed using the Céa method, presented above. The descend direction $h = d\theta$ is given by solving :

$$\begin{aligned}\left\langle \frac{\partial \mathcal{L}}{\partial \theta}, h \right\rangle =< \frac{\partial J^*}{\partial \theta}, h > + \int_\Omega \Bigg(\frac{\partial \sigma}{\partial \theta} \ : \ e(\underline{u}) + (\frac{\partial b}{\partial \theta}\nabla p\ .\ \underline{u}) + \frac{\partial K_D^*}{\partial \theta}\nabla \hat{p}\ .\ \nabla \underline{\hat{p}}\ dx \\ + \frac{\partial k_f^*}{\partial \theta}\nabla T_f\ .\ \nabla \underline{T} + \frac{\partial k_s^*}{\partial \theta}\nabla T_s\ .\ \nabla \underline{T} + (-c_p \underline{T}\frac{\partial K_D^*}{\partial \theta}\nabla p)\nabla T_f + \ell \Bigg) h\ dx,\end{aligned} \tag{4.28}$$

where the descend direction $h = d\theta$ has to satisfy the inequality

$$\left\langle \frac{\partial \mathcal{L}}{\partial \theta}(\theta, u, \underline{u}, p, \underline{p}, T, \underline{T}, \ell), d\theta \right\rangle < 0 \tag{4.29}$$

which is achieved by choosing

$$\begin{aligned}d\theta = -\Bigg(\frac{\partial J^*}{\partial \theta}(\theta) + \frac{\partial \sigma}{\partial \theta} \ : \ e(\underline{u} + \frac{\partial b}{\partial \theta}\nabla p\ .\ \underline{u} + \frac{\partial K_D^*}{\partial \theta}\nabla \hat{p}\ .\ \nabla \underline{\hat{p}}\ dx + \frac{\partial k_f^*}{\partial \theta}\nabla T_f\ .\ \nabla \underline{T} + \\ \frac{\partial k_s^*}{\partial \theta}\nabla T_s\ .\ \nabla \underline{T} + (-c_p \underline{T}\frac{\partial K_D^*}{\partial \theta}\nabla p)\nabla T_f) + \ell \Bigg)\end{aligned} \tag{4.30}$$

At iteration n, the optimal density θ is then updated by performing the projected gradient :

$$\theta^{n+1} = P_{[0,1]}(\theta^n + \delta d\theta), \tag{4.31}$$

where $\delta > 0$ is the step size and $P_{[0,1]}$ is the projection operator on the interval $[0, 1]$. Again, we point out that the value of the Lagrange multiplier ℓ is computed at each

iteration by a dichotomy process designed to respect the volume constraint. Numerically, the partial derivative of the Lagrangian $\frac{\partial \mathcal{L}}{\partial \theta}$ is regularized using an equivalent H^1-norm :

$$\int_\Omega (\frac{\partial \mathcal{L}}{\partial \theta} h + \eta^2 \nabla \frac{\partial \mathcal{L}}{\partial \theta} \,.\, \nabla h)\, dx = < \frac{\partial J^*}{\partial \theta}, h > + \int_\Omega \Big((\frac{\partial \sigma}{\partial \theta} \;:\; e(\underline{u}) + \frac{\partial b}{\partial \theta} \nabla p \,.\, \underline{u}) + \frac{\partial k_f^*}{\partial \theta} \nabla T_f \,.\, \nabla \underline{T} + \frac{\partial k_s^*}{\partial \theta} \nabla T_s \,.\, \nabla \underline{T} + (-c_p \frac{\partial K_D^*}{\partial \theta} \nabla p) \nabla T_f \, \underline{T} + \ell \Big) h \, dx, \tag{4.32}$$

where η is a small coefficient, which typically depends on the size of the elements of the mesh : thanks to this coefficient, we are able to numerically regularize the partial derivative on a length scale of order η and to limit the checkerboard effect on the density θ.

Complete optimization algorithm.

The optimization algorithm is an iterative method, structured as follows :

1. Initialization of the design variable θ such that :

$$\forall x \in \Omega \quad \theta^0(x) = \frac{\Theta}{\int_\Omega 1 \, dx}$$

2. Iteration until convergence, for $n \geq 0$:
   (a) Computation of the state variable p^n through the Biot-Darcy problem (3.12), with the design $(\theta^n, A^*(x))$
   (b) Computation of the state variable T^n through the convection-diffusion equations (4.8), with the design $(\theta^n, A^*(x))$
   (c) Computation of the stress tensor σ^n through the thermal poro-linear elasticity problem (4.11), with the design shape $(\theta^n, A^*(x))$ and the descend direction $d\theta^n$ for a given stress tensor σ^n using formulas (4.30)
   (d) Updating the design variable θ^{n+1} using formulas (4.31) for the descend direction $d\theta^n$ and then updating the design $(\theta^{n+1}, A^*(x))$, by linear interpolation.

Note that, the alternate direction algorithm is apparented to the two known methods in [15, 22, 25].

4.3 Numerical test cases

This section is devoted to the presentation of several 2-d test cases which in particular allow to verify numerically the sensitivity analysis formulas presented in sect.4.2.6 for the three-physic problem. This verification is based on the assumption that their correct implementation should make objective functions decrease and constraints become gradually satisfied, in accordance with the expected behavior of our full alternate

minimization algorithm for the constrained optimization (detailed in chapter 2, section 2.3.1 for linear elasticity case). Here, we demonstrate on various multiphysics examples how the previous ideas can be effectively implemented in order to address a wide range of topology optimization problems.

4.3.1 A few details about the numerical implementation

Our numerical implementation follows algorithm 4.2.7 outlined in chapter 1 for the linear elasticity case. We rely on the open-source **FreeFem++** environment for the resolution of Finite Element problems [80] (see [29, 31] for its use in the context of structural optimization and [45, 49] for its use in the context of fluid flow optimization). Since much more details shall be provide in chapter 5, we content ourselves to provide here only a brief overview of our implementation.

The Biot-Darcy (3.12), convection-diffusion equations (4.8), and the elastic displacement u in (4.11) are solved consequently, where the space functions $V(\Gamma_D^f)$, $V(\Gamma_T^D)$ and $V(\Gamma_D^s)$ are discretized with P_1 finite elements. In all the considered examples, the Young's modulus is set to $\boldsymbol{E} = 12\text{Gpa}$ (i.e., $12 \times 10^9 Nm^{-2}$) and Poisson's ratio to $\nu = 0.35$; volume expressions of shape derivatives are considered for the computation of a descent direction as described in chapter 4 sect.4.2.6. Once the shape derivative $\frac{d\mathcal{L}}{\partial\theta}$ of the considered relaxed objective function J^* (or the constraints) is assembled, the optimization problem is updated using **FreeFem**. In several cases, we observed without explanation that the use of the volume expression was beneficial, either for obtaining better composite shapes or smoother convergence curves for the objective function and constraints. A few comparisons illustrating these facts shall be provided hereafter.

In all our examples, the considered shape and topology optimization problems feature equality or inequality constraints, for instance on the volume of one of the two phases (solid and void). As explained in chapter 2, we do not known how to determine ℓ beforehand, so an alternative computations were performed, where the Lagrange multiplier ℓ is adjusted at each iteration, so that the corresponding value of the optimal density satisfies the volume constraint. In the following, we treat a variety of test cases which are all sub-cases of the full three physics model. The first three examples are benchmark test cases of the literature featuring only two physics : thermoelasticity and heat convection. The final example involves all physics simultaneously.

4.3.2 Minimum compliance problem in thermoelasticity

In this paragraph, we reproduce a test case already been introduced in [13, 108] by Xia and Wang, and Feppon (where level-set method is used) for compliance minimization in thermoelasticity. In this example, the workspace is a 2×1 rectangle. The structure is clamped on the left and right sides of the domain, and subjected to a traction load on the middle of the bottom boundary (i.e., boundary Γ_N^s). It is made of an effective elastic material characterized by Lamé parameters $\lambda^*(\theta)$, $\mu^*(\theta)$, thermoelastic coefficient $\alpha = 0.77$ (independent of the density) and reference temperature $T_{ref} = 0$.

A constant temperature field $T = T_{ref} + \Delta T$ is applied on the whole structure, which induces thermal expansion. The setting is reproduced on Figure 4.3.

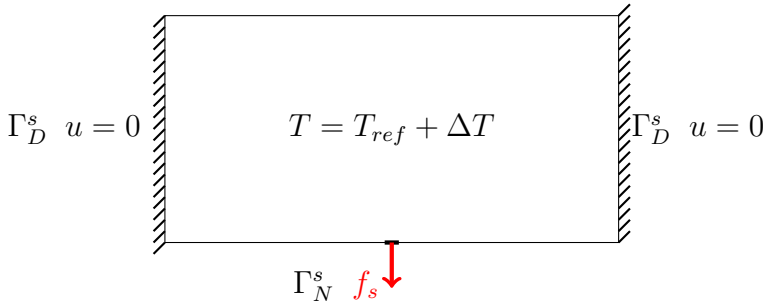

Figure 4.3 – Setting for the thermoelastic compliance minimization problem of (4.3.2) issued from [13, 108]

We seek minimizers of the sum of the elastic compliance, subject to a volume constraint, that is :

$$\min_{\theta} J^*(\theta) = \min_{\theta} \int_{\Omega} A^*(\theta) e(u) \;:\; e(u)\, dx,$$

where u is the unique solution to the coupled thermoelasticity problem :

$$\begin{cases} (i) & T = T_{ref} + \Delta T \\ (ii) & -div(\sigma(u,T)) = 0 \\ (iii) & \frac{1}{|\Omega|} \int_{\Omega} \theta \, dx = \Theta, \end{cases}$$

where

$$\sigma(u,T) = A^*\Big(e(u) - \alpha \Delta T I_2\Big) \quad \text{with } A^* e(u) = 2\mu^* e(u) + \lambda^* \mathrm{Tr}(e(u)) I_2,$$

Note that, all mechanical equilibrium equations are satisfied under small deformation assumption. Strictly speaking, the problem still involves only one physics (the heat conduction problem (4.2.2) does not need to be solved since the temperature field is prescribed). We could have made it multiphysics by applying loads, however we keep the setting in [13, 108]. The force applied in [13, 108] has a value $F = 1$, which is set in our implementation by prescribing a traction force density $f_s = -1/\epsilon$ on a small portion of size $\epsilon = 0.023$ on the boundary. For this calculation, the volume constraint is set to $\Theta = 25\%$

The optimized topologies are shown on Figure 4.4 for each case. For this later, the corresponding deformed mesh for each configuration is displayed on Figure 4.5, while we plot on Figure 4.6, the convergence history for this calculation. Note that our numerical values do not coincide exactly with those in [13, 108] because their original physical parameters and optimization method are different from our algorithm, although we clearly retrieve similar optimized shapes albeit composite shapes.

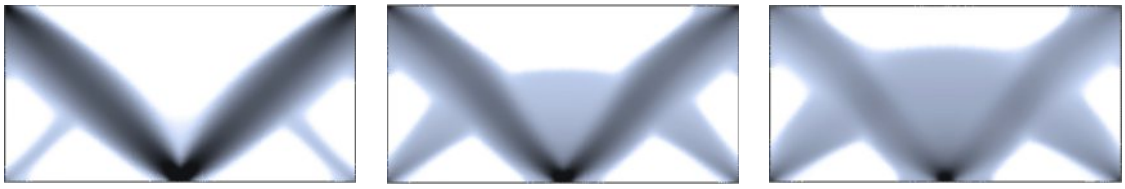

(a) $\Delta T = 0$ (b) $\Delta T = 5$ (c) $\Delta T = 10$

FIGURE 4.4 – (a) The optimal density for each case in the thermoelastic problem (4.3.2)

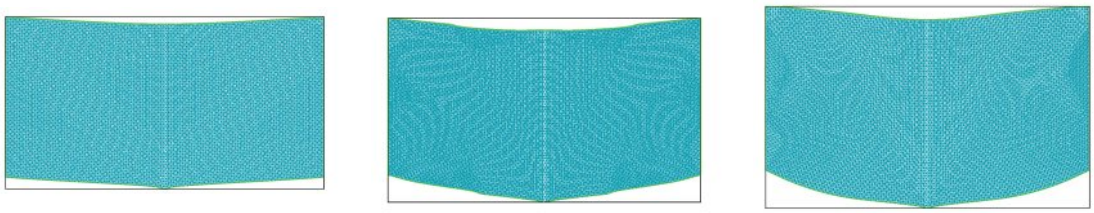

(a) $\Delta T = 0$ (b) $\Delta T = 5$ (c) $\Delta T = 10$

FIGURE 4.5 – (a) The deformed mesh for each case in the thermoelastic problem (4.3.2)

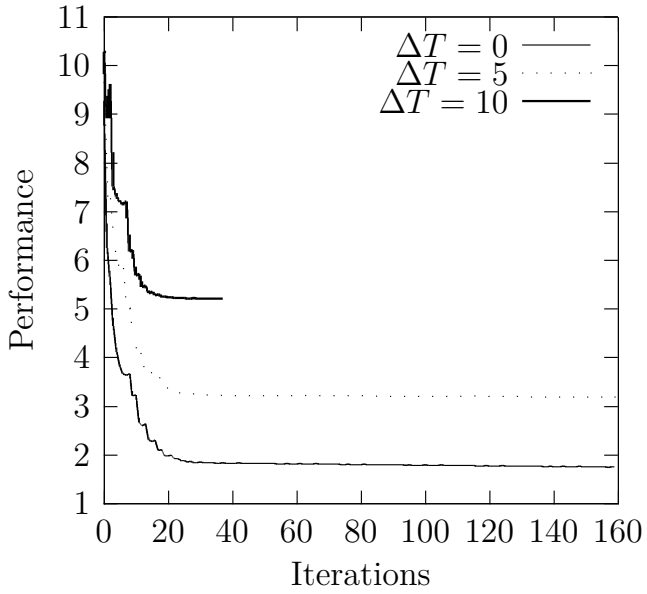

FIGURE 4.6 – Convergence history featuring each case, in the thermoelastic problem (4.3.2

4.3.3 A convective heat transfer problem

Our second example involves only a coupling of the flow (4.6) and heat equations (4.8), i.e., the elastic equation (4.11) is not taken into account. In this test case, the

structure to be found is unit box with two cavities, where a fluid is entering with densities q_0^1, q_0^2 and an inlet temperature T_{in}. The setting is similar to that introduced and solved in [13] (with level-set method) and in [109] (with density based method), although here, we use different flow model, different parameters values ; namely, lower heat capacity of the fluid c_p, conductivity k_s^*, k_f^* (while $c_p = 100, k_s = 10$ and $k_f = 1$). The other regions of the boundary of the cavity are insulated from the outside, i.e. : zero normal fluxes boundary conditions hold for the temperature and zero pressure $p = 0$. The setting is reproduced on Figure 4.7 and numerical values of the parameters involved are displayed on Figure 4.8.

Our aim is to achieve a trade-off between the minimization of the strain hydraulic energy dissipated by the fluid and the maximization of the heat transferred by the fluid, subject to an upper bound on the output pressure drop and a volume constraint, that is :

$$\begin{aligned} &\min_{\theta} J^*(\theta, p(\theta), T(\theta)) = \int_\Omega c_p K_D^* \nabla p \,.\, \nabla T \\ &s.t. \begin{cases} \mathrm{DP}(p(\theta)) = \int_{\Gamma_N^{f_{int}}} p \; ds - \int_{\Gamma_N^{f_{out}}} p \; ds \leq \mathrm{DP}_{static} \\ \frac{1}{|\Omega|} \int_\Omega \theta \; dx = \Theta \end{cases} \end{aligned} \tag{4.33}$$

Note that the objective function J^* is seen as the opposite of heat transferred from the inlet $\Gamma_N^{f_{int}}$ to the outlet $\Gamma_N^{f_{out}}$ upon integration by parts :

$$\begin{aligned} \int_\Omega c_p K_D^* \nabla p \,.\, \nabla T &= \int_\Omega -c_p div(K^* \nabla p) \; T \; dx + \int_{\partial\Omega} c_p (K_D^* \nabla p \,.\, n) \; T \; ds \\ &= \int_{\Gamma_N^{f_{int}}} c_p (K_D^* \nabla p \,.\, n) \; T \; ds + \int_{\Gamma_N^{f_{out}}} q_0 c_p \; T \; ds \end{aligned}$$

where the second term is a constant depending on the inlet data. The upper bound constraint on the static pressure drop is set to $\mathrm{DP}_{static} = 8.4$ and the volume constraint is set to $\Theta = 40\%$ of the volume of the total domain $|\Omega|$ and only the reinforced honeycomb is displayed but the result remains valid for all hexagonal cells. As in [45], we consider two possible configurations , featuring : $T_{up,1}$ and $T_{up,2}$, for the applied temperature T_{up} at the upper wall of the system. In the first case, the upper and lower wall temperatures are equal and higher than the inlet temperature : $T_{in} < T_{up} = T_{low}$, while in the second case, the upper wall temperature is lower than the inlet temperature : $T_{up} < T_{in} < T_{low}$.

remark 19. *The constraint function DP does a priori make sense because the pressure p belongs a priori to $H^1(\Omega)$ and has well defined trace on the boundary.*

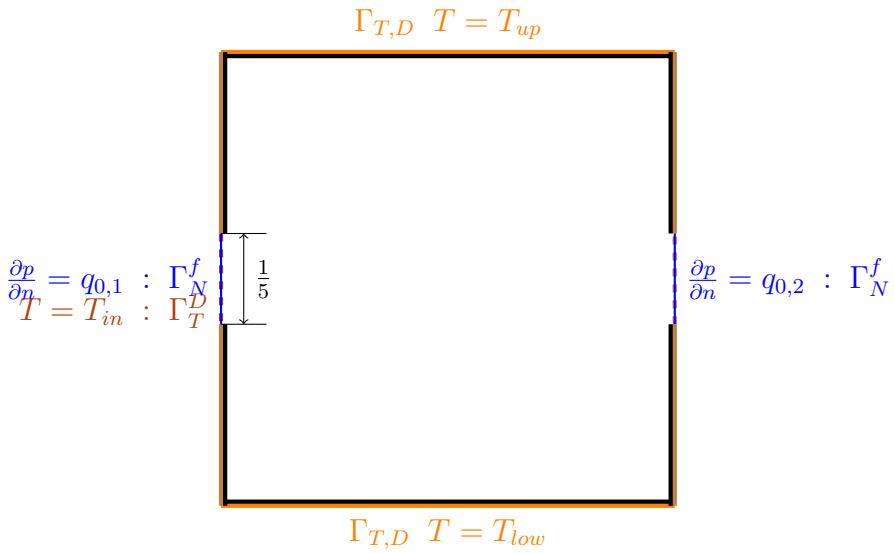

FIGURE 4.7 – Setting of the convective heat transfer test case of Section 4.3.3. The black layers at the walls stand for solid, non optimizable boundaries and the brown stand for zero normal fluxes for the temperature

c_p	$q_{0,1}$	$q_{0,2}$	T_{low}	T_{in}	$T_{up,1}$	$T_{up,2}$	α
50	1	0.5	10	0	-5	10	0.77

FIGURE 4.8 – Numerical values of the physical parameters in the convective heat transfer problem of Section 4.3.3

In this setting, the augmented performance function $\mathcal{L}$ reads as :

$$\mathcal{L}(\hat{\theta},\hat{p},\underline{\hat{p}},\hat{T},\underline{\hat{T}},\ell) = J^*(\hat{\theta}) + \int_\Omega k_f^* \nabla \hat{T}_f \,.\, \nabla \underline{\hat{T}} + \int_\Omega k_s^* \nabla \hat{T}_s \,.\, \nabla \underline{\hat{T}} + \int_\Omega (-c_p \underline{\hat{T}} K_D^* \nabla \hat{p}) \nabla \hat{T}_f + \int_\Omega K_D^* \nabla \hat{p} \,.\, \nabla \underline{\hat{p}}\, dx + \ell\Big(\int_\Omega \hat{\theta}\, dx - \Theta\Big) \tag{4.34}$$

where, $(\hat{\theta},\hat{p},\underline{\hat{p}},\hat{T},\underline{\hat{T}}) \in L^\infty(\Omega) \times H_0^1(\Omega;\mathbb{R})^2 \times H_0^1(\Omega;\mathbb{R})^2$ are independent variables. For this example, the formulas needed for the sensitivities and the definition of the adjoint systems read : for p in direction $\phi_p \in H^1(\Omega)$,

$$\left\langle \frac{\mathcal{L}}{\partial p}, \phi_p \right\rangle = < \frac{\partial J^*}{\partial p}, \phi_p > + \int_\Omega (-c_p \underline{\hat{T}} K_D^* \nabla \phi_p) \nabla \hat{T}_f + \int_\Omega K_D^* \nabla \phi_p \,.\, \nabla \underline{\hat{p}}\, dx, \tag{4.35}$$

and for T in direction $\phi_T \in H^1(\Omega)$

$$\left\langle \frac{\mathcal{L}}{\partial T}, \phi_T \right\rangle = < \frac{\partial J^*}{\partial T}, \phi_T > + \int_\Omega k_f^* \nabla(\phi_T)_f \,.\, \nabla \underline{\hat{T}}\, dx + \int_\Omega k_s^* \nabla(\phi_T)_s \,.\, \nabla \underline{\hat{T}} + \int_\Omega (-c_p \underline{\hat{T}} K_D^* \nabla \hat{p}) \nabla(\phi_T)_f\, dx, \tag{4.36}$$

which when equation (4.35) and (4.36) vanish, are nothing more than the variational formulation associated to the adjoint-systems. The derivatives with respect $\underline{p}$ and $\underline{T}$ in directions $\phi_p \in H^1(\Omega)$ and $\phi_T \in H^1(\Omega)$ are simply the state equations, that are :

$$\left\langle \frac{\partial \mathcal{L}}{\partial \underline{p}}, \phi_p \right\rangle = \int_\Omega K_D^* \nabla \hat{p} \,.\, \nabla \phi_p \, dx, \tag{4.37}$$

and

$$\left\langle \frac{\partial \mathcal{L}}{\partial \underline{T}}, \phi_T \right\rangle = \int_\Omega k_f^* \nabla \hat{T}_f \,.\, \nabla \phi_T + \int_\Omega k_s^* \nabla \hat{T}_s \,.\, \nabla \phi_T + \int_\Omega (-c_p \phi_T K_D^* \nabla \hat{p}) \nabla \hat{T}_f \, dx, \tag{4.38}$$

which when it vanishes, is nothing more than the variational formulation associated to the state equations, i.e., (4.6)-(4.8). Finally, the partial derivative of $\mathcal{L}$ with respect to θ in direction $\bar{\theta} \in L^\infty(\Omega; \mathbb{R})$ at the stationary point $(p, \underline{p}, T, \underline{T})$ is defined by :

$$\left\langle \frac{d\mathcal{L}}{d\theta}, \bar{\theta} \right\rangle = < \frac{\partial J^*}{\partial \theta}, \bar{\theta} > + \Bigg(\int_\Omega \frac{\partial K_D^*}{\partial \theta} \nabla \hat{p} \,.\, \nabla \underline{\hat{p}} \, dx + \frac{\partial k_f^*}{\partial \theta} \nabla \hat{T}_f \,.\, \nabla \underline{\hat{T}} + \frac{\partial k_s^*}{\partial \theta} \nabla \hat{T}_s \,.\, \nabla \underline{\hat{T}} + (-c_p \underline{\hat{T}} \frac{\partial K_D^*}{\partial \theta} \nabla \hat{p}) \nabla \hat{T}_f + \ell \Bigg) \bar{\theta} \, dx \tag{4.39}$$

As in [45], we consider two possible configurations, featuring : T_{up}^1 and T_{up}^2, for the applied temperature T_{up} at the upper wall of the system. In the first case, the upper and lower wall temperatures are equal and higher than the inlet temperature : $T_{in} < T_{up} = T_{low}$, while in the second case, the upper wall temperature is lower than the inlet temperature : $T_{up} < T_{in} < T_{low}$.

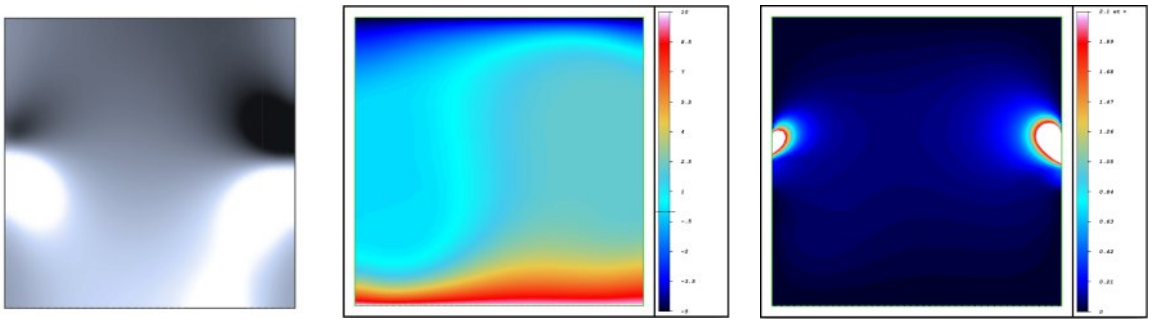

(a) Density (b) Temperature (c) Pressure

Figure 4.9 – (a) The optimal density, (b) temperature field, (c) and pressure field for the first case : $T_{up} < T_{in} < T_{low}$, in the convective heat transfer problem of Section 4.3.3

The optimized density with the corresponding temperature and pressure field at the final state, for the two configurations, i.e. : $T_{up} < T_{in} < T_{low}$ and $T_{in} < T_{up} = T_{low}$ are displayed on Figure 4.9 and Figure 4.10, respectively. The topology of the result is different to that obtained in previous literature [13] because in [13], a steady-state

Navier-Stokes model is used with different settings. Very interestingly, we retrieve the fact that the topology of the result is not far different although its contains a larger composite zone for each configuration. On Figure 4.11, we plot the convergence history for each configuration : $T_{up} < T_{in} < T_{low}$ and $T_{in} < T_{up} = T_{low}$. For this calculation, only the smooth honeycomb cell is displayed but the topology of the results remain valid for all three hexagonal cells.

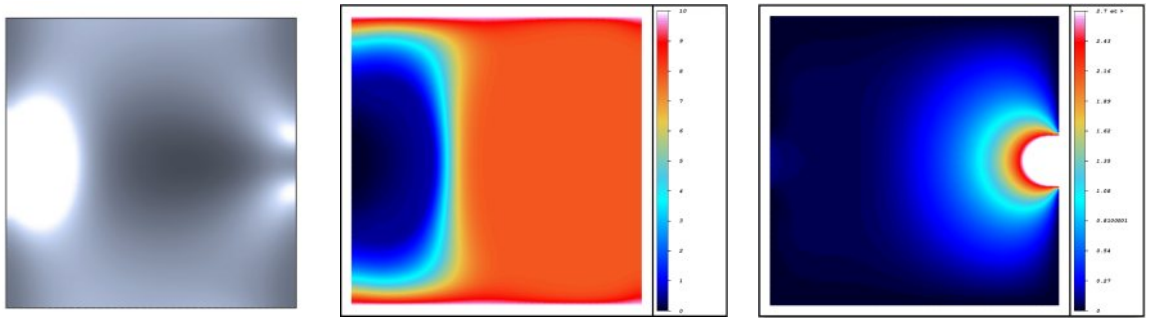

(a) Density (b) Temperature (c) Pressure

FIGURE 4.10 – (a) The optimal density, (b) temperature field (c) and pressure field, for the first case : $T_{in} < T_{up} = T_{low}$, in the convective heat transfer problem of Section 4.3.3

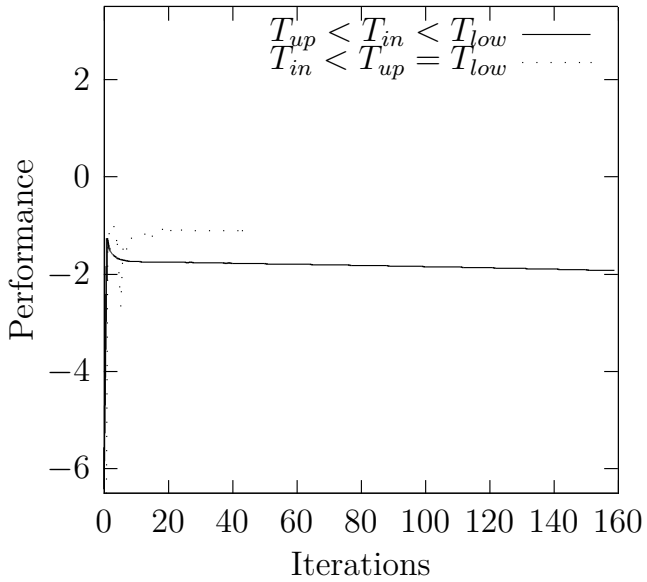

FIGURE 4.11 – Convergence history for each configuration, i.e., $T_{up} < T_{in} < T_{low}$ and $T_{in} < T_{up} = T_{low}$, in the convective heat transfer problem of Section 4.3.3

4.3.4 Thermoelastic solid with fluid-structure interaction

We finally turn to a shape optimization example in the full three-physic setting presented in Section 4.2. The structure to be found is 2×1 rectangle with cavities, fluid is flowing from the left to the right of a two-dimensional pipe, where at the center of this pipe, a solid body is attached to the boundary of a small non optimizable square ω of length ℓ. The flow with densities $q_{0,1}$ and $q_{0,2}$ are entering the pipe at the inlet and outlet, and a prescribed temperature T_{in}, while the solid body receives a thermal flux h_0 applied at the boundary $\partial\omega$ of the square. The reference temperature of the solid material is equal to the fluid inlet temperature : $T_{ext} = T_{in}$. All the other boundaries in this device are insulated from the outside : zero Neumann boundary conditions (i.e., $\frac{\partial T}{\partial n} = 0$) hold for the temperature and also zero Neumann boundary hold for pressure at upper and lower walls. The setting is reproduced on Figure 4.12 and numerical values of the parameters involved are displayed on Figure 4.13. In this case, the role of the fluid is to mitigate the temperature variations induced in the solid phase by the thermal source h_0.

Our aim is to minimize the mechanical efforts induced in the solid structure by the thermal dilation effect and the stress imposed by the fluid, subject to the volume constraint, that is :

$$\begin{aligned} \min_{\theta} J^*(\theta, u(\theta)) &= \int_\Omega \sigma(u, T_s) \ : \ \nabla u \, dx \\ &= \int_\Omega (A^* e(u) \ : \ e(u) - \alpha^*(T_s - T_{ref}) div(u)) \, dx \\ &\qquad s.t. \left\{ \tfrac{1}{|\Omega|} \textstyle\int_\Omega \theta \, dx = \Theta \right. \end{aligned} \tag{4.40}$$

where $\alpha^* = 2\alpha(\lambda^* + \mu^*)$. The objective functional $J^*(\theta, u(\theta))$ corresponds to the internal energy stored inside the structure.

remark 20. *Note that :*

$$A^* : I = 2(\lambda^* + \mu^*)I, \quad \textit{hence} \quad A^* \ : \ \alpha(T_s - T_{ref})I \ : \ \nabla u = \alpha^*(T_s - T_{ref}) div(u)$$

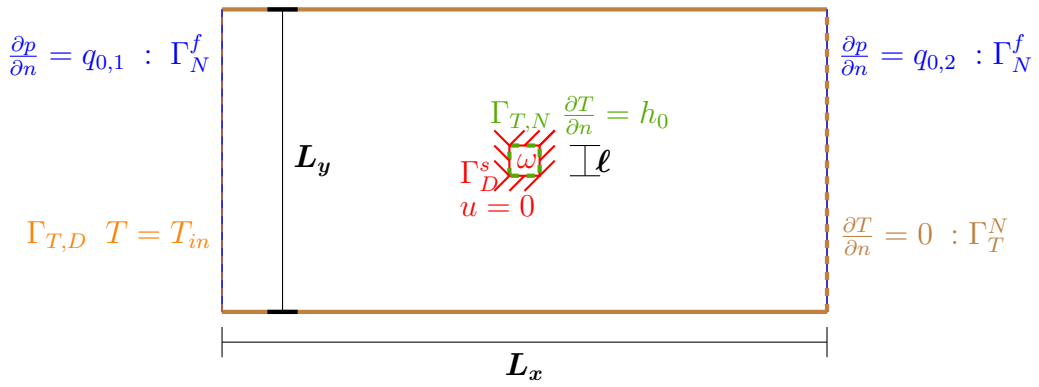

Figure 4.12 – Setting of the thermoelastic fluid-structure problem of Section 4.3.4

L_x	L_y	ℓ	c_p	$q_{0,1}$	$q_{0,2}$	T_{in}	T_{ref}	h_0	α
2	1	0.05	0.1	1.5	1/2	0	0	25	2

FIGURE 4.13 – Numerical values of the physical parameters in the thermoelastic fluid-structure problem of Section 4.3.4

We consider two optimization problems : case the optimization is subject to volume constraint first, and case with no volume constraint, second. As in [45], we took in our Biot-Darcy model, a sufficiently high value of the thermal dilation coefficient α so as to make the thermoelastic effect dominant.

Figure 4.14 shows the optimized density for the two configuration, i.e. : (a) case with volume constraint set to $\Theta = 32\%$ and (b) case with no volume constraint. For this latter, Figure 4.15 depicts the corresponding temperature and pressure field at the final state, for this calculation. For this optimization, only the smooth honeycomb is used but the topology of the results remain valid for all the three hexagonal cells.

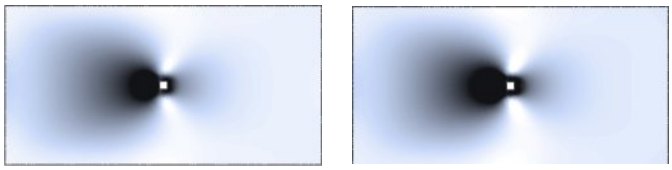

(a) (b)

FIGURE 4.14 – The optimal density for the two cases : (a) with volume constraint $\Theta = 32\%$ and (b) without volume constraint, in the thermoelastic fluid-structure problem of Section 4.3.4. For the second case, the final volume is $\Theta = 37\%$

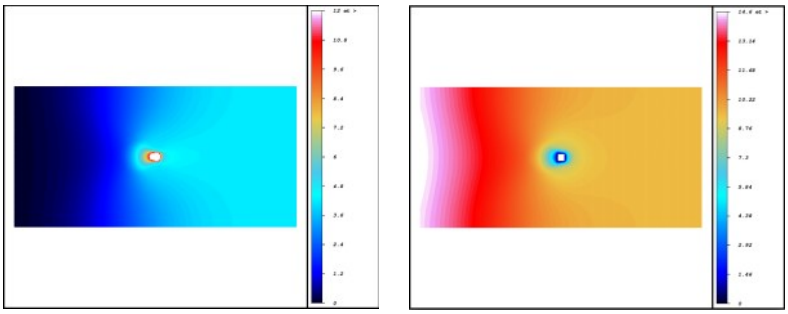

(a) Temperature (b) Pressure

FIGURE 4.15 – (a) The temperature and pressure field, in the thermoelastic fluid-structure problem of Section 4.3.4

Our numerical implementation follows algorithm 4.2.7 outlined in chapter 1 for the linear elasticity case. We rely on the open-source **FreeFem++** environment for the resolution of Finite Element problems [80] (see [29, 31] for its use in the context of structural optimization and [45, 49] for its use in the context of fluid flow optimization

4.3.5 Two dimensional counter-flow heat exchanger problem

This final 2-d example is an attempt to compute a more realistic structure for a validation. The structure to be found is a two-dimensional counter-flow exchanger of dimensions 2×2.2 with cavities. The setup is seen in Figure 4.16. and consists of a fluid flow (of density $\boldsymbol{q}_{0,1}$) entering at the lower-right wall part of the domain, with the corresponding outlet pressure $p_{0,1}$ and temperature $T_{in,1}$ at the opposite lower-left wall, while another fluid flow (of density $\boldsymbol{q}_{0,2}$) is located at the upper-left wall of the domain, with the corresponding outlet pressure p_0^2 and $T_{in,2}$ at the opposite upper-right wall. All the other boundaries in this device are insulated from the outside : zero Neumann boundary conditions (i.e., $\frac{\partial p}{\partial n} = 0$) hold for the temperature, while homogeneous Dirichlet boundary conditions are applied on the boundary of a small non optimizable rectangle ω of dimensions 2×0.2. The reference temperature of the solid material is set to $T_{ext} = 0$; the numerical values of the parameters involved are displayed on Figure 4.17

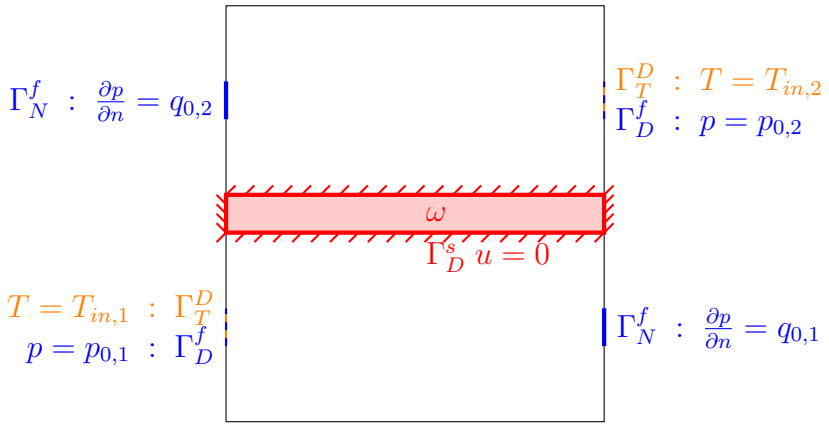

Figure 4.16 – Setting of the 2-d counter-flow exchanger problem of Section 4.3.5. The red small rectangle is non optimizable (full of material). For all other boundaries, homogeneous Neumann boundary conditions hold for the temperature.

α	c_p	$p_{0,1}$	$p_{0,2}$	$q_{0,1}$	$q_{0,2}$	$T_{in,1}$	$T_{in,2}$
1/2	10	3.47	1.06	.149	.149	5.85	10.85

Figure 4.17 – Numerical values of the physical parameters in the 2-d counter-flow exchanger problem of Section 4.3.5

Our aim is to minimize the compliance induced in the solid structure by the thermal dilation effect and the stress imposed by the fluid, subject to the volume constraint, that is :

$$\begin{aligned} \min_{\theta} J^*(\theta, u(\theta)) = \int_\Omega A^* e(u) \ : \ e(u) \, dx \\ s.t. \left\{ \tfrac{1}{|\Omega|} \textstyle\int_\Omega \theta \, dx = \Theta \right. \end{aligned} \tag{4.41}$$

where $\Theta = 32\%$. The objective functional $J^*(\theta, u(\theta))$ corresponds to the internal energy stored inside the structure.

Figure 4.18 displays the optimal density and the corresponding temperature and pressure field at final state : here, only the smooth honeycomb is displayed but the results remain valid for the hexagonal cells. Very interestingly, we retrieve the fact that the topology of the result contains a larger composite zone, formed in such manner that the force contribution from the boundaries exposed to counter-flow appears in all directions, which evidently, prior to the analysis is expected. On Figure 4.19, we plot the convergence history for this computation : smooth and relatively rapid convergence is observed.

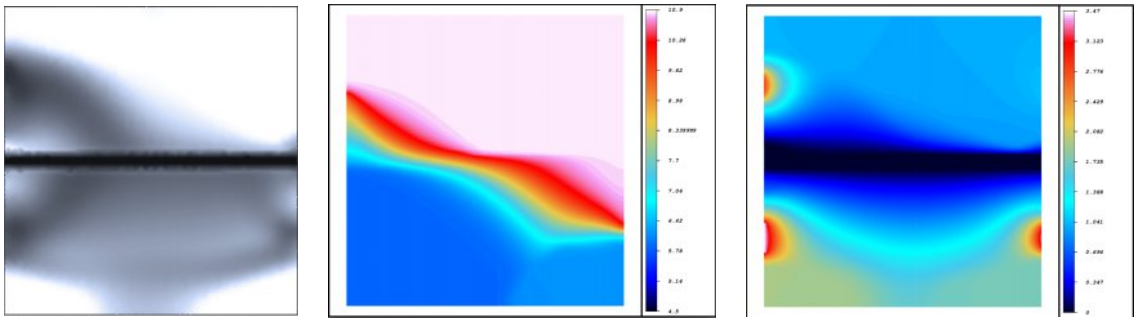

(a) Density (b) Temperature (c) Pressure

FIGURE 4.18 – (a) The optimal density, (b) temperature field, (c) and pressure field, in the 2-d counter-flow exchanger problem of Section 4.3.5

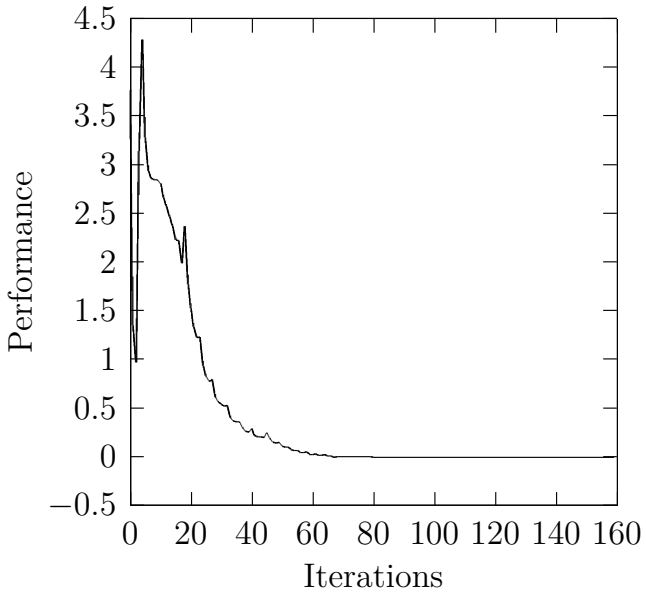

FIGURE 4.19 – Convergence history for the 2-d counter-flow exchanger problem of Section 4.3.5

4.4 Conclusions

In this study, we have demonstrated the relevance of shape and topology optimization for generating unconventional design problems involving thermal fluid-elastic interactions using the homogenization method. As thermal-fluid loads vary with the shape and location of the exposed structural boundary, a main challenge in such problems is to determine design-dependent temperature-pressure field and its design sensitivities. In the proposed method, Biot-Darcy's law and the convection-diffusion equations are used to define the design dependent pressure-temperature field by solving an associated **PDEs** using the standard finite element method. The porosity of each **FE** is related to its material density via a smooth enough function to ensure a smooth transition between void and solid elements. The Biot coefficient and the heat transfer coefficients are also related to material density, explicitly defined in the case of isotropic porous medium, where the determined pressure and temperature field are further used to find the consistent nodal loads. In the early stage of the optimization, the obtained nodal loads are spread out within the design domain and thus, may enhance exploratory characteristics of the formulation and thereby the ability of the optimization process to find well-performing solutions. Furthermore, the Biot-Darcy's parameters and the volumetric heat transfer coefficients, selected a priori to the optimization, affect the topologies of the final density. The method facilitates analytical calculation of the load sensitivities with respect to the design variables using the computationally inexpensive adjoint-variable method. This availability of load sensitivities is an important advantage over various earlier approaches to handle thermal-fluid loads in topology optimization. In addition, it is noticed that consideration of load sensitivities within the approach does alter the final density designs, and that the load sensitivities terms are particularly important when designing thermal-fluid loaded structures. Moreover, in contrast to methods that use explicit boundary tracking, the proposed Biot-Darcy method, together with our simplified heat transfer equation offer the potential for relatively straightforward extension to 3-D problems. The effectiveness and robustness of the proposed method is verified by minimizing several arbitrary objective functionals. The method allows relocation of the thermal fluid-loaded boundary during optimization, and smooth and steady convergence is observed. Extension to 3-D structures and to liquid-liquid heat exchangers problems are presented in chapter 5.

Chapitre 5

TOWARDS 3-D AND INDUSTRIAL APPLICATIONS : IMPLEMENTATION FOR A VARIETY OF NUMERICAL TEST CASES

5.1 Introduction

This chapter attempts to demonstrate the ability of multiphysics shape optimization by the homogenization method (i.e. an alternate minimization method) to deal with 3-d problems approaching industrial test cases. From the numerical point of view, the extension of the shape optimization algorithm outlined in chapter 3 to chapter 4 from 2-d to 3-d is straightforward. However, several additional ingredients are required in order achieve a satisfactory efficiency. The first section 5.2 outlines the most important features of our implementation : we provide beforehand a brief presentation of our FreeFEM implementation, and some details about various technical operations (rarely described in the literature) applied in the course of optimization iterations in order to enforce non-optimizable regions, symmetry and non-degeneracy of composite shapes.

In the next section 5.3, we present a variety of 3-d test cases solved thanks to our implementation. Five examples are considered : the first three examples are two physics application, fluid-structure interactions. The last two are true multiphysics examples ; it is concerned with thermal-fluid interaction and thermal fluid-structure interaction. These test cases are described as moderately large-scale, in the sense that the problems considered make extensive use of preconditioning in order to be run in reasonable CPU time, however their size remains rather small (our largest test case features up to 200 thousand degrees of freedom) when compared to that of industrial problems (reaching about the billion of degrees of freedom).

5.2 Implementation of 3d topology optimization of multiphysics system

In this section, we discuss several aspects of our implementation in **FreeFEM** [80] for 3-d shape and topology optimization of coupled thermal-fluid elastic systems. The first two 5.2.1 and 5.2.1 provide information regarding several choices of programming paradigms. Section 5.2.3 describes several “hidden” operations applied to shapes in the course of optimization iterations, in order to account for non-optimizable regions, symmetry, or to avoid mesh degeneracy.

5.2.1 FreeFem++ programming paradigm for shape optimization

An implementation of the alternate minimization algorithm described in chapter 4, section 4.2.7 is used for both 2-d and 3-d problems, which could in principle be used for any optimization problem set on a manifold as soon as a generic minimal set of

ingredients (below) is provided. Solve the optimization **problem** :

$$\min_{x \in \boldsymbol{V_h}} J^*(x)$$
$$\text{such that} \begin{cases} g_i(x) = 0 & \text{for all } i = 1, .., p \\ h_j(x) \leq 0 & \text{for all } j = 1, .., q \end{cases}$$

where **problem** is an instance of the class solvable. In **FreeFEM**, the finite element space :

$$V_h = \{x \mid x_0\phi_0 + x_1\phi_1 + ... + x_{M-1}\phi_{M-1} + x_M\phi_M,\ x_i \in \mathbb{R}\}$$

is easily created by : fespace IDspace(IDmesh3,<IDFE>) **;** Where **IDspace** is the name of the space (e.g. $\boldsymbol{V_h}$), **IDmesh3** is name of the associated freefem 3-d mesh, i.e. : mesh3, and **<IDFE>** is an identifier of finite element type. Due to an interpolation problem, the degree of freedom is not the vertices but four vertices in 3-d (or three vertices in 2d) which move inside $T(X) = G + .99(X - G)$ where T is tetrahedral in 3-d (or triangle in 2-d) and G is the barycenter. The most important function in **FreeFEM** is the function **problem** which instantiates an abstract class solvable. For **FreeFEM**, a problem must be given in variational form, so we need a bilinear form $a(u, v)$, a linear $l(f, v)$ and possibly a boundary condition form must be added :

- **problem P**$(u, v) = a(u, v) - l(f, v)$+(**boundary** condition) ;
- In 3-d for instance, **problem P**$(u, v) =$

$$\textbf{int3d}(\textbf{Th})(\textbf{...}) + \textbf{int2d}(\textbf{Th}, g_n)(\textbf{...}) - \textbf{int3d}(\textbf{Th})(f\ .\ v) + \textbf{on}(g_d, u = g)$$

where **Th** is a mesh of the three dimensional domain Ω and $\boldsymbol{g_d}$ and $\boldsymbol{g_n}$ are respectively the boundary labels of boundary Γ_d and Γ_n. The parameters are **FE** (Finite Element) functions real or complex, the number n of parameters is even ($n = 2 \times k$) the k first function parameters are unknown, and the k last are test functions. In order to solve problem (5.2.1), it is sufficient that the following information be provided by the supplied instance problem of a solvable **problem** object :

- $J^*, g_i, h_j : \boldsymbol{V_h} \mapsto \mathbb{R}$: objective functions and constraints ;
- $\frac{\partial \mathcal{L}}{\partial x} : \boldsymbol{V_h} \mapsto \mathbb{R}$: the partial derivative of the Lagrangian in the Céa method, regularized using an equivalent H^1-norm.
- **solve** : for a **problem P**, one needs to call : **P** ;

The above ingredients constitute all the necessary information required by any first order optimization algorithm acting on a **FE** space and in particular by the alternate minimization algorithm outlined in sect. 4.2.7. In our implementation for shape optimization, the current guess x^n is obtain by performing the projected gradient

$$x^n = P_{[0,1]}(x^{n-1} + \delta dx),$$

where the descend direction dx has to satisfy the inequality : $\left\langle \frac{\partial \mathcal{L}}{\partial x}, dx \right\rangle < 0$ and δ is an adaptive the step size. This programming paradigm allows us to implement separately 2-d and 3-d test case (which required different solvers for the physical state equations).

remark 21. *In **FreeFEM**, when you want to formulate the problem and solve it in the same time, you can use the keyword solve.*

5.2.2 FreeFEM programming

Our treatment of 2-d and 3-d shape optimization test cases with the alternate minimization method is implemented in **FreeFEM**[80] :

- firstly, the optimization routine of the previous section is conveniently implemented in **FreeFEM**, which is a very user-friendly language and which allows for easy debugging : e.g., it is possible to pause a running instance of the code at any step of the optimization process ;
- secondly, **FreeFEM** is used for all finite element related operations : i.e., the assembly of sparse matrices discretizing variational forms, integration on meshed or boundaries, the resolution of linear systems, and so on. In particular, the language is a C++ idiom which allows to run these operations very efficiently. Furthermore, the syntax of the language is very close to mathematics and it allows to easily implement the expressions of the shape derivatives presented in chapter 3. section 3.3.2 (see also [59], for detailed examples of the use of **FreeFEM** in topology optimization)

An example of a piece code that implements the variational form of chapter 4 section 4.2.5 of (4.15) :

$$\textbf{sthermic}(T,S) = \int_\Omega k_s^* \nabla T \,.\, \nabla S \; dx + \int_{\Gamma_{T,N}} hS \; ds + \int_\Omega h_{vol}^* (T - T_f) S \; dx,$$

$$\textbf{fthermic2}(T,S) = \int_\Omega k_f^* \nabla T \,.\, \nabla S \; dx + \int_{\Gamma_{T,N}} hS \; ds + \int_\Omega h_{vol}^* (T - T_s) S \; dx + \int_\Omega (-c_p S K_D^* \nabla p) \,.\, \nabla T \; dx$$

The above variational form is converted by the following "standard" **FreeFEM** source code :

```
// modèle fluide
problem darcy(pr,pv) =
int2d(Th)(KD*(dx(pr)*dx(pv)+dy(pr)*dy(pv)))+int1d(Th,fNeu)(fluxp*pv)
+on(fDir,pr=Pout);
darcy; //resolution
// modèle thermique pour le solide
problem sthermic(Ts,S) = int2d(Th)(ks*(dx(Ts)*dx(S)+dy(Ts)*dy(S)))+int2d(Th)(-hvol*Ts*S)
+int2d(Th)(hvol*Tf*S)+int1d(Th,tNeu)(fluxT*S)+int1d(Th,tNeul)(fluxTl*S)
+on(tDir,Ts=Tout);
sthermic; //resolution
// modèle thermique pour le fluide
problem fthermic(Tf,S) = int2d(Th)(kf*(dx(Tf)*dx(S)+dy(Tf)*dy(S)))
+int2d(Th)(-hvol*Tf*S)+int2d(Th)(-cp*KD*S*(dx(pr)*dx(Tf)+dy(pr)*dy(Tf)))
+int2d(Th)(hvol*Tf*S)+int1d(Th,tNeu)(fluxT*S)+int1d(Th,tNeul)(fluxTl*S)
+on(tDir,Tf=Tout);
fthermic; //resolution
```

Below is reported a typical output of a running instance of our 2-d code, which offers a clear picture of all the elementary steps of the shape optimization algorithm outlined in chapter 4, algorithm 4.2.7.

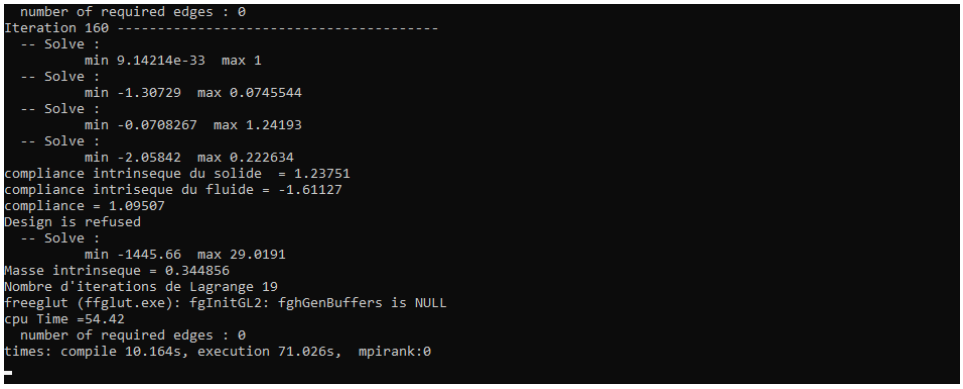

5.2.3 Processing operations : generation of initial designs, taking into account non-optimizable regions, symmetrization and regularization

We now describe a few very classical operations that are implemented in most homogenization based topology optimization codes but which are not often detailed in published works. The context and notation assumed are that of chapter 3, section 3.3 : a workspace $\Omega \subset \mathbb{R}^N$ ($N = 2$ or $N = 3$) is considered, and the goal is to optimize the material density θ of composite microstructures : allow for fine mixtures of void and material on a scale which is much smaller than the mesh used for actual computation. In physical terms admissible designs in our optimization should include periodic micro-perforations of the elastic within the design domain Ω in proportion θ and $1 - \theta$ of solid and void.

Generation of meshes and initial designs.

Our implementation relies on a fully explicit mesh discretization of the work space Ω ; this is very convenient for solving finite element problems in Ω. Note that, in practice the workspace is fill with composite on a scale which is much smaller than the mesh discretization : it is the preprocessing introduced in chapter 2, section 2.2.1, where we explicitly compute the homogenized Hooke's laws using the so-called correctors w_{ij}. It is worth mentioning that generating a mesh featuring a correct geometry respecting user-defined labels on the boundary triangles is an art by itself : there exist several software programs in order to do this (such as **Tetgen** [110] or gmsh [111]). For our purposes, we found very convenient to do it with with the help of the **Tetgen** and **FreeFem** libraries :

- firstly, a mesh **Th** for the computational domain Ω is generated. Usually, Ω is a box-like, so this step is very easily achieved for instance using a **FreeFem** command of the kind

```
// Generate a mesh for the box domain [0,2]*[0,2]*[0,1]
mesh3 Th3 = cube(20,20,10,[2*x,2*y,z]);
```

➢ secondly, the work space is fill with an initial material density θ^0 for a given composite design $A^*(\theta^0)$, satisfying a volume constraint :

$$\forall x \in \Omega \quad \theta^0(x) = \frac{\Theta}{\int_\Omega 1 \, dx}$$

➢ the obtained boundaries $\mathbf{\Gamma_h}$ of **Th** are tagged with specific labels according to the desired boundary conditions (see e.g, on Figure 5.1 below for a 2d mesh or [80] for more details)

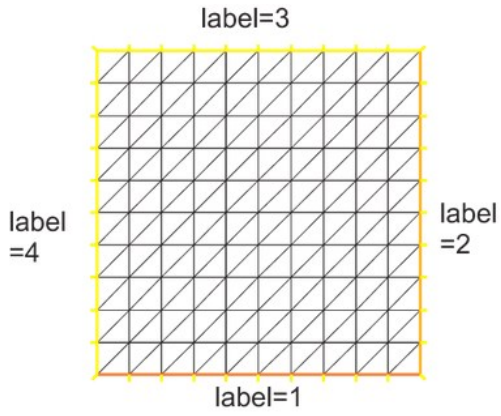

Figure 5.1 – Boundary labels of the mesh **Th = square**(10,10,[x,y]) ; (figure taken from https ://doc.freefem.org/...)

Non optimizable subdomains

It is very customary to impose that some non-optimizable subdomains ω belong either to the fluid/void phase or the solid phase. A particular attention must be given to the treatment of the material density $\theta \in L^\infty(\Omega; [0,1])$ during the optimization process : it should satisfies

$$\theta(x) = \begin{cases} 1 & \text{if } \omega \text{ is full of material,} \\ 0 & \text{if } \omega \text{ is void of material} \end{cases} \tag{5.1}$$

Note that, the constraint 5.1 is ensures also on the boundary $\partial\omega$. In principle, this requirement could be imposed as an additional constraint in the mathematical program determining the current density θ. In practice, in the context of the unconstrained minimization of an objective functional $J^*(\theta)$, an optimal density θ taking into account the non optimizable region ω is performed by penalization of θ at end of each iteration n : by imposing 1 (if ω is full of material) or 0 (if ω is void).

Enforcing symmetries of domain

Many optimization test cases feature inherent domain symmetries ; it is then expected that locally optimal designs for these problems should also be symmetric : in general, symmetry is used to reduce the size of the computational domain ; the overall optimization is performed on only one part of the domain Ω and the optimal design in Ω as whole is inferred by symmetry. However, it is sometimes desirable to perform the computations on the whole domain and performed a post-treatment to symmetrize designs ; such a post-treatment is needed because in general, numerical inaccuracies tend to quickly make optimized designs nonsymmetric when the computational mesh is not symmetric. In our implementation, the symmetry of the design θ is enforced on the displacement $u(\theta)$ on Dirichlet boundary Γ_N^s : e.g., $u_x = 0$ in 2d or $u_x = 0$ and $u_y = 0$ in 3d.

Singularities in the composite Hooke's law

Mathematically, if for instance $\theta(x) = 0$, the homogenized Hooke's law computed at each iteration turn out to be singular, an undesired feature when solving problems of linear elasticity. This singular behaviour has several sources : first, we note that the effective tensor is equal to zero when the density vanishes ; implicitly, the corresponding stress field should vanish simultaneously. This problem, which occurs in 2-d and 3-d, is easily circumvented by imposing a positive threshold on the density. In practice, the smallest admissible value of θ is fixed at $1.e-3$. Numerical experiments suggest that the choice of 10^{-3} is not important.

Preconditioning for 3-d variational problems

Passing from the 2-d implementation to its 3-d counterpart is theoretically straightforward, but it requires in practice a substantial amount of effort. Here, we do not discuss the (quite important) differences between 2-d and 3-d regarding remeshing issues ; we focus instead on the difficulties related to the resolution of variational problems by the finite element method.

The cornerstone of the passage from 2-d to 3-d lies in the assembly and inversion of large sparse linear systems obtained from the discretization of the physical equations of chapter 4, section 4.2.1 to 4.2.3. Generally, linear systems resulting from 2-d applications are sufficiently small so that a direct factorization based method can be used [80]

(e.g., solver LU, Cholesky, Crout, CG, GMRES, UMFPACK, MUMPS, SuperLU). In 3-d, it is possible to use direct methods only for very low resolution problems : indeed, modern direct solvers based on LU factorizations such as MUMPS or UMFPACK, have a complexity of order $O(N)$ (N is the number of degrees of freedom of the finite element approximation) which becomes quickly too expensive in terms of both CPU time and required memory. In our algorithm, we content ourselves to iterative methods merely based on matrix-vector products, which are relatively inexpensive to compute due to the sparsity of the matrices involved in the context of finite element problems. The most popular iterative methods are the conjugate gradient method (CG) for symmetric positive definite problems, and GMRES for the general non symmetric case.

Here, we do not treat the (quite important) preconditioning [112], which may be necessary when dealing with ill-conditioned linear systems : it may take many iterations to converge in reasonable CPU time when using iterative methods ; preconditioning helps to accelerate the resolution of such linear systems. However, the use of these techniques requires a significant amount of effort, because the whole implementation needs to be thought parallel for scalability ; this includes operations ranging from the finite element matrix assembly, the evaluation of volume or surface integrals, up to the numerical assembly and regularization of shape derivatives.

5.3 A few large-scale three dimensional multiphysics applications

In this paragraph, we go back to the three physics setting of Chapter 4, section 4.2 : a working space fill with composite built with periodic tetrakaidecahedron cell 2.2.1. The behavior of the fluid-solid interaction is described by the weakly coupled system of partial differential equations (4.6) to (4.11), which determines the pressure p, the temperature T and the elastic displacement $\boldsymbol{u}$ in the homogeneous domain Ω. The ultimate goal is to optimize the material density θ of composite microstructures built with tetrakaidecahedron cells in order to solve a relaxed unconstrained formulation of original optimal constrained design problems of the form

$$\begin{aligned} &\min_{\theta} J^*(\theta, p(\theta), T(\theta), u(\theta)) \\ \text{s.t} &\begin{cases} g_i(\theta, p(\theta), T(\theta), u(\theta)) = 0, & 1 \leq i \leq p, \\ h_j(\theta, p(\theta), T(\theta), u(\theta)) \leq 0, & 1 \leq j \leq q, \end{cases} \end{aligned} \tag{5.2}$$

where the notation convention is that introduced in 4.2.4. In the following, we treat five moderately 3-d test cases which are sub-cases of the full three physics model. The first three examples are benchmark test cases of the literature featuring only two physics : fluid-structure interaction, which is the 3-d analog of the 2-d test cases treated in chapter 3, section 3.4.3. In the last two cases, we attempt to compute industrial applications for validation : simple 3-d simulation featuring heat conduction and all three physics simultaneously.

The last two cases of interest are very classical problem of finding optimal me-

chanical stiffness while controlling the loss of pressure induced by the system on the input fluid, or the mechanical resistance of the whole structure to the elevated thermal-pressure load. This problem has been the object of much effort in the literature [40, 41, 42, 43, 44, 45] however, these contributions most often consider the original formulation where classical methods of shape optimization, based on boundary motion, level set methods and density based are used. The novelty of our work is the application of our topology optimization method, relying on homogenization method which allows to compute optimal composite designs on a scale much smaller than the mesh used for actual computation : it allows to drastically improve the performance of a candidate optimal shape.

5.3.1 Minimum compliance problem in fluid-structure interaction

Here, Our aim is to devise the least compliant structure compatible with the loads for a given weight of the structure, that is :

$$J^*(\theta) = \int_\Omega A^*(\theta)e(u) \ : \ e(u)\ dx, \tag{5.3}$$

where u is the unique solution (up to a rigid displacement field) to the coupled fluid-elastic problem, that is :

$$\begin{cases} (i) & -div(K^*\nabla p) = 0 \\ (ii) & -div(A^*e(u)) = -b\nabla p \\ (iii) & \frac{1}{|\Omega|}\int_\Omega \theta\ dx = \Theta \end{cases} \tag{5.4}$$

where Θ is the prescribed volume fraction. Note that, all mechanical equilibrium equations are satisfied under small deformation assumption. This example was previously introduced and solved in [49, 93] (in a plan setting, with a density-based method). Here, we neglect the thermal effects (namely, (4.8) is ignored), so that equation (4.11) boils down to a standard linear elasticity system with the forcing induced by the fluid.

In this setting, the augmented performance function known as the Lagrangian $\mathcal{L}$ reads as :

$$\begin{aligned} \mathcal{L}(\hat\theta, \hat u, \underline{\hat u}, \hat p, \underline{\hat p}, \ell) := J^*(\hat\theta) + \int_\Omega (A^*(\hat\theta)e(\hat u) \ : \ e(\underline{\hat u}) + b(\hat\theta)\nabla\hat p \,.\, \underline{\hat u})\ dx \\ + \int_\Omega K\nabla\hat p \,.\, \nabla\underline{\hat p}\ dx + \ell(\int_\Omega \hat\theta\ dx - \Theta), \end{aligned} \tag{5.5}$$

The formulas needed for the sensitivities and the definition of the adjoint systems read :

$$\left\langle \frac{\partial\mathcal{L}}{\partial u}(\hat\theta, \hat u, \underline{\hat u}, \hat p, \underline{\hat p}, \ell), \phi_u \right\rangle = -\int_\Omega b(\hat\theta)\nabla p \,.\, \phi_u + \int_\Omega A^*(\hat\theta)e(\phi_u) \ : \ e(\underline{\hat u})\ dx \tag{5.6}$$

and

$$\left\langle \frac{\partial\mathcal{L}}{\partial p}(\hat\theta, ...,), \phi_p \right\rangle = \int_\Omega (-b\nabla\phi_p) \,.\, u\ dx + \int_\Omega b(\hat\theta)\nabla\phi_p \,.\, \underline{\hat u}\ + \int_\Omega K\nabla\phi_p \,.\, \nabla\underline{\hat p}\ dx \tag{5.7}$$

which when it vanishes, is nothing more than the variational formulation associated to adjoint-systems. In addition, the derivatives with respect $\underline{u}$ and $\underline{p}$ in directions $\phi_u \in H^1(\Omega)^2$ and $\phi_p \in H^1(\Omega)$ are simply the state equations, that are :

$$\left\langle \frac{\partial \mathcal{L}}{\partial \underline{u}}(\hat{\theta}, \hat{u}, \underline{\hat{u}}, \hat{p}, \underline{\hat{p}}, \ell), \phi_u \right\rangle = \int_\Omega \Big(A^* e(\hat{u}) \ : \ e(\phi_u)\, dx + b \nabla \hat{p} \,.\, \phi_u \Big), \tag{5.8}$$

and

$$\left\langle \frac{\partial \mathcal{L}}{\partial \underline{p}}(\hat{\theta}, \hat{u}, \underline{\hat{u}}, \hat{p}, \underline{\hat{p}}, \ell), \phi_p \right\rangle = \int_\Omega K \nabla \hat{p} \,.\, \nabla \phi_p \, dx, \tag{5.9}$$

which when it vanishes, is nothing more than the variational formulation associated to state equations (5.4). Finally, the partial derivative of the Lagrangian $\mathcal{L}$ with respect to θ in direction $\bar{\theta} \in L^\infty(\Omega; \mathbb{R})$ at the stationary point $(u, \underline{u}, p, \underline{p})$, reads as :

$$\begin{aligned} \left\langle \frac{d\mathcal{L}}{d\theta}, \bar{\theta} \right\rangle = \int_\Omega \Bigg(& - e(u)^T \frac{\partial A^*}{\partial \theta} e(u) + \\ & \underbrace{\Big(e(u)^T \frac{\partial A^*}{\partial \theta} e(\underline{u}) + \frac{\partial K^*}{\partial \theta} \nabla p \,.\, \nabla \underline{p} + \frac{\partial b}{\partial \theta}(\theta) \nabla p \,.\, \underline{u} + \ell \Big)}_{\text{Load sensitivities}} \Bigg) \bar{\theta} \, dx \end{aligned} \tag{5.10}$$

The pressurized 3-D piston

In this first example, the structure to be found is a $1.6 \times 0.8 \times 1$ box, fixed on the left-right vertical side (i.e., $u_y = 0$) and on a small square located at the middle-bottom part of the box (i.e.,$u = 0$), on a zone of area $\frac{1}{100}$, while submitted to a pressure load $p = 1$ bar, on the upper wall. For all other regions of the boundary, homogeneous Dirichlet boundary conditions hold for the pressure, namely, $p = 0$: see Figure 5.2, for a schematic of this test case. It is desired to find a stiffest optimum design θ, which can convey the applied pressure loads on the upper wall to the lower fixed support readily.

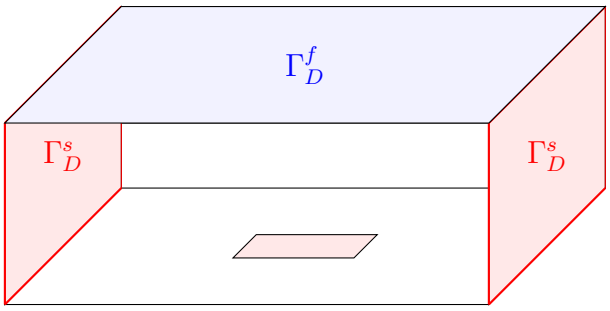

Figure 5.2 – The setting of the 3-d piston problem of Section 5.3.1 subjected to a pressure load. The small red rectangle at middle-lower region correspond to the fixed Dirichlet boundary (i.e.,$u = 0$), together with the red left and right walls of the box (i.e., $u_y = 0$). For all other regions, homogeneous Dirichlet boundary conditions hold for the pressure (i.e., $p = 0$)

The functional J^* is minimized using the alternate minimization algorithm of Section 4.2.7, under the constraint that the volume of the solid phase represent a fraction $\Theta = 23\%$ of that of the total domain $|\Omega|$. We used for all finite element operations a mesh of size 79696 tetrahedral elements and started from an initial configuration $\theta^0 = \Theta$, throughout. The algorithm produces a symmetric layout. The total **FreeFEM** running CPU time (2.60 **GHz**) for this calculation is 21819.8 seconds.

The 3-d pictures are harder to visualize. Figure 5.4 displays a sweep of iso-surface θ of composite density. In this example, the iso-surfaces are smooth and embedded into each other as θ increases.

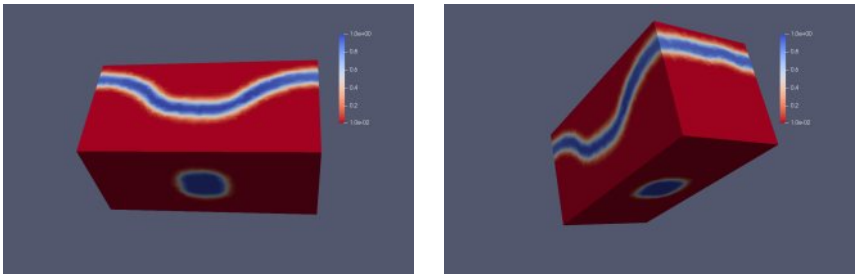

FIGURE 5.3 – Computational domain for the 3-d piston test case of Section 5.3.1 subjected to a pressure load. The red regions correspond to quasi voids and the remaining regions correspond to the optimized iso-density.

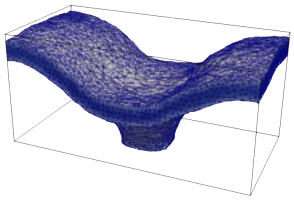

(a) $\theta \geq 40\%$

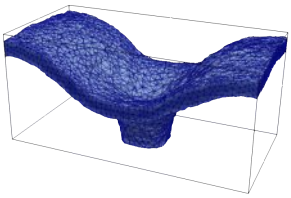

(b) $\theta \geq 70\%$

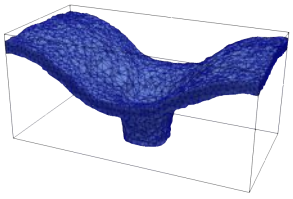

(c) $\theta \geq 75\%$

FIGURE 5.4 – Threshold of the domain according to the optimized density θ, for the 3-d pressurized piston problem of Section 5.3.1

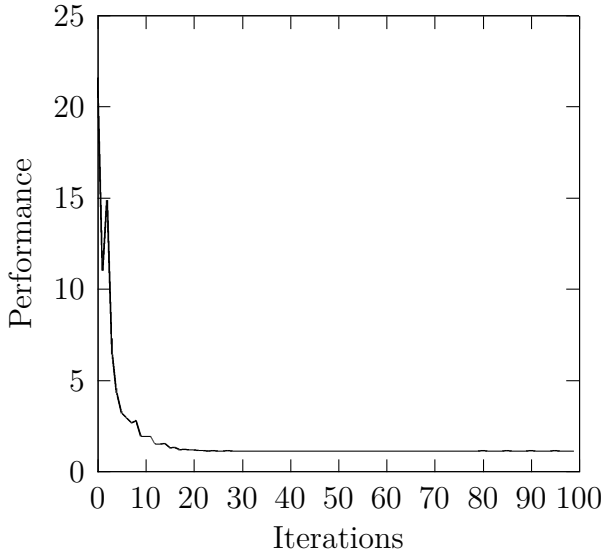

Figure 5.5 – Convergence history for the 3-d pressurized piston problem of Section 5.3.1

The pressurized 3-D arch

This example is a 3-d analog of 2-d case originally introduced and solved in [49, 89]. A structure with dimensions $0.2m \times 0.1m \times 0.1m$ is fixed at the edges of its left and right bottom on a zone of area $\frac{4}{100}$, while a pressure load $p = 1$ bar (i.e., $1 \times 10^5 Nm^{-2}$) is applied to the bottom wall Γ_D^f. For all other regions of the boundary, homogeneous Dirichlet boundary conditions hold for the pressure, namely, $p = 0$: see Figure 5.6, for a schematic of this test case. Evidently, prior to the analysis, the force contribution from the prescribed pressure appears only in z-direction. For this calculation, the volume constraint is set to $\Theta = 23\%$ of the volume $|\Omega|$.

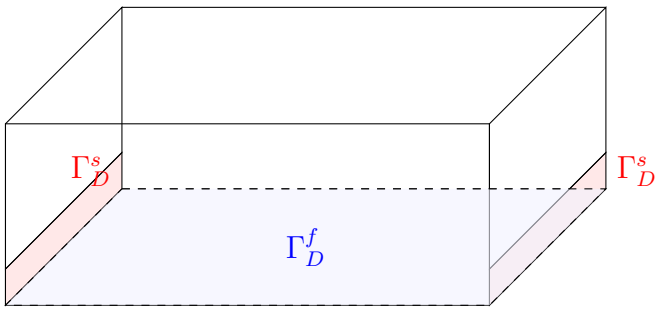

Figure 5.6 – The setting of the 3-d arch problem of Section 5.3.1 subjected to a pressure load. The left-right red rectangles at lower region correspond to the fixed Dirichlet boundary (i.e.,$u = 0$). For all other regions, homogeneous Dirichlet boundary conditions hold for the pressure (i.e., $p = 0$)

Figure 5.7 displays the optimized iso-density for the 3-d arch problem at final state.

For this later, Figure 5.8 shows the corresponding designs for a sweep of iso-surface θ of composite density. The algorithm creates a symmetric arch-like structure. On Figure 5.9, we plot the convergence history for this calculation. The total **FreeFEM** running CPU time (2.60 **GHz**) for this calculation is 20818.5 seconds.

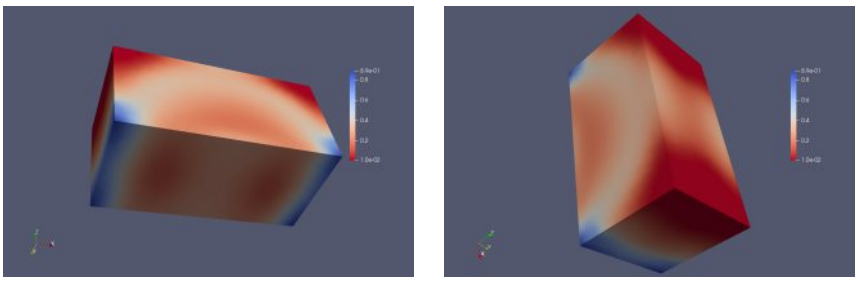

FIGURE 5.7 – Computational domain for the 3-d arch test case of Section 5.3.1 subjected to a pressure load. The red regions correspond to quasi voids and the remaining regions correspond to the optimized iso-density.

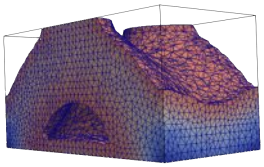

(a) $\theta \geq 10\%$

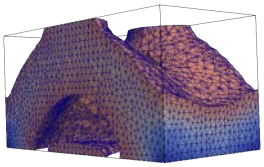

(b) $\theta \geq 20\%$

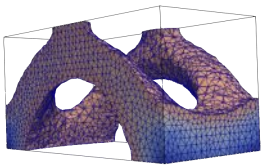

(c) $\theta \geq 30\%$

FIGURE 5.8 – Threshold of the domain according to the optimized density θ, for the 3-d pressurized piston problem of Section 5.3.1

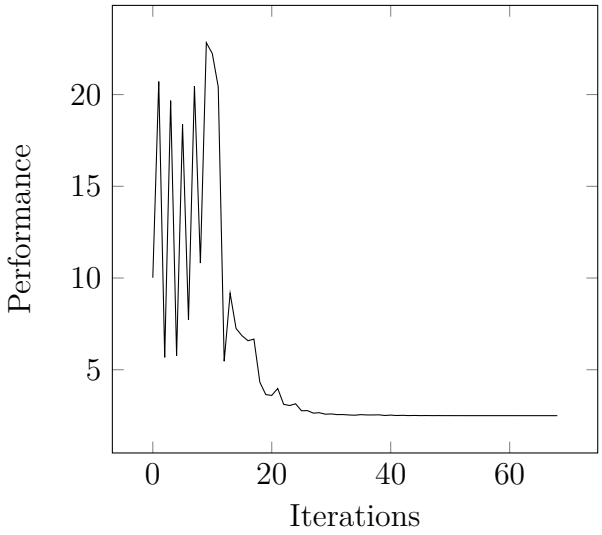

Figure 5.9 – Convergence history for the 3-d pressurized piston problem of Section 5.3.1

5.3.2 Sum of strain energy problem in fluid-structure interaction : 3-D fluid-pressure exchange

This example is an attempt to compute a more realistic structure. The structure to be found is a unit 3-d box with cavities, fixed at the four corners of its upper-lower walls, while submitted to pressure loads on the left-front walls, with corresponding fluids entering on the opposite sides : The setup is seen in Figure 5.10. All the other boundaries in this device are insulated from the outside : zero Neumann boundary conditions hold for the pressure (i.e., $\frac{\partial p}{\partial n} = 0$) ; the numerical values of the parameters involved are displayed on Figure 5.10. It is desired to find the stiffest optimum density θ, which can maximize the exchange surface between void and solid phase, while limiting the output pressure loss and convey the applied pressure loads on the upper-lower walls to the corners fixed support readily. We neglect the thermal effects (namely, (4.8) is ignored), so that equation (4.11) boils down to a standard linear elasticity system with the forcing induced by the fluid.

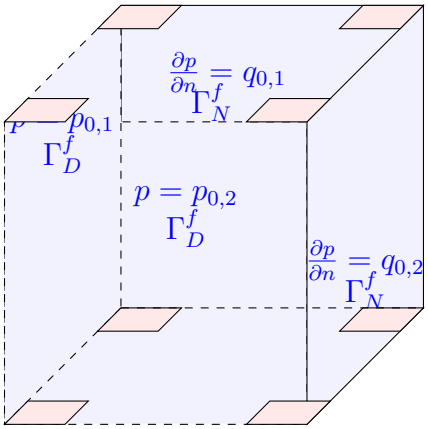

FIGURE 5.10 – The setting of the 3-d fluid-pressure exchange problem of Section 5.3.2 subjected to fluid-pressure loads. The small red rectangles at upper-lower corners correspond to the fixed Dirichlet boundary (i.e.,$u = 0$). For all other regions, homogeneous Neumann boundary conditions hold for the pressure (i.e., $\frac{\partial p}{\partial n} = 0$)

$p_{0,1}$	$p_{0,2}$	$q_{0,1}$	$q_{0,2}$
1.47	1.06	0.149	0.149

FIGURE 5.11 – Numerical values of the physical parameters in the 3-d fluidic pressure exchange problem of Section 5.3.2

Our aim is to achieve a trade-off between the minimization of the compliance imposed by the fluid and the maximization of the hydraulic strain energy, subject to the volume constraint, that is :

$$J^*(\theta, u(\theta)) = \alpha \underbrace{\left(\int_\Omega A^* e(u) \ : \ e(u) \ dx \right)}_{\text{Elastic strain energy}} + (1-\alpha) \underbrace{\left(- \int_\Omega K^* \nabla p \ . \ \nabla p \ dx \right)}_{\text{Hydraulic strain energy}}, \quad s.t. \left\{ \frac{1}{|\Omega|} \int_\Omega \theta \ dx = \Theta \right. \tag{5.11}$$

where $\alpha \in [0, 1]$ is termed as a weighting factor : it measures the relative weight given to each term in (5.11). The objective functional $J^*(\theta, u(\theta))$ corresponds to the internal energy stored inside the structure, under the constraint that the volume of the solid phase represent a fraction $\Theta = 25\%$ of that of the total domain $|\Omega|$. We used for all finite element operations a mesh of size 140656 tetrahedral elements. For this calculation $\alpha = 1/2$.

Figure 5.12 shows the optimized iso-density for the the 3-d fluidic pressure exchange problem. For this later, Figure 5.13 displays the corresponding designs for a sweep of iso-surface θ of composite density. The algorithm creates a tree-like dome. The total **FreeFEM** running CPU time (2.60 **GHz**) for this calculation is 24818.5 seconds.

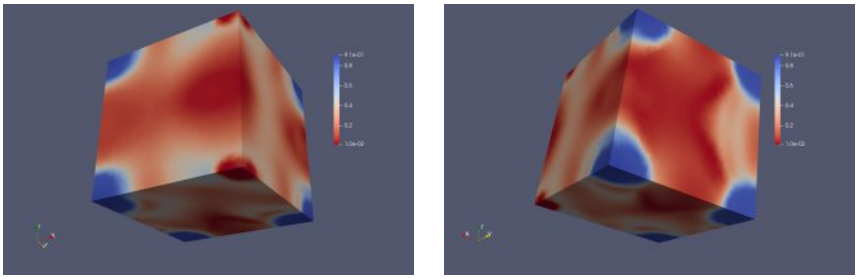

Figure 5.12 – Computational domain for the the 3-d fluidic pressure exchange problem 5.3.2 subjected to a fluid-pressure load. The red regions correspond to quasi voids and the remaining regions correspond to the optimized iso-density.

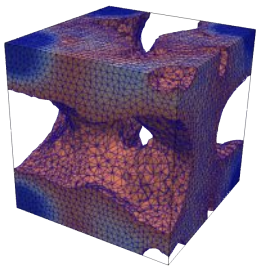

(a) $\theta \geq 10\%$

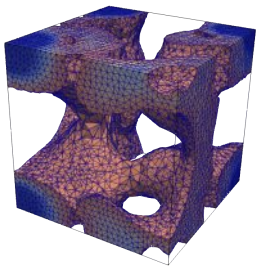

(b) $\theta \geq 20\%$

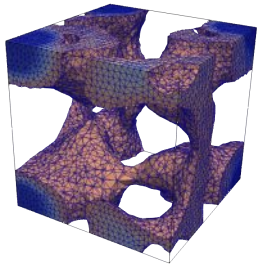

(c) $\theta \geq 28\%$

Figure 5.13 – Threshold of the domain according to the optimized density θ, for the 3-d fluid-pressure exchange of Section 5.3.2, for $\alpha = 1/2$

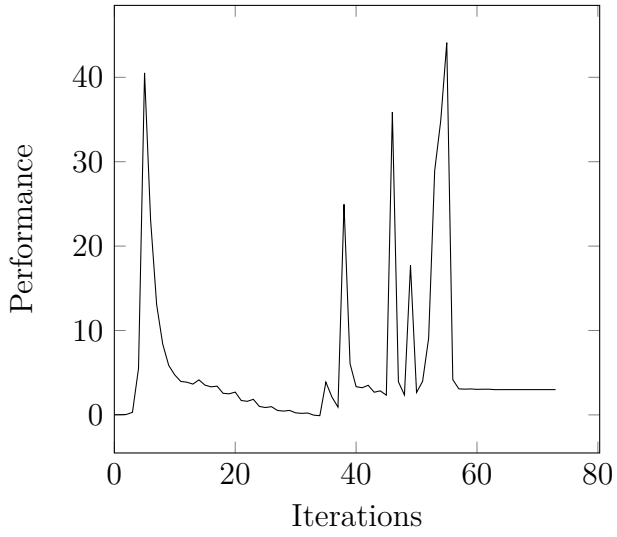

FIGURE 5.14 – Convergence history for the 3-d fluid-pressure exchange of Section 5.3.2

5.3.3 A convective heat transfer : 3-D thermal-fluid loaded L-shape

In this optimization, our aim is maximize the heat transferred by the fluid subject to an upper bound on the output pressure drop and a volume constraint :

$$\begin{aligned} &\min_{\theta} J^*(\theta, p(\theta), T(\theta)) = \int_\Omega c_p K_D^* \nabla p \,.\, \nabla T \; dx \\ &s.t. \begin{cases} \mathrm{DP}(p(\theta)) = \int_{\Gamma_D^f} p \; ds - \int_{\Gamma_N^f} p \; ds \leq \mathrm{DP}_{static} \\ \frac{1}{|\Omega|} \int_\Omega \theta \; dx = \Theta \end{cases} \end{aligned} \tag{5.12}$$

where the objective function J^* is seen as the opposite of heat transferred from the inlet to the outlet upon integration by parts :

$$\begin{aligned} \int_\Omega c_p K_D^* \nabla p \,.\, \nabla T &= \int_\Omega -c_p div(K^* \nabla p) \; T \; dx + \int_{\Gamma^f} c_p (K_D^* \nabla p \,.\, n) \; T \; ds \\ &= \int_{\Gamma_D^f} c_p (K_D^* \nabla p \,.\, n) \; T \; ds + \int_{\Gamma_N^f} q_0 c_p \; T \; ds \end{aligned}$$

where the second term is a constant depending on the inlet data. The upper bound constraint on the static pressure drop is set to $\mathrm{DP}_{static} = 11.4$.

remark 22. *This optimization problem does not take into account the poro-linear equation (4.11) : i.e., we do not solve the elastic problem, so that equation (4.8) boils down to hot fluids, cool down by cold fluids. The constraint function DP (which has a more straightforward interpretation in industrial applications and also considered in topology optimization works [13]) does a priori make sense because the pressure p belongs a priori to $H^1(\Omega)$ and has well defined trace on the boundary.*

In this test case, the structure to be found is a L-like box, i.e., a truncated cubic object, with cavities. An inlet pressure p_{in} and temperature $T_{0,1}$ is entering through

the front wall, while a corresponding flux q_0 and temperature $T_{0,2}$ come in through the left end side. The other regions of the boundary are insulated from the outside, i.e., zero normal fluxes boundary conditions hold for the temperature and pressure. The setting is reproduced on Figure 5.15 and numerical values of the parameters involved are reported in 5.16. For this calculation, the volume constraint is set to $\Theta = 34\%$ of the volume $|\Omega|$.

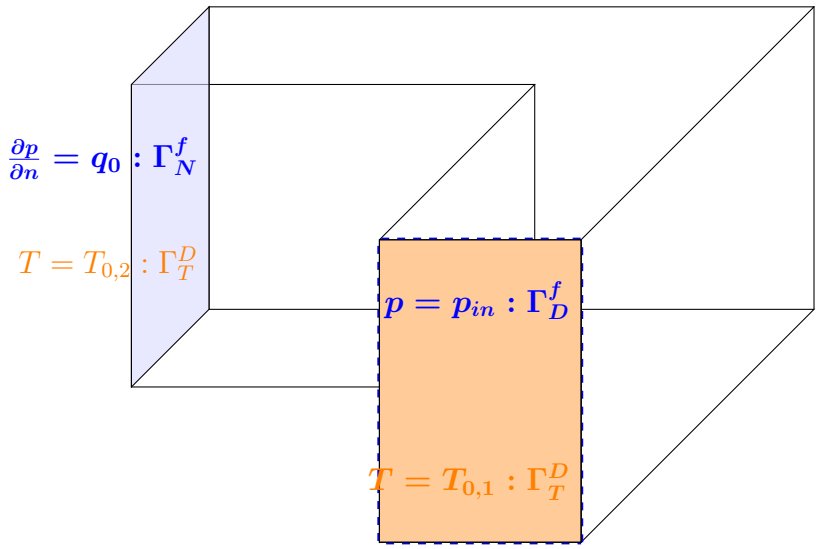

Figure 5.15 – The setting of the 3-d thermal-fluid loaded L-shape problem of Section 5.3.3 subjected to thermal fluid-pressure loads. For all other regions, homogeneous Neumann boundary conditions hold for the thermal-pressure

c_p	α	p_{in}	q_0	$T_{0,1}$	$T_{0,2}$
100	0.77	1	1/2	600.47	100.47

Figure 5.16 – Numerical values of the physical parameters in the convective heat transfer test case 5.3.3

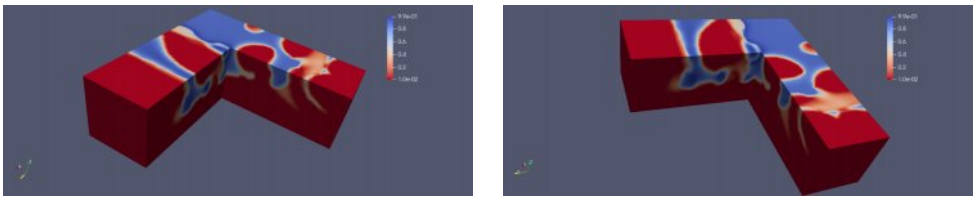

Figure 5.17 – Computational domain for the convective heat transfer test case 5.3.3. The red regions correspond to quasi voids and the remaining regions correspond to the optimized iso-density.

Figure 5.17 shows the optimized iso-density for the 3-D thermal loaded L-shape problem. For this later, Figure 5.18 displays the corresponding designs for a sweep of iso-surface θ of composite density, while Figure 5.19 depicts the iso-temperature and pressure field at the final state. The total **FreeFEM** running CPU time (2.60 **GHz**) for this calculation is 15383.8 seconds.

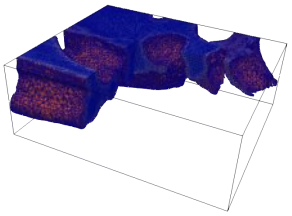

(a) $\theta \geq 10\%$

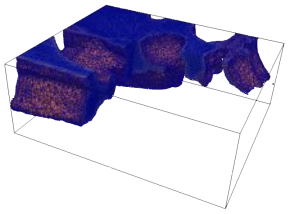

(b) $\theta \geq 20\%$

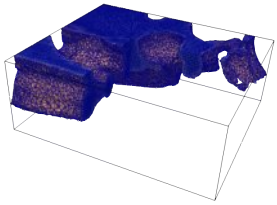

(c) $\theta \geq 30\%$

FIGURE 5.18 – Threshold of the domain according to the optimized density θ, for the 3-D thermal loaded L-shape test case 5.3.3

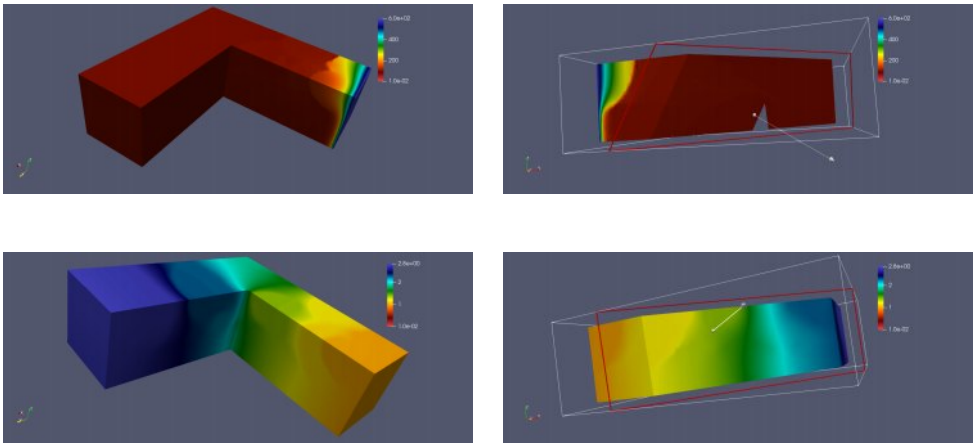

FIGURE 5.19 – (a) The corresponding iso-temperature (top) (b) and iso-pressure field (bottom) at the final state, in the convective heat transfer test case 5.3.3

5.3.4 Thermoelastic with fluid-structure interaction : 3D counter-flow heat exchanger

We finally turn to a shape optimization example in the full three-physic setting presented in Section 4.2. The structure to be found is three-dimensional counter-flow heat exchanger of dimensions $2 \times 0.5 \times 1.1$ with cavities, fixed at the boundary of a small non optimizable box of dimensions $2 \times 0.5 \times 0.1$, while submitted to thermal-pressure loads on the left-lower and right-upper walls, with the corresponding fluids entering at left-upper and right-lower walls : the setup is seen in Figure 5.20. All the other boundaries in this device are insulated from the outside : zero Neumann boundary conditions hold for the pressure and temperature. The numerical values of the parameters involved are displayed on Figure 5.21. It is desired to find the stiffest optimum density, which can convey the applied thermal fluid-pressure loads on the walls to the fixed support readily.

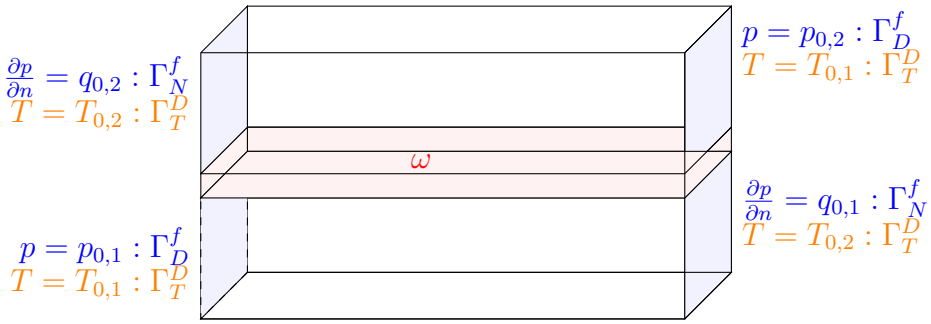

Figure 5.20 – The setting of the 3-d counter-flow heat exchanger problem of Section 5.3.4 subjected to thermal fluid-pressure loads. The small red cubic box ω is non-optimizable, i.e., full of material. For all other regions, homogeneous Neumann boundary conditions hold for the thermal-pressure

c_p	$p_{0,1}$	$p_{0,2}$	$q_{0,1}$	$q_{0,1}$	$T_{0,1}$	$T_{0,2}$	α
50	3.47	1.06	0.149	0.149	192.1	610.8	0.77

Figure 5.21 – Numerical values of the physical parameters in the 3-d counter-flow heat exchanger problem of Section 5.3.4

Our aim is to minimize the compliance of the body induced by the thermal dilation effect and the stress imposed by the fluid, subject to the volume constraint, that is :

$$J^*(\theta) = \int_\Omega A^*(\theta) e(u) \ : \ e(u) \, dx, \tag{5.13}$$

where u is the unique solution (up to a rigid displacement field) to the coupled thermal

fluid-elastic problem, that is :

$$\begin{cases} (i) & -div(K^*\nabla p) = 0, \\ (ii) & \begin{cases} -div(k_f^*\nabla T_f) + h_{vol}^*(T_s - T_f) + (-c_p K^*\nabla p)_f \nabla T_f = 0, \\ -div(k_s^*\nabla T_s) + h_{vol}^*(T_f - T_s) = 0 \end{cases} \\ (iii) & -div(\sigma(u,T)) = -b\nabla p \\ (iv) & \frac{1}{|\Omega|}\int_\Omega \theta \, dx = \Theta \end{cases} \tag{5.14}$$

The functional J^* is minimized under the constraint that the volume of the solid phase represent a fraction $\Theta = 44\%$ of that of the total domain $|\Omega|$. We used for all finite element operations a mesh of size 79696 tetrahedral elements, throughout.

Figure 5.22 shows the optimized iso-density for the 3-d counter-flow heat exchanger problem. For this later, Figure 5.23 displays the corresponding designs for a sweep of iso-surface θ of composite density, while Figure 5.24 depicts the iso-temperature and pressure field at the final state. The algorithm produces a symmetric layout. The total **FreeFEM** running CPU time (2.60 **GHz**) for this calculation is 23066.4 seconds.

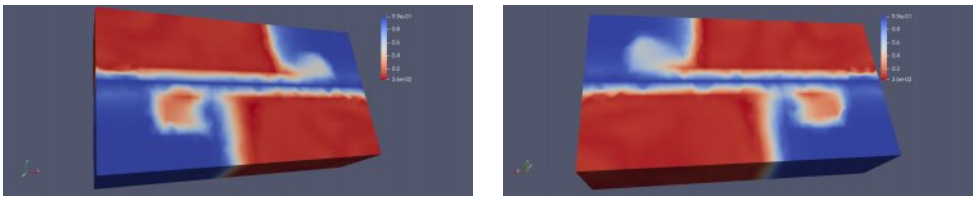

FIGURE 5.22 – Computational domain for the 3-d counter-flow heat exchanger of Section 5.3.4. The red regions correspond to quasi voids and the remaining regions correspond to the optimized iso-density.

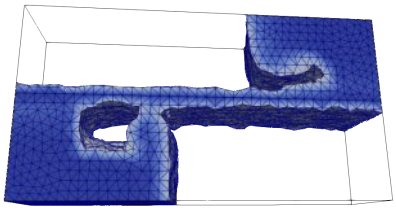

(a) $\theta \geq 30\%$

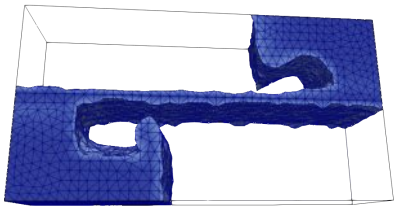

(b) $\theta \geq 40\%$

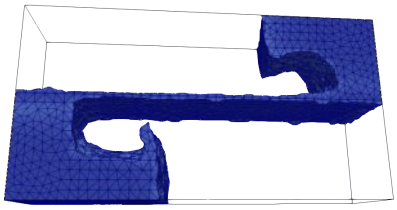

(c) $\theta \geq 50\%$

Figure 5.23 – Threshold of the domain according to the optimized density θ, for the 3-d counter-flow heat exchanger problem of Section 5.3.4.

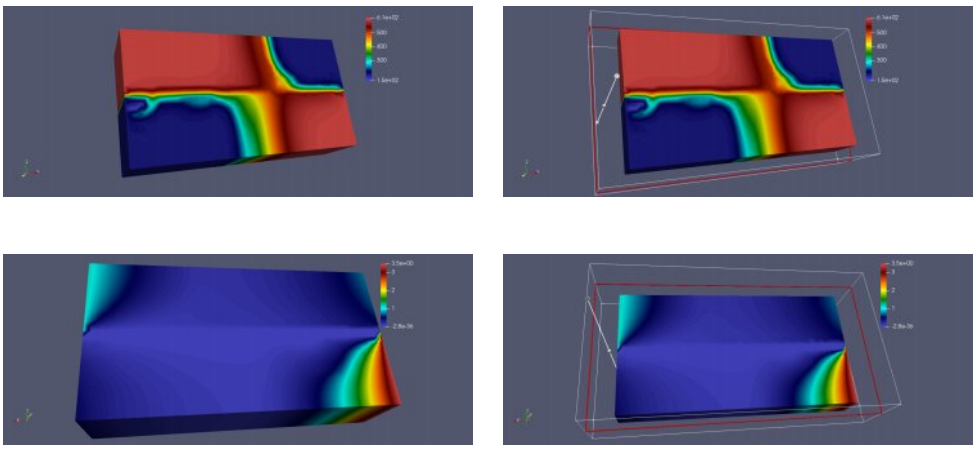

Figure 5.24 – (a) The corresponding iso-temperature (top) (b) and iso-pressure field (bottom) at the final state, in the 3-d counter-flow heat exchanger problem of Section 5.3.4

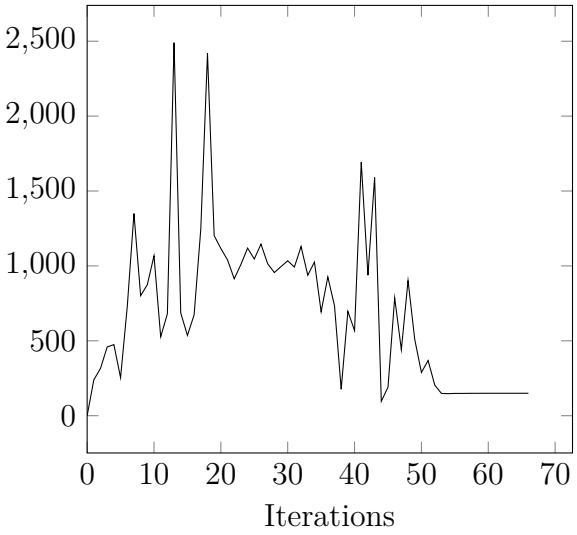

FIGURE 5.25 – Convergence history for 3-d counter-flow heat exchanger problem of Section 5.3.4

5.4 Conclusion and perspectives

In this work, a novel approach to perform topology optimization of design problems involving three physics : thermal fluid-elastic structure, was presented using the homogenization method. The approach permits use of standard finite element formulation and does not require explicit boundary description or tracking ; it allows to verify numerically the sensitivity analysis formulas presented in sect.4.2.6 for the three-physic problem. The method facilitates analytical calculation of the load sensitivities with respect to the design variables using the computationally inexpensive adjoint-variable method. This verification is based on the assumption that their correct implementation make objective functions decrease and constraints become gradually satisfied, in accordance with the expected behavior of our full alternate minimization algorithm for the relaxed optimization problem (detailed in chapter 2, section 2.3 for linear elasticity case). This availability of load sensitivities is an important advantage over various earlier approaches to handle thermal pressure loads in topology optimization.

In the proposed method, Biot-Darcy's law is used to define the design dependent pressure field by solving an associated **PDE** using the standard finite element method (see Appendix A.6). The porosity of each **FE** is related to its material density via a smooth enough function to ensure a smooth transition between void and solid phases. The Biot coefficient is also related to material density, explicitly defined in the case of isotropic porous medium, where the determined pressure field is further used to find the consistent nodal loads. Also, we took the initiative to describe and emphasize separate transport equations for each phase for the convective heat transfer equation.

In the early stage of the optimization, the obtained nodal loads are spread out within the design domain and thus, may enhance exploratory characteristics of the formulation and thereby the ability of the optimization process to find well-performing solutions.

Furthermore, the physical parameters (for the thermal and Biot-Darcy's equations), selected a priori to the optimization, affect the topologies of the final density. In addition, it is noticed that consideration of load sensitivities within the approach does alter the final density designs, and that the load sensitivities terms are particularly important when designing thermal pressure loaded structures. Moreover, in contrast to methods that use explicit boundary tracking, the proposed method offers the potential for relatively straightforward extension to 3-D problems. The effectiveness and robustness of the proposed method is verified by solving several 2-d and 3-d test cases, which in particular allow to verify numerically the sensitivity analysis formulas presented in sect.4.2.6. The method allows relocation of the thermal pressure-loaded boundary during optimization, and smooth and steady convergence is observed.

We emphasize that our proposed model is a simplified version of a genuine thermal fluid-solid coupling between the solid and fluid phases. A more accurate description of fluid-structure interaction would feature a transition regime and inertia regime [102]. However, for sake of simplicity, we opted for simplified version, which is justifiable insofar as we wish to obtain a first qualitative result of microstructure without sizing accurately as possible the system.

In addition, from a fluid point of view, it was established in the work by Feppon [13] that there exist homogenized models of higher order corrections for the Darcy model. Namely, in the low-volume fraction limit where the obstacle size is assumed to be one of the three classical regimes of the literature (i.e., Stokes, Brinkman or the Darcy equation), there exists a so called higher order homogenization which allows to yield a more accurate description of the effective physics characterizing porous media in contexts where the size of the microstructure ϵ (i.e., the periodic size which is assumed to tends to zero in the homogenized model) is not so small (see [13], for more details). Hence, this is an obvious line of research for future work.

Also, as aforementioned in chapter 2, section 2.2.2, we explicitly compute the optimization process on a subset of all possible Hooke's laws G_θ : i.e., composite periodically perforated by hexagonal cells in 2-d and tetrakaidecahedron cell in 3-d. However, restricting the analysis to periodic composites is an acceptable limitation because the set of Hooke's laws of periodic composites is dense in the set of all possible Hooke's laws reachable with composites [59] ; but restricting the set of periodic composites to regular hexagonal cells in 2-d or regular tetrakaidecahedron cell in 3-d, is clearly a loss of generality. Exploring a larger range of periodic microstructures is an obvious line of research for future work (see Appendix 5.4, for composite built with orthotropic cell).

Appendix

A.5 Composite built with orthotropic lattice materials

We provide in this appendix, composite microstructures built with orthotropic cell, in which the geometry of the corresponding periodic cell Y is orthotropic : a square cell perforated by a rectangle hole in 2d or a unit cube perforated by a cubic hole in 3d (see Figure 5.26). The interest for this kind of cell relies on the fact that, in converse to isotropic cells where the local stress of the microstructure is no stronger in particular direction, orthotropic cells are designed in order to support the stress in privileged directions : i.e., the principal directions of the stress. Indeed, orthotropic microstructures can be oriented in order to align its principal directions to the principal directions of the stress.

A.5.1 Cell design

Orthotropic cell in 2d.

The Orthotropic cell in 2d is a square perforated by a rectangle hole, parametrized by the relative linear dimensions of its rectangular hole, together with the orientation α of the cell. let $Y_\alpha(m)$ be the orthotropic cell and $m = (m_1, m_2) \in [0,1]^2$ be the relative linear dimensions of the rectangle hole. Then, m is linked to the density θ as follow :

$$\theta = 1 - m_1 m_2, \tag{5.15}$$

while the orientation α is defined by the y_1-axis of the cell with the x_1 axis of the domain Ω ; see Figure 5.26.(a), for the geometry of the periodic cell.

Orthotropic cell in 3d.

The Orthotropic cell in 3d is a unit cube perforated by cubic holes and like its 2d version this kind of cell is parametrized by the relative linear dimensions of its cubic hole $m = (m_1, m_2, m_3) \in [0,1]^3$; together with the orientation α of the cell defined by the y_1 axis with the x_1 base of the domain Ω ; see Figure 5.26.(b), for the geometry of the periodic cell.

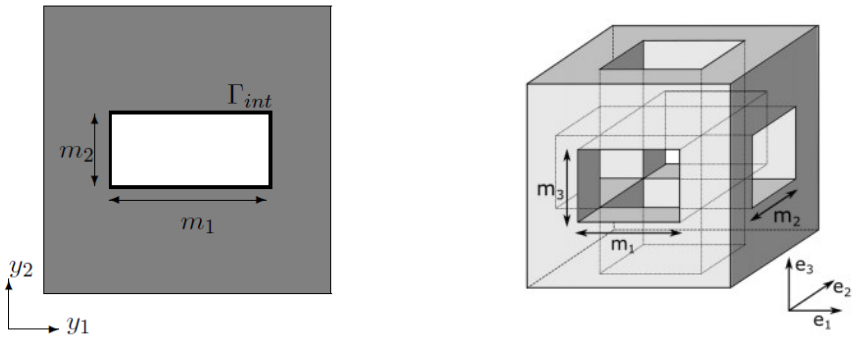

(a) 2-d orthotropic cell

(b) 3-d orthotropic cell

FIGURE 5.26 – Anisotropic cell Y

A.5.2 Homogenized Hooke's laws of the microstructures

Like in section 2.2.1, the homogenized Hooke's laws of the microstructure built with orthotropic cells is computed using the so called correctors 2.8. We emphasize that the microstructure built with orthotropic cells as well as its Hooke's laws are not very far from those of rank-2 laminates with orthogonal lamination directions, which are known to be optimal for the single-load compliance minimization problems [29]. The rank-2 laminates are intrinsically multiscale : they feature two well separated microscopic scales, and thus hard to manufacture.

Note that, periodicity of the orthotropic cell in 2d or 3d is defined by the same displacement on two opposite and parallel faces ; hence, there are two directions of periodicity for the square cell and 3 directions of periodicity for the cubic cell.

A.5.3 Sensitivity of the homogenized elasticity tensor

The sensitivity of the homogenized tensor with respect to the parameters of the orthotropic cell $Y_\alpha(m)$ will be based on the notion of shape derivative. We briefly introduce this notion for the $2d$ case but it remains valid for any dimensional $N \geq 2$.

Definition A.5.1. *Let $\theta \in W^{1,\infty}_{\#}((0,1)^2, \mathbb{R}^2)$ be a periodic Lipschitz function, with values in $\mathbb{R}^2$. The shape derivative of a function $F(Y_0)$ is defined as the Fréchet derivative in $W^{1,\infty}_{\#}$ at 0, of the application $\theta \mapsto F((Id+\theta)Y_0)$; namely :*

$$F((Id+\theta)Y_0) = F(Y_0) + < F'(Y_0), \theta > + o(\theta), \quad \textit{with} \quad \lim_{\theta \to 0} \frac{o(\theta)}{|\theta|_{W^{1,\infty}_{\#}}} = 0$$

where $F'(Y_0)$ is a continuous linear form on $W^{1,\infty}_{\#}((0,1)^2, \mathbb{R}^2)$.

Let $\mathcal{M}_2$ be the set of matrices of order 2 and $\mathcal{M}_2^s$ be the subset of all symmetric ones.

Lemma A.5.1. *The shape derivative of the homogenized coefficients A^*_{ijkl} is defined by :*

$$\begin{aligned}\Big\langle (A^*_{ijkl})', \theta \Big\rangle = &\int_{Y_0} A(e_{ij} + e(w_{ij})) \ : \ (e_{kl} + e(w_{kl}))\ div(\theta)\ dy \\ &- \int_{Y_0} A(e_{ij} + e(w_{ij})) \ :< de(w_{kl}), \theta > \ dy \\ &- \int_{Y_0} A(e_{kl} + e(w_{kl})) \ :< de(w_{ij}), \theta > \ dy\end{aligned} \tag{5.16}$$

where $de(w)$ is a linear operator from $W^{1,\infty}_{\#}((0,1)^2, \mathbb{R}^2)$ to $L^2(Y_0; \mathcal{M}^s_2)$, defined for every $w \in H^1_{\#}((0,1)^2, \mathbb{R}^2)$ by

$$\Big\langle de(w), \theta \Big\rangle = \frac{1}{2}(\nabla w \nabla \theta + (\nabla w \nabla \theta)^T)$$

Démonstration. One should refer to [113], for a complete proof : its relies on the Lagrangian method of Céa [107], which amounts to introduce a Lagrangian defined as sum of formula (3.34) and the variational formulation (3.36). Differentiating with respect to the state variable gives the adjoint system. It turns out that the problem is self-adjoint, so no adjoint appears in equation (5.16). □

A.5.4 Computation of the homogenized elasticity tensor

As in section 2.2.2, featuring isotropic cells, the set of homogenized elasticity tensors $\Big\{ A^*_\alpha(m) \mid (m, \alpha) \in L^\infty(\Omega, [0,1] \times \mathbb{R}) \Big\}$ has to be characterized. Again, the proposed strategy consists in computing the material properties for a discrete sample of parameters values and using the collected data to construct a surrogate model for the effective tensor by linear interpolation.

A.5.5 Cell orientation

The considered cells $Y_\alpha(m)$ are not isotropic, nor are theirs corresponding homogenized elasticity tensors $A^*_\alpha(m)$, which are orientation-dependent. Let $R(\alpha)$ be the fourth-order tensor defined by :

$$\forall \xi \in \mathcal{M}^s_2,\ R(\alpha)\xi = Q(\alpha)^T \xi Q(\alpha),$$

where $Q(\alpha) \in \mathcal{M}_2$ is the rotation matrix of angle α. Then, the dependency of the effective elasticity tensor $A^*_\alpha(m)$ with respect to the orientation α is explicitly defined by :

$$A^*_\alpha(m) = R(\alpha)^T A^*_0(m) R(\alpha). \tag{5.17}$$

Unlike the parameters $m = (m_1, m_2)$, the dependency on α of $A^*_\alpha(m)$ and its derivatives wrt. α are explicitly known. The computation of $A^*_\alpha(m)$ can thus be restricted to the case $\alpha = 0$. Its is noted that, the rotation of the cell by an angle π does not change its Hooke's law as $R(\pi) = -Id$; hence the optimal orientation is defined modulo π.

A.5.6 Derivatives of the homogenized elasticity tensor

In order to compute the derivative of the homogenized tensor wrt. the parameters of the cell $Y_\alpha(m)$: i.e., the relative linear dimensions of its rectangle hole $m = (m_1, m_2)$, we choose a specific deformation field θ in the shape derivative formula (A.5.1).

Let θ_1 and θ_2 be the smooth $(0,1)^2$-periodic vector fields, defined by :

$$\theta_1 = c_1\Big(sin(2\pi y_1), 0\Big)^T,\ \theta_2 = c_2\Big(0, sin(2\pi y_2)\Big)^T,$$

where $c_1 = -sin(\pi m_1)^{-1}$ and $c_2 = -sin(\pi m_2)^{-1}$ are rescaling coefficients. We emphasize that $Y_0(m_1 + \delta m_1, m_2 + \delta m_2) = (Id + \delta m_1\theta_1 + \delta m_2\theta_2)Y_0(m)$, where $(\delta m_1, \delta m_2)$ is small increment in the directions y_1 and y_2 axis, respectively. It follows that, for $i = 1, 2$,

$$\frac{\partial A_0^*(m)}{\partial m_i} = \left\langle \Big(A_0(m)\Big)', \theta_i \right\rangle \tag{5.18}$$

Thus, by applying formula (5.17), we get the sensitivity of the homogenized tensor $A_0^*(m)$ wrt. the parameters m_1 and m_2 of the periodic cell $Y_0(m)$.

A.6 Finite element formulation

This section presents the FE (Finite Element) formulation of the proposed pressure load based on Darcy's law, wherein the approach employs the standard FE method using the provided FreeFEM language [80] [1], to solve the associated boundary value problems to determine the pressure p and displacement u. Standard 2-d triangular elements with bilinear shape functions are employed to parameterize the design domain. First, in addition to the Darcy equation (3.14), the equation of state using the law of conservation of mass in view of incompressible fluid is derived. Thereafter, the consistent nodal loads are determined from the derived pressure field.

A.6.1 State equation

In view equation (3.6) t0 (3.7), we get :

$$div(K\nabla p) + Q_{drain} = 0, \quad \text{in } \Omega_\epsilon, \tag{5.19}$$

Now, for the finite element formulation, we use the Galerkin approach to seek an approximate to solution $p(x)$ such that :

$$\sum_{e=1}^{n_{elem}} \left(\int_{\Omega_e} \nabla\ .\ (K\nabla p(x))w(x)\ dV + \int_{\Omega_e} Q_{drain} w(x)\ dV \right) = 0 \tag{5.20}$$

1. FreeFEM offers a large list of finite elements, like the Lagrange, Taylor-Hood, etc., usable in the continuous and discontinuous Galerkin method framework

for every $w(x)$ constructed from the same basis functions as those employed for $p(x)$. The total number of elements is denoted n_{elem}. In the discrete setting, within each $\Omega_e|_{e=1,\dots,n_{elem}}$, we have

$$p_e = \mathbf{N}_p \mathbf{p}_e, \quad w_e = \mathbf{N}_p \mathbf{w}_e, \tag{5.21}$$

where $\mathbf{N}_p = [N_1, N_2, N_3]$ are the bilinear shape functions in a physical element and $\mathbf{p}_e = [p_1, p_2, p_3]$ is the nodal pressure. Now, with integration by parts and Green's theorem, Equation (5.20) becomes on elemental level :

$$-\int_{\Omega_e} K(\nabla w(x) \,.\, \nabla p(x))\, dV + \int_{\Omega_e} Q_{drain} w(x)\, dV = \int_{\Gamma_e} w(x) \mathbf{q}_\Gamma \,.\, \mathbf{n}_e\, dA, \tag{5.22}$$

where n_e is the boundary normal on surface Γ_e and therein, $\mathbf{q}$ changes to $\mathbf{q}_\Gamma$. In view of equation (5.19) to (5.21), equation (5.22) gives :

$$\underbrace{-\int_{\Omega_e} K \mathbf{B}_p^T \mathbf{B}_p\, dV}_{\mathbf{A}_e^h}\ \mathbf{p}_e = \underbrace{\int_{\Omega_e} b \frac{\partial e_{vol}}{\partial t} \mathbf{N}_p^T\, dV + \int_{\Gamma_e} \mathbf{N}_p^T \mathbf{q}_\Gamma \,.\, \mathbf{n}_e\, dA}_{\mathbf{f}_e}, \tag{5.23}$$

where $\mathbf{B}_p = \nabla \mathbf{N}_p$ and $\mathbf{q}_\Gamma$ is the Darcy flux through the boundary Γ_e. In global sense, i.e., after assembly, equation (5.23) is written as :

$$\mathbf{A}^h \mathbf{p} = \mathbf{f}, \tag{5.24}$$

where $\mathbf{A}^h$ is termed the global flow matrix, $\mathbf{p}$ and $\mathbf{f}$ are the global pressure vector and loading vector, respectively. We emphasize that, $\mathbf{q}_\Gamma = 0$ on the interior boundaries Γ_e of the periodic domain Ω_ϵ but not on the exterior boundary $\Gamma = \partial\Omega_\epsilon$, which is the case we have considered while solving design problems in this work. Note that,

$$\mathbf{f}_{\mathbf{s},e} = \int_{\Omega_e} b \frac{\partial e_{vol}}{\partial t} \mathbf{N}_p^T\, dV = \int_{\Omega_e} b(\nabla \,.\, \mathbf{N}_u^T)\mathbf{N}_p^T\, dV\ \frac{\partial \mathbf{u}_e^*}{\partial t} = \mathbf{H}_{\mathbf{s},e} \frac{\partial \mathbf{u}_e^*}{\partial t}, \tag{5.25}$$

is the weakly coupled term which amount to solve a linear poro-elasticity problem of solution $\mathbf{u}^*$. Thus, from Eq. (5.25), one can rewrite Eq. (5.24) as :

$$\mathbf{A}^h \mathbf{p} = \mathbf{f} = \mathbf{H}_\mathbf{s} \frac{\partial \mathbf{u}^*}{\partial t} + \mathbf{f}_h, \tag{5.26}$$

where $(\mathbf{f}_h)_{e=1,\dots,n_{elem}}$:

$$\mathbf{f}_{h,e} = \int_{\Gamma_e} \mathbf{N}_p^T \mathbf{q}_\Gamma \,.\, \mathbf{n}_e\, dA, \tag{5.27}$$

is the loading vector on an exterior boundary of $\Gamma_e \cap \Gamma_N^f$, submitted to a Neumann condition. We denote by $N_u = [N_1\mathbf{I}, N_2\mathbf{I}, N_3\mathbf{I}]$ with $\mathbf{I}$ as the identity matrix in $\mathbb{R}^2$. It is noted that $\mathbf{H}_\mathbf{s}$ is design-dependent ; the design-dependence enters through the Biot's coefficient b.

A.6.2 Pressure field to consistent nodal loads

The force resulting from the pressure field is expressed as an equivalent body force. Writing the force equilibrium equations, one obtains :

$$\begin{pmatrix} pdydz - pdydz - \frac{\partial p}{\partial x} dydz \\ pdxdz - pdxdz - \frac{\partial p}{\partial y} dxdz \\ pdxdy - pdxdy - \frac{\partial p}{\partial z} dxdy \end{pmatrix} = \begin{pmatrix} b_x \\ b_y \\ b_z \end{pmatrix} dV \tag{5.28}$$

where, b_x, b_y and b_z are the components of the body force in x, y and z directions respectively. Equation (5.28) can be rewritten as :

$$\mathbf{b}\, dV = -\nabla p\, dV \tag{5.29}$$

In the discretized setting, $-\nabla p\, dV = -\mathbf{B}_p \mathbf{p}_e$. In general, the external elemental force originating from the body force $\mathbf{b}$ and traction $\mathbf{t}$ in a FE setting, can be written as :

$$\mathbf{F}^e = -\int_{\Gamma^e} \mathbf{N}_u^T \nabla p\, dA + \int_{\Omega_e} \mathbf{N}_u^T \mathbf{b}\, dV, \tag{5.30}$$

where, $N_u = [N_1\mathbf{I}, N_2\mathbf{I}, N_3\mathbf{I}]$ with $\mathbf{I}$ as the identity matrix in $\mathbb{R}^2$ herein. Note, $\mathbf{t} = 0$ on the interior boundaries Γ_e of the periodic domain Ω_e. Thus, equation 5.30 gives the consistent nodal loads on elemental level as :

$$\mathbf{F}^e = \underbrace{-\int_{\Omega_e} b\mathbf{N}_u^T \mathbf{B}_p\, dV}_{\mathbf{H}_e} \mathbf{p}_e \tag{5.31}$$

Next, in the global form, the consistent nodal loads $\mathbf{F}$ can be evaluated from the global pressure vector $\mathbf{p}$ using the global conversion matrix $\mathbf{H}$ obtained by assembling all such $\mathbf{H}_e$ as :

$$\mathbf{F} = -\mathbf{H}\mathbf{p} \tag{5.32}$$

Note that $\mathbf{H}$ is design-dependent ; the design-dependence enters through the Biot's coefficient b, such that pressure drops to zero when $\rho_e = 1$.

Bibliographie

[1] A.G.M. Michell. "The limits of economy of material in frames structures". In : *Philosophical Magazine*. T. 8. 6. 1904, p. 589-597.

[2] J. Hadamard. "Mémoires sur le problème d'analyse relatif à l'équilibre des plaques encastrées". In : *Bulletin de la société mathématique de france, Oeuvres choisies, III, Ed. du CNRS, Paris,* 1907.

[3] O. Pironneau. "Optimum design for elliptic systems". In : *Springer-Verlag, Berlin,* 1984.

[4] J. Céa. "Optimisation, théorie et algorithmes". In : *Dunod, Paris,* 1971.

[5] D. Chenais. "On the existence of a solution in a domain identification problem". In : *J. Math. Anal. Appl.* T. 52. 1975, p. 189-289.

[6] J. Sokolowski et J.P. Zolésio. "Introduction to shape optimization. Shape sensitivity analysis". In : *Springer Series in Computational Mathematics*. T. 16. Springer, Berlin, 1992.

[7] F. Murat et L. Tartar. "Calcul des variations et homogénéisation". In : *Les lectures de l'homogénéisation : théorie et applications en physique*. Eyrolles, 1985, p. 319-369.

[8] F. Murat et L. Tartar. "Optimality conditions and homogenization". In : *Marino A. et al., editor, Nonlinear Variationnal problems. Pitman Advanced Publishing program*. Boston, 1985, p. 1-8.

[9] M.P. Bendsøe. "Methods for optimization of structural topology, shape and material". In : *Springer Verlag*. 1985.

[10] A. Cherkaev et R.V. Kohn. "Topics in the mathematical modelling of composite materials". In : *A. Cherkaev R.V. Kohn, editor, Progress in Nonlinear Differential Equations and their Applications*. T. 31. Birkhaüser, Boston, 1997.

[11] H.A. Eschenauer, V.V. Kobelev et A. Schumacher. "Bubble method for topology and shape optimization of structures". In : *Structural optimization*. T. 8. 1994, 42-–51.

[12] D. Chenais. "Why does it seem difficult to avoid homogenization type methods in order to change topology in shape optimization?" In : *M.P. Bendsøe and C.C. Mota Soares, editors, Topology design of structures*. T. 227 of Nato ASI Series. Kluwer Academic Publishers, 1993, p. 331-336.

[13] F. Feppon. "Optimisation topologique de systèmes mutiphysiques". In : *Hal, archives-ouvertes.fr*. Thèse, École Polytechnique Université Paris Saclay 2019.

[14] L. Tartar. "Estimation de coefficients homogénéisés". In : *Lecture notes in mathematics*. T. 704. Springer Verlag, Berlin, 1977, p. 364-373.

[15] M.P. Bendsøe et N. Kikuchi. “Generating optimal topologies in structural design using a homogenization method”. In : *Comp. Meth. Appl. Mech. Eng.* T. 71. 1988, p. 197-224.

[16] R.V. Kohn et G. Strang. “Optimal design and relaxation of variational problems i-ii-iii”. In : *Comm. Pure Appl. Math.* T. 39. 1986, p. 113-137, 139-182, 353-377.

[17] K. Lurie et A. Cherkaev. “Exact estimates of the conductivity of a binary mixture of isotropic materials”. In : *Proc. Royal Soc. Edinburgh.* T. 104(A). 1986, p. 3-81.

[18] W. Prager et G. Rozvany. “Optimal layout of grillages”. In : *Struct. Mech.* T. 5. 1977, p. 1-18.

[19] F. Murat. “Contre-exemples pour divers problèmes où le contrôle intervient dans les coefficients”. In : *Ann. Mat. Pura. Appl.* T. 112. 1977, p. 49-68.

[20] P. Geoffrey-Donders. “Homogenization method for topology optimization of structures built with lattice materials”. In : *PhD thesis, Université Paris Saclay (COmUE).* 2018.

[21] M.P. Bendsøe. “Optimal shape design as a material distribution problem”. In : *Struct. Opt.* T. 1. 1989, p. 193-202.

[22] K. Suzuki et N. Kikuchi. “A homogenization method for shape and topology optimization”. In : *Computer methods in applied mechanics and engineering.* T. 93. 1991, p. 291-318.

[23] K. Suzuki et N. Kikuchi. “Layout optimization using homogenization method”. In : *G.I.N Rozvany, editor, Optimization of large structural systems,I of NATO ASI Series.* T. 231. Kluwer Academic Publishers, 1993.

[24] P. Pedersen. “Optimal orientation of anisotropic materials-optimal distribution of anisotropic materials-optimal shape design with anisotropic materials-optimal design for a class of non-linear elasticity”. In : *G.I.N. Rozvany, editor, Optimization of large structural systems, volume II of Nato ASI Series.* T. 231. Kluwer Academic Publishers, 1991, p. 649-681.

[25] G. Allaire et R.V. Kohn. “Optimal design for minimum weight and compliance in plane stress using extremal microstructures”. In : *Europ. J. Mech. A/Solids.* T. 12. 6. 1993, p. 839-878.

[26] L. Gibianski et A. Cherkaev. “Microstructures of composite of extremal rigidity and exact estimates of provided energy density”. In : *Ioffe Physicotechnical Institute preprint ,in russian.* Ioffe Physicotechnical Institute ,1987.

[27] M. Avellaneda. “Optimal bounds and microgeometries for elastic two-phase composites”. In : *SIAM J. Appl. Math.* T. 47. 6. 1987, p. 1216-1228.

[28] R.V. Kohn. “Recent progress in the mathematical modelling of composites materials”. In : *G. Sih, C. Smith, and I.H. Marshall, editors, Composite material response : Constitutive relations and damage mechanism. Elsevier Applied Science, London and NewYork*. 1988, 155-177. Chap. 11.

[29] G. Allaire et al. “Shape optimization by the homogenization method”. In : *Numerische Mathematik*. T. 76. 1997, p. 27-68.

[30] K. Suzuki et N. Kikuchi. “Generalized layout optimization of shape and topology in three dimensional shell structures”. In : *Computer methods in applied mechanics and engineering*. T. 28. 1992, p. 63-80.

[31] G. Allaire, P. Geoffrey-Donders et O. Pantz. “Topology optimization of modulated and oriented periodic microstructures by the homogenization method”. In : *Computers and Mathematics with Applications, Elsevier*. T. 78. 2019, 2197-–2229.

[32] J. Céa et al. “The shape and topological optimizations connection”. In : *Computer Methods in Applied Mechanics and Engineering*. T. 188. IV WCCM, Part II (Buenos Aires, 1998), 713—726.

[33] G. Allaire, F. Jouve et A.-M. Toader. “Structural optimization using sensitivity analysis and a level-set method”. In : *Journal of Computational Physics*. T. 194. 2004, 363—393.

[34] M.Y. Wang, X. Wang et D. Guo. “A level set method for structural topology optimization”. In : *Computer methods in applied mechanics and engineering*. T. 192. 2003, 227—246.

[35] X. Duan, Y. Ma et R. Zhang. “Optimal shape control of fluid flow using variational level set method”. In : *Physics letters A*. T. 372. 2008, 1374-–1379.

[36] A. Takezawa, S. Nishiwaki et M. Kitamura. “Shape and topology optimization based on the phase field method and sensitivity analysis”. In : *Journal of Computational Physics*. T. 229. 2010, 2697—2718.

[37] I.G. Jang et B.M. Kwak. “Evolutionary topology optimization using design space adjustment based on fixed grid”. In : *International Journal for Numerical Methods in Engineering*. T. 66. 2006, 1817—1840.

[38] M.P. Bendsøe et O. Sigmund. “Topology optimization”. In : *Theory, methods and applications*. Springer-Verlag, Berlin, 2003.

[39] G. Allaire, F. Jouve et G. Michailidis. “Thickness control in structural optimization via a level set method”. In : *Structural and Multidisciplinary Optimization*. T. 53. 2016, 1349-–1382.

[40] V.B. Hammer et N. Olhoff. “Topology optimization of continuum structures subjected to pressure loading”. In : *J. Structural and Multidisciplinary Optimization*. T. 19. 2. 2000, p. 85-92.

[41] P. Papazoglou. “Topology optimization of heat exchangers”. In : *Master's thesis, TU Delft*. 2015.

[42] M. Pietropaoli, F. Montomoli et A. Gaymann. “Three-dimensional fluid topology optimization for heat transfer”. In : *J. Structural and Multidisciplinary Optimization*. T. 59. 2019, p. 801-812.

[43] D. Saltzman et al. “Design and evaluation of an additively manufactured aircraft heat exchanger”. In : *J. Applied Thermal Engineering*. T. 138. 2018, 254—263.

[44] K.R. Saviers et R. Ranjan. “Design and validation of topology optimized heat exchangers”. In : *AIAA Scitech 2019 Forum*. 2019, p. 1465.

[45] F. Feppon et al. “Shape Optimization of a Coupled Thermal Fluid-Structure Problem in a Level Set Mesh Evolution Framework”. In : *J. Boletin de la Sociedad Española de Matemática Aplicada, Springer*. T. 76. 3. 2019, p. 413-458.

[46] G. Allaire et R.V. Kohn. “Explicit optimal bounds on the elastic energy of a two-phase composite in two space dimensions”. In : *Quart. Appl. Math.* T. 51. 1993, p. 675-699.

[47] D. Hübner et al. “Optimization of the porous material described by the Biot model”. In : *International Journal of Solids and Structures*. T. 156–157. January 2019, p. 216-233.

[48] V.A. Beck et al. “Computational design of microarchitected porous electrodes for redox flow batteries”. In : *Journal of Power Sources*. T. 512. 15 November 2021.

[49] P. Kumar, J.S. Frouws et M. Langelaar. “Topology optimization of fluidic pressure-loaded structures and compliant mechanisms using the Darcy method”. In : *Structural and Multidisciplinary Optimization*. T. 61. 2020, 1637—1655.

[50] L.C Høghøj et al. “Topology optimization of two fluid heat exchangers”. In : *International Journal of Heat and Mass Transfer*. T. 163. 2020.

[51] T. Dbouk. “A review about the engineering design of optimal heat transfer systems using topology optimization”. In : *Applied Thermal Engineering*. T. 112. 2017, 841—854.

[52] S.B. Dilgen et al. “Density based topology optimization of turbulent flow heat transfer systems”. In : *Structural and Multidisciplinary Optimization*. T. 57. 2018, 1905—1918.

[53] C. Dilgen et al. “Topology optimization of turbulent flows”. In : *Computer Methods in Applied Mechanics and Engineering*. T. 331. 2018, 363—393.

[54] G.H. Yoon. “Topological layout design of electro-fluid-thermal-compliant actuator”. In : *Computer Methods in Applied Mechanics and Engineering*. T. 209—212. 2012, 28—44.

[55] J. Nocedal et S.J. Wright. “Numerical optimization”. In : *Springer Science*. T. 35. 1999.

[56] K. Svanberg. “The method of moving asymptotes|a new method for structural optimization”. In : *International Journal for Numerical Methods in Engineering*. T. 24. 1987, p. 359-373.

[57] A. Wächter et L.T. Biegler. “On the implementation of an interior-point filter line-search algorithm for large-scale nonlinear programming”. In : *Mathematical programming*. T. 106. 2006, p. 25-57.

[58] G. Allaire et R.V. Kohn. “Optimal lower bounds on the elastic energy of a composite made from two non-well-ordered isotropic materials”. In : *Quart. Appl. Math.* T. 52. 1994, p. 311-333.

[59] G. Allaire. “Shape optimization by the homogenization method”. In : *Springer Science & Business Media*. T. 146. 2002.

[60] S. SPAGNOLO. “Bulla convergenza di soluzioni di equazione paraboliche ed ellitiche”. In : *Ann. Sc. Norm. Sup. Pisa*. T. 22. 1968, p. 577-597.

[61] S. SPAGNOLO. “Convergence in energy for elliptic operators, Numerical solutions of partial differential equations III Synspade 1975”. In : *B. Hubbard ed.,Academic Press New York*. 1976.

[62] E. DE GIORGI et T. FRANZONI. “Su un tipo di convergenza variazionale”. In : *Atti Acad. Naz. Lincei Rend. Cl. Sei. Fis. Mat. Natur.* T. 58. 1975, p. 842-850.

[63] L. TARTAR. “Quelques remarques sur l’homogénéisation”. In : *Proc. of the Japan-France Seminar 1976 "Functional Analysis and Numerical Analysis"*. T. 58. Japan Society for the Promotion of Sciences,1978, p. 469-482.

[64] F. MURAT et L. TARTAR. “H-convergence”. In : *Seminaire d’Analyse Fonetionnelle et Numerique de l’Universite d’Alger, mimeographed notes*. 1978.

[65] L. Tartar. “Compensated compactness and partial differential equations”. In : *Nonlinear Analysis and Mechanics: Heriot-Watt Symposium*. T. IV. Pitman,1979, p. 136-212.

[66] Z. Hashin et S. Shtrikman. “A variational approach to the theory of the elastic behaviour of multiphase materials”. In : *Journal of the Mechanics and Physics of Solids*. T. 11. 2. 1963, p. 127-140.

[67] G.A. Francfort et F. Murat. “Homogenization and optimal bounds in linear elasticity”. In : *Archive for Rational mechanics and Analysis*. T. 94. 4. 1986, p. 307-334.

[68] R.V. Kohn et G. Milton. “Variational bounds on the effective moduli of anisotropic composites”. In : *J. Mech. Phys. Solids*. T. 36. 6. 1988, p. 597-629.

[69] W. Milton. “The theory of composites”. In : *Cambridge University Press*. May,2002.

[70] L. Tartar. “Estimations fines de coefficients homogeneises”. In : *In Ennio De Giorgi's Colloquium. Pitman Research Notes in Math.* London,1985.

[71] S. Vigdergauz. “Energy-minimizing inclusions in a planar elastic structure with macroisotropy”. In : *Structural optimization*. T. 17. 2-3. 1999, p. 104-112.

[72] G. Michailidis. “Manufacturing constraints and multi-phase shape and topology optimization via a level-set method”. In : *PhD thesis, Ecole Polytechnique X*. 2014.

[73] S. Hyun et S. Torquato. “Optimal and manufacturable two-dimensional, Kagome-like cellular solids”. In : *Journal of Materials Research*. T. 17. 1. 2002, p. 137-144.

[74] O. Sigmund. “Design of material structures using topology optimization”. In : *PhD thesis, Technical University of Denmark*. 1994.

[75] J.K. Guest et J.H. Prévost. “ Optimizing multifunctional materials: design of microstructures for maximized stiffness and fluid permeability.” In : *International Journal of Solids and Structures*. T. 43. 22–33. 2006, 7028—7047.

[76] C.Y. Lin, N. Kikuchi et J. Hollister. “A novel method for biomaterial scaffold internal architecture design to match bone elastic properties with desired porosity”. In : *Journal of biomechanics*. T. 43. 5. 2004, 623—636.

[77] O. Pantz et K. Trabelsi. “A post-treatment of the homogenization method for shape optimization”. In : *SIAM Journal on Control and Optimization*. T. 47. 3. 2008, p. 1380-1398.

[78] H. Neuber. “heory of notch stresses: principles for exact calculation of strength with reference to structural form and material”. In : *USAEC Office of Technical Information*. 1961, p. 4547.

[79] K.M.E. Abad, A.S. Khanoki et D.F. Pasini. “Fatigue design of lattice materials via computational mechanics: Application to lattices with smooth transitions in cell geometry”. In : *International Journal of Fatigue*. T. 47. 2013, 126-–136.

[80] F. Hecht. “New development in freefem++”. In : *J. Numerical Mathematics*. 2012, 251—266.

[81] M.P. Bendsøe, A. Diaz et N. Kikuchi. “Topology and generalized layout of elastic structures”. In : *M.P. BENDSØE and C.C. Mota SOARES, editors, Topology Optimization of structures*. T. 227 of Nato ASI Series. Kluwer Academic Publishers,1993, p. 159-205.

[82] C. Jog, R. Haber et Bendsoe M. “A displacement-based topology design method with self-adaptive layered materials”. In : *Topology design of structures, Nato ASI Series E, Bendsoe M., et al. (eds.)* Kluwer, Dordrecht 1993, p. 219-238.

[83] C. Jog, R. Haber et Bendsoe M. “Topology design with optimized, self-adaptative materials”. In : *Int. Journal for Numerical Methods in Engineering*. T. 37. 1994, 1323-–1350.

[84] P. Zhang et al. “Efficient design-optimization of variable-density hexagonal cellular structure by additive manufacturing: theory and validation”. In : *Journal of Manufacturing Science and Engineering*. T. 137. 2015, p. 021004.

[85] J. Du et N. Olhoff. “Topological optimization of continuum structures with design-dependent surface loading - Part I: New computational approach for 2D problems”. In : *J. Structural and Multidisciplinary Optimization*. T. 27. 3. 2004, 151—165.

[86] M.B. Fuchs et NNY. Shemesh. “Density-based topological design of structures subjected to water pressure using a parametric loading surface”. In : *J. Structural and Multidisciplinary Optimization*. T. 28. 1. 2004, 11—19.

[87] E. Lee et JRRA. Martins. “Structural topology optimization with design-dependent pressure loads”. In : *J. Computer Methods in Applied Mechanics and Engineering*. T. 40-48. 2012, p. 233-236.

[88] Zm Li, J. Yu et L. Xu. “Topology optimization of pressure structures based on regional contour tracking technology”. In : *J. Structural and Multidisciplinary Optimization*. T. 58. 2. 2018, 687—700.

[89] B. Zheng, C.J. Chang et H.C. Gea. “Topology optimization with design-dependent pressure loading”. In : *J. Structural and Multidisciplinary Optimization*. T. 38. 6. 2009, 535—543.

[90] X. Gao, K. Zhao et Y. Gu. “Topology optimization with design-dependent loads by level set approach”. In : *10th AIAA/ISSMO Multidisciplinary Analysis and Optimization Conference*. 2004, p. 4526.

[91] C. Li et al. “Distance regularized level set evolution and its application to image segmentation”. In : *J. IEEE Transactions on Image Processing*. T. 19. 12. 2010, 3243—3254.

[92] Q. Xia, M.Y. Wang et T. Shi. “Topology optimization with pressure load through a level set method”. In : *J. Computer Methods in Applied Mechanics and Engineering*. T. 283. 2015, 177-–195.

[93] B. Bourdin et A. Chambolle. “Design-dependent loads in topology optimization”. In : *ESAIM: Control, Optimisation and Calculus of Variations*. T. 9. 2003, 19—48.

[94] B.C. Chen et N. Kikuchi. "Topology optimization with design-dependent loads". In : *Finite elements in Analysis and Design*. T. 37. 1. 2001, 57-–70.

[95] H. Panganiban, G.W. Jang et T.J. Chung. "Topology optimization of pressure-actuated compliant mechanisms". In : *Finite elements in Analysis and Design*. T. 46. 3. 2010, 238-–246.

[96] O. Sigmund et P.M. Clausen. "Topology optimization using a mixed formulation: An alternative way to solve pressure load problems". In : *J. Computer Methods in Applied Mechanics and Engineering*. T. 196. 13-16. 2007, 1874-–1889.

[97] S. Vasista et L. Tong. "Design and testing of pressurized cellular planar morphing structures". In : *AIAA journal*. T. 50. 6. 2012, 1328-–1338.

[98] H. Zhang, X. Zhang et S.T. Liu. "A new boundary search scheme for topology optimization of continuum structures with design-dependent loads". In : *J. Structural and Multidisciplinary Optimization*. T. 37. 2. 2008, 121-–129.

[99] C. Wang, M. Zhao et T. Ge. "Structural topology optimization with design-dependent pressure". In : *J. Structural and Multidisciplinary Optimization*. T. 53. 5. 2016, 1005—1018.

[100] R. Picelli, A. Neofytou et H.A. Kim. "Topology optimization for design-dependent hydrostatic pressure loading via the level-set method". In : *J. Structural and Multidisciplinary Optimization*. T. 60. 4. 2019, 1313-–1326.

[101] O.C. Zienkiewicz et R.L. Taylor. "The Finite Element Method for Solid and Structural Mechanics". In : *Butterworth-heinemann*. 2005.

[102] Y. Jobic et al. "Transport properties of solid foams having circular strut cross section using pore scale numerical simulations". In : *Heat Mass Transfer*. T. 54. 2018, p. 2351-2370.

[103] G. Batchelor. "An introduction to fluid dynamics". In : *Cambridge university press*. 2000.

[104] C. Jog, R. Haber et M. Bendsoe. "A displacement-based topology design method with self-adaptive layered materials". In : *Topology design of structures, Nato ASI Series E, Bendsoe M., et al. (eds.)* 1993, p. 219-238.

[105] C. Jog, R. Haber et M. Bendsoe. "Topology design with optimized, self-adaptative materials". In : *Int. Journal for Numerical Methods in Engineering*. T. 37. 1994, 1323-–1350.

[106] F. Duval, F. Fichot et M. Quintard. "A local thermal non-equilibrium model for two-phase flows with phase-change in porous media". In : *Int J Heat Mass Transf*. T. 47. 2004, p. 613-639.

[107] J. Céa. "Conception optimale ou identification de formes, calcul rapide de la dérivée directionnelle de la fonction coût". In : *ESAIM: Mathematical Modelling and Numerical Analysis*. T. 20. 6. 1986, p. 371-402.

[108] Q. Xia et M.Y Wang. "Topology optimization of thermoelastic structures using level set method". In : *Computational Mechanics*. T. 42. 2008, 837—857.

[109] G. Marck et Y. Privat. "On some shape and topology optimization problems in conductive and convective heat transfers". In : *OPTI 2014, An International Conference on Engineering and Applied Sciences Optimization*. M. Papadrakakis, M. Karlaftis, and N. Lagaros, eds., June 2014, 1640-–1657.

[110] H. Si. "A quality tetrahedral mesh generator and three-dimensional delaunay triangulator". In : *Weierstrass Institute for Applied Analysis and Stochastic, Berlin, Germany*. T. 81. 2006.

[111] C. Geuzaine et J.F. Remacle. "Gmsh: A 3-D finite element mesh generator with built-in pre-and post-processing facilities". In : *International journal for numerical methods in engineering*. T. 79. 2009, p. 1309-1331.

[112] G.H. Golub et C.F. Van Loan. "Matriz computations". In : *The Johns Hopkins University Press, Baltimore, USA*. 1989.

[113] G. Michailidis. "Manufacturing constraints and multi-phase shape and topology optimization via a level-set method". In : *PhD thesis,Ecole Polytechnique X*. 2014.